Neutrophils on the Hunt: Migratory Strategies Employed by Neutrophils to Fulfill Their Effector Function

By

Julian A. Stopp

September, 2023

A thesis submitted to the
Graduate School
of the
Institute of Science and Technology Austria, Klosterneuburg, Austria
in partial fulfillment of the requirements
for the degree of
Doctor of Philosophy

Committee in charge:
Prof. Dr. Maximillian Jösch, Chair
Prof. Dr. Michael K. Sixt
Prof. Dr. Gasper Tkačik
Prof. Dr. Milka Sarris



The dissertation of Julian A. Stopp, titled

"**Neutrophils on the Hunt: Migratory Strategies Employed by Neutrophils to Fulfill Their Effector Function**",

is approved by:

Supervisor: Prof. Dr. Michael K. Sixt, ISTA, Klosterneuburg, Austria

Signature:_____

Committee Member: Prof. Dr. Gasper Tkačik, ISTA, Klosterneuburg, Austria

Signature:_____

Committee Member: Prof. Dr. Milka Sarris, University of Cambridge, Cambridge, UK

Signature:_____

Exam Chair: Prof. Dr. Maximillian Jösch, ISTA, Klosterneuburg, Austria

Signature:_____

Signed page is on file

© by Julian A. Stopp, September 2023
All rights reserved

ISTA Thesis, ISSN: 2663-337X
ISBN: 978-3-99078-038-1

I hereby declare that this thesis is my own work and that it does not contain other people's work without this being so stated; this thesis does not contain my previous work without this being stated, and the bibliography contains all the literature that I used in writing the dissertation.

I declare that this is a true copy of my thesis, including any final revisions, as approved by my thesis committee, and that this thesis has not been submitted for a higher degree to any other university or institution.

I certify that any republication of materials presented in this thesis has been approved by the relevant publishers and co-authors.

Signature: _____

Julian A. Stopp

September, 2023

Signed page is on file

To the cherished memory of my brother.

To the happiness of my son.

To the people I love.

To life.

Da steh' ich nun, ich armer Tor,
Und bin so klug als wie zuvor!
Heiße Magister, heiße Doktor gar,
Und ziehe schon an die zehen Jahr'
Herauf, herab und quer und krumm
Meine Schüler an der Nase herum –
Und sehe, daß wir nichts wissen können!

Johann Wolfgang von Goethe (1749 - 1832)

Source:

Goethe, Faust. Der Tragödie erster Teil, 1808. Scene: Nacht, Faust allein in seinem gotischen Zimmer

Abstract

During my Ph.D. research, I managed a series of projects, each focused on the mechanisms underlying cell migration. My work involved an in-depth examination of the complex strategies employed by neutrophils, with a specific focus on their ability to synchronize spatial-temporal cues and optimize their gradient perception. However, it is essential to acknowledge that not all projects yielded successful results, as some ideas were discontinued and are archived for future reference within this thesis.

My main project investigated how neutrophils decode spatial cues for precise navigation. Human neutrophils showcased distinct movement patterns based on source type – linear or point-like. By combining single-cell tracking in 3D environments with proxy dyes, this project linked cell behaviors to gradient changes, revealing a stronger response to semi-exponential gradients from point sources. In addition, neutrophils exhibited oscillating migration speeds, using speed minima to adjust trajectories toward sources. Experiencing continuous concentration changes, they accelerated over time and employed a "Run and Fumble" strategy, alternating between consistent runs and strategic "tumbles" for efficient navigation.

The project extended to the possibility of cells amplifying perceived gradients by enclosing their immediate surroundings, pushing attractants forward for enrichment while depleting it at the cell rear. Microfluidic devices were employed, and various experimental parameters configurations were optimized. Although significant differences in migratory efficacy were detected across pore sizes and device heights, quantifying gradient manipulation effects proved challenging.

The "Laser-Assisted Protein Adsorption by Photobleaching" (LAPAP) project was promising, as it allowed the printing of gradients. Initially successful with dendritic cells, we aimed to adapt it for neutrophils. Through extensive experimentation with multiple parameters, we attempted to trigger responses from neutrophils. Despite these efforts and collaboration, the project failed due to practical challenges and limitations.

Facing a lack of neutrophil-like cells at IST, we initially established the SCF-HoxB8 primary murine cell line. Despite their existence, their migratory behavior was largely unexplored due to potential limitations. Through differentiation protocol refinements we enhanced their migratory capabilities, though their capacity still lagged behind human neutrophils. Despite this, the improved migration potential of these cells pointed toward their utility for *in vitro* murine neutrophil migration studies.

Acknowledgments

This work, spanning multiple years, would not have been possible without the ongoing support of so many people. This Ph.D. journey was filled with discovery, challenges, and especially growth. The unwavering support, guidance, and encouragement of so many have been instrumental in shaping every step of this endeavor.

To my dedicated advisor, Michael Sixt, and committee member, Gašper Tkačik, for your invaluable expertise and mentorship throughout this pursuit, I extend my heartfelt thanks. I deeply appreciate your patience, insightful feedback, and vast knowledge, as well as the freedom you granted me to truly make this project my own. This experience has not only enriched my scientific comprehension and understanding of data analysis but has also been a wellspring of inspiration, motivating me to consistently pursue excellence. I want to especially thank Michl for his unwavering support and understanding during “my dark times” when my physical and mental health deteriorated. And to Gašper for taking the time to explain complex mathematical concepts to me, essentially teaching a quantitative illiterate the art of numbers.

I am indebted to my lab mates for their camaraderie, shared insights, and countless discussions that have fueled my curiosity and broadened my horizons – both scientific and philosophical. Your collaborative spirit and willingness to share your knowledge have been invaluable for this work. You not only enriched my Ph.D. journey scientifically but also brought an abundance of fun and inspiration that I deeply appreciate. I knew I could always entrust you with my cell culture when I was not at ISTA!

My family and friends, your unwavering belief in me, your continuous encouragement, and your tireless support have been the pillars of my strength – and therefore also of this thesis. Your presence in my life has given me the courage to overcome my personal challenges and pursue my aspirations with determination. Especially to you, Amika, your steadfast support acted as the bedrock upon which I built my journey through these challenging and rewarding times. A heartfelt shoutout goes to my friend Michele Nardin, whose wizardry in data analysis not only massively contributed to this thesis but also unveiled connections that seemed to elude my grasp.

Finally, I extend my profound gratitude to all the participants who generously contributed to this study. Your involvement and participation have paved the way for this piece of work. Each of you has played an integral role in shaping the outcome of this work, especially Christoph Sommer from the imaging facility, without whom my data would still be “trapped” within the microscope images.

I acknowledge and appreciate the financial support for this project from the European Union's Horizon 2020 research and innovation programme under the Marie Skłodowska-Curie Grant Agreement No. 665385.

About the Author

Julian completed his Bachelor's in "Pharmaceutical Biotechnology" at the University of Applied Sciences in Biberach, which was a joint study program with the pharmaceutical company Boehringer Ingelheim. His passion for immunology and infectious diseases subsequently led him to pursue a master's degree in "Molecular Biosciences – Major Infectious Diseases" at the University of Heidelberg. Throughout his studies, Julian completed multiple internships and worked in seven different research facilities in Germany and Finland, focusing on optimizing biotechnological processes, immunology, virology, and parasitology.

Julian joined IST Austria in September 2016 as a Ph.D. student, becoming part of Michael Sixt's group in 2017. His Ph.D. work primarily revolved around understanding how neutrophils integrate chemotactic signals in a spatiotemporal manner to locate their targets. During his Ph.D., Julian transitioned from a wet lab scientist to a more data science-driven approach. He actively participated in workshops where he presented his work and was accepted into the "Expert Internship" program of the Ludwig Boltzmann Society, allowing him to work in a Data Science department in a pharmaceutical company for two months.

Throughout his academic life, he actively participated in various professional societies, including the "German Society for Immunology", the "German Biotechnological Student Society", and the "Austrian Society for Molecular Biosciences and Biotechnology", organizing and attending workshops and meetings. Additionally, since 2017, Julian has held the position of treasurer at the Graduate School Association at IST Austria. Julian received multiple grants and prizes for his academic and scientific achievements, including the Bruno Frey Scholarship, the Prize of Boehringer Ingelheim Pharma KG for an excellent bachelor's thesis, the MINT Excellence Grant in the category "Science Excellence", and the competitive DKFZ fellowship.

In addition to his research, Julian engaged in various outreach activities at IST Austria, such as the "Zoom a Scientist" initiative, where he was answering scientific questions from high school students, and the "Open Campus Day", where he was explaining the research conducted in the Sixt lab to interested citizens.

List of publications

a) Published publications at ISTA:

Sitarska E., Almeida S.D., Beckwith M. S., **Stopp J.**, Schwab Y., Sixt M., Kreshuk A., Erzberger A-. Diz-Munoz A., "*Sensing their plasma membrane curvature allows migrating cells to circumvent obstacles*". Nature Communications (in print)

Alanko J., Ucar MC, Canigova N., **Stopp J.**, Schwarz J., Merrin J., Hannezo E., Sixt M.; "*CCR7 acts as both a sensor and a sink for CCL19 to coordinate collective leukocyte migration*". Science Immunology (2023)

Stopp J., Sixt M.; "*Plan your trip before you leave: The neutrophils' search-and-run journey*". Journal of Cell Biology Spotlight (2022)

Reversat A., Gärtner F., Merrin J., **Stopp J.**, Tasciyan S., Aguilera J., de Vries I., Hauschild R., Hons. M., Piel M., Callan-Jones A., Voituriez R., Sixt M., "*Cellular locomotion using environmental topography*". Nature (2020)

Renkawitz J., Kopf A., **Stopp J.**, de Vries I., Driscoll M., Merrin J., Hauschild R., Welf E., Danuser G., Fiolka R.; "*Nuclear Positioning Facilitates Amoeboid Migration Along the Path of Least Resistance*". Nature (2019)

b) Published publications before ISTA:

Stopp J.*, Balta E., Castelletti L., Kirchgessner H., Samstag Y., Wabnitz GH. "*Qualitative and quantitative analysis of PMN/T-cell interactions by InFlow and super-resolution microscopy*". Methods (2017); *Co-Author

A manuscript with the working title "Migratory Strategies Employed by Neutrophils to Fulfill Their Effector Function" is currently in preparation, encompassing the findings presented in chapter 2 of this thesis.

Table of Contents

Abstract i
Acknowledgments ii
About the Author iv
List of publications v
Table of Contents vi
List of Figures ix
List of Tables x
List of Symbols/Abbreviations xi
1 General Introduction 1
1.1 The Immune System 1
1.1.1 Neutrophils – The First Line of Active Defense 1
1.2 (Directional-) Cell Migration 2
1.2.1 Forms of Cell Migration and its Regulation 2
1.2.1.1 Migratory Strategies 3
1.2.1.2 Directional Guidance Mechanisms 4
1.2.2 Physiological Gradients 5
1.2.3 The Cytoskeleton 6
1.2.3.1 Components of the Cytoskeleton 6
1.2.3.2 The Cytoskeleton During Cell Migration 7
1.2.3.3 Cell Polarity 7
1.2.4 Receptors and Their Regulation 8
1.2.5 Spatial and Temporal Sensing 9
1.2.5.1 Migratory Memory 11
1.2.6 Current Models of Directed Cell Migration 12
1.3 Directional Cell Migration of Neutrophils 13
1.3.1 Chemotaxis of Neutrophils is Essential for an Effective and Guided Early Immune Response 13
1.3.2 Neutrophils Respond to Multiple Divergent Attractants for Guidance 13
1.3.3 Sequential Attractant Sensing is Guiding Neutrophils Toward Their Prey 14
1.4 Thesis Aims 16
1.4.1 The Missing Links 16
1.4.2 Aim 1 – Gradient Effects on Cell Trajectories: Cyclical Behavior and Memory Utilization 17
1.4.3 Aim 2 – Local Geometry and Cell Count Influence Gradient-Induced Persistence and Directionality in Cell Migration 17
2 Run and Fumble – What Eukaryotes Learnt From Bacteria 18
2.1 Summary 18

2.2 Introduction 18
2.3 Results 19
2.3.1 Establishment of Sixt Neutrophils and how They Differ From Dendritic Cells 19
2.3.2 Effect of Point and Line Sources on Persistence and Migratory Efficiency 20
2.3.3 The Potential Role of Desensitization 23
2.3.4 Interventions on Migratory Persistence 25
2.3.5 Differences in Gradient Dynamics Between Point and Line Sources 27
2.3.6 Migratory Speed Minima and how Cells Utilize Them for Informed Trajectory Adjustments 31
2.3.7 Influence of Experienced Gradients on Trajectory Readjustments around Speed Minima 33
2.3.8 Speed and Acceleration Differences Between Gradients und Uniform Concentrations 36
2.4 Discussion 39
3 Make Your Body Count – How Local Environment can Help Neutrophils Shape the Local Gradient 47
3.1 Summary 47
3.2 Introduction 47
3.3 Results 48
3.3.1 Device and Experimental Design 48
3.3.2 Influence of Pore Size and Device Height on Efficiency of Maze Solving 50
3.3.3 Linking Maze Solving Efficiency With Cell Derived Gradient Manipulation 54
3.4 Discussion 57
4 Additional Work 63
4.1 Own Projects 63
4.1.1 To Light the way – Use of Laser-Assisted Protein Adsorption by Photobleaching to Print Gradients for Neutrophils 63
4.1.1.1 Summary 63
4.1.1.2 Introduction 63
4.1.1.3 Results 66
4.1.1.3.1 Chemotactic Potential of LAPAP Attractants 66
4.1.1.3.2 Protocol Adjustment Screening for Neutrophils 66
4.1.1.4 Discussion 70
4.1.2 To Make Them Move – Chemotaxis in Immortalized SCF-HoxB8 Neutrophils 73
4.1.2.1 Summary 73
4.1.2.2 Introduction 73
4.1.2.3 Results 74

4.1.2.3.1 Generation and Differentiation Efficiency and Handling 74
4.1.2.3.2 Migratory capabilities 75
4.1.2.4 Discussion 77
4.1.3 Discontinued Projects and Negative Results 80
4.2 Collaborations 84
4.2.1 CCR7 acts as both a sensor and a sink for CCL19 to coordinate collective leukocyte migration 84
4.2.2 Sensing their plasma membrane curvature allows migrating cells to circumvent obstacles 86
4.2.3 Plan your trip before you leave: The neutrophils' search-and-run journey 88
4.2.4 Cellular locomotion using environmental topography 89
4.2.5 Nuclear Positioning Facilitates Amoeboid Migration Along the Path of Least Resistance 91
5 Materials and Methods 93
5.1 Cell Culture 93
5.2 Flow Cytometry 94
5.3 3D Collagen Migration Assay 94
5.4 Under Agarose Assay 95
5.5 Microfluidics 95
5.6 Laser-Assisted Adsorption by Photobleaching (LAPAP) 96
5.7 Imaging and Microscopy 97
5.8 Image and Data Analysis 97
5.9 Statistics and Data Visualization 102
6 References 103
7 Appendix 111
7.1 Collaboration References 111
7.1.1 Sensing their plasma membrane curvature allows migrating cells to circumvent obstacles 112
7.1.2 CCR7 acts as both a sensor and a sink for CCL19 to coordinate collective leukocyte migration 138
7.1.3 Plan your trip before you leave: The neutrophils' search-and-run journey 162
7.1.4 Cellular locomotion using environmental topography 164
7.1.5 Nuclear Positioning Facilitates Amoeboid Migration Along the Path of Least Resistance 182

List of Figures

Figure 1: Modes and mechanisms of cancer cell migration. 3
Figure 2: Common types of directed cell migration. 4
Figure 3: Surface molecules and receptors on neutrophils. 14
Figure 4: Neutrophil chemotaxis toward a *Staphylococcus aureus* cell. 16
Figure 5: Point sources outcompete line sources in fMLF chemotaxis. 21
Figure 6: Desensitization and chemoattractant titration. 23
Figure 7: Visualization of (maximal-)gradient experiences of cells during chemotaxis via fluorescence proxy values. 28
Figure 8: Speed oscillations and their influence on angle changes. 30
Figure 9: Neutrophils employ speed extrema to adjust their angle changes. 34
Figure 10: Speed differences over time for gradient fields and uniform concentrations. 37
Figure 11: Model of the run and fumble cycle. 44
Figure 12: Theoretical impact of cell migration and local geometric environment on local gradients. 48
Figure 13: Microfluidic designs and experimental setup to study local environment effects on gradients. 49
Figure 14: Pore size and device height effects on maze solving efficiency of cells. . 51
Figure 15: Influence of migrating cells on gradients within microfluidic devices and subsequent measurement challenges. 55
Figure 16: LAPAP methodology and proof of concept. 64
Figure 17: LAPAP attractants and their chemotactic potential on PLB-985 cells. 66
Figure 18: LAPAP protocol adjustments for neutrophil migration. 67
Figure 19: LAPAP conceptual problems and potential solution. 71
Figure 20: Optimization of differentiation efficiency and handling of immortalized SCF-HoxB8 neutrophils. 75
Figure 21: Migratory capabilities of differentiated SCF-HoxB8 cells. 77
Figure 22: Dendritic cells migrate persistently and CCR7 dependent also in uniform CCL19 field. 85
Figure 23: Loss of the curvature-sensing protein Snx33 impacts adaptive motility. . 87
Figure 24: Model for neutrophil search-and-run strategy *in vivo*. 88
Figure 25: Force transmission of PLB-985 in varying microfluidic geometries. 90
Figure 26: Nuclear positioning enables cells to take the path of least resistance. ... 92

List of Tables

Table 1: A compilation of various methodological interventions to improve the migratory persistence of cells in 3D collagen assays. 25
Table 2: Migratory persistence of dPLB-985, dHL-60 and neutrophils cells in different assays. 47
Table 3: LAPAP protocol adjustment parameters. 69

List of Symbols/Abbreviations

C5a:	Complement factor 5a
CCL19:	Chemokine (C-C motif) ligand 19
CCR7	Chemokine receptor 7
Cdc42:	Cell division control protein 42
CI:	Chemotaxis index
DC:	Dendritic cells
dHL-60:	Differentiated HL-60 (human leukemia)
DMF:	Dimethylformamide
DMSO:	Dimethyl sulfoxide
DNA:	Deoxyribonucleic acid
dPLB:	Differentiated PLB-985 (promyelocytic leukemia blast)
ECM:	Extracellular matrix
EDTA:	Ethylenediaminetetraacetic acid
EtOH:	Ethanol
FITC:	Fluorescein isothiocyanate
fMIFL:	fMet-Ile-Phe-Leu
fMIVIL:	fMet-Ile-Val-Ile-Leu
fMLF (fMLP):	N-formyl-met-leu-phe (*fMLP is a misnomer*)
fNLFNTK:	N-formyl-nle-leu-phe-nle-tyr-lys
FPR:	Formyl peptide receptors
G-CSF:	Granulocyte-colony stimulating factor
GM-CSF:	Granulocyte macrophage-colony stimulating factor
GPCR:	G protein-coupled receptors
HoxB8:	Homeobox B8
IL-8:	Interleukin-8
INF-γ:	Interferon-gamma
IQR:	Interquartile range
KO:	Knockout
LAPAP:	Laser-Assisted Protein Adsorption by Photobleaching
LEGI:	Local Excitation, Global Inhibition
LPS:	Lipopolysaccharide
LTB4:	Leukotriene B4
NET:	Neutrophil extracellular trap

NK-cell:	Natural killer cell
PAMP:	pathogen-associated molecular patterns
PDMS:	Polydimethylsiloxane
PEG:	Polyethylene Glycol
PTEN:	Phosphatase and tensin homolog
PVA:	Polyvinyl alcohol
ROS:	Reactive Oxygen Species
SCF:	Stem cell factor
SEM:	Standard error of the mean
T cells:	Thymus cells
TLR:	Toll-like receptor
TNF-α:	Tumor necrosis factor-alpha
VACF:	Velocity autocorrelation function
WT:	Wild type

1 General Introduction

This chapter begins with the foundational principles of immunity, with a particular emphasis on the role of neutrophils. Subsequently, fundamental concepts related to (directional) cell migration are introduced, before the chapter concludes with the migratory principles of activated neutrophils and this thesis aims.

1.1 The Immune System

Immunity is a highly intricate defense mechanism utilized by nearly all living organisms as a means of self-protection. Whether it is a multi-layered defense system employed by large mammals or a more limited system used by small bacteria, immunity takes on various forms and functions [1]. It is important to note that the immune system has not only evolved over millions of years but is also continuously shaped by the ongoing interactions between pathogens and immunity. These interactions play a critical role in the ongoing development and refinement of the immune system [2,3].

The human body relies on a multi-layered system to protect itself against invading pathogens. The first line of defense is the skin, a continuous layer of endothelial cells that act as a barrier to prevent organisms from entering. Only if these barriers are breached does the immune system become triggered and respond to the foreign intruder to prevent an infection. The human immune system is divided into two branches: the adaptive and the innate immunity. The adaptive immune response is highly specialized and can remember pathogens, resulting in an improved effector function. However, it is a slow process. The innate immune response, on the other hand, is quickly responding but has rather unspecific modes of action. The innate immune system primarily detects pathogens via non-self-molecules, called pathogen-associated molecular patterns (PAMP), through their pathogen recognition receptors. Adequate and effective immune responses to persistent pathogens often require interactions between the innate and adaptive immune systems, as important information is passed from one to the other. However, in most cases, the innate immunity is enough to prevent the establishment of an infection. This is demonstrated by disease-related impairments of the innate immunity, which are often far more severe than those of the adaptive immunity. Thus, the innate immunity plays a crucial role as the "first responder" to foreign organisms in the body [4].

1.1.1 Neutrophils – The First Line of Active Defense

One of the initial defense mechanisms of the innate immunity is the group of polymorphonuclear leukocytes, commonly referred to as granulocytes. Comprising four different subtypes, namely neutrophils, eosinophils, basophils, and mast cells, each granulocyte subset has unique effector functions and plays a crucial role in the body's response to foreign invaders. Among these subtypes, neutrophils are particularly important, acting as the first line of active cellular defense [5].

They play an especially crucial role as the first responder in the innate immunity against bacterial or fungal infections in humans. Being the most abundant type of leukocytes in humans, neutrophils rapidly migrate to the site of inflammation upon activation, precisely locate foreign invaders, and employ various effector functions to neutralize them. These effector functions include phagocytosis, degranulation of vesicles with lytic enzymes, the release of reactive oxygen species, or the formation of Neutrophil Extracellular Traps (NET), a combination of DNA and proteins that trap pathogens [6–10]. In many instances, the prompt and initial response by neutrophils is sufficient to prevent infections. This is shown by the fact that patients with neutropenia, a disorder

defined by significantly decreased numbers of neutrophils, are much more susceptible to various types of infections [11–13].

Although neutrophils are often viewed as primitive, short-lived, and suicidal – due to their various self-damaging effector functions that can cause their death – recent research has shown that they possess several other immune effector and regulatory functions. Neutrophils are now known to interact with various immune effector cells, such as B-cells, dendritic cells, T cells, and NK cells in a contact-dependent or contact-independent (via released mediators) manner [9]. These interactions can happen at the site of infection and/or in other tissues such as secondary lymphoid organs and the bone marrow [8]. Therefore, neutrophils are capable of orchestrating immune responses at multiple levels, producing various chemoattractants, cytokines, and other pro-inflammatory mediators. Neutrophils can even differentiate and acquire the ability to act as antigen-presenting cells to instruct T cells upon stimulation with interferon-γ and granulocyte-macrophage colony-stimulating factor [7,14].

Apart from their biological function, neutrophils can also be used as biomarkers for the onset of some diseases. The group of Daniel Irimia could show that neutrophils of hospitalized patients, who suffered from major burns, displayed significantly altered migratory patterns days before the onset of sepsis [15].

Data show that neutrophils play a crucial role in regulating the immune response beyond their primary effector functions which makes them essential responders and guides for the human immune system. Moreover, they could serve as potential biomarkers for certain diseases.

1.2 (Directional-) Cell Migration

Cell migration is a critical process for various physiological functions, such as development and wound healing, where cells need to move to different locations to perform their respective functions effectively [16].

Efficient and quick host defense in immunity depends especially on the migratory ability of leukocytes as effector cells need to reach sites of infection and follow intruding organisms in the body. Depending on their function, immune cells either migrate away from inflammatory sites to recruit and activate specialized effector cells (e.g., dendritic cells), or move toward pathogens (e.g., bacteria) to neutralize them (e.g., neutrophils). The migratory distances of immune cells vary extensively, with neutrophils typically traveling short distances from the blood to inflamed tissue, whereas T cells circulate between lymph nodes, entering all lymph nodes of the body once a day [17,18].

Cell migration is not only crucial for physiological functions but also for pathogenesis. For instance, tumor metastasis formation or infections heavily rely on the motility of cells. In the case of infections, pathogenic organisms like bacteria can enter a host through a wound and then disseminate via cell migration. These bacteria can use various migratory mechanisms, such as flagella-dependent swimming, swarming, or pilus-driven twitching, to invade specific host tissues and establish an infection [19–22].

1.2.1 Forms of Cell Migration and its Regulation

Cell migration is a broad term that encompasses various processes and concepts related to how a single cell or a group of cells can move from one location to another. Cells differ in their speed, migratory patterns, directional cues, and whether they migrate alone or collectively. For instance, some cells migrate in a straight line, while others move in a zigzag pattern, and they may follow different cues, such as chemotaxis or durotaxis (see subchapter 1.2.1.2).

1.2.1.1 Migratory Strategies

When looking at the different possible migratory strategies, one can in general distinguish three distinct ones: mesenchymal, amoeboid, and collective (see figure 1).

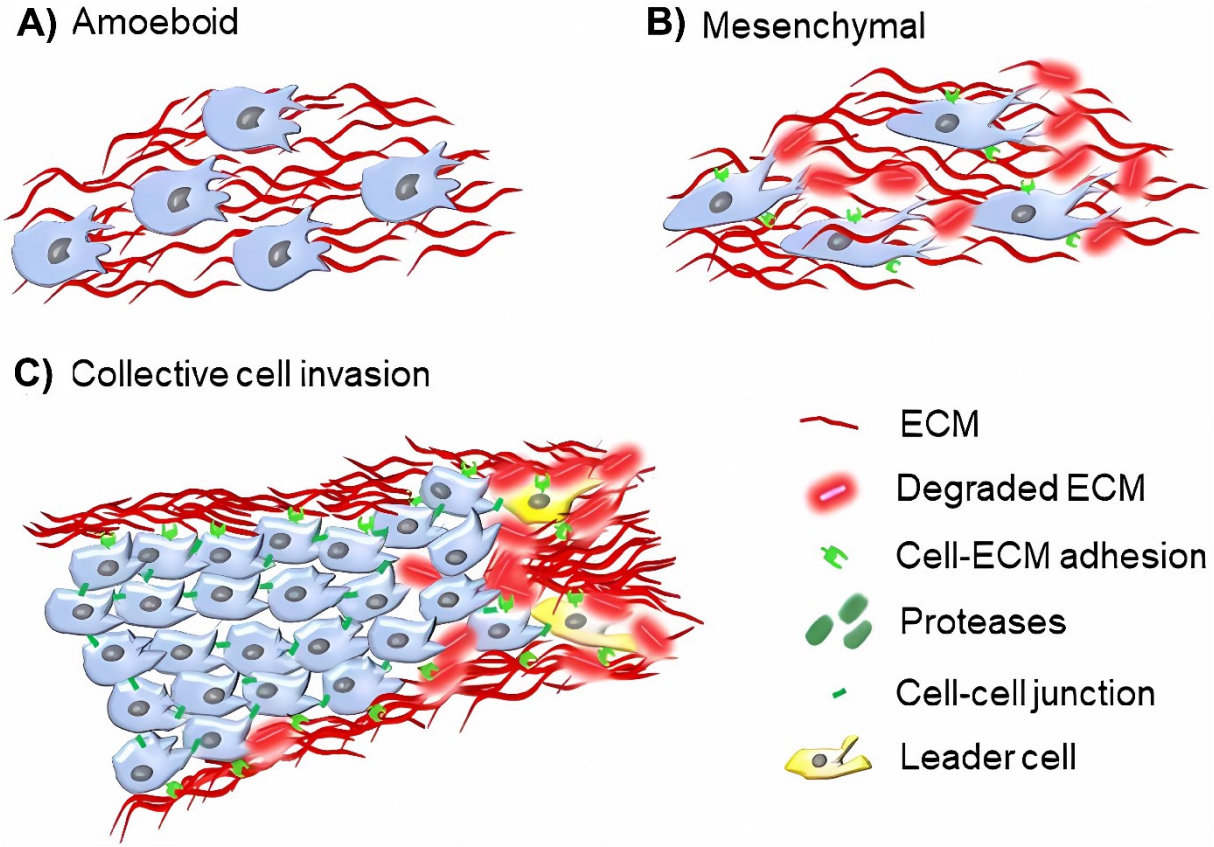


Figure 1: Modes and mechanisms of cancer cell migration. **A)** Amoeboid migrating cells are characterized by roundish and highly deformable cell morphology with bleb-like protrusions, high Rho-directed actomyosin contraction, weak extracellular matrix (ECM) interaction as well as lack of intercellular adhesion, and proteolytic degradation of the surrounding matrix. **B)** For movement, mesenchymal cells with elongated morphology require cytoskeletal contractility, integrins-mediated ECM adhesion, and pericellular proteolysis. **C)** Collective migrating cell groups retain high intercellular adhesion and front–rear polarity. This type of motility depends on actin dynamics, integrin-mediated cell-ECM adhesion, and pericellular proteolysis-mediated ECM reorganization. Figure and legend taken and adapted from Jia-shun Wu et al [23].

Mesenchymal cells, such as fibroblasts, exhibit elongated morphologies and require adhesion to a substrate to generate the necessary cytoskeletal contractility for migration. These cells are slow migrators and use proteolytic cleavage to create a path for their migration. In contrast, amoeboid cells, like leukocytes, are very fast-migrating cells that exhibit a highly deformable but roundish morphology. They are polarized with a clear leading edge as well as a uropod (i.e., cell back) and do not require adhesion for movement. While moving through tissues, they prefer to migrate through existing gaps rather than creating space through proteolytic cleavage. Collective migration involves the formation of strong interconnected clusters (e.g., through adherent junctions) that establish a front-rear polarity between all cells. The cluster relies entirely on proteolytic cleavage of the substrate to enable migration through tissue. Interestingly, many cells possess the ability to switch between the various strategies which allows the cells to adapt to the local environment [23–26].

1.2.1.2 Directional Guidance Mechanisms

The guidance mechanism for directional cell migration is another crucial factor to consider when thinking about directional cell migration. This relates to how cells are guided in a particular direction, or more broadly, how they locate the intended destination. There are numerous approaches that cells can use for this purpose, and the most prominent ones will discuss here (see figure 2).

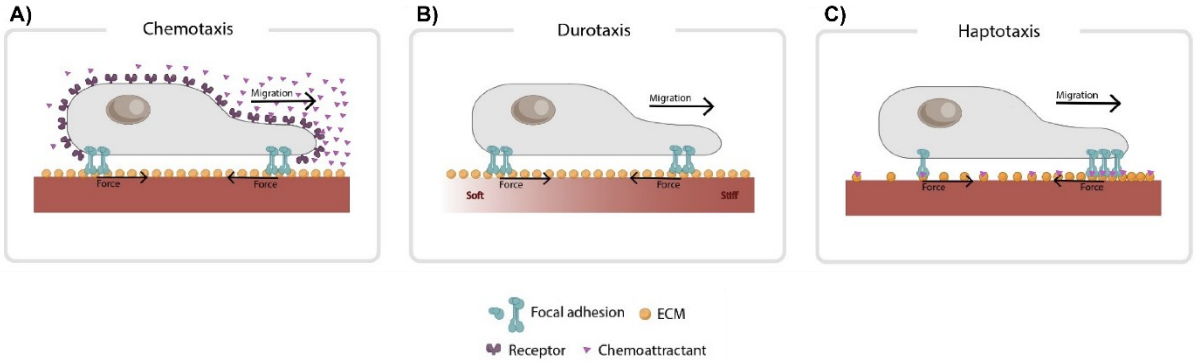


Figure 2: Common types of directed cell migration. **A)** In chemotaxis, cells follow gradients of chemical factors dissolved in the medium. **B)** In durotaxis, cells follow gradients of stiffness in the extracellular matrix. **C)** In haptotaxis, cells follow gradients of chemical factors immobilized in the matrix. These gradients can be made of ECM proteins such as fibronectin or collagen. Figure and legend taken and adapted from Isabela C. Fortunato et al [27].

Chemotaxis refers to the mechanism where migrating cells follow a gradient formed by an attractant produced by a source. The responsive cells recognize the attractant, usually via surface receptors, and process its information via biochemical network reactions. This leads to a coordinated response by adapting cellular adhesions, cell morphology, and mechanical force to migrate toward the source of the gradient. A significant factor in chemotaxis is that the attractant must be soluble to form a gradient in a fluid [28].

Haptotaxis is a process similar to chemotaxis, but the attractant is immobilized on a surface or substrate either through direct local expression or binding from the surrounding liquid. The migrating cell may need to cleave the attractant before being able to recognize it and follow its gradient [29].

Durotaxis is a strategy that is guided by substrate stiffness or rigidity. It is based on the concept that cells can sense and respond to the mechanical properties of their environment, such as the stiffness of the substrate they are adhered to. In durotaxis, cells preferentially migrate toward stiffer regions of the substrate, in a process that involves the formation and contraction of focal adhesions and cytoskeletal rearrangements [30].

Barotaxis is a type of cell guidance where cells migrate in response to mechanical forces exerted by the surrounding fluid, such as fluid flow or pressure. This can occur in various biological contexts, such as in blood vessels where endothelial cells can sense and respond to fluid shear stress. Another occurrence can happen if cells enter “dead ends” in tissues where liquid pressure is exerted against the migrating cell. In this scenario, the cell is guided away from the high-pressure region toward an area of lower pressure where migration can continue. In barotaxis, cells may use specialized mechanosensitive receptors or signaling pathways to sense the mechanical forces and adjust their migration accordingly [31].

Chemokinesis is a cellular response to chemical stimuli that can affect the speed, amplitude, frequency, or direction of cell migration. It is different from chemotaxis in that it does not involve directional guidance toward a specific source, resulting in a

random, non-vectorial movement. While chemokinesis does not have a specific directionality, changes in cell speed can still affect the overall migration toward areas of higher chemical concentration. This is because cells that are moving faster are more likely to encounter and ultimately accumulate at areas of higher chemical concentration, even if their movements are still somewhat random [32]. Interestingly, a single attractant can induce chemokinesis and/or chemotaxis in the same type of cell. When a substantial concentration gradient is present, cells tend to exhibit chemotaxis, aligning their movement with the gradient's direction. Conversely, in the absence of a distinct gradient (e.g., in uniform concentrations), cells may opt for chemokinesis [33].

Cells have evolved various mechanisms to navigate through complex environments, and they can switch between different guidance mechanisms depending on the availability of the cues in the environment or the cells' internal state. Additionally, cells can integrate multiple signals from different sources to make decisions about their direction of migration. These mechanisms provide cells with the ability to navigate and migrate toward specific locations in response to a variety of signals.

1.2.2 Physiological Gradients

Especially for chemotaxis, the presence of a gradient is crucial for cells to follow the guidance cue, but knowledge about gradient properties in this process remains poorly understood. Many studies have used arbitrary gradients to investigate cell migration, but it is becoming increasingly clear that different gradient properties, such as strength, stability, and shape, can have profound effects on the migratory behavior of cells [34,35]. In many experiments, a “source-sink” system is used, where on one side a fresh attractant is supplied whereas it is removed on the other side. Over time this generates a stable linear gradient between the two sides [36]. Modifying this setup by removing the sink would also generate an unstable linear gradient which would increase the overall concentration with time, making the gradient shallower. Changing the concentration input also affects the steepness and propagation time of the gradient.

Despite many efforts, it remains challenging to identify gradient properties that accurately mimic natural gradients in (inflamed) tissues as it is not fully known how physiological gradients look like. This is due to several experimental complications, including the inability to label some attractants (e.g., leukotriene B4 - LTB4) and the altered affinity of labeled attractants to their corresponding receptors, which can affect cellular responses. Additionally, most liquid within tissues and between cells is bound to the extracellular matrix and the glycocalyx, reducing the amount of available free liquid and making it difficult to determine the gradient concentration [37,38]. This reduced liquid volume generates specific problems for determining the gradients. First, the gradient concentration can reach very high levels although the actual molecular number of molecules is below the detection limit. Second, combining the first problem with the concept of “self-generating gradients” complicates matters further, as some cells can alter local concentrations by removing molecules, especially when using a decoy receptor with no intracellular signaling [39,40]. These problems can lead to significant differences between the gradients a cell detects and the measured gradients. Another challenge arises when cells are capable of a relay function, releasing the same or additional attractants on top of an existing gradient [41,42]. Furthermore, it is important to note that within tissue environments, the presence of chemoattractants and other signaling cues is actively regulated. These molecules are subject to active removal processes, such as uptake by resident cells or enzymatic degradation in the interstitium. Through these mechanisms, the concentration and availability of these cues are carefully controlled, influencing the behavior and migration of cells within the tissue microenvironment. Without proper labeling or knowledge of these relay molecules, it can be difficult to

measure the physiologically relevant gradient, particularly if the relay gradient is the primary guidance cue.

These limitations explain why the properties of natural gradients remain largely unknown. As of now, there is no clear evidence of how gradients look within tissue – what is the gradient shape (linear or more exponential), how high is the concentration (absolute and relative), how stable are they, and how quickly do they propagate? However, the development of new and sophisticated techniques may enable us to gain deeper insights into gradient properties in the future. For instance, new methods that label the respective signaling pathway instead of the attractant itself may provide clues as to the gradients that cells are sensing [43].

1.2.3 The Cytoskeleton

The proper translation of guidance cues into movement output is crucial for effective migration in biological systems. Even the most sophisticated migratory strategies and guidance mechanisms will ultimately be ineffective without this translation. The ability of cells to convert guidance signals into appropriate movements is a key factor in successful migration. This process can be thought of as similar to how humans use their skeletal system and muscles to generate movement, but on a smaller scale, as cells rely on their cytoskeleton to achieve this task.

1.2.3.1 Components of the Cytoskeleton

The cytoskeleton is a complex network of protein filaments that provides shape, structure, and support to cells and plays a critical role in cell migration. There are three main types of cytoskeletal filaments: microfilaments, intermediate filaments, and microtubules.

Microfilaments, also known as actin filaments, are the thinnest filaments in the cytoskeleton, with a diameter of about 7 nanometers. They are made up of actin proteins, which form a double helix structure that provides strength and rigidity to the cell's structure. Microfilaments play a key role in cell migration by providing the force necessary for cell movement.

Intermediate filaments are the middle-sized filaments in the cytoskeleton, with a diameter of about 10 nanometers. They are made up of various proteins, including keratin, vimentin, and lamin, and provide mechanical support to the cell's structure. Intermediate filaments are important in maintaining the integrity of the cell's nucleus and are also involved in anchoring cells to their surroundings.

Microtubules are the largest filaments in the cytoskeleton, with a diameter of about 25 nanometers. They are made up of tubulin proteins and provide structure and support to the cell's shape. Microtubules also play a crucial role in cell migration by helping to organize and transport intracellular components, such as organelles and vesicles.

These cytoskeletal filaments work together to provide the cell with its structure and movement capabilities. The cytoskeleton is a dynamic structure that can rapidly reorganize in response to changes in the cell's environment, allowing the cell to adapt to its surroundings [44].

Aside from the cytoskeletal protein filaments, there exist various protein families that assist in the modulation and arrangement of the cytoskeleton's movement. Notably, the actin-binding proteins and the Rho GTPases are considered two of the most significant protein families involved in this process.

Actin-binding proteins include a diverse range of proteins such as myosins, α-actinin, tropomyosin, filamin, fimbrin, and spectrin, among others. Two important types of actin-binding proteins involved in actin nucleation and polymerization are Arp2/3 complex and formins. Arp2/3 complex is a protein complex that nucleates actin filaments

and creates a branched actin network. Formins, on the other hand, promote actin polymerization by binding to the barbed end of actin filaments and elongating them. Both proteins play crucial roles in the regulation of actin dynamics and the generation of force and movement within cells [45].

The Rho GTPases are a crucial family of cytoskeletal proteins that regulate the cytoskeleton and play a vital role in cell migration. This group includes RhoA, Rac1, and Cdc42, with each playing a specific role in cell migration. RhoA, for example, promotes the formation of contractile actin filaments at the cell's rear end, while Rac1 and Cdc42 promote the formation of protrusive actin structures at the cell's leading edge. Together, these proteins help to coordinate the dynamic rearrangement of the cytoskeleton necessary for cell migration [46,47].

1.2.3.2 The Cytoskeleton During Cell Migration

One of the key steps in cell migration is the formation of filopodia and lamellipodia, which are thin, actin-rich protrusions that extend from the cell's leading edge and generate the force needed to propel the cell forward. These protrusions provide the initial contact with the extracellular matrix and allow the cell to explore its environment. The formation and extension of these protrusions require the coordinated assembly and disassembly of actin filaments, which are regulated actin-binding proteins, such as Arp2/3, cofilin, and profilin [48–50].

Another important step in cell migration is the adhesion of the cell to the extracellular matrix. This is mediated by integrins, which are transmembrane receptors that bind to extracellular matrix proteins such as fibronectin and collagen. Integrins link the cytoskeleton to the extracellular matrix and play a crucial role in regulating the mechanical properties of the cell. Once the cell is attached to the substrate, it begins to generate force to move forward. This involves the coordinated contraction of the cell's rear end, which is mediated by myosin motors that interact with actin filaments. This contraction pulls the cell forward, and the cycle repeats as the cell moves in a coordinated and directional manner. It is important to note that not all modes of cell migration require adhesion to the extracellular matrix. For instance, in amoeboid migration, cells move by deforming their cell membrane and squeezing through tight spaces without the need for adhesion [25,51–53].

Overall, cell migration is a complex process that involves the coordinated regulation of multiple factors, including the cytoskeleton, cell adhesion molecules, signaling pathways, and environmental cues. Dysregulation of any of these factors can lead to abnormal cell migration and is associated with various pathological conditions [54].

1.2.3.3 Cell Polarity

Cell polarity is a hallmark of cell migration, distinguishing migrating cells from their non-migrating counterparts. In resting cells, which often exhibit a spherical shape, polarity is not apparent. However, during migration, cells develop a distinct polarity characterized by the presence of a distinct cell front and a cell rear. This polarity is essential for directional movement and efficient navigation through complex environments. The front of the cell, known as the leading edge, extends protrusions such as lamellipodia and filopodia, which interact with the environment and provide traction for forward movement. At the rear, called the trailing edge, the cell retracts and releases adhesions to facilitate movement. The establishment and maintenance of cell polarity during migration involve intricate signaling pathways and the coordinated regulation of cytoskeletal dynamics. Proper cell polarity ensures efficient migration and is critical for the migratory ability of cells. During polarization, an early event involves the generation of opposing gradients of Cdc42 and RhoA activity, which occur simultaneously at the cell front and rear. At the front, Cdc42 and Rac proteins promote actin polymerization, while

at the rear, RhoA regulates myosin II contractility. These front and rear signaling modules operate independently of each other and are regulated by positive feedback loops that contribute to self-amplification and maintenance of cell polarity. Furthermore, it has been observed that tension exerted by the plasma membrane acts as a long-range inhibitor, mechanically preventing the formation of multiple cell fronts [55,56].

The front-rear polarity of migrating cells, such as chemotactic neutrophils, is generally considered to be relatively stable. Instead of repolarizing, these cells tend to steer their leading edge toward a cue even if the cue originates from the cell's rear. This stability in polarity allows cells to maintain a persistent direction of migration in response to external cues [57]. Indeed, a study conducted by Hadjitheodorou et al. provided intriguing insights into the relationship between cell polarity strength and cell behavior during migration. They demonstrated that the strength of polarity, quantified by the ratio of Cdc42 activity between the front and back of the cell, not only influenced the speed of cell movement but also affected the responsiveness of cells to repolarize. Through optogenetic stimulation experiments, they observed a positive correlation between polarity strength, cell speed, and the likelihood of repolarization. This suggests that the strength of cell polarity plays a crucial role in governing both the migratory speed and the ability of cells to adjust their polarity in response to external cues [58].

1.2.4 Receptors and Their Regulation

For the detection of molecules that comprise gradients, cells rely on specialized structures capable of sensing these molecules. Receptors play a crucial role in this process, particularly in chemotaxis, where G-protein-coupled receptors (GPCR) are primarily involved. GPCR are transmembrane receptors characterized by seven transmembrane domains. These receptors possess an extracellular tail responsible for ligand recognition, along with seven internal loops that participate in the regulation and recruitment of secondary effectors and specific G-proteins. These proteins, on the other hand, are multi-subunit complexes consisting of alpha, beta, and gamma subunits, each with distinct functions and comprising various subunit families. The signaling cascade triggered by each GPCR can be highly intricate, as different G-proteins and their subfamilies contribute to specific functions and drive diverse biological outcomes. The complexity of these signaling pathways underscores the intricate nature of cell response to gradients [59].

Remarkably, all the receptors known to be involved in inducing directed migration through chemotaxis belong to the family of GPCR [60]. It is worth noting that PAMP, such as lipopolysaccharide (LPS), cannot induce directed migration but instead elicit random migration through toll-like receptors (TLRs), which belong to the Interleukin-1 receptor superfamily [32,61].

To effectively respond to various factors such as absolute concentration, the cellular environment, and gradient shape, receptors need to dynamically adapt. Cells employ regulatory mechanisms to adjust the activity of GPCR in response to specific cue properties. The regulation of GPCR can occur through diverse mechanisms, each leading to different outcomes in cue detection:

- Up-regulation – Cells can increase the synthesis of receptors or release them from intracellular pools, such as vesicles, to enhance their availability on the cell surface.
- Down-regulation – Receptor synthesis can be reduced, or receptors can be internalized through endocytosis, leading to a decrease in their presence on the cell surface.

- Modification – Receptors can undergo chemical modifications that alter their affinity for ligands or modify downstream signaling pathways, thereby affecting their overall responsiveness.
- Oligomerization – Some receptors require oligomerization, where multiple receptor units come together, while others can switch their functions based on whether they act alone or within a cluster of receptors.
- Recycling – Receptors can be internalized through endocytosis and subsequently recycled back to the cell surface, allowing for a dynamic regulation of their availability.
- Trafficking – Receptors can undergo trafficking along the cell surface or within the cell, allowing them to be transported to specific cellular compartments or regions.

These various regulatory processes – alone or as a combination – enable cells to fine-tune the responsiveness of receptors, adapt to changing environmental conditions, and optimize their ability to detect and respond to cues [62,63].

In the absence of specific cues, cells exhibit a characteristic distribution of receptors, with an even distribution across their entire surface. This even distribution ensures that receptors are uniformly accessible to the surrounding environment, enabling the cell to detect signals from all directions. By evenly distributing the receptors, cells can achieve a comprehensive and unbiased detection capability across the entire circumference of the cell. This allows for a broader sensitivity to the surrounding environment, facilitating responses to various stimuli in a more balanced manner [57]. The distribution of receptors in chemotactic cells, specifically regarding whether they are evenly distributed or skewed toward the cell front, is still an area of ongoing research. While the exact distribution pattern is not fully understood, some experimental evidence suggests that cells may indeed exhibit a skewed distribution of unoccupied receptors toward the cell front. This skewed distribution would enhance the sensitivity of the leading edge to gradient cues. A study conducted by Subramanian et al. focused on neutrophils and demonstrated that upon binding of formyl-methionyl-leucyl phenylalanine (fMLF) to FPR1, multiple receptors cluster and undergo trafficking along the cell surface toward the trailing edge. These receptor clusters are then endocytosed, recycled, and transported forward to the leading edge of the cell [64]. This mechanism potentially contributes to the cell's ability to "lock in" on the gradient. By maintaining a highly sensitive leading edge while reducing sensitivity in the rest of the cell, the likelihood of noise-induced formation of new leading edges or unintended cell turning is diminished.

In addition to receptor distribution, the morphology of the cell's leading edge can also contribute to an imbalance in receptor availability. The leading edge of a migrating cell is often characterized by its ruffled and layered structure, which results in a relatively higher surface area compared to the rest of the cell [65]. This increased surface area at the cell front alone can create an increased local concentration of receptors, even if the overall receptor availability per unit surface area is equal throughout the cell. By spatially concentrating receptors at the leading edge, cells may achieve a higher sensitivity to gradient cues in the direction of migration while minimizing unnecessary responses to cues from other directions. This localized receptor distribution, in conjunction with other mechanisms of receptor regulation and signaling, contributes to the complex process of gradient sensing and cell migration.

1.2.5 Spatial and Temporal Sensing

During cell migration, cells employ various strategies to interpret extracellular signals, including gradients, and respond accordingly. A critical question in this process is how cells sense the gradient and integrate its spatial and temporal components

across their length to determine the gradient's direction. Spatial and temporal sensing are two essential mechanisms used by cells to detect and respond to gradient cues.

Spatial sensing refers to the ability of cells to detect differences in the concentration of a chemical or physical cue across space. For example, when a cell is exposed to a gradient of a chemoattractant, it can sense the direction of the gradient and migrate toward higher concentrations of the attractant. Spatial sensing involves the ability of cells to compare the concentration of the cue at different locations of their own cell body and determine which location has the higher concentration. Eukaryotic cells are capable of spatial sensing due to their relatively large size, while small bacterial cells cannot accurately differentiate between two locations due to their small size.

Temporal sensing is a mechanism by which cells can detect changes in the concentration of a cue over time. It allows cells to respond to dynamic changes in their environment. For instance, when a cell is exposed to a rapid increase in the overall concentration of a chemoattractant around the cell, it can sense the temporal change and modify its behavior accordingly. Temporal sensing enables cells to adapt their responses based on the changing concentration gradients, allowing for integration over time and thus ignoring noise in the gradient. Bacteria, being too small to rely on spatial sensing, employ temporal sensing as a key mechanism for their motility. Through a fascinating strategy known as "run and tumble," bacteria navigate their environment. During the "run" phase, they move in a straight line to explore their surroundings. Periodically, they transition to a "tumble" motion, reorienting randomly while simultaneously assessing the concentration of cues. Subsequently, bacteria adjust their behavior by comparing the current concentration with the previous tumble location. If the concentration is higher, they extend the run phase, and if it is lower, the run phase becomes shorter.

Spatial and temporal sensing play significant roles in cell migration and other cellular processes that rely on chemical and/or physical cues. Spatial sensing offers the advantage of an immediate response to a gradient cue, making it advantageous when a quick response is needed. In contrast, temporal sensing requires integrating over time to obtain accurate interpretations, which may take longer. However, spatial sensing may be more prone to errors as noise in the gradient or environmental fluctuations can obscure the gradient, while temporal sensing can help to reduce these artifacts by integrating over time [66].

In recent years, there has been growing evidence suggesting that eukaryotic cells can harness the advantages of both spatial and temporal sensing mechanisms to enhance their sensing capabilities. Theoretical work by Hegemann and Peter, for instance, proposes a model where cells combine spatial and temporal information through stochastic local concentration sampling to determine the source of gradient signals [67]. Supporting this idea, studies conducted by Aronin et al. on murine immune cells demonstrate that stable gradients are insufficient to promote persistent migration, whereas rising concentrations can. This implies that cells employ spatial sensing to establish the direction of the gradient and then utilize temporal sensing to sustain their migratory responses [68]. Another intriguing study by Merlini et al. focuses on fission yeast and their alignment during mating. They reveal the presence of a polarity patch within yeast cells, which undergoes a biased random walk along the membrane upon contact with pheromones from the opposite sex. Like bacteria, this random walk incorporates "run and tumble" phases that adapt according to the pheromone concentration. Once the highest concentration is detected, the cell extends in that direction to initiate mating. In this novel hybrid mechanism, eukaryotic cells utilize their entire cell surface by facilitating a searching agent's random walk, rather than relying on complex and error-prone calculations of receptor occupancy differences [69].

These studies highlight the fascinating interplay between spatial and temporal sensing in eukaryotic cells, revealing their ability to employ diverse strategies for effective signal detection and response.

1.2.5.1 Migratory Memory

The presence of temporal sensing in eukaryotic cells appears to significantly enhance their capacity to perceive and interpret gradients, thereby facilitating their responsiveness to chemotactic cues. By incorporating temporal sensing mechanisms, eukaryotic cells can greatly improve their proficiency in accurately detecting and interpreting the dynamics of gradients, enabling them to navigate toward the desired direction dictated by the cues more readily.

Of personal note, regarding nomenclature, it is important to clarify the distinctions between "memory", "momentum", and "inertia" in the context of cell behavior. Memory effects typically involve the integration of information over time and an active comparison between different time points or the integration of specific signals over time. A classic example is the "Run and Tumble" behavior of bacteria, where concentrations at different time points are actively compared. On the other hand, momentum comes into play once a cell has initiated a specific process and can only respond after that process is complete. An example of momentum could be a highly polarized cell that exhibits persistent movement in one direction, even in the presence of cues from the back of the cell. Inertia, on the other hand, refers to cellular processes that require time to manifest their effects. For instance, the up-regulation of actin or receptors after reaching a specific cue concentration may result in an observable effect, such as increased cell speed, but this effect may only become evident minutes after the initial trigger. While the outcome may appear similar for all three processes, the triggering mechanisms differ. For example, some groups refer to the ongoing persistence of a cell as "memory," attributing it to the stability of the cytoskeleton in a specific orientation. However, this could be better described as an inertia or momentum effect since it lacks a temporal component.

In a study conducted by Nandan et al., it is proposed that single cells utilize a "working memory" mechanism to aid in persistent and directional migration. The research demonstrated that cells continued to follow a previous chemotactic cue even after the cue was no longer present. However, when a new cue was introduced at a different location, the cells responded promptly to the new cue. The underlying model suggests that this behavior arises from a metastable state of receptor activity, which persists even when the attractant is no longer bound to the receptors. This metastable state of receptor activity not only enables rapid responses to new cues but also aids the cell in "remembering" the origin of the attractant. By maintaining their dynamic nature, the receptors retain the ability to swiftly respond to changes in the environment while retaining information about the previous cue source [70].

In a study conducted by Haastert, it was discovered that non-chemotactic eukaryotic cells exhibit a correlated random walk pattern instead of purely random migration. This finding suggests the presence of a memory system within these cells. Haastert identified two distinct memory systems: a short-term memory lasting up to 20 seconds and a long-term memory lasting up to 2 minutes. The short-term memory is regulated by modifications in F-actin, while the long-term memory relies on cGMP-binding proteins located at the back of the cell. The interaction between these two memory systems enables the cells to maintain persistence in their movement, even in the absence of a chemotactic cue [71].

In recent years, several independent studies have demonstrated the involvement of cytoskeletal components in memory effects. For example, Prentice-Mott et al. found

that the long-lived cytoskeletal asymmetry in cells plays a role in maintaining cell persistence. Specifically, they identified the presence of moesin at the cell rear, and they observed that stabilizing moesin increased the directional memory of the cell. Conversely, disrupting moesin resulted in a reduction of directional memory. These findings highlight the significance of cytoskeletal dynamics in regulating memory effects during cell behavior [72]. Meanwhile, in a study by Georgantzoglou et al., it was shown that leukocyte migration occurs through a two-step process. Firstly, cells undergo an initial search phase where they orient themselves toward the gradient. This is followed by a run phase characterized by high cell speed and persistence up the gradient. Notably, when the actin flow was disrupted, the cells were unable to accurately sense the gradient, suggesting that the actin flow itself may serve as a memory for persistent migration [73].

In summary, eukaryotes demonstrate the utilization of temporal components in cell migration to navigate complex gradient environments. Theoretical studies provide insights into how these temporal mechanisms contribute to their navigation abilities, while biological studies aim to identify the specific proteins or complexes responsible for these effects. Although potential candidates have been identified, the exact mechanism or protein involved in implementing temporal sensing remains unknown.

1.2.6 Current Models of Directed Cell Migration

There is a wide range of models available for conceptualizing cell migration, each focusing on different aspects and incorporating various factors related to gradient detection. In the context of gradient sensing, Endres and Wingreen developed a simple model that explores the physical limitations of this process by comparing two hypothetical cell types: perfect absorbers and perfect monitors. In the model, perfect absorbers represent cells that infer the gradient by absorbing surface molecules, while perfect monitors allow particles to freely diffuse through their membrane for direct measurement. The researchers found that the perfect absorber outperforms the perfect monitor in terms of gradient sensing efficiency, primarily because the absorber avoids re-measuring the same particles [74]. This comparison highlights the potential advantages of utilizing a mechanism where cells extract information from absorbed molecules rather than continuously monitoring the environment. By avoiding redundancy in measurements, the perfect absorber model suggests a more efficient strategy for gradient sensing.

The "Local Excitation, Global Inhibition" (LEGI) model is a widely recognized and influential model for understanding eukaryotic cell migration. It provides insights into how cells detect and respond to chemical gradients in their environment. The LEGI model proposes that cells utilize a combination of local excitation and global inhibition mechanisms to sense and interpret chemical gradients accurately. It suggests that when a cell encounters a higher concentration of a chemical signal at a particular location, it undergoes local excitation, which involves the activation of receptors or signaling molecules specific to that signal. Simultaneously, the cell also experiences global inhibition, which acts globally across the entire cell to suppress excitation in other regions. The key idea behind the LEGI model is the establishment of a feedback loop between local excitation and global inhibition. Local excitation reinforces itself, leading to a stronger response in the region with higher signal concentration. At the same time, global inhibition prevents excessive excitation in other parts of the cell, maintaining polarity and allowing for directed migration. The LEGI model provides a conceptual framework for understanding how cells generate and maintain a polarized response to chemical gradients. It helps explain how cells establish a leading edge,

where excitation is strong, and a trailing edge, where inhibition dominates, enabling efficient migration toward or away from specific cues [28,75].

As highlighted in earlier discussions, the limited understanding of the intricate processes involved in cell migration poses challenges in constructing comprehensive and accurate models. Consequently, many existing models tend to be simplistic and lack the necessary level of detail. Furthermore, the identification of all the key players involved in cell migration remains an ongoing pursuit, and there are still unknown factors that contribute to this complex phenomenon.

1.3 Directional Cell Migration of Neutrophils

Until now, the theoretical aspects of cell migration and the underlying mechanisms were reviewed. With the following chapter the focus turns on the migration of neutrophils, a type of fast-moving amoeboid leukocyte that relies on chemotaxis as its primary guidance mechanism to navigate toward specific destinations.

1.3.1 Chemotaxis of Neutrophils is Essential for an Effective and Guided Early Immune Response

During infections, the recruitment of neutrophils to the sites of pathogens is crucial for their effective response. Chemotaxis plays a pivotal role in this process, as neutrophils follow various cues originating from the host (e.g., chemokines) and the pathogens themselves (e.g., formylated peptides). To track and locate motile pathogens, also accounting for Brownian motion, neutrophils rely on a soluble chemotactic agent as the ultimate attractant. This is due to the fast and dynamic nature of the neutrophil steering process, which can be best explained by the involvement of soluble mediators. Chemotaxis serves multiple purposes for neutrophils, including their recruitment from the bloodstream and their directed migration toward the vicinity of pathogens [76]. Therefore, in the context of immunity, chemotaxis plays a fundamental and crucial role in guiding neutrophils toward sites of inflammation to neutralize pathogens. It serves as a vital mechanism to effectively respond to and combat infections.

1.3.2 Neutrophils Respond to Multiple Divergent Attractants for Guidance

Neutrophils play a critical role as the immune system's first responders, and to fulfill their functions, they rely on a diverse array of receptors for activation, pathogen recognition, adherence, and selective detection of various chemoattractants (see figure 3). Directed migration of neutrophils involves the utilization of different receptor families and their corresponding attractants. Among these, chemokines, which are potent attractants for many leukocytes, are produced by host cells to recruit immune effectors to infection sites. Chemokines are recognized by chemokine receptors, with interleukin-8 (IL-8 or CXCL8) being a primary attractant recognized by the chemokine receptor CXCR1 on neutrophils. Another important group of receptors on neutrophils are the "classical chemoattractant receptors," which include the LTB4 receptors BLT1 and BLT2, as well as the complement receptors C5aR and CR. LTB4 serves as a critical relay for neutrophils, as it is secreted by initially arriving neutrophils to recruit additional neutrophils from distant locations [77]. Especially for the final guidance of neutrophils toward pathogens, the complement factors C3a, and more dominantly C5a, play an important role. Both factors belong to the family of anaphylatoxins and C5a is the most potent chemoattractant to date. Unlike most attractants produced by cells, C3a and C5a are released by the complement system upon cleavage of their precursor molecules in an activation cascade. This release occurs on the surface of opsonized pathogens. It is noteworthy that the release of these factors is dependent on the

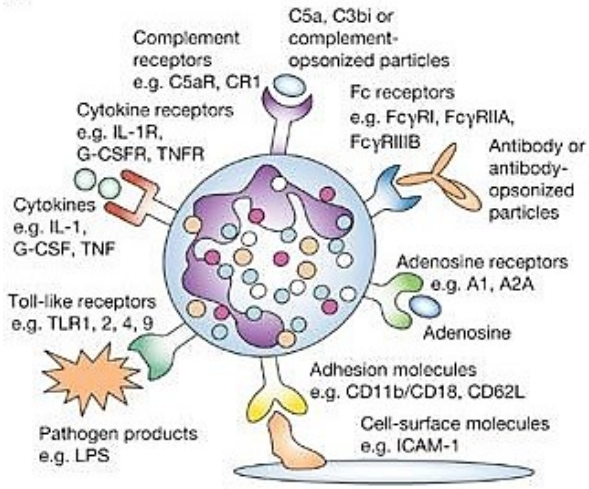


Figure 3: Surface molecules and receptors on neutrophils. Depicted are receptor families (e.g., complement receptors), relevant examples of them (e.g., C5aR), and their corresponding ligands (e.g., C5a). Of note, chemokine receptors belong to the cytokine receptor family. Figure taken and adapted from Jo L Eyles et al [78].

presence of heat-sensitive complement factors in the serum or blood [79,80]. The formyl peptide receptors (FPR1-3) constitute another significant family of chemotactic receptors. These receptors specifically bind to N-formyl peptides. N-formyl peptides are typically produced by bacteria and are recognized by the immune system as both PAMP and chemotactic cues. One well-known example of a PAMP is fMLF, which is released by bacteria. Neutrophils are guided toward bacteria by recognizing fMLF through FPR1 [81]. In addition to these important receptors, neutrophils possess a variety of other receptors which are linked with chemotaxis.

1.3.3 Sequential Attractant Sensing is Guiding Neutrophils Toward Their Prey

During an infection, recruited neutrophils are exposed to multiple attractants simultaneously and in a sequential manner. Despite this complex scenario, neutrophils possess the ability to process and interpret these competing signals rapidly and efficiently. This enables them to accurately navigate toward pathogens. To ensure precise tracing and localization of pathogens, neutrophils must not only sense the diverse mixture of attractants originating from different sources but also prioritize them. Initially, neutrophils are recruited from the bloodstream by primary attractants such as IL-8, which are released by activated tissue-residing cells to recruit neutrophils toward sites of infection [82–84]. Once neutrophils extravasate, they encounter a combination of intermediate attractants, such as LTB4, which are secreted by infiltrated immune cells. These attractants guide the neutrophils toward the vicinity of the pathogen. At the site of infection, end-point attractants, including fMLF and C5a released by the pathogen, play a crucial role in directing the neutrophils toward their target. These attractants often act on neutrophils simultaneously but with varying concentrations, gradient shapes, and sometimes even opposing gradients. As a result, neutrophils must possess the ability to process and interpret diverse attractant information, as well as prioritize them, in order to navigate toward the pathogen efficiently and rapidly. This sequential processing and interpretation of different attractants, culminating in the attack on its prey, is made possible by the spatiotemporal hierarchy of chemoattractant sensing employed by neutrophils [85–87]. Although the specific mechanisms underlying the prioritization of attractants by neutrophils are not yet well understood, these processes likely occur at the downstream signaling levels. Generally, primary, and intermediate attractants activate a different signaling pathway than end-point attractants. The former

pathway involves the phosphatidylinositol-3-OH (PI3K) phosphatase and tensin homolog (PTEN) pathway, while the latter activates the p38 mitogen-activated protein kinase (p38 MAPK) pathway. There is a crosstalk between these pathways that leads to the prioritization of end-point attractants through the recruitment of PTEN, an antagonist of PI3K, to the cell circumference because of p38 MAPK activation. When a neutrophil encounters an end-point attractant, the signaling hierarchy suppresses the response to primary and intermediate attractants and directs the cell's focus toward the specific end-point attractant. Importantly, this suppression occurs independently of the concentration of the primary or intermediate attractant. Interestingly, not all involved signaling pathways are known yet, as when PTEN was inhibited, neutrophils were still able to prioritize fMLF to IL-8 in PTEN knockouts, showing that PTEN-independent pathways exist. Additionally, the PI3K-independent pathway, which gets inhibited by PTEN, for sequential sensing in neutrophil migration is yet not known [87–89]. Despite the prioritization of end-point attractants, there is still an ongoing competition between primary and intermediate attractants that is not fully understood. Recent studies suggest that neutrophils exhibit a preference for more distant attractants and can switch and oscillate between different attractants. This indicates a dynamic decision-making process by neutrophils, where they continually assess and respond to the changing gradient landscape in their environment. The underlying mechanisms and factors influencing this preference and switching behavior are subjects of ongoing research [85,87,90].

The precise localization of motile pathogens by neutrophils involves the accurate interpretation of diverse soluble gradients. While the primary recruitment and relay functions of neutrophils are relatively well understood, the mechanisms underlying the final localization of motile pathogens remain a subject of investigation. It is crucial to determine which attractants are important and how neutrophils rapidly detect and respond to them, especially in the case of motile bacteria where a prompt reaction is necessary to prevent the bacterium from changing its location before the neutrophil reaches it. Recent research by Heinrich et al. suggests that C5a, a component of the complement system, plays a key role in enabling the final chemotaxis of neutrophils toward pathogens. This conclusion is supported by experiments using complement-inactivated serum, which failed to elicit a chemotactic response in single neutrophils toward various single or clustered microorganisms, even over very short distances [80,91,92]. The observation that other end-point attractants, such as fMLF, do not appear to be involved in the final stages of pathogen localization is intriguing. It suggests that different types of attractants may play distinct roles in neutrophil migration and pathogen targeting. However, the study by Dahl and Lindroos in 1978 provides evidence that factors other than the complement system are important for the final migratory adjustment of neutrophils, particularly in the context of clusters of microorganisms. In their bulk experiments with complement inactivation, neutrophils showed directed migration toward bacterial supernatant and zymosan particles, which mimic fungal surfaces, indicating that at least for clusters of microorganisms other factors than the complement system are important for the final migratory adjustment [93]. These findings suggest that the mechanisms involved in the final localization of pathogens by neutrophils are complex and multifaceted. While the complement system, including C5a, is likely crucial for neutrophil chemotaxis, there may be additional factors at play, especially in situations involving clustered microorganisms or specific types of pathogens.

1.4 Thesis Aims

The study of cell migration principles and mechanisms holds significant importance in comprehending various physiological and pathological processes. It provides valuable insights into the intricate workings of cells during development, tissue repair, immune responses, and cancer metastasis, among others. By unraveling the fundamental aspects of cell migration, one can uncover potential targets for therapeutic interventions and develop novel strategies to modulate cell behavior.

1.4.1 The Missing Links

Cell migration and chemotaxis have been subjects of scientific investigation for centuries, starting with the pioneering observations of cellular movement by Leeuwenhoek in 1703 and the introduction of the concept of chemotaxis by Engelmann in 1881. While significant progress has been made in understanding the molecular aspects of cell migration in recent years, many mechanisms remain poorly understood. Researchers have identified and characterized various receptors and biochemical signaling cascades involved in migration. However, the spatiotemporal sensing and interpretation of chemoattractants by leukocytes, which guide their movement toward targets, remains a complex and elusive process.

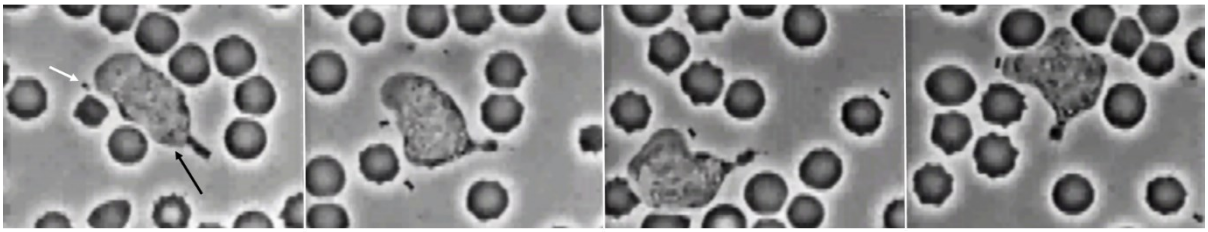


Figure 4: Neutrophil chemotaxis toward a *Staphylococcus aureus* cell. Depicted is one of the first movies where a neutrophil hunts and ultimately phagocytoses (not shown) its prey. A *S. aureus* culture was added to a human blood film and the original idea was to study the capability of *S. aureus* to survive within neutrophils. The movie was recorded in the 1950s by David Rogers and was made public in 1999 by Thomas Stossel. A montage was created by the original published (1999) video and contrast as well as sharpness were enhanced. The black arrow highlights a human neutrophil while the white arrow highlights the *S. aureus* cell [94].

A notable example illustrating this challenge is the work of David Rogers in the 1950s, where he demonstrated that a neutrophil could track and ultimately phagocytose a *Staphylococcus aureus* pathogen, despite the random Brownian motion of the pathogen (see figure 4). The video demonstrates the remarkable capability of a neutrophil to quickly adjust its trajectory dynamically to keep up following its prey. By doing so, the neutrophil keeps following a bacterium for multiple minutes while traversing a distance that is a multitude of its length. Interestingly, in the video, the neutrophil also encounters a second bacterium but ignores it as it seems to be locked on the initially encountered bacterium. The close correlation between changes in bacterial trajectories and the corresponding adjustments in the neutrophil's trajectory raised questions about the precise mechanisms underlying the spatiotemporal control. It is intriguing how the neutrophil swiftly responds to even the slightest changes in the bacterial path, ensuring its continuous pursuit. This dynamic interplay suggests the existence of intricate signaling and sensing mechanisms that enable the neutrophil to effectively track and respond to the movements of its target. Exploring the spatiotemporal control underlying this observation could unveil valuable insights into the complex coordination and regulation of cell migration and chemotaxis.

The complex dynamics of gradients and their impact on neutrophil perception raise numerous unresolved questions. Our understanding of the actual sources and

appearance of *in-vivo* gradients is limited, and the formation and characteristics of gradients in physiological contexts remain largely unknown. Furthermore, the influence of different gradient shapes, strengths, and the local tissue environment on chemotactic cell responses, as well as the influence of gradient properties on receptor regulation, are still elusive. The dynamic nature of migrating cells suggests the involvement of temporal factors in fine-tuning their migratory behavior and the concept of "self-generating" gradients adds another layer of complexity, as cells can actively shape the surrounding gradient landscape. The mechanisms underlying gradient sensing, symmetry breaking, and polarization, and their interplay with gradient properties and front versus back signaling, remain poorly understood, emphasizing the need for further investigation in this field. Especially when looking at the possibility of a temporal component, several intriguing questions arise: Which specific molecules or signaling pathways are involved? What are the underlying molecular mechanisms controlling this temporal component? Is this temporal component consistently present or dependent on specific conditions? Within what timeframe does the integration of this component occur?

The objective of this thesis is to tackle some of the existing knowledge gaps and shed light on unanswered questions regarding gradient integration and the subsequent adaptation of cell trajectories. This research aims to elucidate how cells effectively utilize the spatiotemporal information of gradients to adjust their paths and navigate toward the source of the cue. Furthermore, we seek to investigate the role of the local geometric environment in facilitating the accurate interpretation and navigation of gradients by individual cells as well as cell groups. With this thesis, we aim to contribute insights into the fundamental processes of gradient interpretation by neutrophils.

1.4.2 Aim 1 – Gradient Effects on Cell Trajectories: Cyclical Behavior and Memory Utilization

The first main project of this thesis focuses on investigating how neutrophils interpret information from dynamic gradient fields. In this project, we employ a combination of unlabeled single-cell tracking in collagen and intensity measurement of proxy dyes to establish a correlation between concentration changes and cell behavior.

In the initial phase, we investigate the impact of different source types (line vs. point sources) and source concentrations on various migratory properties, like persistence or speed, of chemotactic neutrophils.

Subsequently, we are interested in understanding the role of memory in their gradient sensing capabilities. We study whether neutrophils "remember" the concentration they encountered earlier and if this memory aids them in navigating the gradient more efficiently.

1.4.3 Aim 2 – Local Geometry and Cell Count Influence Gradient-Induced Persistence and Directionality in Cell Migration

The second major focus of our research was to investigate whether neutrophils can utilize their local geometric environment to enhance their local gradient. Specifically, we study whether neutrophils can concentrate the gradient in front of them by pushing, either individually or collectively, against the gradient. To address this question, we employed custom-made microfluidic devices to examine the combined impact of cell number and pore sizes within a pillar maze on the navigational efficiency of neutrophils in completing the maze.

2 Run and Fumble – What Eukaryotes Learnt From Bacteria

2.1 Summary

For the primary focus of this thesis project, we explored how neutrophils integrate spatial-temporal signals to navigate toward their target location. Our preliminary results showed the presence of distinct migratory patterns among human neutrophils depending on the nature of the originating source, whether it is line or point-like. To investigate further, single-cell tracking in 3D environments and proxy dyes were combined to correlate various cell behaviors to fluorescence changes in different source types and concentrations. Our data revealed that neutrophils react more persistently to the semi-exponential gradient created by point sources than to the linear gradient of the line sources. we also observed that the migration speed of neutrophils oscillates within a given frequency, and that speed minima are utilized to adjust their trajectories toward the source. Moreover, if cells are exposed to continuous concentration changes, they accelerate over time but do not respond to higher absolute concentrations. In contrast to bacterial chemotaxis, characterized by an alteration of bacterial run length in accordance with ambient concentration and a random tumble phase, our results indicate that neutrophils adopt an intelligent "Run and Fumble" strategy. This approach combines a consistent run interval with making intelligent "fumbles" toward the source, ultimately guiding cells quickly and efficiently toward their prey. In addition, as the cells approach the source, they encounter a continual alteration in gradient, leading to an augmented cellular speed, therefore facilitating a quick arrival at their targeted location. Our study sheds light on the navigation skills of neutrophils, which is important for understanding the immune response to inflammatory stimuli.

2.2 Introduction

Inspired by David Rogers' captivating 1950s movie, which depicted a single neutrophil's relentless pursuit of a bacterium within a droplet of blood, we found ourselves intrigued by the dynamics underlying this extended chase. Upon repeated viewings of the video, the interplay of spatial and temporal factors intrigued us profoundly. Whenever the bacterium altered its trajectory, the neutrophil responded immediately, adjusting its path to keep track of the bacterium. Even over distances spanning multiple cell lengths, the neutrophil remained fixed on the bacterium. This observation underscores that successful navigation in such challenging scenarios demands not only the rapid integration of external signals but also the quick execution of decisions to adapt to a moving target's unpredictability. Hence, this mesmerizing movie ignited our curiosity about the intricacies of cellular decision-making and navigational strategies, especially about the spatiotemporal components involved. Consequently, we started this project to investigate the spatiotemporal signal interpretation, and in addition, also to explore the question if neutrophils possess a form of "cellular migratory memory".

When investigating cellular responses to attractant stimuli in a spatiotemporal context, the role of gradients becomes inherently significant. As previously noted, our comprehension of gradient profiles *in vivo* is limited, along with our understanding of their impact on cellular signaling and behavior. Existing research suggests that cells exhibit optimal gradient sensitivity when transitioning from no concentration to any concentration [35]. This is attributed to the potentially infinite change in the relative concentration between the timepoints. The formula $(\Delta c_1 - \Delta c_0) / \Delta c_0$, compares the change in concentration at a later time point (Δc_1) to the concentration at the initial time point (Δc_0), where Δc_0 represents the time of no concentration. Since Δc_0 is close to 0, the resulting difference can approach infinity, highlighting the significant change from the initial

absence of concentration to any concentration at Δc_1. Moreover, steeper, or exponential gradients tend to elicit more robust responses compared to shallower or linear gradients, respectively, again due to the potentially higher relative change in the concentration [95]. The gradient aspect is particularly pivotal since cells rely solely on the attractant and its associated gradient as their environmental cues to ascertain any information about their target destination. Consequently, when studying the spatiotemporal cellular response, examining gradients becomes paramount, as they encompass all the essential information for guiding cellular behaviors. By investigating gradient fields and individual cell trajectories, and establishing correlations between the two, valuable insights into how cells utilize gradient information to steer their migratory responses can likely be unveiled. This approach would enable us to utilize gradients and the corresponding behavioral responses as a measurable indicator for deciphering the underlying spatiotemporal dynamics governing these effects.

Our exploration also revolved around the idea that neutrophils might possess the capacity to retain a trace of their previous encounters with a concentration, gradient, or stimuli, helping them to form a navigational memory. Such a memory mechanism could potentially enable these cells to not only react in the moment via spatial sensing but also to extrapolate from past signals with the help of temporal sensing. Combining both, temporal and spatial sensing, might help them to make more informed migratory decisions. In terms of temporal sensing, this concept raises a series of interesting questions: How do neutrophils store this information? Do they prioritize recent encounters or maintain a comprehensive record and average it? How does the temporal aspect integrate with the predominantly spatial sensing mechanism?

Hence, through this study, we aimed to elucidate the complex way neutrophils integrate gradient differences within physiological 3D environments via spatiotemporal mechanisms, while also exploring how the incorporation of a migratory memory could enhance their ability to reach the specific stimuli sources.

We employed label-free cell tracking within 3D collagen assays, using both varied fMLF gradient and uniform concentration configurations, alongside a fluorescent proxy for the attractant. Subsequently, we established correlations between the measured proxy concentration changes experienced by cells and diverse observed cellular responses of individual cells. This innovative analytical approach allowed us to uncover intriguing insights into the spatiotemporal dynamics of migrating neutrophils, along with the potential presence of a migratory memory mechanism.

2.3 Results

2.3.1 Establishment of Sixt Neutrophils and how They Differ From Dendritic Cells

Upon project start, the absence of established protocols for primary neutrophils or neutrophil-like cells within the research group necessitated the initial task to create or adapt protocols. This included securing an ethical approval for the isolation and handling of primary human neutrophils, as well as initiating the cultivation of diverse cell lines such as HL-60 and PLB-985. Additionally, SCF-HoxB8 cells, an immortalized murine neutrophil cell line, were successfully implemented and their motility enhanced (as detailed in chapter 4.1.2). The establishment of these cell lines also involved fine-tuning various parameters for our diverse cell migratory assays, including optimal cell quantities and the identification of the most effective chemoattractants and their respective concentrations.

Given that the research group primarily focuses on dendritic cells (DC), DC were used as a benchmark for adapting protocols for neutrophils. Remarkably, in collagen assays, while DC exhibited a slow but very persistent acceleration toward a

chemotactic stimulus for many hours, neutrophils and neutrophil-like cells displayed an initial rapid burst in speed, followed by a transition into random migration after approximately 30 minutes to a maximum of 2 hours (see figure 22 in chapter 4.2.1). The observed burst behavior involves swiftly migrating toward the attractant source, followed by a transition to random movement. This initial phase is characterized by accelerated, directed motion toward the attractant's origin, showcasing the rapid response of neutrophils to the signaling cue. However, this focused migration is short-lived, and the cells subsequently adopt a more random pattern of movement.

Intriguingly, all tested cell lines, including SCF-HoxB8 cells, showed random migration when there was no attractant. However, primary human neutrophils were initially non-motile, yet triggered a pronounced "La Ola" response once exposed to an attractant (data not shown). Despite the gradient fields for the attractants theoretically being equivalent, this divergent response to the attractant between neutrophils and DC highlights distinct spatial and temporal dynamics employed by these cell types, which likely contribute to the observed disparate behaviors.

As notable spatiotemporal dynamics between DC and neutrophils in 3D collagen assays were discernible during the initial establishment phase, these assays were selected for the subsequent experiments. This decision was further supported by their capability to closely mimic *in vitro* physiological migratory conditions and effectively reveal migratory deficiencies in cells. Subsequently, fMLF was selected as the primary attractant and for the choice of cell line, PLB-985 cells were picked, considering their greater accessibility compared to primary neutrophils. Additionally, based on empirical data, PLB-985 cells exhibited superior migratory capabilities compared to HL-60 or SCF-HoxB8 cells (data not shown).

2.3.2 Effect of Point and Line Sources on Persistence and Migratory Efficiency

To investigate the spatiotemporal migration dynamics across different gradient configurations, experiments employing various setups were conducted. These included experiments without any chemoattractant (i.e., control), setups involving a line source with concentrations of either 5 or 20 nM of fMLF, and experiments utilizing a pipette containing 1000 nM of fMLF embedded into the collagen matrix. The selection of 5 and 20 nM concentrations was based on their ability to induce a semi-persistent directional migration response, with 5 nM serving as a lower threshold and 20 nM as an upper threshold. Of note, prolonged chemotactic responses were not observed for concentrations lower than 5 nM and between the concentration range of 25 – 50 nM cells initially migrated toward the gradient, followed by a brief phase of random migration before entering an anergy phase where migration stopped (see figure 6 A). While the line sources aimed to generate relatively linear gradient fields, the point source should generate a radial gradient pattern and was previously used in the laboratory for cells, such as macrophages, that did not respond well to line sources. The point source, provided at 1000 nM, was also tested at lower concentrations but higher concentrations resulted in recruitment across the entire field of view (~ 2400 µm, with cell lengths of ~ 19 µm), while concentrations of 100-200 nM produced recruitment coverage of less than half the field of view (data not shown).

Upon visual examination of the single-cell tracks, distinct differences between the experimental setups already became evident (see figure 5 A). Control cells exhibited predominantly random migration with minimal total displacements. Conversely, cells exposed to fMLF displayed markedly enhanced directionality and covered greater distances. Although subtle differences existed between the two-line sources, both seemed to initially follow the gradient but then shift to random migration. Interestingly, cells exposed to point sources exhibited a distinct behavior from control or line sources,

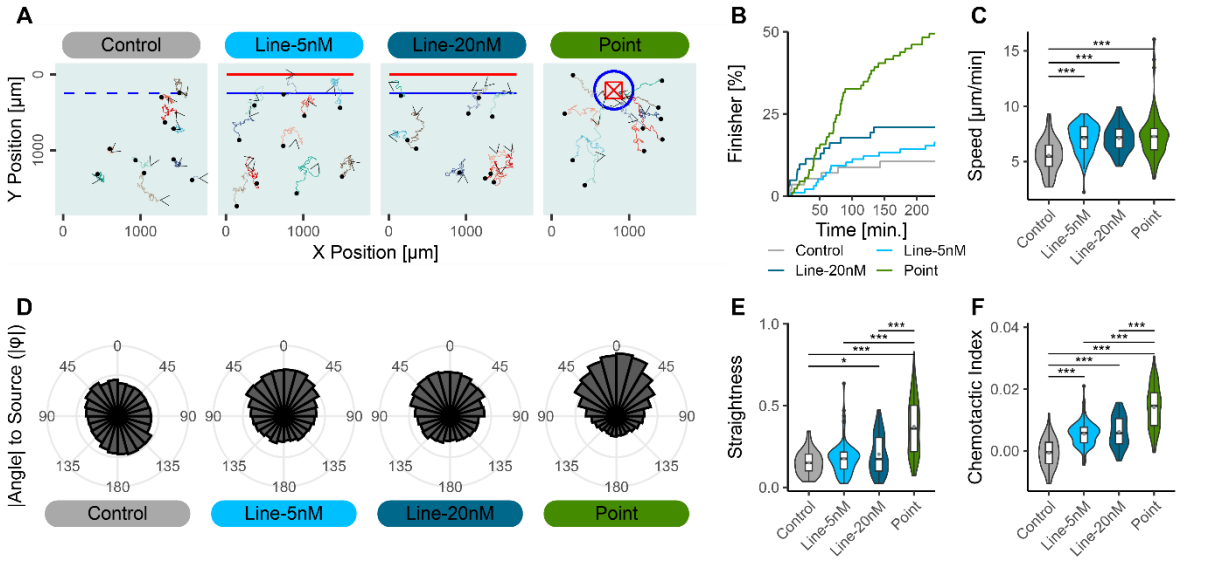


Figure 5: Point sources outcompete line sources in fMLF chemotaxis. **A)** Trajectories of 10 random cells of each control (0 nM), Line-5nM, Line-20nM, and point (1000 nM) are shown. Black dots indicate the track start and arrowheads show the orientation of the last time point. Red lines and the red box show the position of the respective source of chemoattractant. Blue lines and blue circle indicate the 250 µm finishing range for B). **B)** Percentage of finishers over time. Finishers are cells that reached within the range of 250 µm around the source (see blue line in A). **C)** Median speed of whole cell tracks over the course of the experiment (≙ 240 minutes). Pairwise Wilcoxon rank sum test with continuity correction (Bonferroni), ***, P < 0.001. Non-significant values (P > 0.05) are not shown. **D)** Absolute angle to source distribution (Φ) of cells at each time point in the range of 0 to 180 degrees. The closer the value is to 0, the better-aligned cells are. The right hemisphere shows angles in the rightwards direction whereas the left hemisphere shows leftwards angle directions in relation to the respective source. Values are over the course of the experiment (≙ 240 minutes). **E)** Median straightness of cell tracks. Straightness is defined as the Euclidean distance (the shortest path between track start and end) divided by the total traveled distance. The total traveled distance was calculated based on the distance a cell traveled throughout the duration of the experiment (≙ 240 minutes). Pairwise Wilcoxon rank sum test with continuity correction (Bonferroni), *, P = 0.025, ***, P < 0.001. Non-significant values (P > 0.05) are not shown. **F)** The summarized chemotaxis index (CI) of all cells. The CI is defined as the total distance a cell travels toward the source in relation to its total traveled distance. The total traveled distance was calculated based on the distance a cell traveled throughout the duration of the experiment (≙ 240 minutes). Pairwise Wilcoxon rank sum test with continuity correction (Bonferroni), ***, P < 0.001. Non-significant values (P > 0.05) are not shown.

showing a consistent and persistent gradient-following trajectory without noticeable phases of random migration. Upon conducting a more comprehensive analysis of the distinct experimental configurations, our initial observations were supported. After approximately three hours, nearly half (49 %) of the cells tracked in point sources had successfully entered a predetermined finishing zone spanning 250 µm around the source origin (see figure 5 B). In contrast, by chance only 11 % of cells in the control group reached this zone. Both line sources performed better than the control but significantly worse than the point source as line-5 and line-20 setups had corresponding finishers of 16 % and 21 %, respectively.

When comparing the median speeds of all tracked cells, it became evident that gradient experiments consistently exhibited markedly higher speeds than the control. However, no statistically significant differences in speed were observed between any of the gradient experiments (see figure 5 B). Analyzing the distribution of angles toward the source at each time point, a discernible pattern emerged (see figure 5 D). Control cells exhibited a nearly uniform distribution, whereas cells subjected to gradient experiments displayed distributions skewed toward lower angle offsets. This observation

indicated that, at any given time, cells in gradient conditions were more consistently oriented toward the respective source. Intriguingly, no significant distinction in distribution was observed between the two-line sources. However, the point source exhibited a notably stronger alignment toward the source compared to both line sources. This is particularly intriguing because achieving better alignment for point sources is comparatively more challenging. Whereas for line sources, any movement in the y-direction (i.e., upward the gradient) results in alignment toward the source. In contrast, point sources are defined by a single pixel as the target, granting them more degrees of freedom to deviate from the alignment.

The observation of better alignment among cells exposed to point sources was also captured by using the straightness metric (see figure 5 E). This metric quantifies the straightness of a cell's trajectory by comparing the total distance traveled to the shortest Euclidean distance between the starting and ending point of a track, a higher index, therefore, indicating a straighter trajectory. Notably, the point source (0.36) exhibited significantly better alignment compared to both line sources and the control. While no significant difference was found between line-5 (0.17) and the control (0.15), a slight yet significant difference was observed between the control and line-20 (0.17). Nevertheless, both line sources displayed higher straightness values than the control, indicating a trend of being more directional when an attractant is present. It is noteworthy that by selecting only the initial 30 to 60 minutes, the straightness of line sources would exhibit a significant increase (data not shown). This observation implies that cells encountering line sources display considerable persistence during the initial stages as well. However, the subsequent phase of random migration contributes to a substantial offset when considering the entire timespan.

Upon assessing the chemotactic index, which normalizes the overall distance traveled by the distance covered solely in the direction of the source, it is evident that all gradient experiments substantially surpass the control group (-0.0003). While both line-5 (0.0059) and line-20 (0.0058) exhibited similar chemotactic indices, the point source (0.0146) again significantly surpassed both line sources.

Remarkably, restricting the analysis to the initial 30 minutes reveals intriguing variations in behavior. Line-20 exhibits a higher number of finishers compared to both the point source and line-5. Although speed remains consistent across all samples with attractant, the point source demonstrates a lower distribution of angles toward the source and slightly higher straightness and chemotactic index, albeit with a notably smaller difference compared to the analysis considering the entire track duration (data not shown). Notably, as the analysis time interval expands, the distinction between the point source and line sources becomes more pronounced, showing a substantial difference even within the initial 60 minutes (data not shown). When comparing various time windows, it is observed that throughout the experiment, values for point sources remain consistent, while line sources exhibit a decrease in their respective values.

In summary, our initial observations reveal that when neutrophils perceive a gradient, their speed significantly increases. However, while cells exposed to line sources exhibit only initially a gradient-tracking behavior, those exposed to point sources demonstrate a higher level of sustained and efficient gradient-following. Our comprehensive analysis of diverse parameters, measuring persistence and directionality, showcases a superior performance of neutrophils exposed to point sources compared to those exposed to line sources. This also includes the proportion of cells successfully reaching the target location. Of note, for the remainder of this study, the term "persistence" is a composite measure best explained by encompassing various factors such as straightness, chemotactic index, and angle distribution. In essence, this term denotes the duration a cell maintains its trajectory. It represents a collective assessment

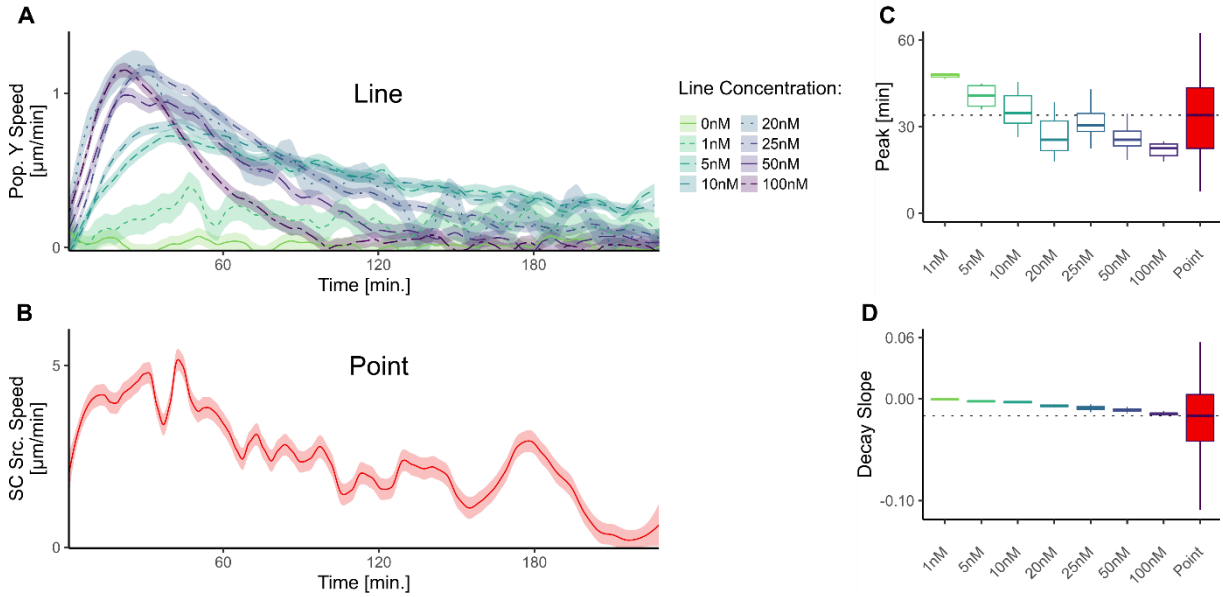


Figure 6: Desensitization and chemoattractant titration. **A)** Speed in y direction (source is the top y-axis) of whole populations in collagen with various fMLF concentrations for line sources. Only the displacement in y direction between two frames was computed and divided by the framerate. Lines show a LOESS fit with a span of 0.1. Ribbons show the 95 % CI. *Pop*: Population. **B)** Speed in source direction for the point source. While A) shows whole population tracks, this shows the speed toward the source of tracked single cells. Only the displacement in source direction was computed between two frames and divided by the framerate. Lines show a LOESS fit with a span of 0.1. Ribbons show the 95 % CI.*SC*: single cell; *Src*: source. **C)** The time when populations (line sources) or single cells (point sources) reach their directional speed (population y speed or single cell source speed) peak. Dotted lines indicate the median of the point source. **D)** The decay slope of populations (line sources) or single cells (point sources) for the continuous decrease in speed after the peak time. The respective peak of each cell in C) was used as a starting point to compute a linear fit from the peak to the last time frame, and the slope of the decaying line was extracted and is shown here. Dotted lines indicate the median of the point source.

of how consistently and for how long a cell persists in a particular direction over extended periods of time. The quantitative proxy for persistence in this context considers the interplay of multiple parameters, reflecting the overall tendency of a cell to maintain its course. The term "directional persistence" further integrates this concept with directionality, capturing how long a cell migrates toward the attractant source.

2.3.3 The Potential Role of Desensitization

A possible explanation for the reduced persistence in line sources could be related to receptor desensitization and/or oversaturation. This occurs when the concentration of fMLF becomes too high, leading to a state where the receptors on the neutrophil's surface become less responsive to the gradient of the attractant. Essentially, the receptor's ability to detect the gradient might be diminished due to an overwhelming concentration of fMLF. One could hypothesize that point sources, despite starting with a higher concentration of fMLF (1000 nM), have a smaller reservoir of the attractant (around 4-10 µL). On the other hand, line sources have a larger reservoir (about 100 µL). As a result, in the case of point sources, the concentration of fMLF might be very high near the pipette but rapidly diminishes as the distance from the source increases. In contrast, for line sources, cells might experience higher concentrations of fMLF in general, even when farther away from the pipette. This difference in concentration distribution could contribute to the observed differences in cell behavior between point and line sources. Neutrophils encountering point sources may experience a rapid change in concentration, leading to a more focused and persistent migratory

response. Conversely, for line sources, the more evenly distributed concentrations could result in a less pronounced migratory response over time.

To test this hypothesis, a straightforward approach is to conduct a titration assay for line sources, wherein the source concentrations of fMLF are varied. If desensitization or oversaturation of neutrophil receptors is indeed contributing to the observed behavior, one would anticipate reaching a concentration threshold at which the persistence of cells in line sources approaches that of point sources. To investigate this, a series of collagen assays with varying concentrations for the line source was performed, ranging from 0 nM to 100 nM (see figure 6 A, C, D).

The experiments showed that in general concentrations lower than 3 nM did not induce a persistent migration toward the source; rather, they increased the overall speed of the cells (data not shown). Among the tested concentrations, 5 nM emerged as the lowest concentration capable of generating a sustained migration, surpassing the effects observed at lower concentrations. Remarkably, two discernible trends became evident. Firstly, as the concentration increased, the acceleration phase (burst phase) of migration was faster, leading to reaching the maximum y-directional displacement earlier. Secondly, at higher concentrations, the rate of decay in y-directional displacement was more pronounced, resulting in decreased persistence. Consequently, higher concentrations facilitated faster acceleration toward the source but concurrently caused a quicker transition into random migration.

Nonetheless, irrespective of the used concentration, cells exhibiting the same level of persistent gradient-following behavior as seen with point sources was never observed. Directly comparing the datasets of the shown line sources and the point sources is not feasible due to the differing analytical methods. In figure 6, the data for line sources is generated through a script that analyzes the x and y displacements of entire cell populations between frames. Conversely, point sources lack a fixed source axis, such as y = 0 for lines, and cells migrate toward a singular point. Therefore, using the same script would yield random migration for point sources. This arises from the fact that any directional movement, such as a cell migrating from the bottom left to the center, would be entirely counteracted in the employed script by another cell migrating from the top right to the center. Although we attempted to correct this using a polar transformation, this approach introduced significant artifacts, rendering the script unsuitable for point sources. To allow some comparison, the displacement speed toward the source of single cell tracks in point sources was employed as a parameter (i.e., the displacement solely toward the source of single cells between two consecutive timepoints was divided by framerate to obtain this speed value). This analysis reveals that point sources outperform all line source concentrations below 10 nM in acceleration and all line sources in persistence (see figure 6 C, D). It is important to note that the data are not directly comparable, as line sources used population-wide analysis while point sources utilized single-cell trajectories. Despite these limitations, the analysis underscores some degree of comparability. Furthermore, our analysis approach presents its challenges. A maxima detection was utilized to find the first peak and assess the slope thereafter to measure the decay of directional persistence. However, this procedure may result in artifacts. For instance, the 1 nM sample displays minimal response to the attractant, leading to a near-flat curve close to the control, thus explaining its low slope. Additionally, the first peak for the 1 nM sample most likely originates from noise, as the largest peak can be seen shortly before 60 minutes.

Based on these findings, it was concluded that desensitization plays a limited role. While lower line source concentrations do induce a slight increase in persistence, no persistent chemotaxis was observed reaching the same extended level as seen with point sources. Furthermore, even in the vicinity of the 1000 nM point source, where the

fMLF concentration should be exceptionally high, one can still observe directional movement toward the pipette. This suggests that oversaturation and desensitization are not the predominant factors at play here.

2.3.4 Interventions on Migratory Persistence

Throughout this project, we engaged in discussions with various fellow scientists and reviewed numerous research papers that discussed strategies to potentially enhance cell persistence or presented data suggesting such effects (see table 1). Recognizing that cell persistence likely connects to spatiotemporal dynamics of receptors, any successful alteration of directional cell persistence could also offer valuable insights into the underlying components involved. Throughout this project, a multitude of diverse interventions was performed, each targeting distinct fundamental concepts that could plausibly impact cell persistence. Due to the substantial extent of this list and the associated figures, a concise summary is presented, outlining the intervention, its underlying rationale, and the resultant outcomes. For the analysis, line sources at varying concentrations were employed and evaluated differences using the previously mentioned script, which uses population y displacements between successive timeframes.

Given our predominant use of fMLF, alternative formylated peptides were explored that exhibit higher affinities for FPR, like fMIFL and fMIVIL [96]. Surprisingly, using these peptides resulted in decreased persistence and a more subtle burst pattern, characterized by a less pronounced peak and a smoother displacement curve. The observed burst behavior of neutrophils involves rapid migration toward the attractant source, followed by a shift to random movement. As previously described, this initial phase is marked by accelerated, directed motion, emphasizing the swift response of neutrophils to the signaling cue, yet it is short-lived, and the cells subsequently adopt a more random pattern of movement.

Intervention	Expected Outcome	Measured Effect
Use agonists with higher affinity → fMIFL and fMIVIL	Higher affinity could correlate with persistence & directionality	„Smoother“ burst; Decreased persistence
Use other attractants → IL8, C5a and LTB4	Persistence depends on the type of attractant	No effect
Block relay function → LTB4 & IL8 block	Relay overlays primary gradient	No effect
Block p38 (FPR internalization ↑) → Use pharm. inhibitors	Less Persistent (less receptor available)	Stronger burst; Same persistence
Block Erk (FPR internalization ↓) → Use pharm. inhibitors	More Persistent (more receptor available)	Stronger burst; Same or decreased persistence
Increase FPR amount → Nutridoma-CS	More Persistent (more receptor available)	No effect
Prevent fMLF oxidation → Add β-mercaptoethanol	Methionine gets oxidized and cannot bind to FPR	No effect
Test other “neutrophils” → PLB, HL, primary	Potentially altered proteome affecting chemotaxis	No effect

Table 1: A compilation of various methodological interventions to improve the migratory persistence of cells in 3D collagen assays. The list also contains the potential outcome of each intervention as well as each outcome.

Recognizing that persistence could be influenced by the nature of the attractant, the corresponding receptors, and the subsequent signaling cascades, various attractants were investigated. Representatives of primary (IL-8), intermediate (LTB4), and end-point (C5a) attractant families were incorporated, which have been postulated to engage distinct signaling pathways. Despite the variation in attractants, and thus receptors and signaling pathways, the same pattern as with fMLF was consistently observed – an initial burst of directed migration followed by a decay in directionality. These findings suggest that the specific directional persistence is not solely regulated by the type of attractant or the subsequent receptor and signaling pathway.

To address the potential impact of relay functions mediated by LTB4 and IL-8, which could introduce additional gradients potentially interfering with our attractant gradients, experiments were conducted where both relay functions were inhibited by blocking the respective receptors. However, these interventions did not yield any discernible effects on the observed cellular behaviors or directional persistence.

The most promising intervention was inspired by a study conducted by Lui et al., in which they demonstrated altered persistence through inhibition of Erk or p38 [97]. Following their approach, the same pharmaceutical inhibitors were used, but our results for the Erk inhibition yielded a slightly reduced persistence and an augmented burst, contrary to the anticipated increase. Regarding p38 inhibition, our experiments similarly revealed a stronger burst phase, yet no discernible impact on persistence was detected. It's worth noting that we encountered substantial challenges with drug precipitation, especially when using the concentrations reported by Lui et al, even under adequate temperatures and with varying solvents. Adjusting inhibitor concentrations failed to yield any consistent effects. A noteworthy distinction between our work and theirs lies in the assay setup, while they employed a 2D coated migration assay, our study utilized a 3D collagen assay. This variation may contribute to the observed differences in cellular response.

The potential influence of receptor quantity was also studied, as the availability of receptors might be crucial for controlling the spatiotemporal dynamics. In exploring various differentiation protocols for PLB-985 cells, a method involving Nutridoma-CS was identified that can enhance the FPR1 expression, which is the main receptor for formylated peptides [98]. However, despite achieving elevated FPR1 expression levels, no impact on directional persistence was measured.

Research showed that the methionine's formyl group can undergo oxidation, rendering the oxidized version undetectable by FPR [99]. It is possible that fMLF may undergo oxidation during the experiment, leading to a diminished response to fMLF over time. However, using β-mercaptoethanol to prevent oxidation did not yield any noticeable effect on cell persistence.

Finally, different neutrophil types were explored, including primary human and murine neutrophils, as well as PLB-985 and HL-60 cells. This investigation aimed to rule out the possibility that genetic mutations within specific cell types were causing the observed persistence. Despite the variations in persistence between these neutrophil types (with primary human and PLB-985 cells exhibiting higher persistence), the results remained consistent within each neutrophil type. Concentration variations in line sources did not lead to prolonged directional persistence. However, this experimentation did highlight that inherent cellular differences play a role in modifying the spatiotemporal response to gradients. This distinction was particularly evident as murine neutrophils exhibited significantly lower directional persistence and only responded at higher concentrations (see chapter 4.1.2).

In summary, the various tested interventions did not increase the directional persistence and, at best, decreased it. Most interventions had no effect at all on the

persistence, but instead, the observed outcomes primarily involved modifications in the initial burst behavior. This alteration resulted in either a quicker burst or a less abrupt and smoother burst response. It appears that the factors governing persistence are part of a more intricate system, whereas burst behavior likely stems from the initial reactions of receptors and cells to the newly encountered attractant. Consequently, while persistence seems to be a longer-term process, the initial burst behavior may be influenced by shorter-term factors.

2.3.5 Differences in Gradient Dynamics Between Point and Line Sources

As it was not possible to enhance the persistence of cells in line sources to match that of cells in point sources, we wondered what caused the significant difference in directional persistence between these setups. As mentioned in the introduction, the primary difference between the two lies in how, and to some extent how much of the attractant is delivered to the cells. Based on this premise, the dissimilarity should be rooted in the gradient encountered by the cells. Consequently, for the next step, it was aimed to visualize, and subsequently analyze the gradient within the collagen assays.

However, cell migration is a delicate process that is often very sensitive to interference from reactive oxygen species (ROS) induced by the photo-instability of labeled proteins involved in the cell migration apparatus or by having dyes very close to them. To circumvent this, a label-free experimental setup was selected where a proxy dye for fMLF was used. Of note, our experiments with labeled fMLF variants indicated that cells progressively decelerated over time and exhibited reduced persistence even without illumination (data not shown, but a similar trend is evident in figure 17). This phenomenon is likely attributed to modifications in the chemical or physical properties, as well as the size, of the labeled fMLF. These alterations can impact the affinity of the molecule to the FPR. To facilitate the visualization of low concentrations over prolonged durations and thereby ensure the accurate tracking of gradient propagation

at the single-cell level, the use of a dye that is both photostable and very bright was necessary. These attributes are commonly found in Atto-tec dyes which are used extensively in super-resolution microscopy. It was also aimed for a dye that closely approximated fMLF in size to ensure similar gradient propagation, given that the diffusion coefficient is largely governed by molecule size. Combining all the required

attributes, the Atto-488 (590 – 804 Da) and Atto-633 (552 – 652 Da) were selected as proxy dyes for the experiments, with Atto-633 being predominantly used in the results of this thesis due to its enhanced reliability. However, the observed gradients were analogous for both Atto-488 and Atto-633. Notably, though slightly larger, the diffusion of Atto dyes should only marginally decrease according to the Stokes-Einstein equation. For instance, fMLF has a radius of approximately 0.678 nm, while Atto-488, the larger dye, can reach up to 0.827 nm in radius. Consequently, the diffusion coefficient for fMLF would be around 2.96e-9 cm^2/s, and for Atto-488, it would be 2.42e-09 cm^2/s.

To understand what concentrations a cell experiences within the respective experiments, and to potentially correlate it with cell behavior, the proxy gradient field around single cells was measured. As a first step, the length of dPLB-985 cells in collagen was measured across various concentrations and experimental setups, which resulted in a median length of 18.6 µm (see figure 7 A). Additionally, the center of mass of single cells was manually tracked to ensure an accurate and consistent tracking throughout all experiments. This was crucial, as the measured length and the single-cell tracks formed the basis for the subsequent computational script. This script used the center of mass of each cell to assess an area in front and rear of the cell, from which proxy values were extracted. The cell's estimated orientation, obtained by a spline

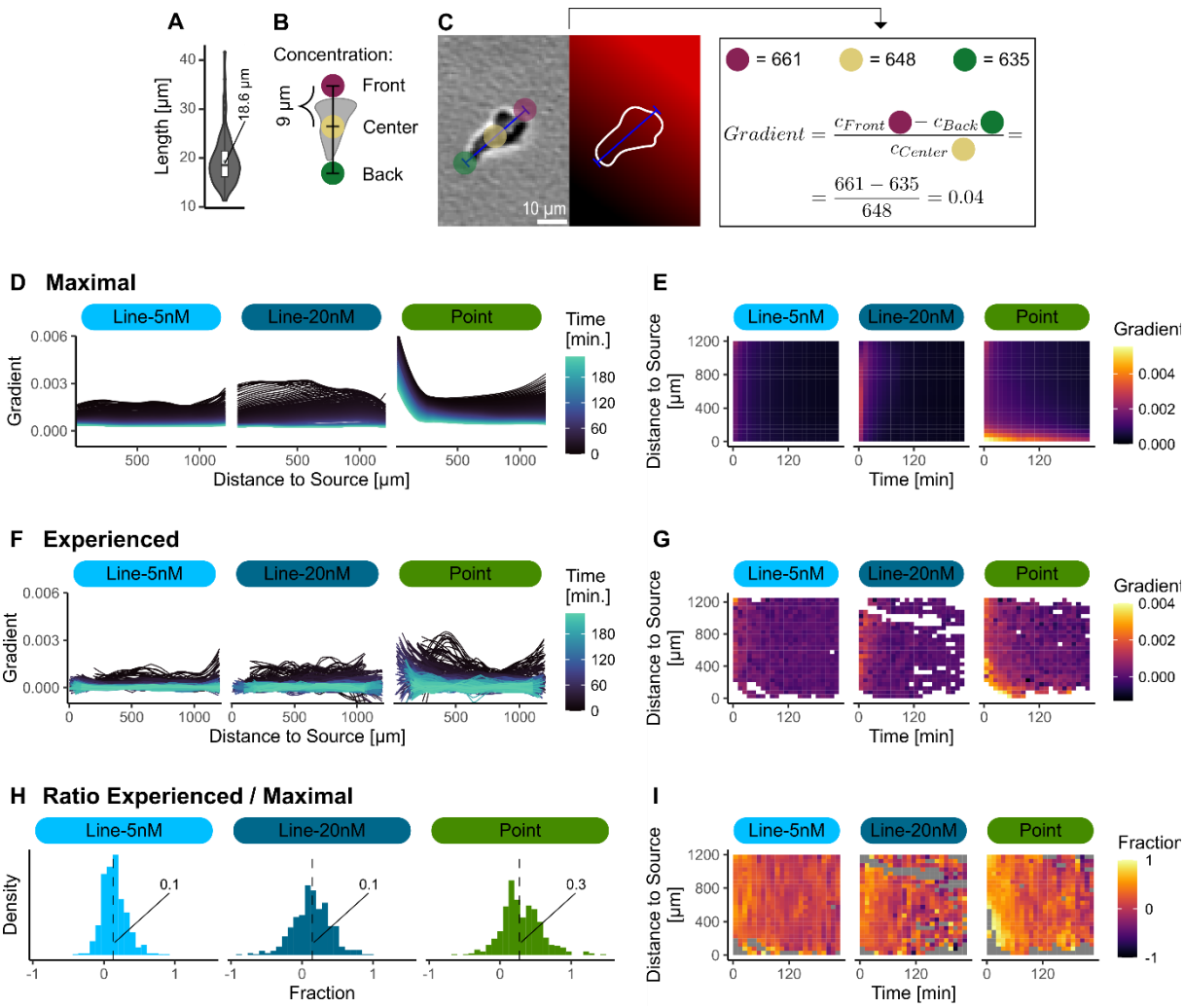


Figure 7: Visualization of (maximal-)gradient experiences of cells during chemotaxis via fluorescence proxy values. **A)** Median length of cells in collagen, n = 124. **B)** Schematic of proxy fluorescence extraction around migrating cells. The center of mass (≙ cell center; yellow area) was tracked where the center concentration was extracted. Additionally, extractions happened 9 µm in the front (red) and 9 µm at the back (green) of the cell with respect to the center location. Orientations for the front and back of cells were derived from spline interpolations (see figure 8 F). **C)** Example of a fluorescence extraction and gradient calculation of a migrating cell. *Left*: A migrating cell and areas where the smoothed proxy values are extracted are shown. The white line shows the outline of the cell. The blue line indicates the cell length. Due to the use of widefield microscopy the cell shape is not creating a shadow within the proxy field. *Right*: A typical ∆c calculation with the extracted values is shown in the box. **D - G)** Maximal (*top*) and experienced (*bottom*) gradient values as indicated in 2C. Maximal gradients were calculated at each pixel of the movie over all time frames with a 0-degree angle to source deviation (i.e., perfectly aligned). Experienced values are calculated from tracked cells. *Left*: The front–back difference plotted against the distance to the source with color showing how the magnitude develops over time. Values were smoothed using a loess fit (span 0.4) before plotting. The y-axis range was set to -0.001 and 0.006. *Right*: Time and distance to source are binned (10 min. and 50 µm, respectively) and median gradient values of these bins are calculated. Values were smoothed using a loess fit (span 0.4) before binning. **H - I)** The difference as a ratio (Experienced / Maximal) of the respective heatmaps is shown as a density histogram (H) or as a heatmap (I). The dashed line in H represents the median value of the fraction, which is also shown.

interpolation of its actual tracks (see figure 8 F), determined each cell's front and rear. With the cell length measured at 18.6 µm, a 9 µm difference between the center to the front as well as the center to the rear was set to still encompass the cell's body rather than being just outside it (see figure 7 B). The gathered data were subsequently utilized to calculate a gradient value for each cell. This process involved subtracting

the rear value from the front value and normalizing it using the center concentration (as demonstrated in figure 7 C). This calculated gradient value represented the "experienced" gradient, reflecting the actual exposure of cells to the gradient. Additionally, an investigation was conducted into what a cell might experience if it were consistently optimally oriented toward the source within the collagen assay. The "maximal" gradient was assessed using a script that virtually placed cells at every pixel and time point within the collagen, optimally oriented them, and extracted concentrations in the same manner as for the experienced gradient (front, center, back at 9 µm distance). This calculated gradient value was termed the "maximal gradient," mirroring the "experienced gradient". The comparison of the "maximal gradient" with the actual "experienced gradient" provided insights into the potential gradient's strength and persistence for each experimental scenario.

Notably, the "maximal gradient" analysis revealed that point sources exhibited significantly higher gradient strength and better gradient retention than line sources (see figure 7 D, E). Interestingly, throughout the experimental time, the maximal gradient observed in point sources consistently surpasses that of any of the line sources. In addition, the gradient profile near the pipette's vicinity displayed an exponential shape, indicative of a robust gradient potential with substantial Δc values. While line-20 initially showed a stronger gradient than line-5, it quickly dissipated into an indiscernible gradient, eventually converging with line-5's maximal gradient.

Strikingly similar outcomes were observed when analyzing the real "experienced gradient" (see figure 7 F, G). Cells within point sources experienced markedly stronger gradients than those within line sources, with significantly better retention over time. Although line-20 initially exhibited a higher gradient potential than line-5, its strength diminished to levels like line-5, yet it maintained a superior gradient potential over time. When analyzing experienced gradients, it becomes evident that they exhibit greater variability, occasionally even yielding negative gradients when cells move in the opposite direction of the source. Additionally, these experienced gradients tend to yield considerably lower average gradient values compared to the maximal potential values.

Directly comparing the "experienced" and "maximal" gradient values for each experimental setup demonstrated that while both line sources approximated only around 10 % of the maximal potential, point sources reached 30 % (see figure 7 H, I). This indicated that cells within point sources approached the possible maximum values more closely than cells within line sources.

It's worth highlighting that a notable valley-like pattern is particularly observable in both “maximal” and “experienced” gradients for point sources. This phenomenon potentially arises due to the intense gradient near the source, and a similar sharp change from no concentration to some concentration on the opposite side. This can lead to elevated gradient values in these regions.

Examining the raw proxy intensity values obtained from each pixel of the movie further reveals interesting insights (data not shown). Notably, both line sources exhibit a transient exponential gradient at the beginning, which subsequently transforms into a linear gradient over time. Intriguingly, the proxy values from the line-20 configuration indicate that the gradient propagation is quicker compared to line-5, yet it also decays more rapidly into a linear form. In contrast, the point source consistently maintains an exponential shape throughout the entire duration of the experiment.

Combining all these observations, it can be concluded that in light of concentration differences (Δc), cells within point sources consistently experience a significantly higher gradient than those in any of the line sources. This effect is particularly pronounced for cells positioned near the source. Furthermore, the data also highlight an initial higher gradient for cells in the line-20 experimental setup compared to the line-5

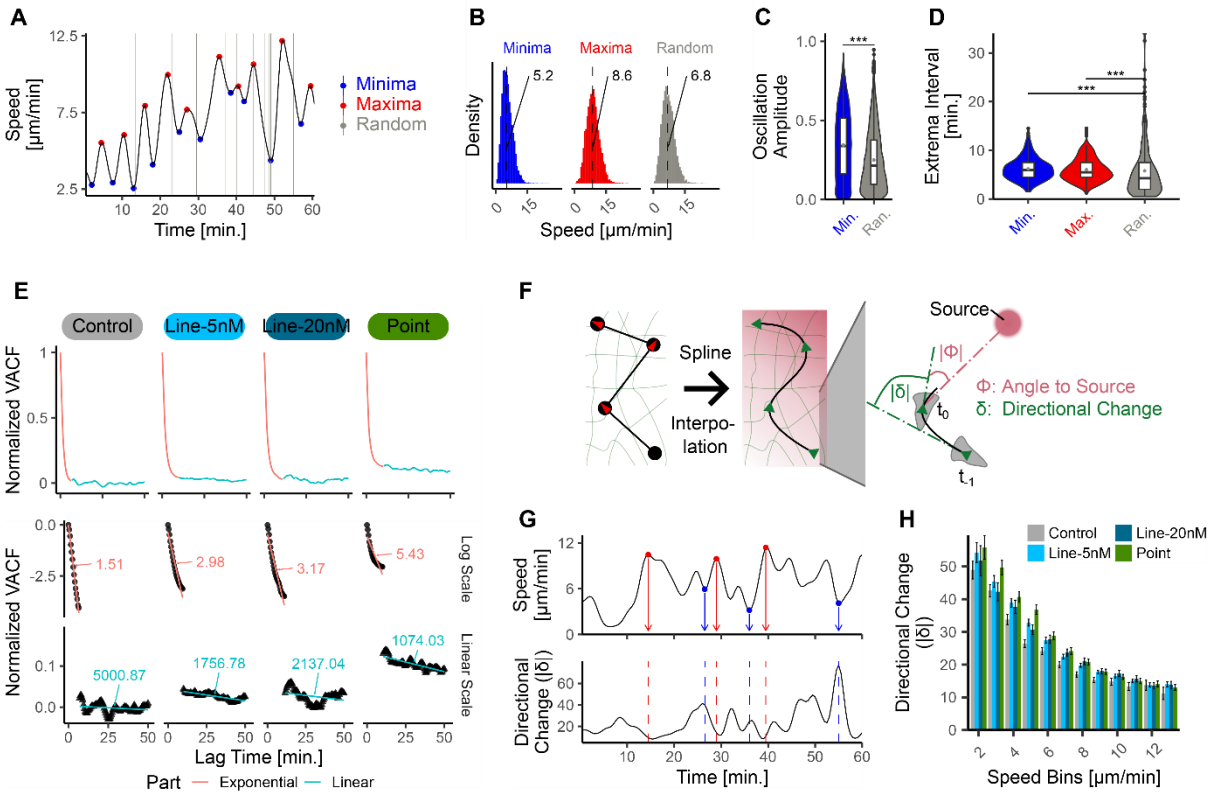


Figure 8: Speed oscillations and their influence on angle changes. **A)** The oscillation of the smoothed speed of an example cell. Minima (blue), maxima (red), and random spots are highlighted. Random time points are sampled randomly, and the total count of randomly selected points matches the number of minima present. **B)** Distribution of speed around the extrema. Values shown are the median of the respective extrema. **C)** Proportion of the amplitude change indicating how much the speed changed at any minima compared to the previous maxima ($\frac{speed_{max} - speed_{min}}{speed_{max}}$) or between two randomly sampled time points. Pairwise Wilcoxon rank sum test, ***, P < 0.001. **D)** Time interval between two consecutive extrema (e.g., minima to minima). Pairwise Wilcoxon rank sum test with continuity correction (Bonferroni), ***, P < 0.001. Non-significant values (P > 0.05) are not shown. **E)** *Top*: Modified normalized velocity autocorrelation function (VACF) shown in linear scale, red lines indicate the initial exponential decay and blue lines show the stationary phase. For the calculations, the unit vector was used to reduce the effect of speed oscillations and focus on vector orientation changes. This means that the analysis exclusively considered the direction of the velocity vectors and did not take into account the magnitude (i.e., speed) associated with those vectors. *Bottom*: For the exponential decay a linear fit in the logarithmic scale was performed and the corresponding persistence time in minutes is shown. For the stationary phase, the linear fit was done within the linear scale. **F)** Schematic of track processing and calculated angular parameters. *Left*: Single-cell trajectories typically are in a "zig-zag" pattern with points not depicting the true directions of cells at the respective time point (red arrows within black circles). Using a spline interpolation more realistic orientations of cells at each time point are available (green arrows on black line). *Right*: Cell orientations are used to calculate the directional change (δ) of a given time point (t_0) to its previous time point (t_{-1}) as well as the current angle to source (Φ) at the current time point. **G)** Stacked graphs of an exemplary cell showing speed (*top*) and directional change (δ; *bottom*) over time. Three speed minima (blue) and maxima (red) were chosen at random and dashed lines indicated their location in the speed as well as in the directional change plot. **H)** Correlation of speed and directional change (δ). Speed was binned in 10 uniform-sized bins and the respective bin median of the directional change is shown with the 95 % CI. Values on the x-axis represent the mean value of the speed bin.

configuration. These findings potentially provide an explanation for the more robust and rapid burst observed in cells subjected to line-20 experiments compared to line-5, as well as explain why cells within point sources surpass any line source concentration in terms of directional persistence.

2.3.6 Migratory Speed Minima and how Cells Utilize Them for Informed Trajectory Adjustments

Upon discovering the significant differences in gradients, our investigation extended to analyzing various parameters of single-cell trajectories. When the speed of individual cells over time was studied, it revealed a rather intriguing phenomenon – cell speeds consistently exhibited oscillatory patterns (see figure 8 A). This observation led us to wonder whether these fluctuations originated from inherent cellular noise or if they represented a tracking-related artifact. Consequently, a comprehensive exploration was performed to determine whether this phenomenon was random in nature or if it held meaningful biological implications.

First, both the minima and maxima points within the speed trajectories of individual cells were identified. As a control, a random sampling of time points was also performed so that the number of random points matched the count of minima for each cell. As expected, distinct speed distributions between the extrema were observed. The median speed around minima was the lowest (5.2 µm/min), around maxima it was the highest (8.6 µm/min), and random time points exhibited an intermediate value (6.8 µm/min) that fell between the two (see figure 8 B). When the amplitude change from a minima to a maxima or from one random point to another was examined, data showed that the median change at extrema was approximately 34 %, whereas random points exhibited an estimated change of 21 % (see figure 8 C). A notable observation emerged when considering the oscillation interval between the corresponding extrema (e.g., minima to minima, maxima to maxima, and random to random). The median interval was measured at 6.0 minutes for minima, 5.5 minutes for maxima, and 4.5 minutes for random points (see figure 8 D). More intriguingly, the interval distribution spread for minima and maxima is considerably smaller (~ 1 – 14.5 minutes), whereas randomly sampled timepoints exhibit a nearly exponential spread (~ 0.5 – 31.5 minutes). Of note, observations regarding the interval between extrema remained consistent across all experimental setups (i.e., line and point sources; data not shown). The employed methodology here (i.e., distance measures between extrema) is susceptible to noise but as two consecutive smoothing kernels were used, the influence of noise was mitigated to a minimum.

As a next step, the modified velocity autocorrelation function (VACF) was analyzed. The VACF is a commonly used particle analysis method that helps distinguish between random walks and active transport. Thus, the VACF provides insights into the persistence of movement in a given direction. It's important to note that unit vectors were employed for the analysis, which reduced the impact of the observed oscillating velocities and allowed us to focus on the orientation of each vector. This means that the analysis focused solely on the orientation of the velocity vectors, without taking into consideration their magnitude (i.e., speed). Our findings revealed that the VACF for all samples exhibited two distinct phases – an initial exponential decay followed by a slower, constant linear decay. Each of these phases was used to extract persistence times through linear fitting. Intriguingly, during the exponential decay phase, the control group displayed the shortest persistence time (1.51 minutes), followed by line-5 (2.98 minutes) and line-20 (5.43 minutes), while the point source exhibited the longest persistence time (5.43 minutes). Notably, all subsequent linear decay phases had persistence times exceeding 1000 minutes. Since only the initial decay corresponds to the time an object spends moving into a relatively similar direction, the linear decay time does not hold significant relevance here. Moreover, the data are non-stationary at this scale during the linear decay time, further underscoring their lack of relevance. Of note, when the analysis was restricted to the first 90 minutes of the experiments, the VACF

for both line sources notably improved, reaching levels comparable to the point source (data not shown). While the VACF data supported the conclusions drawn from figure 5, where cells in point sources displayed superior directional persistence compared to line sources and the control, it's also insightful to compare the VACF findings with the extrema interval data from figure 8 D. Interestingly, while the extrema intervals remained consistent across all experimental setups, the VACF data showed a clear trend of higher persistence for the point source in comparison to both line sources and the control. An approximate time difference of 6 minutes was identified between successive minima or maxima in the speed trajectories. Given that the midpoint between them corresponds to the opposite extrema, it follows that the time interval between minima and maxima is approximately 3 minutes. Consequently, one could reasonably regard any time interval within the range of 3 to 6 minutes as a potential run phase. Combining this with the made observations is intriguing, as it suggests that cells in point sources are utilizing their run phases more effectively than cells in line sources or the control. While cells in point sources use the upper limit of the run phase to migrate in the same direction, cells in line sources operate on the lower scale. Hence, cells in line sources appear to deviate more from their optimal trajectories during this time.

Given that both minima and maxima exhibited significant differences from randomly sampled points, it was concluded that they are neither noise nor artifacts. Hence, it was subsequently explored whether these extrema hold a biological meaning. Specifically, the focus was on the angular changes of the cell's trajectory. As the raw trajectories do not accurately represent the cell's actual migratory path, due to only showing endpoints at specific times, a spline interpolation was utilized to estimate the cell's true orientation at any given time (see figure 8 F). This estimated orientation was then employed to calculate the angle to the source (Φ), a measure of how much a cell deviates from an optimal path toward the source at any given time point. Additionally, the directional change (δ) was calculated, a parameter reflecting the degree of turning a cell underwent between two consecutive time points. In essence, the angle to the source provides insight into the cell's directionality, while the directional change informs about how persistent a cell migrates.

Upon examining the speed trajectory alongside the directional change, a distinct pattern emerged – they appeared to be inversely related (figure 8 G). When the cell's speed reached its maxima, the directional change tended to be minimized, and conversely, when the speed dipped to its minima, the directional change was often at its maximum. This inverse relationship between speed and directional change was consistently observed across all cells and experimental setups (see figure 8 H). This consistent pattern suggests that as the speed of the cell increases, the amount of directional change tends to decrease, and conversely when the speed decreases, the directional change tends to increase. Remarkably, this trend remained consistent regardless of the presence of a gradient, suggesting that the observed negative correlation between speed and directional change is a widely conserved phenomenon.

In summary, the data strongly suggest that the observed oscillations in cell speed are not a result of random noise or an artifact, as both minima and maxima show significant differences from randomly sampled points. These oscillations appear to be a conserved phenomenon in terms of frequency and are independent of the presence of an attractant. However, during the run phase between consecutive minima, cells in point sources seem to utilize their time more efficiently to migrate toward the source compared to cells in line sources. Furthermore, there seems to be a negative correlation between the directional change and the speed of cells. When cells are moving at higher speeds, they tend to make smaller angle changes, whereas speed minima are associated with larger angle changes.

2.3.7 Influence of Experienced Gradients on Trajectory Readjustments around Speed Minima

As observed, it appears that cells utilize speed minima to make angle changes, while using the time between consecutive minima as a run phase. The next question explored was whether the directional change (δ) that a cell performs is random or if it is oriented toward the source. Hence, this investigation included analyzing the angle to the source (Φ) around the extrema, as this parameter provides insights into the extent to which a cell's orientation deviates from the direction of the source.

Interestingly, when plotting the directional change against the angle to the source for all samples, most directional change values tend to be below 45 degrees (data not shown). Additionally, the presence of a gradient seems to significantly influence the distribution of the angle to the source, causing it to skew toward the lower end (i.e., a lower angle to the source means less deviation from optimal orientation to the source). These observations indicate that cells tend to avoid making substantial angle changes in their migration and when encountering a gradient, their trajectories appear to adjust to align with the gradient.

To analyze this phenomenon more thoroughly, the median directional change and angle to source were calculated at each time point around each extrema for every cell (see figure 9 A, top). This approach allowed to examine how the angle to the source changed both before and after each extrema.

From a cell’s perspective, while they slow down around speed minima, they increase their directional changes. Conversely, fewer angle adjustments are performed around speed maxima when cell speed is high. Taking the angle to source into account, it appears that the deviation from the source is largest at speed minima, but the larger angle changes at low speeds are used to correct their path towards the source during the upcoming run phase. Interestingly, cells seem to also use the local gradient (i.e., Δc) to reduce their directional change with an increased local gradient. More specifically, analyzing the directional change (δ), a conserved pattern across all experimental setups was observed, with consistent values for all samples (see figure 9 B, top). Around randomly sampled time points, the directional change values remained relatively steady, showing no distinctive pattern. Around minima, the directional change exhibited a distinct behavior as it began to rapidly increase approximately 1 minute before reaching the minima, peaked at the extrema, and then returned to its original value within about 1.5 minutes. On the other hand, around maxima, the directional change was highest roughly 2 minutes before and after the maxima, but it reached its lowest value at the maxima time point. This observation aligns with the findings from figure 8 H, indicating that when cells exhibit maximum speed, their angular changes are minimal, and vice versa. Furthermore, our observations suggest that as cells approach a minima, their angle changes become more pronounced, and as they approach a maxima, their angle changes become less pronounced. Of note, due to the roughly 3-minute distance between different extrema (minima to maxima), there is no overlap shown in the plot.

This observation becomes more intriguing when combined with the angle to source (Φ), which indicates the degree of alignment to the source of a cell, with lower values indicating better alignment (see figure 9 B, bottom). As only deviations up to 180 degrees in each hemisphere were considered, a randomly migrating cell would show an angle to source of 90 degrees. This is what was observed for all extrema in the control environment, indicating random migration for cells in the control. For the experimental setups involving a gradient, a consistent trend was noticed, although with varying strength. In comparison to the control, setups with a gradient exhibited

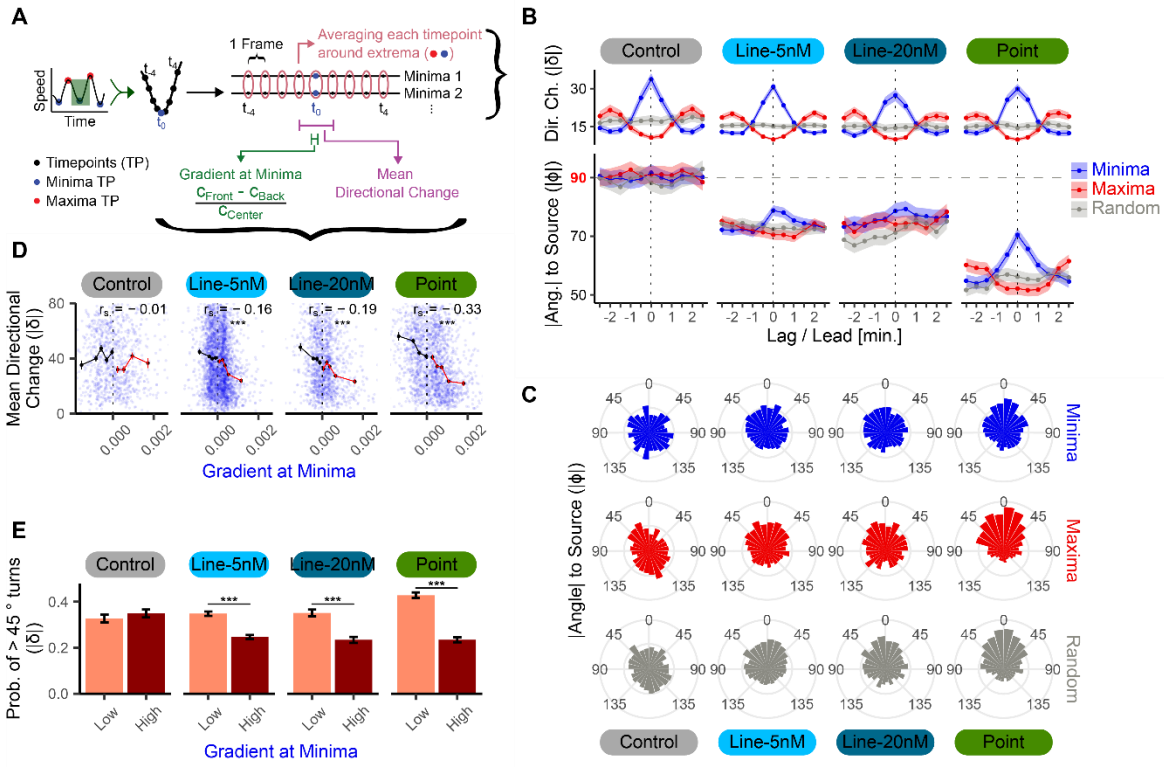


Figure 9: Neutrophils employ speed extrema to adjust their angle changes. **A)** Schematic to illustrate the data processing for subsequent plots. *Red (top)*: Values around each extrema, including the extrema, are averaged across all cells and time points, and are displayed in B). *Bottom (green and magenta)*: To study the potential effect of concentration changes on directional changes (δ), the gradient at each minima and the average directional change around the minima were calculated. The gradient value was obtained as shown in figure 7 C. Briefly, the proxy concentration at the cell back was subtracted from the concentration at the cell front and divided by the concentration at the center of the cell. As seen in figure 8 G) the extrema of the directional change (δ) does not fully overlap with the extrema of the speed but can also appear shortly before or after. Therefore, to obtain an average directional change, directional change values (δ) one time point before and after the extrema, as well as at the extrema, were extracted and the average was computed. Results are shown in D). **B)** The averaged directional changes (δ; *top*) and absolute angle to source (Φ, *bottom*) around extrema. Ribbons around the lines are SEM. The extrema are at lag/lead of 0 on the x-axis and are highlighted by a vertical dotted line. The absolute angle to source (Φ) is comprised of values between 0 to 180 degrees, hence a random orientation would be at 90 degrees. To highlight this, a dashed horizontal line and the 90-degree value in red are shown on the y-axis. **C)** Absolute angle to source distribution (Φ) at all extrema in the range of 0 to 180 degrees. The closer the value is to 0, the better-aligned cells are. The right hemisphere shows angles in the rightwards direction whereas the left hemisphere shows leftwards angle directions in relation to the respective source. **D)** The gradient at minima against the average directional change around minima as indicated by A) is shown. Blue dots represent single time points of cells while red and black dots and lines are median post-directional change values of gradient values created by forming nine quantile bins, so each bin has an equal amount of data points. Error bars represent SEM. The black dotted line indicates a gradient of 0, black lines and dots represent negative gradient values while red represents positive gradient values. A Spearman correlation was calculated over all values and rho (r_s) as well as significances are shown, ***, P < 0.001. Non-significant values (P > 0.05) are not shown. Control cells had no chemoattractant but contained the same amount of proxy as the 5 nM line control. **E)** The probability of cells to have a directional change (δ) value around the minima (t_{-1} - t_1) which is higher than 45 degrees after having a high or low gradient value (25 % highest and lowest gradient values) during their run. Control cells had no chemoattractant but contained the same amount of proxy as the 5 nM line control. Pearson's Chi-squared test, **, P < 0.01, ***, P < 0.001.

significantly lower angle-to-source values. Specifically, both line sources had angle-to-source values of around 70 degrees, while the point source showed a deviation

of around 55 degrees. Interestingly, the trend shows that as cells approach a minima, they deviate more from the source, but this angle to source value decreases again after the minima. Among the line sources, the angle to source around random time points remained relatively constant. However, for the angle to source around maxima, while it was nearly consistent for line-20, line-5 showed a gradual decrease around the maxima. In the case of the point source, angle-to-source values also remained roughly constant around random time points, but interestingly, around maxima, the angle-to-source decreased the closer the cells were to the source. Overall, while the observed effects are more pronounced for point sources compared to line sources, the general trend around minima, and to some extent around maxima, can be observed in all set-ups. This suggests that as cells approach a speed minima, they exhibit more oscillatory behavior, causing them to deviate more from the source. Conversely, as they approach speed maxima, they seem to align more with the source. This observation is further supported when examining the distributions of angles to the source around the respective extrema for each experimental setup (see figure 9 C). Minima had the lowest number of angles facing the source, whereas maxima had the highest, with random points falling in between. Remarkably, cells in point sources were so well aligned that even during random sampling, a distinct trend of alignment toward the source was evident. In summary, the data suggest that when cells reach a speed minima, they tend to slow down and make informed large angle changes toward the source. During the subsequent run phase, the trajectory is fine-tuned through smaller angle changes while approaching the maxima.

Also, of interest was whether these informed angle changes were influenced by the experienced gradient of the cells, especially given the pattern of initial stronger angle changes at the minima followed by finer adjustments. As minima exhibited the most pronounced angle changes, the focus of this analysis was on this aspect. The approach involved calculating the gradient at the minima (front – back, normalized by center) and then determining the mean directional change based on directional change values at the minima, as well as one time point before and after (see figure 9 A, bottom). Including time points around the minima was essential because, as depicted in figure 8 G, the extrema values of speed did not entirely align with the corresponding peaks or troughs of the directional change, which can be shifted by one time point. For intrinsic control purposes, a collagen assay was employed where no fMLF, but the proxy dyes were included in the same concentration as in the line-5 setup. This control was designed to account for any potential artifacts that might arise in our measurements. When the computed mean directional change was plotted against the calculated gradient, a remarkable pattern emerged. While the control exhibited no discernible relationship, all gradient samples displayed highly significant negative correlations. Notably, this correlation held true for all extrema, albeit with reduced directional change values for the maxima and randomly sampled points (data not shown). This finding suggests that when a cell encounters a higher gradient, it tends to execute smaller angle changes around the minima.

To investigate this observation further, the lowest 25 % (low) and highest 25 % (high) concentration gains were categorized for each cell and examined the likelihood of a turn exceeding 45 degrees. The selection of 45 degrees is based on the idea that deviations exceeding 45 degrees signify significant turns, while those surpassing 90 degrees denote actual changes in direction. In this context, maintaining a deviation of 45 degrees or less would indicate an approach toward the source, while larger deviations would suggest divergence from the source over time. Surprisingly, in the control group, there was no significant distinction between the two groups (low: 32 %, high: 35 %). However, within all gradient-exposed samples, a substantial distinction was

evident. Cells exposed to the lowest concentrations exhibited a notable tendency to perform turns exceeding 45 degrees (line-5: 35 %, line-20: 35 %, point: 43 %). Intriguingly, cells experiencing the highest gradients displayed a markedly reduced probability of such turns (line-5: 25 %, line-20: 24 %, point: 24 %). This pattern persisted when considering maxima and randomly sampled points, even though the likelihood of turns exceeding 45 degrees was further diminished in these cases, particularly at high concentrations (data not shown). This discrepancy can likely be attributed to the overall lower angle changes that typically occur during both maxima and random sampling points.

In summary, our findings suggest that cells strategically utilize speed minima to execute informed, substantial angle changes aimed at aligning themselves with the source. Conversely, as cells approach maxima, they tend to make only minor adjustments in their direction toward the source. Interestingly, the current concentration experienced by a cell appears to significantly influence its tendency to turn at extrema. Specifically, lower concentrations appear to amplify the likelihood of larger angle turns during these events, while higher concentrations decrease the likelihood. These observations are intriguing because it seems that cells nearing the speed minima are potentially making deliberate choices about their upcoming running direction for the run phase, deviating only slightly from the path they have selected.

2.3.8 Speed and Acceleration Differences Between Gradients und Uniform Concentrations

While the focus has largely been on migratory persistence and directionality, another intriguing aspect was also noted when examining cell speeds over time. As depicted in figure 8 A, our observations did not only reveal oscillatory patterns but also a general trend, where speed gradually increase over time. While the median speed in figure 5 B provides a concise summary, figure 6 offers insight into directionally biased speed changes. However, due to the directional bias in figure 6, it does not fully depict a normal velocity. Thus, both representations still lack a thorough analysis of how individual cell speeds develop over time. To address this, an averaged and smoothed instantaneous speed was computed between successive time points for all cells across the experimental setups.

When examining the averaged speed over time, a pattern similar to the previous results of median speed becomes evident. Cells without attractant generally exhibit slower speeds compared to cells experiencing a gradient and the speed trajectories of all gradient-exposed samples are quite similar, displaying no significant distinctions (see figure 10 A). However, when looking into the temporal dynamics of speed, it reveals an intriguing trend that persists for approximately 60 minutes across all experimental conditions – a shared acceleration phase. Notably, this shared acceleration phase is also observed in the control group. This suggests that the initial acceleration could be attributed to cells adapting to the collagen environment, transitioning from their prior 2D culture to the more confined setting within collagen. This adjustment likely involves the adjustment of their migratory machinery, resulting in this initial acceleration. While the control group's speed level reaches a plateau after this early acceleration phase, the gradient-exposed samples continue to accelerate, notably up to around 120 minutes of experimentation. However, also for cells in gradients, the most rapid acceleration primarily takes place within the initial 0 to 60 minutes.

An intriguing observation that caught our attention was the absence of any significant speed or acceleration differences between the line concentrations and the point source. This finding led us to formulate a hypothesis that the gradient's impact on speed is much more pronounced than the specific absolute concentration levels. To

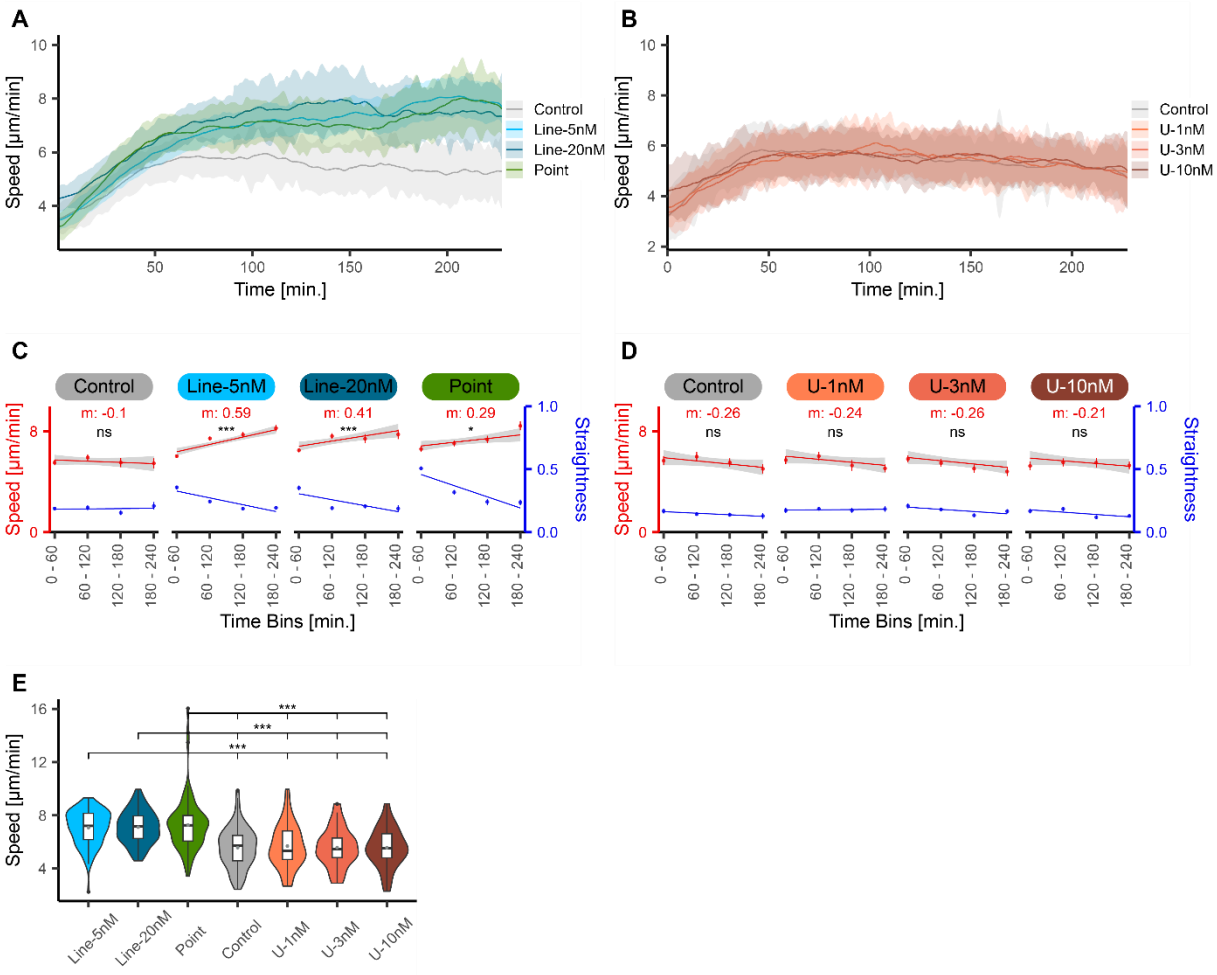


Figure 10: Speed differences over time for gradient fields and uniform concentrations. **A & B)** Median speed of cells at each time point smoothed with a moving average of 100 time points (exponential kernel). Colored bands represent the 95 % CI. **C & D)** Time points were merged into bins of 60 minutes and the median speed and straightness of each bin were calculated and plotted (red dots and blue dots, respectively). A linear regression was fitted with the regression lines (red and blue line) and the respective 95 % CI (grey area) shown. The slope of the linear fit for the speed is given on top of each graph (m). P values < 0.05 show that the slope is likely not randomly different than zero, *, P < 0.05, ***, P < 0.001. **E)** Median speed of whole cell tracks. Controls of cells in gradients and uniform concentrations were pooled and are shown between experiments in gradients and uniform concentrations. Pairwise Wilcoxon rank sum test with continuity correction (Bonferroni), ***, P < 0.001.

test this hypothesis, collagen assays using uniform fMLF concentrations were conducted. Notably, due to the collagen's need to polymerize and the intention to avoid fMLF pre-stimulation, no fMLF was added to the collagen but a substantial volume of medium with fMLF was added onto the collagen after polymerization. This should rapidly establish an equilibrium, but this approach did introduce an initial gradient until equilibrium was reached. Moreover, while the uniform concentrations listed were used in the medium, a slight reduction in concentration occurred due to the neglected collagen volume itself, although this impact is considered negligible (200 µL collagen compared to 5 mL medium). Upon analyzing the averaged speed over time for the uniform concentrations, an entirely unexpected outcome emerged (see figure 10 B). Despite a similar initial phase of adaptation to the collagen for all samples, no discernible distinctions in speeds between the tested concentrations or to the control were observed. Interestingly, while the gradient samples reached and maintained a speed plateau, it appeared that the speed of cells in uniform concentrations was gradually diminishing

over time after reaching its peak. These unexpected findings implied that all uniform concentration samples behaved in a remarkably similar manner. Notably, the adaptation phase's acceleration appeared slightly shorter in duration and less pronounced. Several factors could contribute to this phenomenon. First, cells in the collagen assay are essentially serum-starved due to the absence of serum in the master mix. Second, the gradient assays involve a relatively small interface between the collagen and the added medium, whether with or without fMLF. Conversely, the uniform concentration assay covered the entire collagen area. It was therefore speculated that this observed effect could be attributed to cells reacting to serum-related factors present in the medium, thus contributing to the adaptation phase. However, this adaptation phase appears to occur more rapidly for uniform concentrations due to the larger interaction area between the collagen and the added medium.

The obtained results were interesting, prompting to investigate whether cells subjected to uniform concentrations might experience challenges in distinguishing the attractant gradient due to its consistent distribution. These challenges might lead the cells to switch to a fully random migratory mode, which might cause increased angle changes and subsequently a general reduction in speed. To explore this hypothesis, the time was divided into 60-minute bins for all experimental setups and computed the median speed as well as the track straightness for each bin. Subsequently, linear fits were performed to observe how speed and straightness developed over time. As expected, the control groups for both assay types did not reveal any notable trends (see figure 10 C, D). However, while the gradient samples exhibited a significant positive speed trend over time, this trend was also accompanied by a gradual decrease in track straightness over time. In contrast, the uniform concentration assays did not showcase any significant slope for either speed or straightness, albeit showing a trend for decreasing speed over time. An intriguing observation emerged from the gradient samples, as their cells demonstrated their highest speeds precisely when their straightness was at its lowest point. Remarkably, these straightness values were similar to those exhibited by the cells in uniform concentrations. This finding was particularly interesting, as it removed the notion that the absence of speed differences in uniform concentrations was due to cells migrating more randomly. Furthermore, it opposed the conventional assumption that faster cells also tend to migrate more directionally persistent, as in the context of the gradient samples, the speed peak coincided with the least persistent cells. A plausible explanation for this phenomenon is that despite their reduced persistence in migration, cells with higher instantaneous speeds can cover more ground more quickly. Consequently, such cells may not necessarily need to exhibit a higher degree of trajectory straightness to achieve greater speeds.

Furthermore, the made observations were also supported when considering the median speed across all time points. In this regard, all gradient samples exhibited significantly higher speeds compared to any of the uniform concentrations and the control, and none of them showed any significant difference between each other. Conversely, there were no significant differences among the uniform concentration samples, and none of them displayed a significant distinction from the control group (see figure 10 E).

Interestingly, the data here suggests that faster cells may not necessarily exhibit greater persistence, whereas the data in figure 9 B & C suggests the opposite – namely, that faster cells are more directional. The distinction between the two analyses lies in the respective time windows of analysis. Figure 9 examines short time frames between consecutive extrema (~ 5 minutes), while figure 10 employs much larger time frames (1 hour). This temporal difference can account for the disparate observations. On small time scales, cells during the run phase have limited opportunities for significant angle changes, whereas on larger time scales, they are entirely capable of doing

so. Additionally, larger time scales encompass minima time points, contributing to an overall reduction in persistence. To illustrate, consider a very fast-driving car: when observed in small time windows, the car appears to have very persistent motion, as substantial angle changes are constrained by various forces. However, when observed over a much larger time scale, the car is likely to navigate curves, potentially turning around, and not necessarily following a straight path.

The gathered data strongly implies that cells primarily respond to relative and temporal concentration gradients (i.e., changes in Δc over time: $(\Delta c_1 - \Delta c_0) / \Delta c_0$) rather than absolute concentrations. Even within gradient setups, cells did not exhibit increased speed in the presence of a higher gradient (point vs. line gradients, as shown in figure 7) or a higher concentration gradient in general (e.g., line-5 vs. line-20 with a fourfold difference). When uniform concentrations were employed, the absence of a gradient led to no acceleration of cell speeds beyond an initial adjustment phase, and no uniform concentration generated faster cells than the control. Furthermore, cells in gradient environments demonstrated significantly higher speeds compared to those in uniform concentrations. Notably, this effect cannot be attributed to increased random migration, as instances where cells in gradient environments exhibited the highest speeds also saw similar levels of straightness compared to cells in uniform concentrations. The descending speed trend seen in uniform concentrations likely arises from a sustained overstimulation resulting from the constant presence of the uniform concentration. This raises the intriguing question, if this situation is analogous to frustrated phagocytosis where cells fail to engulf a particle, or if it is due to the absolute concentration approximating the receptor's dissociation constant (K_d), leading to excessive stimulation. The observed negative correlation between speed and straightness in gradient environments could also provide insights into cell trajectories. As experiments progress in time, gradients might become more difficult to discern and noisier, potentially prompting cells to switch to a more exploratory mode. In this scenario, cells would migrate in a more randomized manner, yet potentially maintain higher speeds.

2.4 Discussion

Inspired by the dynamic yet consistent way neutrophils hunt bacteria, the aim of this project was to explore the intricate spatiotemporal aspects of this process. This study employed collagen assays to investigate how two distinct forms of gradient application (line and point sources) affect the migratory behavior of neutrophils. Additionally, it was examined how the concentrations of the respective attractants (line-5 and line-20) influence this migratory pattern. To establish a correlation between observed cellular behavior and the corresponding gradients, two distinct proxies for fMLF were utilized without labeling the cells or the attractant. Of note, while cells were migrating in a 3D environment (i.e., xyz), the imaging and subsequent tracking of these cells were exclusively conducted in a 2D plane (i.e., xy). This tracking discrepancy introduces some degree of noise into the data, as cells can move along the z-axis, causing an underestimation of their actual speeds in this study. However, our approach partially compensates for this by tracking the shadow of cells when they are not in the plane of focus, ensuring robust and consistent tracking of individual cells over extended periods. Moreover, any potential errors stemming from this method would be systematic and consistent across devices, allowing for reliable and standardized analysis.

The data showed noteworthy differences in directional persistence between dendritic cells (DC) and neutrophils or neutrophil-like cells, even when employing similar attractant concentrations within the same assay. While these differences initially surprised us, they are conceptually sound. In the context of immunity, distinct cell types serve specific effector functions, thus varying behaviors among different cell types are

to be anticipated. For instance, DC must precisely navigate toward lymph nodes during inflammation, whereas neutrophils must exit the bloodstream and transition into a search-and-run mode. Consequently, it's reasonable that neutrophils exhibit lower persistence compared to dendritic cells, as their responsiveness to new stimuli in their vicinity takes precedence over prolonged guidance. Moreover, considering that the gradient and attractant carry most of the information for cells to inform their actions, even identical information can yield different outcomes in distinct cell types.

The choice of fMLF as the primary chemoattractant in our experimental setup stems from several practical and scientific considerations. Firstly, fMLF is a cost-effective option in comparison to other chemoattractants such as chemokines like IL-8. Its widespread usage in numerous research groups indicates its reliability and established track record in various experimental settings [85,87,100,101]. Importantly, fMLF has robustly demonstrated the most potent and favorable cellular response within collagen assays compared to other attractants tested, making it the optimal choice for our specific context. It is important to highlight that our experimentation involved testing various other attractants, and the obtained results mirrored those obtained with fMLF, reinforcing its reliability and effectiveness within the scope of our study. Nevertheless, it's important to acknowledge that while other attractant-receptor pairs could potentially offer distinct advantages, within our tested context, we observed no discernible differences.

Across the conducted experiments, significant differences in the directional persistence of neutrophils was consistently observed, with point sources exhibiting a considerable advantage over line sources. Despite various interventions to achieve similar directional persistence in line sources as observed in point sources (see to table 1), the ability to increase persistence was not feasible. Instead, the persistence often experienced only slight decreases. The predominant focus on interventions targeting the sensing aspect (e.g., receptor desensitization), coupled with the absence of direct perturbations to the myosin or actin network, raises a pertinent question. Is persistence less closely tied to sensing the attractant and more connected with the polarization or motion-generating mechanisms of the cell? As discussed in the introduction (see 1.2.5.1), modifications to the cytoskeleton, involving polarizing factors and the motion-generating system, can exhibit bidirectional effects on persistence – either enhancing it (e.g., stabilizing moesin at the cell back) or diminishing it (e.g., actin inhibition) [73,102]. However, many interventions in the literature are conducted without chemoattractants, and those combining both suggest impairment of chemoattraction itself, rendering cells unable to read the gradient. This emphasizes the delicate and finely tuned nature of directional persistence, regulated at multiple levels. Intriguingly, the time window for calculating persistence times significantly influences the results. In the initial 30-minute period, both line sources and point sources exhibit similar directional persistence, but line sources experience a relatively quick decline in their persistence, as depicted in figure 10 C. Expanding the time window for analysis reveals that point sources higher alignment characteristics (i.e., a lower angle distribution, better straightness, and chemotactic index), whereas line sources show a decline in these values. This trend could potentially be attributed to the fact that cells within line sources initially encounter strong gradients, including exponential ones to a certain extent, before the gradients become indiscernible later. The gradient field, being the only variable differing between the experimental setups, must inherently encapsulate all the cues guiding cellular responses. When analyzing the gradients, it becomes evident that cells within point sources not only experience higher and sustained gradient values (Δc: front – back, normalized by center) but also encounter gradients that exhibit more of an exponential shape. On the other hand, cells within line sources predominantly encounter linear gradients with varying degrees of steepness. This distinction holds important

significance in the context of cell migration, as numerous models propose that cells measure and perceive gradients by assessing the Δc, subsequently shaping their responses accordingly [103]. When a cell migrates along an upward linear gradient, the absolute concentration increases along the migratory axis, yet the Δc ($\frac{c_{Front}-c_{Front}}{c_{Mean}}$) decreases as $c_{Front} - c_{Front}$ remains constant and c_{Mean} increases. In contrast, within an exponential gradient, a cell would measure a constant Δc over time ($c_{Front} - c_{Front}$ and c_{Mean} increase), potentially facilitating the process of gradient tracking. Notably, if one were to use $c_{Front} - c_{Front}$ alone, a linear gradient would display a constant difference, while the exponential gradient would show a constant increase as a cell migrates upward. It's essential to acknowledge that Δc ($\frac{c_{Front}-c_{Front}}{c_{Mean}}$) remains a hypothesis, implemented based on a fully understood *E. coli* temporal sensing mechanism [104]. Biologically, in *E. coli*, division by c_{Mean} is achieved through receptor adaptation via methylation, which adjusts the effective K_d to match the mean concentration [105]. Previous work in our laboratory has already demonstrated that dendritic cells have increased directional persistence in steeper linear gradients compared to shallower ones [34]. Furthermore, that research also showed that exponential gradients outperform linear ones, further underscoring the crucial role of gradient shape in cell behavior.

The significance of the gradient's role becomes more apparent when examining the attempted interventions. None of the numerous interventions, targeted at different molecular mechanisms, managed to enhance persistence, instead, some only led to its reduction. This underscores the challenge of improving biological processes artificially and highlights the tendency for interventions to have a diminishing effect. Moreover, this observation reinforces the idea that directional persistence is subject to stringent regulation through potentially diverse mechanisms. However, the simple transition from a line to a point source exhibited a remarkable impact on directional persistence. As previously mentioned, this alteration solely modifies the gradient characteristics that cells are exposed to, consequently influencing the information they perceive.

When focusing on Δc, one might argue why not a simple front–back difference was computed without normalization. In fact, this normalization by the center concentration serves both technical and biological purposes. From a technical perspective, variations in brightness can occur between different experiments, even when using the same microscope settings. If the absolute difference in concentrations were to be used, the magnitudes of differences between experiments might differ significantly. However, as the relative gradient propagation is the same between all devices of the same setup, normalizing by the center concentration helps standardize the relative gradient propagation across all devices, thereby addressing this technical variability. Biologically, the choice of using normalized Δc is crucial as well. Consider two scenarios: In the first, a cell encounters a concentration of 20 at the front and 10 at the back; in the second, it faces 210 at the front and 200 at the back. The absolute difference is the same in both cases, yet the gradient perception for the cell in the second scenario is vastly different due to the higher overall concentration. By employing normalized Δc, one can account for this distinction. This biological significance is supported by studies using gradient modifications in microfluidic systems. For instance, cells exhibit higher chemotactic indexes when migrating on the lower side of a linear gradient compared to the higher side [35]. In a purely linear gradient scenario where cells do not normalize by central concentration, their behavior would be similar across all locations within the gradient, which is not in line with experimental observations.

The negative correlation between speed and directional changes (δ) appears to be a conserved mechanism in which high speed and large angle changes are mutually exclusive. This principle aligns with common sense – just as you wouldn't drive at high

speed while taking a tight corner, cells seem to decelerate when making large angle changes. This is further supported by theoretical and experimental work which showed that not only do animals themselves decelerate when turning, but also single cells [106]. However, at the microscopic scale, it remains uncertain whether the same principles apply. At the beforementioned macroscopic scales inertia plays a significant role, and performing high-speed turns involves managing substantial forces and centripetal/centrifugal forces. Yet, at small scales where viscous forces outweighs inertial forces, the applicability of the same physical intuition from the macroscopic world becomes less obvious. Therefore, the process of turning at the cellular level raises an empirical question about the actual mechanisms involved. The observation that the distance between minima and maxima is relatively constant across concentrations and experimental setups suggests the presence of an intrinsic pacemaker of this oscillation. Cells appear to strategically use this oscillation to make informed decisions on direction changes, using the minima phase to adjust their trajectory for the subsequent run phase, where large angle changes are less feasible. However, the identity of this intrinsic pacemaker remains a question. One potential candidate are actin waves, which propagate through cells and exert a pushing force on the cell membrane once they reach the cell perimeter [107]. The dynamics of actin waves could potentially account for the observed behavior – accelerating as the wave progresses, reaching maximum speed when the wave reaches the membrane, and subsequently decelerating before the next wave forms. While actin waves are a likely contributor given the crucial role of actin in regulating cell speed, the timing of actin wave formation might not fully match the observed speed oscillations, as actin wave dynamics can vary significantly across cell types, with neutrophils being more in the seconds to lower minutes range [108–110]. Another possibility is the involvement of hem-1 waves, which regulate Arp2/3 activity and consequently actin polymerization at the leading edge of cells [111]. However, hem-1 waves in neutrophils are relatively short-lived, typically lasting around 30 seconds, which also does not align with the observed oscillations that occur over longer time intervals [112]. Nonetheless, considering that neutrophil migratory behavior heavily relies on the cytoskeleton and its regulators, it is highly plausible that a component of the cytoskeleton, or a regulator thereof, causes the observed speed oscillations. Further investigation is needed to elucidate the precise mechanism at play.

Our most significant finding from this project centers on how cells utilize the information from the experienced gradient to guide their turning behavior. Strong correlations between the currently perceived gradient and the corresponding angle change around the speed minima were observed. This process likely involves a temporal component, as the meaningfulness of this correlation only becomes apparent within a temporal context. Our experiments with uniform concentrations and higher line source concentrations revealed that cells appear to respond to relative concentrations in a spatial and temporal context (Δc for spatial and $(\Delta c_1 - \Delta c_0) / \Delta c_0$ for temporal integration) rather than absolute concentrations. This observation raises the question of how a cell could make decisions about turning based solely on a specific gradient measurement at a given moment. Without the context of previous time points, such a measurement would essentially represent an absolute concentration reading. Interestingly, when past time points of the gradient were included into the analysis, a negative relationship between gradient and directional change was also observed, although this correlation was not as strong (data not shown). Incorporating past gradient values introduces technical complexities, particularly since gradients can be negative, and including more time points might mitigate their influence, leading to convergence toward zero. As a result, lower correlations were observed. We are currently in the process of fitting various mathematical models, such as generalized linear models (GLMnet), to the data to

explore whether including past time points might enhance the predictive power of models. Preliminary results suggest that including past time points could indeed improve the model's predictive capabilities.

In addition to the potential memory aspect for angular changes, another temporal component may play a role in the detected behaviors. Our observation that cells increase their speed in gradients but not in uniform concentrations indicates that they respond to relative temporal concentration differences ($(\Delta c_1 - \Delta c_0) / \Delta c_0$) rather than absolute concentrations, which argues for the involvement of an additional temporal factor. This is rooted in the fact that comparing relative changes requires the ability to compare them against each other. It could be argued that the presence of any gradient increases cell speed rather than the relative change a gradient provides over time. In the context of uniform concentrations, where the Δc remains at a constant 0, cells might need to detect any non-zero Δc to initiate an acceleration. In this scenario, cells might not require memory but rather need to surpass a specific threshold. For future projects, it would be interesting to examine how cell speeds would develop within stable gradient fields, as in our study the gradients are non-stationary and highly dynamic in nature. Furthermore, the observed higher speeds in gradients might also originate from a different source. As our data suggest, cells appear to adjust themselves to the collagen as also control cells experience a speed increase over time after they were placed in collagen assays. Preliminary data from our colleagues suggests that when cells are transitioned from high-density matrixes to low-density matrixes after an equilibration time, those transferred to low-density matrixes exhibit higher speeds than cells newly placed in such environments. This suggests that cells indeed adjust their migratory machinery to their immediate environment, and it is quite likely that maneuvering through more confining environments provides them with advantages when transitioning to larger pore areas. It is plausible that cells in gradient setups are compelled to move even through smaller pores to track the gradient. In contrast, cells in uniform concentrations, not guided by a gradient, might favor the path of least resistance, choosing to move through larger pores. If true, cells in gradient setups might experience the acceleration due to being compelled to navigate through smaller pores, which would result in better collagen adjustment of the migratory system. Although this theory has been subject to discussion among lab members, ongoing experiments using under-agarose assays and open microfluidic devices with both uniform concentrations and gradients are being conducted to investigate this further. These experiments eliminate the variable of pore size adjustments and might provide a clearer picture of the observed speed variations.

Considering that both the gradient and the attractant contain all the essential information for a cell to make informed migratory decisions opens intriguing possibilities for migratory cells within multicellular organisms. Depending on the specific requirements, the same attractant could be employed but presented in the form of different gradients with varying strengths and dynamics to guide cells in accomplishing distinct tasks. For instance, imagine a scenario where an exponential-like gradient is established over longer distances to bolster persistence, enabling cells to reach designated areas effectively. Subsequently, a shift to a more linear gradient might occur, reducing persistence but intensifying the random migration of cells. This adjustment could enhance the search strategy employed by cells, fostering their ability to explore and interact within their environment. This dynamic adaptability of gradient profiles could facilitate the precise control of cellular movements and behaviors within multicellular organisms.

Based on our findings and drawing an analogy to bacterial chemotaxis, we propose a "run and fumble" model for neutrophil migration (refer to figure 11). Similar to

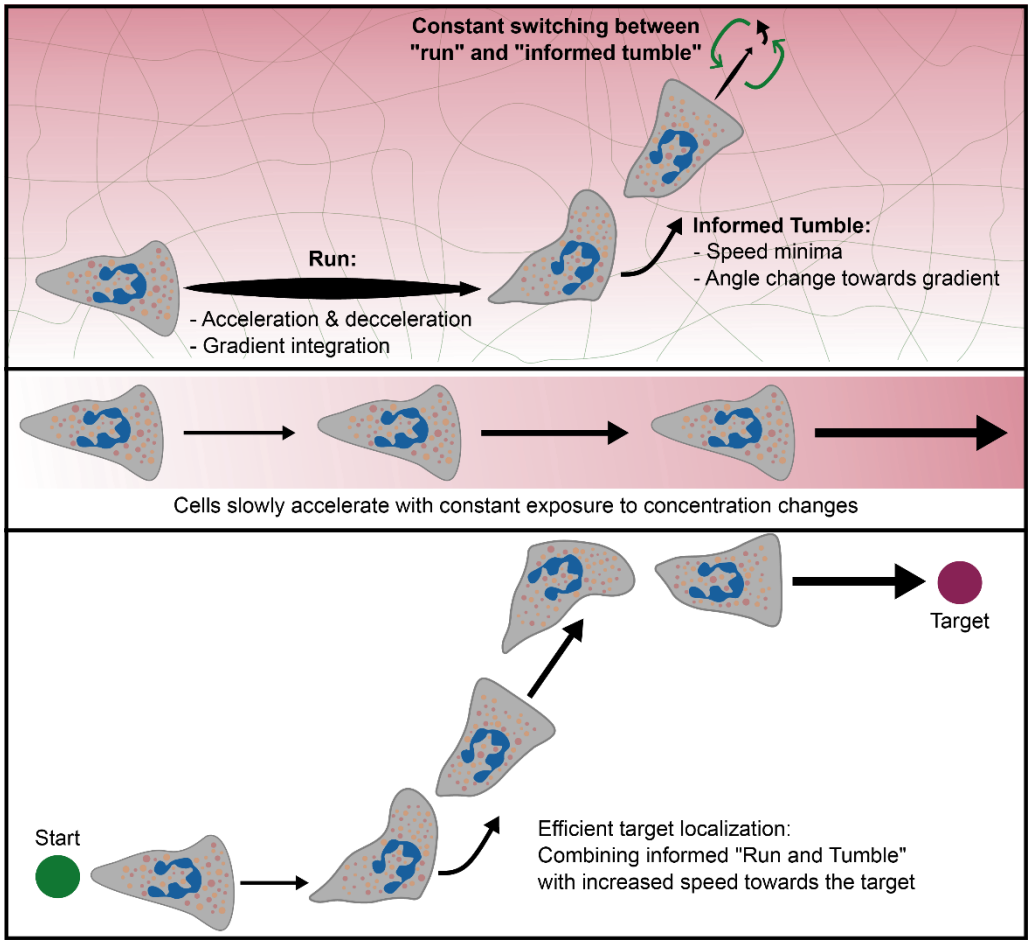


Figure 11: Model of the run and fumble cycle. ***Top***) Short-term memory for informed angle changes. During the run phase, neutrophils initially accelerate and integrate the traversed gradient. At the end of the run, neutrophils slow down and make an informed angle change toward the source. These phases are likely to be repeated until they reach their destination and/or fulfill their function. ***Mid***) Long-term integration of concentration changes leads to increased speed. ***Bottom***) Combining smart angle changes, which are based on measured gradient differences, with a continuous speed increase based on constitutively experiencing a concentration change, helps the cell to find its target more efficiently.

bacterial "run and tumble", where the run phase adjusts in duration based on chemoattractant concentrations – prolonged for higher concentrations and shortened for lower concentrations – but the tumble is completely random [113]. The "run and fumble" model maintains the notion that during the fumble phase, a stochastic process is introduced, which, although not completely random, can be biased by the gradient.

Furthermore, unlike bacteria, which actively adjust their run length, it seems that neutrophils maintain a mostly constant run length concerning the duration of the run phase. More specifically, neutrophils harness the consistent speed oscillations in two distinct ways. First, the interval between consecutive speed minima serves as a run phase, marked by initial acceleration and subsequent deceleration after reaching the speed maxima. Second, during this run phase, cells potentially integrate concentration cues across the gradient field, aiding them in making informed angle changes (referred to as "tumble" or "fumble") at each minima. Additionally, the gradient (Δc) or its change induces gradual acceleration, progressively boosting cell speed. This synergy between informed angle changes and the gradient's influence on speed combines chemotaxis and chemokinesis, leading to a highly effective strategy for neutrophils to locate their target or to reach desired locations. In this model, neutrophils employ spatial sensing

with a temporal component, optimizing their angular adjustments while gradually gaining speed as they approach their target, thereby reaching it faster compared to either mechanism operating independently.

This model also appears to apply to a more general context. Considering a hunting neutrophil, it's advantageous to incorporate a certain level of memory utilization, but not excessively, as an over-reliance on memory would leave the cell incapable of reacting to trajectory changes of the hunted bacterium. For instance, if a bacterium suddenly deviates from its current path, a neutrophil that relies too much on memory cannot quickly adjust its own trajectory and will follow the bacterium's historical trajectory. However, a balanced approach is essential due to the inherent variability introduced by natural environments on signals. In these cases, a memory mechanism would provide additional guidance cues in situations characterized by weak, noisy, or temporary absence of signals.

The proposed model for temporal integration in neutrophils could potentially explain additional observed phenomena. Specifically, when examining line sources in later time intervals, an interesting pattern emerges with a notable increase in cellular velocity accompanied by a significant reduction in track straightness. This combination suggests an increased occurrence of random migration, a trend that becomes more evident when examining individual migration trajectories. The increased random migration, combined with accelerated speeds, results in greater overall cellular displacement. Consequently, this enables cells to temporally integrate the attractant concentration of a larger area. Through this temporal accumulation of concentration data, a more pronounced gradient field emerges, potentially facilitating informed migratory decisions. Furthermore, based on empirical observations, instances arise in which cells exhibit circular trajectories as they navigate the gradient field. This type of migratory behavior also aligns with the concept of temporal integration. Specifically, these circular movements could be interpreted as an effective strategy for cells to survey a relatively small area, thus enhancing their understanding of the gradient field's properties.

When exploring the integration of the memory effect within the migratory mechanism, it is crucial to establish a clear distinction. As mentioned earlier in the introduction, differentiating between inertia and cellular memory can be challenging. In my perspective, memory involves a continual comparison of information at discrete time intervals, akin to saving and recalling data. On the other hand, inertia initiates a process once a specific threshold is reached, and its outcomes become apparent only later, effectively "retaining" information due to its resistance to deactivation once set in motion. For example, consider a cell responding to a chemotactic signal. In this scenario, memory would entail the cell continuously assessing the chemical gradient at intervals and adjusting its movement, accordingly, resembling the process of saving and retrieving information. In contrast, inertia would involve the cell initiating a persistent movement once it detects a certain level of the chemical signal, with the consequences of this action becoming noticeable only after some time. This distinction becomes essential in experimental setups, as addressing memory would require analyzing the cell's response over distinct time points, while inertia might involve observing delayed effects following a specific triggering event. In essence, a memory effect is part of a continuous process involving constant assessment and adjustment over time, while inertia represents a one-time triggering event with delayed consequences.

In his research, Haastert proposed a dual memory system employed by *Dictyostelium* cells. This system involves a short-term memory lasting up to 20 seconds, facilitated by F-actin modifications, and a long-term memory lasting 2 minutes, mediated by a cGMP binding protein [71]. The former contributes to the formation of new pseudopods at the leading edge of the cell, while the latter inhibits pseudopod formation at the rear.

The synergy between both mechanisms enables a persistent migratory capacity for the cell. Notably, Haastert's investigations solely encompassed analyzing random migrating cells, leaving uncertainty regarding the potential influence of chemotactic agents. It's possible that when an attractant is detected, a faster and more dynamic system takes precedence over the described memory-based system here. Chemotaxis is generally quicker and more dynamic than random migration, so a chemotactic cell might switch to a more responsive strategy. This could mean that the described memory system becomes less relevant in the face of chemotaxis. The work of Prentice-Mott et al. delves into the behavior of neutrophil-like cells within microfluidic devices [72]. They show that Moesin at the cell's rear is a pivotal factor in driving memory. Their findings indicate that enhancing Moesin stability augments directional memory, while Moesin destabilization diminishes it. In this context, one could argue that one observes inertia, given that the system likely just retains information about prior signals without integrating it, thereby constraining the cell's movement along a specific trajectory. Similarly, the study conducted by Georgantzoglou et al. appears to highlight an effect rooted in inertia [73]. They identify actin flow itself as a functional memory, sustaining directional consistency for up to three minutes. Here again, the flow appears to solely retain the information once initiated, and information integration seems unnecessary. Noteworthy is their assertion that actin flows undergo a reset before renegotiating the direction, further indicating a reliance on inertia-like mechanisms.

Determining the key components responsible for the memory effect is challenging, as various groups propose different regulators for the temporal aspect. These components could involve actin, microtubules, receptors, or potentially a combination of all three. The regulators might operate near the involved processes or further downstream from them. At the moment, there is a lack of comprehensive understanding of the specific molecular players and their precise roles within this phenomenon. Spatial sensing in eukaryotes most likely dominates the migratory machinery. Nevertheless, there might be scenarios where temporal sensing is needed or where it supersedes spatial sensing. If temporal sensing is indeed present, it remains uncertain whether it operates consistently or only becomes active when gradients become erratic and challenging to interpret. Additionally, the timeframe of temporal sensing remains unidentified. Although our data suggests a lower range in minutes (up to 6 minutes), it's plausible that the range could be much shorter. Moreover, temporal sensing might be differential, implying that newer data might hold varying degrees of importance compared to integrated older data.

3 Make Your Body Count – How Local Environment can Help Neutrophils Shape the Local Gradient

3.1 Summary

For this project, we investigated the hypothesis that cells can exploit their immediate surroundings to locally amplify their perceived gradient. If a cell possesses the ability to enclose its vicinity entirely, it could potentially exert a pushing force on the attractant, leading to its depletion at the rear and enrichment at the front. In this manner, a migrating cell might continually augment its Δc. If an individual cell cannot achieve path closure on its own, a cell collective could potentially achieve it collaboratively. Thus, we designed and optimized various microfluidic configurations featuring a pillar maze with varying pore sizes and different device heights. Through experimentation with different cell densities, a novel analytical approach was formulated to assess the efficacy of cells in navigating the maze. While significant differences in the efficacy were detected between diverse pore sizes and device heights, we encountered challenges related to the quantification of gradient manipulation effects on the cellular level. As addressing the challenge of gradient manipulation by cells would have demanded a substantial investment of time, this project was temporarily suspended to shift the focus toward the "run and fumble" project.

3.2 Introduction

Throughout this doctoral research, various migration assays were performed and quickly a recurring trend was recognized: the migratory persistence of neutrophils and neutrophil-like cells consistently exhibited fluctuations between the assays, even when employing identical concentrations of attractants (table 2). Nevertheless, utilizing the same assay, the migratory persistence remained relatively consistent regardless of the attractant concentration employed.

	Collagen Line	Collagen Point	Under-Agarose	Microfluidic Pillar Forest
Persistence [min.]	< 2 h	~ 6 h	< 1 h	~ 6 h

Table 2: Migratory persistence of dPLB-985, dHL-60 and neutrophils cells in different assays.

When considering potential mechanisms, two significant distinctions emerged – the differences in gradient shapes (line vs. point) and the geometric constraints cells encounter. Chapter 2 of this thesis already investigated gradient properties, where it was observed that point sources generated steeper and more exponential-shaped gradients, a configuration that has been suggested to be more favorable for cellular responses. In this chapter, the impact of geometric constraints is further explored.

Collagen and under-agarose assays predominantly involve open spaces, considering that pores in collagen are closely positioned to each other and do not form a fully enclosed environment (see figure 12 A). In contrast, microfluidic devices can generate environments that become partially enclosed when cells enter channels or pores. In this context, a cell that fully encloses its surroundings can propel the attractant forward, leading to its depletion behind the cell and enrichment ahead (see figure 12 B). This dynamic could contribute to maintaining a higher Δc, resulting in a migrating cell consistently enhancing its chemotactic response. If an individual cell is unable to enclose a path entirely, a collective of cells might collaboratively achieve this effect (see figure 12 C).

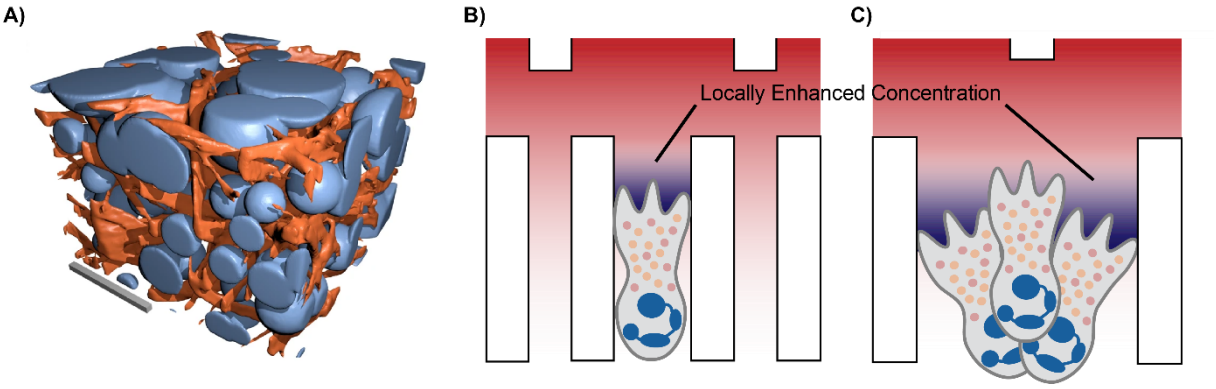


Figure 12: Theoretical impact of cell migration and local geometric environment on local gradients. **A)** 3D visualization of detected spherical bubbles: Orange depicts segmented collagen fibers and blue represents determined bubbles. The scale bar is 20 µm. Image and legend taken from Fischer et al. [114]. **B & C)** Schematic representation of the proposed hypothesis in microfluidic devices. When cells respond to a chemotactic cue (red gradient) and can enclose their immediate environment – whether individually **(B)** or as a group **(C)** – they can locally enhance the attractant concentration (purple gradient).

To address the hypothesis, a series of microfluidic devices featuring a pillar maze with a defined pore size were generated for a comparative analysis. Multiple device iterations were designed, fabricated, and assessed, encompassing variations in pore size, device heights, and loaded cell quantities. Subsequently, cell trajectories were used to analyze their migratory efficiency in each maze.

3.3 Results

3.3.1 Device and Experimental Design

The final design of the microfluidic devices (see figure 13 A) featured a variable central analysis zone, consisting of a pillar maze with a consistent pore size that varied across different devices. Meanwhile, certain features were maintained in each device configuration. This included two puncture holes, enabling consistent and reliable punctures at the same location to maintain consistent gradient propagation across experiments. The puncture holes served as reservoirs for loading cells and the attractant (fMLF). These two reservoirs were interconnected via a bypass, allowing for rapid volume exchange between them. This design choice was motivated by the need to counteract the hydrostatic pressure generated by slight loading variations in the reservoirs. Despite careful pipetting practices and the use of appropriate pipettes and tips, inherent pipetting errors can still create loading disparities, consequently triggering uneven flow. This phenomenon, which was observed in all devices without a bypass, is especially evident in devices with larger heights, wherein cells tend to be carried along with the flow rather than exhibiting migration. This outcome aligns with fluid dynamics principles, as smaller devices offer not only enhanced cell adhesion to the upper surface but also minimize liquid flow due to reduced fluidic dynamics. It's important to note that the bypass and puncture holes were designed to be a different height (100 µm) compared to the rest of the device. This differential height allowed for effective volume exchange in the case of the bypass and facilitated alignment for puncture devices with the holes. Lastly, structural support pillars were integrated around the device, excluding the analysis zone, to prevent PDMS collapse and maintain structural integrity.

Another critical aspect of the design phase was ensuring that the pores encountered by cells within the analysis zone maintained uniform dimensions in all directions. Consequently, the pores were configured to have identical sizes across all pillars (see

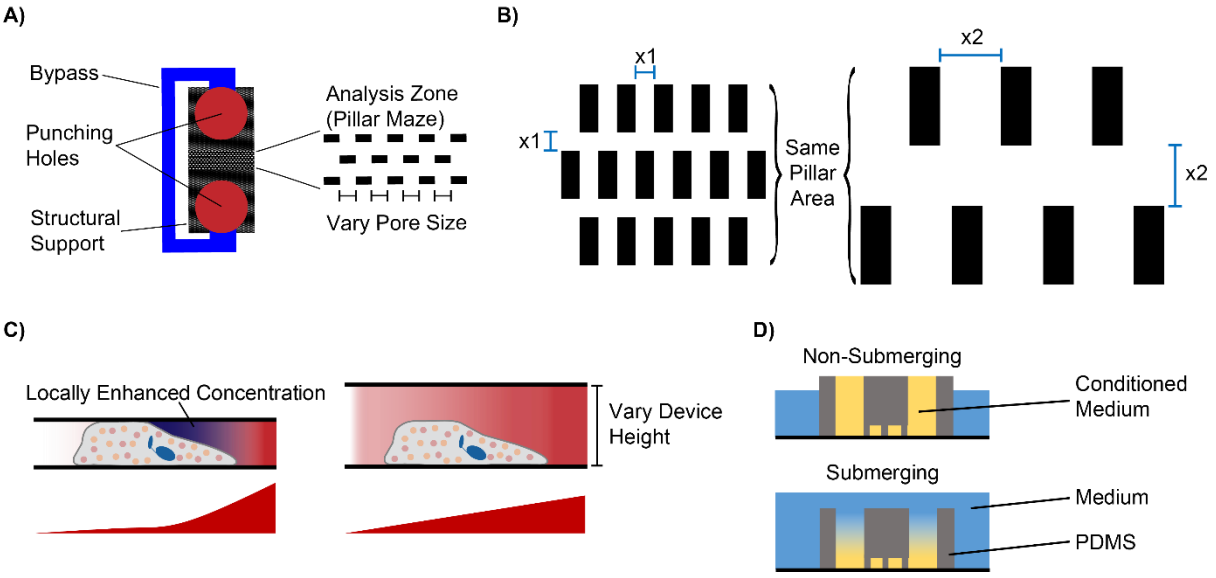


Figure 13: Microfluidic designs and experimental setup to study local environment effects on gradients. **A)** Final layout of microfluidic devices. All devices featured constant elements (left), encompassing a bypass for flow removal through the analysis zone, designated hole-punching regions for standardized experiments, and supportive pillars around these punching holes. Each device incorporated an individual analysis zone composed of a pillar maze (right) that established consistent pore sizes throughout the analysis area. Tested pore sizes were 5, 10, 15, 20 and 40 µm. **B)** Design of the analysis zone. During the design phase, attention was paid to ensuring uniform pore sizes in all directions within the device (x1 = x1; x2 = x2). Furthermore, adjustments were made to the pillar dimensions for all devices to maintain a roughly equivalent total occupied pillar area. This was done to ensure that the variation in pore sizes had minimal impact on the propagation of gradients. **C)** Device heights as intrinsic control for the observed phenomenon. Varying the height of the device served to examine the impact of cells' ability to enclose space between pillars on gradient enhancement (left). Higher device heights (right) eliminated the potential for cells to enhance the gradient by enclosing their surroundings, acting as a control in the experimental setup. **D)** Experimental design of (non-)submerging the devices in medium. In our microfluidic assays, one can either submerge the device in medium or not. Submerging the device in medium results in the conditioned medium, along with the attractant, diffusing out, leading to the development of an unstable gradient over time. On the other hand, choosing not to submerge the device can potentially lead to flow-related challenges within the device due to subtle loading differences and subsequent hydrostatic pressure.

figure 13 B). Furthermore, as the pore size increased, the dimensions of the pillars were correspondingly enlarged to maintain a consistent total pillar area within each device. This strategic design choice was important in maintaining a relatively uniform gradient propagation across devices, mitigating potential variations arising from differences in volume occupancy. For instance, if the pillars were kept at a constant area, enlarging the pore size would result in increased volume capacity in devices with larger pores. This would consequently lead to a decelerated gradient propagation, as the identical amount of attractant molecules would need to spread across a larger volume.

During the initial device design phase, we opted for circular pillars within the analysis zone. However, this choice posed challenges as cells encountered difficulty in fully enclosing their surroundings due to the need to navigate the curvature of the pillars on both sides at the same time. Moreover, the smaller size of circular pillars led to faster diffusion around them, thereby largely negating the potential of a locally enhanced concentration (data not shown).

For an effective intrinsic control, the heights of the devices were varied (see figure 13 C). In scenarios where individual cells could enclose the space between two pillars, they could potentially create a locally enhanced concentration within the gradient. However, elevating the device height would render cells incapable of enclosing their

surroundings, thus nullifying this enhancement effect. For instance, a device with smaller pores exhibiting a robust locally enhanced gradient due to migrating cells would promptly lose this effect in a taller device, as cells would be unable to push the gradient forward as it would just diffuse around the cells' top. Consequently, a range of device heights was integrated to ensure a consistent control across all designed devices. This control also effectively incorporated a control for cell quantities, as even an increased cell number couldn't bridge the gap in the z-axis. Hence, varying the device height served as a clever approach to establish a control for both pore size and cell numbers simultaneously.

During the establishment of the experimental setup an important observation was made. Within the research group two distinct approaches for handling microfluidic devices are employed – either submerging the device in a surrounding medium or placing liquid around the device to ensure adequate humidity (see figure 13 D). Both methods offer their own advantages and caveats. Submerging the devices guarantees a consistent nutrient supply from the surrounding medium. This is particularly critical given the minuscule liquid volumes within microfluidic devices, where the presence of numerous cells can rapidly deplete nutrients while concurrently leading to the accumulation of waste products. Instances of slowed migration or cell death after several hours of experimentation have been observed in cases where the device was not submerged, often due to this issue. Furthermore, submerging has the benefit of eliminating the need for a bypass mechanism, as loading discrepancies are swiftly canceled out once both reservoirs are connected to the ambient medium. Nevertheless, the submerged approach brings with it challenges about gradient stability. As both reservoirs maintain connections to the surrounding medium, substances within the device experience gradual outward diffusion. Consequently, an unstable gradient forms that diminishes over time. In contrast, the non-submerged approach ensures a highly stable gradient over extended periods, but it introduces issues related to flow between the reservoirs and the potential for nutrient depletion and waste product accumulation.

Given the necessity for a stable gradient to facilitate robust study outcomes, we opted for the non-submerging technique for this project. To counteract the resultant flow within the analysis zone, the bypass mechanism was integrated, which rapidly equalized pressure between the two reservoirs. However, in cases where significant differences in reservoir volumes existed, this pressure equalization could inadvertently transport substances from one reservoir to the other. To mitigate this effect, the attractant was consistently loaded first and subsequently introduced the cells. This approach established a pressure gradient from the cell reservoir toward the attractant reservoir, minimizing the likelihood of cells encountering the attractant before entering the analysis zone. An additional challenge associated with the bypass was the occurrence of diffusion through its channel. Consequently, after approximately 4 to 6 hours, the attractant would also diffuse through the bypass and reach the cell reservoir. Despite this phenomenon, it provided ample time for numerous cells to traverse the analysis zone.

3.3.2 Influence of Pore Size and Device Height on Efficiency of Maze Solving

With the refined design iterations of the microfluidic devices, experiments were started to investigate the influence of the local environment on cells and how this phenomenon could potentially enable them to amplify their perceived gradient response.

Our initial analysis of cell speeds across various pore sizes showed that a distinct trend emerged: higher pore sizes appeared to correlate with faster cell migration (see figure 14 A). Notably, cells in 5 µm pores exhibited the slowest speeds, while those in

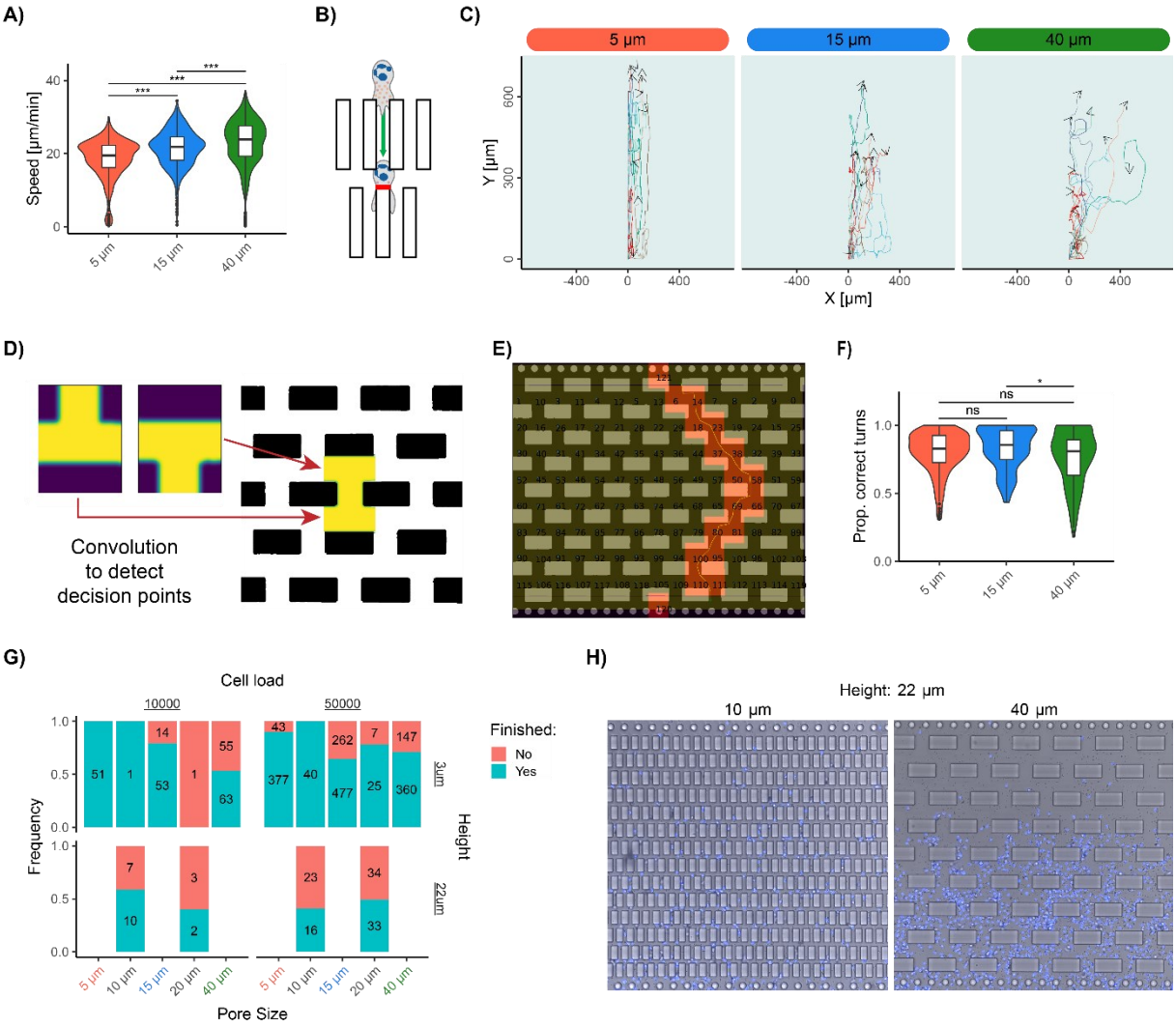


Figure 14: Pore size and device height effects on maze solving efficiency of cells. **A)** Median speed of whole cell tracks within the analysis zone for the 4, 15, and 40 µm pore sizes. Data represent cells in 3 µm high devices with 50,000 cells loaded. Pairwise Wilcoxon rank sum test with continuity correction (Bonferroni), ***, P < 0.001. **B)** Schematic of a migrating cell in a device with small pore sizes. A cell follows the migratory path along the pore (green arrow) and encounters a subsequent pore in close succession (red bar) which requires constant reshaping and adjustment of the cell. **C)** Spider plots of 10 random cells for the 4, 15, and 40 µm pore sizes. Black arrowheads show the orientation of the cell for the last time point they were tracked. Data represent cells in 3 µm high devices with 50,000 cells loaded. **D)** Automated detection of decision nodes was achieved through a convolution algorithm. This algorithm identified both the "downward-facing T" (left) and the "upward-facing T" (middle) structures within each device. These detected "T points" served as decision nodes for cells (right). By using these detected decision nodes, automatic mapping of decision points was generated for each device. **E)** A sample image of a device with a 40 µm pore size is depicted, showcasing semi-automated node detection. Each detected node is marked with blue dots with a corresponding black number, while the starting and ending nodes were manually added for each device. The cell trajectory is shown in yellow with a green dot and arrow indicating the track start and end, respectively. Nodes entered by the cell are highlighted in red. **F)** Proportion of correct turns for the 4, 15, and 40 µm pore sizes. Correct turns were calculated in a way that every second decision node the cell needed to move toward the maze finish. The proportion was calculated as follows: $\frac{Correct\ decicions}{Total\ decicion}$. Data represent cells in 3 µm high devices with 50.000 cells loaded. **G)** Frequency of maze finishers for various conditions. Preliminary results for all tested devices (5, 10, 15, 20, and 40 µm pores) with different heights (3 and 22 µm; secondary y-axis) and cell loads (10.000 and 50.000; secondary x-axis). Cells from the last 30 min. and cells that had less than 600 µm total displacement were removed from the analysis. To qualify as a finisher, cells had to surpass a minimum total y-displacement equivalent to the analysis zone length minus 200 µm. **H)** Snapshot after 2h for 22 µm high devices with 10 (left) or 40 µm (right) pore sizes. The blue signal indicates nuclear Hoechst staining.

15 and 40 µm pores demonstrated significantly higher speeds. Interestingly, cells in 40 µm pores were also faster than those in 15 µm pores. A plausible explanation for this phenomenon is the challenge posed by smaller pores. As a cell exits a pore, it's immediately confronted by the wall of the subsequent pore (see figure 14 B). This demands constant readjustment and repolarization of cells to navigate the maze effectively. Furthermore, as small pores are smaller than cells, cells experience significant compression. Consequently, when leaving a pore, cells simultaneously enter multiple downstream pores with multiple lamellipodia, triggering the need for informed decisions regarding which pore to enter next. This phenomenon likely results in cells slowing down within devices with smaller pores compared to larger ones, as cells in bigger pores have reduced contact with pore walls.

When attempting to analyze the impact of pore size on cell efficiency in solving the microfluidic maze, unexpected analysis complexities were encountered. The conventional method employed in cell migration studies is commonly cell straightness, which produced intriguing results. Notably, cells within smaller pores exhibited remarkably straighter trajectories compared to those within larger pores (see figure 14 C). In devices with 5 µm pores, cells displayed nearly linear migration paths, whereas cells in 40 µm devices exhibited more convoluted migratory routes, with trajectories in 15 µm pores lying between the two. However, this outcome is somewhat deceptive, as it can be attributed to the inherent characteristics of the pores themselves. In smaller pores, cells are effectively constrained to follow relatively straight paths due to reduced degrees of freedom. This is particularly pronounced given cells' affinity for maintaining contact with surfaces and migrating along them. In small pores, cells maintain constant contact with the pore walls, providing them a distinct advantage in terms of maintaining straighter paths. Conversely, in larger pore devices cells have less frequent contact with walls, leading to more varied trajectories. Furthermore, even if a cell were to frequently deviate from the intended path in smaller pores, the impact on trajectory appearance would be minimal. For instance, a one-pore deviation in 5 µm pore devices would result in a discrepancy of roughly 10-15 µm, whereas the same deviation in 40 µm pore devices would lead to an offset of nearly 80 µm (incorporating both pore and pillar sizes). Consequently, a single incorrect decision has a more pronounced effect on trajectory straightness in larger pores.

To refine the analysis, various corrective methodologies were explored, such as implementing "corrected straightness" metrics (data not shown). One approach involved using the geodesic distance, a method that calculates the shortest path between two points while accounting for obstacles, to determine the corrected straightness value. However, this approach encountered comparable challenges to the conventional straightness analysis, as trajectories closely following the walls proved to be more optimal for this algorithm. Consequently, this corrected straightness metric still exhibited a bias toward smaller pores, reflecting the consistent influence of the confined geometries on the cell trajectories. In another tested metric the "best migrator" was identified in each experiment – a cell that navigated the maze the quickest or followed the shortest trajectory – and used its displacement values as a reference for other cells. However, this approach introduced a significant drawback as it heavily skewed the analysis toward a single cell's behavior. For instance, if the "best cell" completed the entire maze from start to end, it would yield an optimal path longer than that of cells entering the analysis zone from a side point or cells whose initial trajectory point was already within the analysis zone. Consequently, this led to calculated straightness values exceeding 1. While it was possible to address this issue by applying stringent filtering criteria, doing so would result in the loss of a substantial number of eligible cells. Ultimately, our focus was on assessing how effectively cells made

decisions at each decision point, rather than shaping filtering methods to align with the analysis approach. Several other alternative metrics were explored to achieve a "corrected" measure of straightness. However, each of these approaches presented considerable limitations, making the analysis of track straightness complex and possibly prone to misinterpretation.

A more effective approach emerged when decision nodes were defined at each location where a cell needed to choose a path. This method involved assessing the efficiency of turns by comparing the number of optimal decisions with the total decisions made. For instance, a cell encountering a decision node could opt to move up into a pore, thereby progressing toward completing the maze, or choose to backtrack or bypass the pore, potentially entering another pore further down. In this analysis, the first choice would be considered an "optimal decision," while the second would be deemed a "wrong" decision as it prolonged the cell's presence within the maze. To execute this analysis, machine learning segmentation on the bright-field images of each device was employed to generate a microfluidic mask encompassing the pillars and pores. This mask, in conjunction with a convolution algorithm, helped identify decision nodes within each microfluidic device (see figure 14 D). Manual addition of start and end points completed the process for each device. Each node was uniquely identified, enabling the tracking of all nodes entered by cells during their migration paths. This allowed for the calculation of the proportion of correct turns for every cell in each device (see figure 14 E). Utilizing this analytical approach, it was observed that 15 µm pores exhibited notably better decision performance than the 40 µm pores. The proportion of correct decisions for the 5 and 40 µm pores were 0.83 and 0.81, respectively, while the proportion for the 15 µm pore was 0.86. It is essential to acknowledge that although the differences may appear slight, there is a discernible trend indicating that smaller pores tend to yield a higher overall proportion of correct turns compared to larger pores. Additionally, it's important to note that the analysis script remains a work in progress, as certain caveats persist, and alterations to the method can result in significant discrepancies in the obtained values. For example, omitting the starting and finishing lines yielded non-significant differences between the 5 and 15 µm pores, but both were significantly different from the 40 µm pore (data not shown).

In addition to evaluating the efficiency of cells in making correct migratory choices to navigate the maze, the number of cells that completed the maze was also investigated. This comprehensive analysis encompassed a broader dataset, incorporating 3 µm and 22 µm high devices, cell loads of 10,000 or 50,000, and pore sizes of 5, 10, 15, 20, and 40 µm (see figure 14 G). The findings unveiled two distinctive outcomes. Firstly, and most striking, in 22 µm high devices, generally less than half of the cells managed to finish the maze. This observation aligned with our empirical observations across all experiments. It appears that cells tend to become disoriented or entrapped midway through the mazes, with the completion of the maze being a rarer occurrence. Though not evident in the data, empirical observations suggest that cells in smaller pores within 22 µm high devices advance further into the maze compared to cells in devices with larger pores (see figure 14 H). Secondly, there seems to be a trend wherein fewer cells complete the maze as pore sizes increase. This phenomenon is more pronounced in devices with a height of 3 µm. Interestingly, no clear trend for the variations in loaded cell numbers was observed. However, upon empirical evaluation of the videos, it seems that cells in devices with higher cell numbers perform better. It's essential to acknowledge that analyzing finishing cells heavily depends on filtering criteria and the definition of "finishing". The present approach excludes cells that entered the analysis zone during the last 30 minutes, eliminating cells that lack adequate time to complete the maze. Additionally, cells with very short trajectories are removed, as

these might enter the maze briefly but then exit the field of view. However, the criterion for being classified as a "finisher" is based on traversing the entire analysis zone, allowing a 200 µm margin, which cells need to pass via their calculated total y displacement (defined per cell as: $Y_{Start} - Y_{End}$). Altering this threshold significantly influences the count of finishing cells, and upon closer examination of excluded cells, many considered non-finishers actually completed the maze. Alternative methods to define finishing cells were explored as well (data not shown). One strategy was to define an approximately 100 µm area around the finishing line, and cells entering this zone would be regarded as finishers. While this approach seems conceptually sound, its practical implementation would be time-consuming, requiring individual adjustments for each maze due to the distinct x/y coordinates of the analysis zone in each microscopy experiment. Attempting to define a common finishing coordinate resulted in unfavorable outcomes. Another approach involved using the cumulative sum of all movements in the y-direction toward the maze's finishing line as a filter for cells that traversed the entire length of the analysis zone. However, this method also failed to provide a perfect differentiation between finishers and non-finishers. Nevertheless, the potential for error in defining finishers and non-finishers should be systematic across all devices, ensuring the reliability of observed trends. These trends underscore the challenges cells face in completing higher devices and their reduced efficiency in larger pore sizes.

An intriguing additional observation that emerged from the experiments is related to the collective behavior of cells when devices were initially submerged. It was frequently observed that cells exhibited a collective behavior, forming a cohesive front and migrating in unison upward the gradient. Interestingly, this phenomenon was absent in non-submerged devices and was also absent in devices loaded with only 10,000 cells.

In summary, the collected data implies that larger pores promote faster cell migration, while smaller pores enhance the efficiency of cell navigation within the mazes. Furthermore, as the device height increases, the task of solving the maze becomes progressively more demanding for migrating cells.

3.3.3 Linking Maze Solving Efficiency With Cell Derived Gradient Manipulation

Besides the observed behavioral alterations in migrating cells across the array of tested devices, we intended to establish a connection with the theoretical variations in locally enhanced gradients. However, this endeavor again presented a significant challenge.

Upon manual examination of the gradients around cells in pores, when a cell entered into a pore, there was a discernible increase in concentration within this pore compared to a neighboring pore without a cell (data not shown). This phenomenon became notably more pronounced when the cell was positioned within the pore (see figure 15 A). The concentration in front of the cell experienced a slight elevation, while the concentration in the back of the cell diminished more markedly. Intriguingly, upon the cell's exit from a pore, the concentration within the pore did not exhibit a pronounced gradient until it began to recover (data not shown). The fact that one could discern these subtle nuances is noteworthy, particularly considering that the measured intensities correspond to a volume of approximately 0.45 pL (assuming dimensions for the front peak area: length of 10 µm, width of 15 µm, and height of 3 µm).

This observed phenomenon was also noticeable for groups of cells, particularly when an individual cell was unable to enclose its surroundings to manipulate the gradient (see figure 15 B). When a cluster of cells simultaneously enters a larger pore, it becomes apparent that they concentrate the gradient ahead of them while depleting it behind them. Interestingly, as soon as the front of the cell cluster breaks open upon

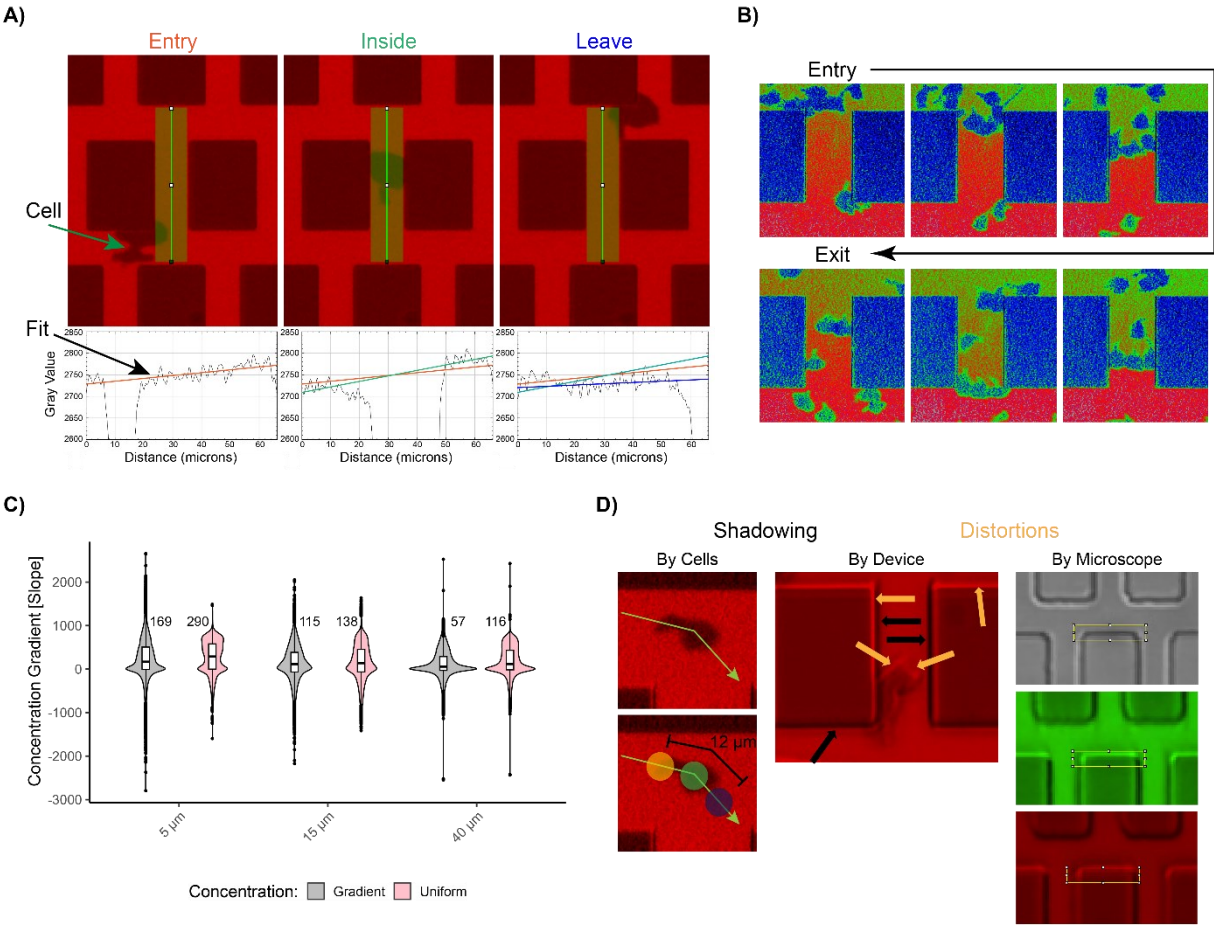


Figure 15: Influence of migrating cells on gradients within microfluidic devices and subsequent measurement challenges. Approximate proxy signal intensity around a cell within a 15 µm pore. Snapshots represent the entry (red; left), being inside (green; middle) and when leaving (blue; right) the pore. The intensity was measured (green rectangles; top) and subsequent intensity profiles were plotted (bottom). A manual basic estimated linear fit was assessed and projected onto the profiles for the respective locations of the cell (i.e., entry, inside, or leave). Projections were kept within the profile to compare to previous locations. The red signal and the respective intensity profile correspond to the Atto-644 signal, and the shadow of the cell was highlighted with a green arrow (left). The time difference between snapshots is 1 minute. **B)** Snapshots of a collective gradient manipulation within a 40 µm pore device are shown. The time difference between snapshots is 1 minute. High signal intensities are illustrated as red, while low are blue. The arrow from “Entry” to “Exit” illustrated the order of images. **C)** Average concentration gradient around cells for experimental assessment. To assess the efficacy of our automatic gradient extraction script, experiments were run with 5, 15, and 40 µm pore size devices that had either a uniform concentration (pink) or gradient (grey). Trajectories of cells were used to extract the corresponding proxy values at the front and back of the cell (both at 12 µm distance), as well as at the center of the cell. Values (proxy concentration at front, center, and back) were subsequently used to calculate a linear fit, and the slope of the resulting fit of each cell was plotted. The numbers next to the plots correspond to the respective median values. **D)** Challenges in automatic gradient extraction due to optical aberrations. Three primary sources of aberrations were identified, leading to difficulties in automated gradient extraction. Cells casting shadows (left) resulted in the exclusion of signals where cells were positioned. The analysis script leveraged cell trajectories (green arrow) to extract gradient values from the center of the current cell location (green dot), as well as proxy values ahead of the cell's path (blue dot) and behind it (yellow dot) at 12 µm distance. Consequently, when a cell's body was within these regions, the extracted intensity was reduced. Of note, the extraction took the microfluidic mask into account so that pillars should be excluded. Additionally, not a single pixel was extracted but a radial area which was smoothed via a Gaussian blur, and the resulting average was extracted. Device-induced shadows (middle; black arrows) arose from optical distortions at the pillar borders. When cells were close to walls, this method generated lower values within these zones. Device distortions (middle; yellow arrows) often led to increased brightness around pillars or cells, despite the signal

Continuation of figure 15 legend: being consistent with the surrounding area. Extracting proxy values from these regions yielded higher values. Microscope distortions (right; yellow rectangles) stemmed from differences in detection wavelengths. The depicted squares occupied identical x/y positions, but they did not coincide in the distinct detectors. Mask generation relied on brightfield images, causing disparities in coordinates within proxy intensity fields and thus partial extraction of values within pillars.

leaving the pore, the concentration swiftly diffuses back into the pore. It's noteworthy that, analogous to the observations of cell behavior in submerged and non-submerged devices, a distinction was observed here as well. While the direct manipulation of the gradient by multiple cells was frequently observed in submerged devices, this behavior was never witnessed in non-submerged devices (as seen in figure 15 B). Despite this, one could still manually quantify gradient differences in non-submerged devices (as seen in figure 15 A).

To quantify the locally enhanced gradient of cells within pores automatically and correlate it with maze-solving efficiency, a script leveraging cell trajectories to extract gradient values was developed. At each time point, the script extracted proxy values from the current cell location, considering the microfluidic mask to exclude pillar areas. To ensure accurate results, the script averaged values over a radial area, applying a Gaussian blur for smoothing. The trajectory was also considered, extracting values both 12 µm ahead (front of the cell) and behind (back of the cell) along the trajectory path. These values were utilized to calculate a linear fit, representing the experienced gradient around cells. To validate the script's accuracy, experiments were conducted in which a chemotactic gradient of fMLF was maintained, but the proxy dyes were presented either in a gradient or uniform concentration (see figure 15 C). Intriguingly, the results revealed discrepancies. Not only did the uniform concentration extraction consistently show higher slopes for all devices, but there was also a significant reduction in the slope as pore size increased. For instance, in the 5 µm pore, the median slope for the gradient was approximately 169, while the uniform concentration exhibited a slope of around 290. Similarly, for the 15 µm pore, the values were around 115 to 138, and for the 40 µm pore, they ranged from 57 to 116. These discrepancies, however, raised doubts about the script's accuracy and its ability to produce meaningful and plausible outcomes.

To understand why multiple iterations of the script consistently produced similar results, the raw data were investigated to identify potential underlying reasons. This exploration revealed the presence of several optical and chromatic aberrations, posing substantial challenges for any “simple” analysis script (see figure 15 D). Firstly, optical issues arising from the cells themselves were observed, particularly in devices with small heights. The confined cells pushed the proxy dye out of the space they occupied, leaving behind a shadow of their own cell volume. Since the script utilized cell trajectories for value extraction, if the extraction area coincided with the cell's shadow, the extracted values were therefore significantly lower. This is aggravated by the fact that cells typically have a longer uropod compared to a longer lamellipodia. As a result, the extraction of values from the cell's back often contained remnants of the shadow, artificially generating gradients even within uniform concentrations. Furthermore, the microfluidic device itself contributed to optical aberrations. Depending on the microscope's lighting configuration and the specific microfluidic device, shadows or areas of increased brightness could appear around pillar and cell edges. Although the mask usually excluded pillar areas, these optical artifacts around cells could still lead to problems in the script, yielding abnormally low or high extracted values. Lastly, chromatic aberrations introduced by the microscope also played a role. In wide-field microscopy, brightfield and fluorescent images may not perfectly overlap at the same x/y

coordinates. While these differences are generally minor, using brightfield images for mask creation could cause significant issues – particularly in devices with small pores. Areas that should be masked might remain unmasked due to these chromatic discrepancies, leading to extractions within pillar regions which can either increase or decrease the obtained intensity values. Considering these various optical aberrations, it becomes evident why our previous automatic attempts yielded unsatisfactory results. Overcoming these challenges would require substantial image-analysis efforts to counteract each of these factors comprehensively.

In summary, our manual observations revealed that both individual cells and groups of cells could locally enhance their perceived gradient within the microfluidic devices. However, automating the analysis of this phenomenon has proven challenging due to a combination of analysis limitations and various optical aberrations.

3.4 Discussion

During this Ph.D., we conducted various migratory assays with neutrophils, as well as neutrophil-like cells, and noticed variations in cell persistence despite using similar concentrations of attractant. This led us to investigate the underlying reasons for these significant differences and we formulated two hypotheses. The first hypothesis was related to the differences in gradient fields experienced by cells in different assays, a subject already explored and discussed in chapter 2. The second hypothesis assumed that individual cells or cell collectives could strategically exploit their local environment. By enclosing their immediate surroundings, they could push the gradient forward, depleting it at their rear while enhancing it in front. This action would lead to a substantial increase in their experienced Δc (front-back concentration). Our subsequent analysis with microfluidic devices yielded several intriguing findings.

Our analysis of cell speeds revealed a significant trend – as pore size increased, cells exhibited higher speeds. This phenomenon appeared to be tied to the mechanical constraints imposed by pore sizes. In smaller pores, cells experienced tight confinement, resulting in increased squeezing from all sides and a subsequent increase in their effective occupied area. Besides the mechanical effects, this expansion in cell area introduced additional challenges. As cells exited a pore, they immediately encountered the wall of the next pore, leading to a deceleration in their movement. Moreover, the close proximity of adjacent pores, combined with the larger cell area, caused cells to enter multiple pores downstream from their current location. This introduced decision-making complexities as cells needed to select the appropriate lamellipodia to follow downstream. A related study by Renkawitz et al. supported these observations [115]. Their work demonstrated that not only did cells require longer times to traverse constrictions in narrower pores, but when faced with decisions regarding which pore to enter, their speed decreased compared to following a straight channel.

Another intriguing finding is that larger pore sizes appear to correlate with decreased efficiency in navigating the maze optimally. This trend, combined with the reduced speed observed in smaller pores, presents an interesting connection. A related study by Skoge et al., who orchestrated the Dicty World Race, revealed that among various (mutated) cell types from all competitors, the cells that excelled in maze-solving were not the fastest, but rather slightly slower cells with enhanced sensing capabilities [116]. Surprisingly, being slower grants cells the advantage of better adjustment and repolarization in response to stimuli. For instance, a fast cell might overshoot the correct turn due to its speed, while a slower cell has the time to accurately perceive and interpret the gradient, enabling precise adjustments in trajectory. In essence, it seems that slower cells possess the ability to make more intelligent, informed, and efficient decisions.

Among all the investigated parameters, the height of the microfluidic device emerged as the most influential factor affecting the cells' ability to navigate the maze. Notably, devices with a height of 22 µm had fewer than half of the tracked cells managing to solve the maze. Interestingly, even within higher devices, cells in devices with smaller pores displayed greater progress into the maze. This suggests that even in higher devices, smaller pores might still contribute to a partial enhancement of the gradient. Alternatively, smaller pores might help in better wall adhesion, aiding the navigation of cells. Another potential factor could be that cells require confinement within microfluidic devices to propel themselves effectively, with smaller pore sizes facilitating contact-based propulsion along the walls when confinement is not given. However, this observation alone fails to explain why cells in taller devices can advance approximately halfway through the maze before their progress halts. This is particularly intriguing since the number of cells completing the maze is nearly the same between small and large pores in higher devices – a scenario where smaller pores should logically result in more finishers if confinement and wall adhesion was the primary factor. We hypothesize that cells struggle to locally enhance the gradient significantly in taller devices, contributing to the observed differences. An alternative explanation could involve the gradient field itself. In confined environments (e.g., small height devices), cells experience concentrations primarily at their front and back. In contrast, higher devices expose cells to concentrations at their top as well. Additionally, while the loaded concentrations were the same, larger devices inherently possess more volume, potentially affecting the diffusion of attractants. Although one might intuitively assume that gradients propagate faster in larger devices due to increased reservoir cross-sections, allowing more molecules to enter, the exact relationship is complex and might not yield a straightforward answer (to be frank, one could also argue the propagation is the same or that the smaller heights have a faster propagation due to the smaller volume – we have asked various physicists and got different answers from each…). This leads us to consider the concept of self-generated gradients proposed by the Insall lab, where cells can modify gradients directly through external means (e.g., released proteases) or on a surface level (e.g., scavenger receptors) [39]. If neutrophils possess the ability to directly alter gradients, beyond the described pushing mechanism, it introduces another layer of complexity. In larger devices with more volume, altering the surrounding gradient might be challenging due to the higher total molecule count within the same area of the device. While our lab has explored self-generated gradients for dendritic cells (see chapter 4.2.1), the capabilities of generating their own gradients remain uncertain for neutrophil-like cells. Although we have not yet observed this capability for neutrophil-like cells by ourselves, considering the abundance of neutrophils *in vivo*, especially on sites of inflammations, and their migration through tight tissue spaces, the potential to directly modify gradients could significantly enhance their gradient-sensing abilities. In conclusion, several gradient-related factors likely contribute to the observed differences between smaller and taller microfluidic devices, influencing neutrophil navigation outcomes.

Another interesting observation made includes the distinctions between submerged and non-submerged devices. While the direct manipulation of gradients by cell collectives and the collective migration of cells were clearly evident in submerged devices, similar behavior was never observed in non-submerged devices. Of note, while we were able to manually measure gradient differences in non-submerged devices, we never observed these differences through visual observation alone when watching the recorded videos. We propose three key differences that might contribute to this contrast: gradient stability, nutrient supply, and waste material accumulation. While we believe the latter two factors are less likely to be responsible for the observed behavior,

gradient instability stands out as a plausible causative factor. In submerged devices, the proxy concentration continuously diffuses out of the source, resulting in fewer proxy molecules available to replenish the locally manipulated gradients around cells. This dynamic makes it easier for us to detect gradient manipulation, particularly because we could best observe these manipulations at the entry points of the maze, which are the farthest locations from the source. However, as one moved closer to the source, it became increasingly challenging to observe or measure these manipulations. Approaching the source, the gradient became more pronounced and stable, resulting in a higher concentration of molecules available to restore the displaced proxy. This led to increased difficulty in discerning gradient manipulations in those regions. The observed collective behavior of cells is also likely influenced by the gradient's instability. Collectively migrating cells also contribute to the gradient's instability as they push and displace it while potentially directly altering it. This results in a gradient that is highly dynamic and locally noisy. Given that collective migration is known to enhance gradient reading compared to individual cells, this aligns with our observations, where the noisy gradient leads to the formation of a collective cell front. [117,118]. Notably, our collective of cells did not form tight clusters but migrated as a cohesive front. This could also support our hypothesis, as the collective itself has the capability to push the gradient forward, enhancing it locally and thus making it more discernible through the improved Δc. Moreover, instances were noticed where cells reached the maze entry but paused before entering, seemingly waiting for other cells to align at the entry before the entire collective proceeded. This behavior underscores the role of gradient properties in steering collective responses among leukocytes, allowing them to dynamically adapt to varying gradient scenarios. Overall, these findings underscore the intricate interplay between gradient properties and cell behavior in complex microenvironments.

Interestingly, when this project was initiated, no existing publications were addressing the observed behavior of cells creating a locally enhanced gradient through pushing in confining spaces. Several years later, Wang et al. published a study confirming the validity of our hypothesis [119]. They investigated neutrophils *in vivo* and discovered that when two neutrophils entered a bifurcation consecutive, the first one chose one path while the second one predominantly took the alternative route. Wang and colleagues then replicated this scenario using microfluidic devices featuring bifurcations and subsequent long channels, where they indeed measured a significant gradient manipulation – intensification ahead of the cells and depletion behind them. However, their experiments focused on individual cells and lacked consideration for collective gradient manipulation. In addition, experiments were conducted in setups where gradient restoration was improbable due to the extended channel length. In contrast, our microfluidic devices aimed to replicate an *in vivo* environment where cell collectives could potentially alter the gradient, reflecting tissue structures more akin to mazes than individual vessels. Despite these differences, their study validated the fundamental principle of our hypothesis. We also successfully observed and quantified gradient manipulation by both single cells and cell collectives within our pillar-based mazes. Additionally, in certain experiments where exclusively long straight channels were employed that cells could completely seal off with their bodies, we were able to replicate the results of Wang et al. In these instances, we observed cells effectively depleting the attractant concentration behind them and significantly amplifying it in front of them, thus not only supporting their findings but also our hypothesis (data not shown).

While we were able to manually observe and measure the local enhancement of gradients, automating the gradient extraction proved challenging. The automated script employed a microfluidic device mask to block pillar areas and utilized cell tracks to extract proxy concentrations along their trajectories. However, technical limitations led

to optical aberrations altering the extracted signal erroneously. The observed higher gradients around cells in uniform concentrations likely resulted from a combination of the uniformly high proxy concentrations throughout the device, and the shadowing effects of the uropod (i.e., the displaced proxy concentration by the cells' body). In relation to the tracked nucleus, cells tend to be longer in the rear, leading to a more pronounced shadowing effect during proxy extraction at the back of the cell compared to the front. Given the overall higher proxy signal in uniform experiments, this shadowing phenomenon had a more significant impact than in scenarios with gradients. Furthermore, smaller pore sizes led to increased cell compression within the pores, resulting in larger cell areas. This increased area amplified the potential for shadowing effects, contributing to the observed higher gradient in smaller pore sizes. An additional challenge arises from the inherent shadowing effect associated with the center concentration, given the direct presence of the cell body in that region. As such, using the center concentration for gradient normalization isn't advisable, as it's prone to extracting mostly noisy signals. Another limitation of the existing script is its indiscriminate extraction of values at all locations, regardless of whether a cell is within a pore or not. This approach includes proxy values even when cells are not located within a pore, potentially resulting in a significant reduction of the gradient. This concern is particularly relevant for the 40 µm pore, where substantial portions lie outside of the pore and are therefore less likely to be enclosed by the respective cells. To establish a strong connection between the observed cell behaviors and their underlying causative factors, this project must develop a reliable and efficient method for extracting the observed gradient manipulation. Hence, a significant optimization of the gradient extraction process is imperative. Manual methods, while informative, tend to yield lower sample numbers and lack robustness. A potential solution lies in the implementation of machine learning techniques, such as cellpose, to segment the shadows created by cells at each time point. Integrating this segmentation as a mask for extraction could help exclude signal interference caused by shadows. However, the application of this approach might still face challenges in addressing both shadowing and areas where cell perimeters appear brighter. Given that these optical aberrations predominantly occur just beyond the cell's circumference, it remains uncertain whether a cell mask generated by machine learning algorithms would effectively encompass these aberrant regions, as distinguishing different cell borders can often pose challenges for reliable detection. Therefore, further investigation and adaptation are necessary to overcome these complexities.

The implemented analysis of maze finishers is strongly biased by the corresponding filtering parameters used, as well as by challenges with cell tracking. Manual adjustments to these filtering parameters could lead to categorizing any cell as a finisher or none at all. Determining optimal settings requires substantial manual effort to define a finishing area for each maze individually. The tracking process is also affected when numerous cells are confined within the maze, causing them to frequently bump into each other and potentially disrupting tracking algorithms. Consequently, some tracks might be fragmented, resulting in cells being counted as non-finishers due to incomplete tracking data and insufficient y displacement for classification as finishers. Moreover, cells could exit the field of view on the sides, and although they might complete the maze just beyond the view, the current analysis would categorize them as non-finishers. Notably, addressing tracking challenges through more accurate manual finishing zones would not correct split tracks (one part of the track would still be counted as a non-finisher) or sidetracked cells (would never reach the finishing zone within the field of view). Despite these limitations, this systematic error should be consistent across device variations, providing a level of reliability to the obtained trend results.

The most optimal analysis method currently available is the established track efficiency script, which utilizes the maze mask to create nodes and assesses whether a cell follows an optimal trajectory. In this analysis, it doesn't matter whether a cell completes the maze or gets sidetracked, nor is it affected by fragmented tracks – it solely focuses on evaluating whether the cell consistently makes correct migration decisions toward the maze finish. However, this script also has limitations. Firstly, it does not penalize cells that continuously move back and forth within a single node, which can be especially problematic in larger pore sizes where nodes are significantly larger. Secondly, and more importantly, the script only considers a cell's trajectory if one of the tracked time points falls within a node. This can lead to issues with fast-moving cells that pass through multiple nodes between timeframes. This issue becomes particularly pronounced in smaller pore sizes, where cells can traverse multiple nodes within a single timeframe. These shortcomings could be resolved by adjusting the script to penalize cells residing within a node for an extended period and by implementing interpolation of cell trajectories between tracked points to account for positions between frames.

For a single cell or a group of cells to effectively enhance the gradient locally in an informative way, certain prerequisites must be met. First, the cell or cell collective must be able enclose the local environment to a degree that significantly alters diffusion, effectively blocking the path of diffusion towards the back of the cell. In *in vivo* migration of most leukocytes inside tissues during an infection, the local geometry often allows for complete blockage of diffusion locally, as pores are typically smaller than the cell diameter, and cells need to adjust their shape to navigate through pores and capillaries. Secondly, the cell membrane should not be permeable to the attractant, as its diffusion through the cell would render the cells or collective incapable of locally enhancing the gradient. Since most attractants require receptor-mediated endocytosis, it is likely that attractants cannot diffuse through the membrane without active cellular efforts to do so. In an open environment, this proposed mechanism would not be possible, as attractant molecules would simply diffuse around the cells. Interestingly, when a cell or cell cluster encounters a bifurcation, the smaller-sized bifurcation is likely where the cells would enter, as the enhancing effect would be more significant. In the case of similar sizes, it is assumed that the leading cell would enter one randomly, but following cells would consistently choose the opposite bifurcation. This choice is driven by the slight depletion of the gradient in the occupied channel, providing less incentive for cells to enter those channels. This behavior has been demonstrated by Wang et al., where in both tissue and microfluidic devices, cells consistently entered the opposite channel compared to the cell before them [119].

Certain mentioned improvements are simple to implement but require an adequate time and testing. However, the project is currently on hold to prioritize the main project of this thesis. Despite this current pause of the project, my strong belief in its potential persists. The project has uncovered intriguing effects and results that suggest a wealth of concealed information within the data. Fine-tuning the efficiency script promises to unveil more pronounced distinctions between pore sizes. While time and technical constraints have delayed these improvements, it's worth noting that manual measurements have already substantiated the existence of a gradient manipulation effect induced by cells. In addition, our observations indicate that cells tend to show better performance in smaller pores and devices, likely attributable to an improved ability to enhance gradients in these conditions. This link between observed behavior and the gradient effect is established, even if not fully quantified due to present limitations. Indeed, there remain numerous avenues for future analysis within this project. Exploring how cells perform when in proximity to other cells, whether in clusters or not, could

shed light on the dynamics of collective cell migration. Particularly, the comparison between submerged and non-submerged devices holds promise for insights into collective cell migration dynamics. I remain steadfast in my belief in the project's potential and the valuable contributions it can make to our understanding of cell behavior in complex microenvironments.

4 Additional Work

In the following chapter, projects are presented that I have been personally worked on. The first part contains projects that are still in the preliminary stages of development and do not warrant separate chapters. Subsequently, projects conducted by colleagues or collaborative partners will be discussed, where I was providing assistance, contributing to the resulting publications (see 7.1 for reference). Finally, a brief list and summary of projects that yielded no or negative results will be provided.

4.1 Own Projects

4.1.1 To Light the way – Use of Laser-Assisted Protein Adsorption by Photobleaching to Print Gradients for Neutrophils

4.1.1.1 Summary

The "Laser-Assisted Protein Adsorption by Photobleaching" (LAPAP) technique was initially successfully established in our laboratory to create immobilized soluble gradients on surfaces for investigating chemotaxis/haptotaxis behaviors in dendritic cells. With this project, our goal was to adapt the LAPAP protocol and reagents to human neutrophils or neutrophil-like cells, such as PLB-985 cells, to study their responses in terms of chemotaxis/haptotaxis. As a result, various click chemistry reagents (Azide-Alkyne and Alkyne-Azide pairs), as well as patterning reagents (fluorescein; LAPAP variants for fMLF) and surface coating strategies (e.g., Polyvinyl alcohol - PVA), were tested with varying concentrations and patterning procedures (altering duration and intensities). As an outcome, the patterning effect on primary human neutrophils as well as on differentiated PLB-985 and HL-60 cells was investigated. Despite extensive experimentation, involving collaborations with experts in the field, we encountered various challenges. Unfortunately, even after multiple rounds of parameter adjustments and testing, including collaborative efforts with experienced colleagues and a company that uses LAPAP, we were unable to elicit a response from neutrophils to patterned gradients or uniform concentrations of fMLF. This project extended over a span of approximately 2 to 3 years, during which concerted efforts were made to establish the technique. Unfortunately, a proof-of-principle for neutrophils was not achieved. Additionally, discussions with former lab members who had used LAPAP for dendritic cell research led us to understand that they also ceased working with the LAPAP system due to limitations it presented for studying chemotaxis/haptotaxis. As a result, it was eventually decided to discontinue this project due to the lack of positive outcomes and practical challenges associated with using LAPAP for studying neutrophil migration.

4.1.1.2 Introduction

A range of assays are available to explore the impact of soluble or immobilized attractants on cellular migration. These assays encompass methodologies like the under-agarose assay and filter-based techniques such as the Boyden chamber and Zigmond chamber, which enable *in vitro* migration analysis [120,121]. However, these assays often rely on dynamically changing gradients of soluble chemoattractants, which come with inherent limitations, as discussed in the introductory section. Notably, microfluidics-based migration assays have emerged in recent years, providing enhanced gradient manipulation capabilities [35,122]. Nevertheless, their implementation can be intricate due to the incorporation of valve systems and the need for an active flow in the system. Traditional assays that utilize surface-bound cues have historically been employed to study axonal guidance in neurons [123]. However, these assays have more recently been

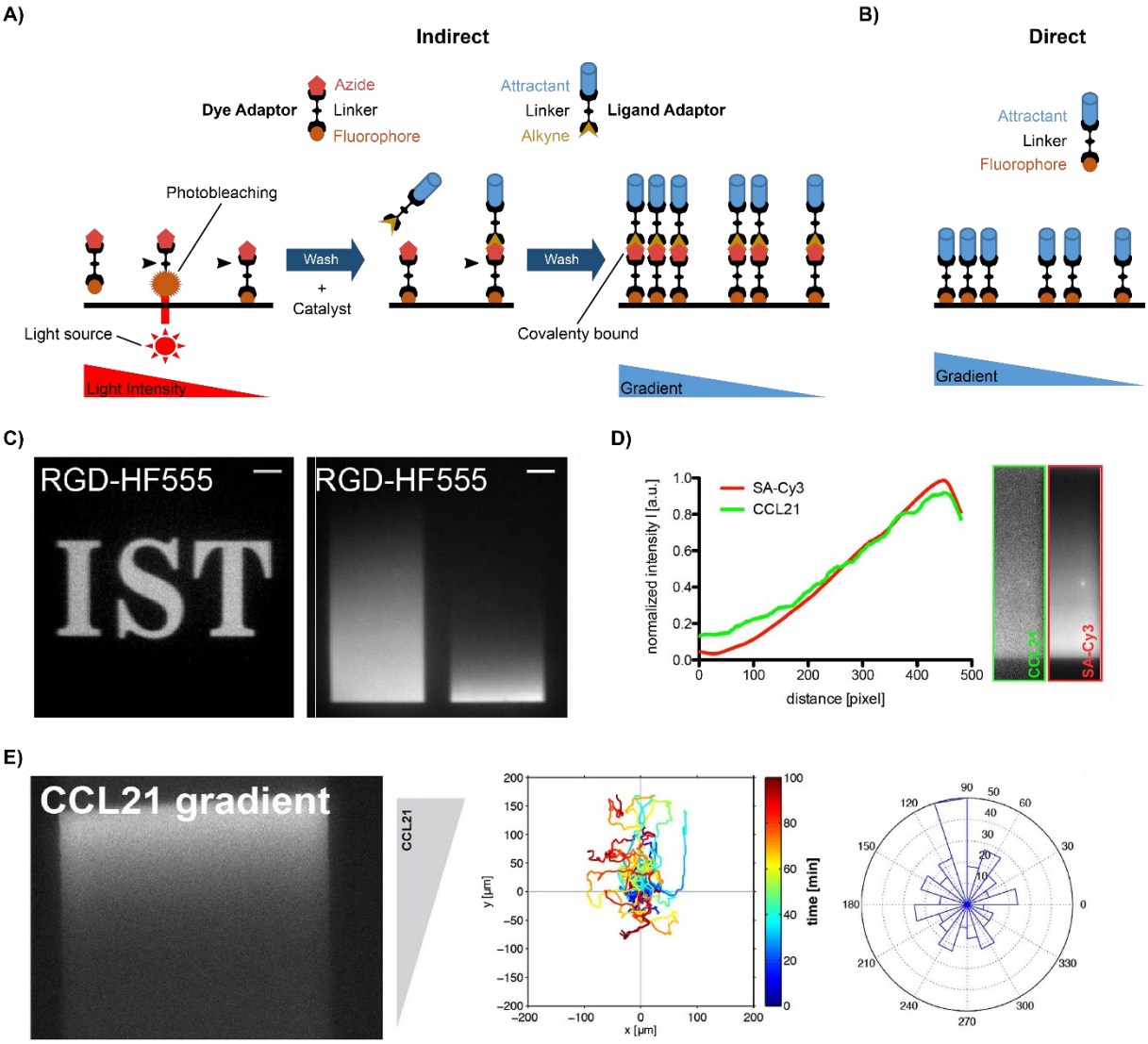


Figure 16: LAPAP methodology and proof of concept. **A)** Indirect LAPAP method. The LAPAP procedure entails the utilization of two distinct click partners: a fluorophore tethered to the first click partner via a linker, and a second click partner linked to an attractant through another linker. Importantly, azide and alkyne functionalities can be exchanged, and the attractant can be replaced by any suitable fluorophore for gradient visualization. The process commences with the use of a light source to photobleach the fluorophore associated with the dye adaptor, which subsequently binds covalently to the substrate's surface. The extent of this binding is influenced by the intensity and duration of the light exposure – greater values result in more dye adaptor proteins being immobilized. The unbleached fluorophore is then removed through washing, and the ligand adaptor is introduced along with the click chemistry catalyst. This leads to the formation of a covalent linkage between both adaptors. After the removal of unbound ligand adaptors, a gradient is generated that mirrors the initial gradient in light intensity. **B)** Direct LAPAP method. Similar to A) but instead of using click chemistry, the fluorophore and the attractant are directly linked on the same adaptor. This enables the direct patterning of the respective attractant. **C)** Fluorescence images of RGD-HF555 patterns and gradients on PVA surfaces. Scale bar 50 µm. Figure and legend taken and adapted from unpublished data of Jan Schwarz. **D)** Immunostaining of a linear CCL21 gradient printed in a migration chamber. SA-Cy3 image (red line and right image) and anti-CCL21/anti-goat AF 488 image (green line and left image). Fluorescence intensities were normalized to the respective maximum. Figure and legend taken and adapted from Schwarz et al [34]. **E)** DCs migrating on a SA-Cy3 stained CCL21 24-98 bio gradient printed in a microfluidic channel. Left panel: Representative images of the SA-Cy3 stained patterns. Middle panel: Trajectories of all cells in the respective field of view, with trajectories plotted to a common starting point [dimensions in µm; time is color-coded]. Gradient direction and pattern shape are indicated in grey. Right panel: Rose plot visualizing the distribution of angles of all cell tracks in an angular sector field with tracks split into 3 minutes intervals. Figure and legend taken and adapted from Schwarz et al [34].

adapted to investigate leukocyte migration. Nevertheless, these assays and various other protein micropatterning techniques, like mask-bound photolithography or micro-contact printing, often lack the necessary spatial resolution to accurately replicate the uniform and continuous gradients essential for such studies [124,125].

In recent years, the LAPAP technology has emerged as a promising solution that aims to combine the benefits of the aforementioned methods while circumventing their limitations [126]. LAPAP offers a unique approach capable of creating highly reproducible substrate-bound gradients of attractant concentrations at microscale resolution. Depending on the research question, these gradients can be adjusted in terms of steepness, strength, and shape. The general principle underlying LAPAP is the covalent surface immobilization of dye molecules, such as fluorescein, through photoactivation. By modulating the intensity of light, the quantity of immobilized fluorescein can be controlled, enabling the generation of homogeneous, continuous gradients. This is achieved using photomasks or movable lasers, thus providing the capacity to immobilize chemokine patterns with arbitrary gradients or uniform concentration patches.

In more detail, the indirect LAPAP technique involves a two-step process to immobilize molecules onto a surface, forming a bioactive monolayer. In the initial step, a fluorescent dye-labeled adapter molecule is covalently anchored to the surface through photobleaching (figure 16 A left). In the subsequent step, a catalyst is employed to facilitate a click chemistry reaction that covalently links the ligand adaptor to the surface-bound dye adapter molecule (figure 16 A middle & right). This separation of the photobleaching and ligand binding steps prevents any degradation of the ligand during the photobleaching phase. Consequently, only active, and accessible ligands are presented on the surface, ensuring optimal bioactivity. Given its covalent nature, versatility, and specificity, the alkyne/azide 'click' system is preferred as the chemical adapter system for linking the surface-immobilized adapter with the corresponding ligand [127]. In this system, molecules or proteins labeled with azide groups are covalently affixed to photo-immobilized alkynes, or vice versa, creating a robust and effective binding configuration. For a simpler and quicker approach, the attractant can be directly attached to the fluorophore through a linker and then patterned onto the surface without the requirement for click chemistry (figure 16 B). However, this method could result in the attractant adopting unconventional conformations, rendering it inaccessible to interacting cells. Moreover, this approach may exhibit reduced specificity and sensitivity, potentially leading to higher levels of background noise.

The LAPAP technique had previously been successfully implemented within the laboratory by several group members for creating both uniform concentration patches and gradients for dendritic cells (figure 16 C) [29,34,95]. They effectively demonstrated that when using direct antibodies against the immobilized chemokine to visualize the LAPAP gradient, a clear resemblance between the actual gradients and the LAPAP-generated gradients was evident (figure 16 D). Additionally, as the LAPAP methodology was effectively adapted for use with murine dendritic cells, and upon introducing these cells to the LAPAP gradients, they aligned themselves quickly with the immobilized surface gradients (figure 16 E).

Given the promising success of the LAPAP method in facilitating leukocyte migration, our focus in this project was to adapt the established protocols for human neutrophils. Our goal was to investigate the impact of diverse gradient attributes – ranging from concentration strength to shape (linear vs. exponential) and the presence of noise – along with other gradient parameters including the effect of changing uniform concentrations. Furthermore, it was aspired to refine the method to integrate it into microfluidic devices under cell confinement and extend its application within collagen assays and cell-derived matrices.

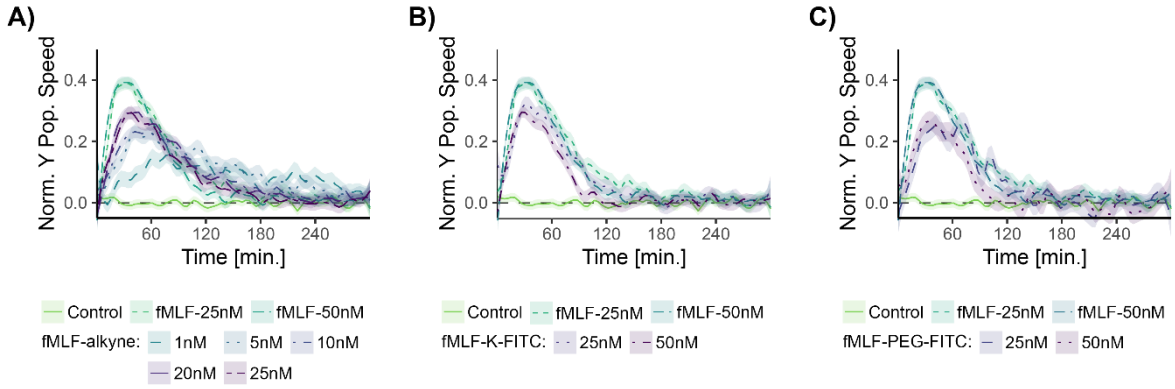


Figure 17: LAPAP attractants and their chemotactic potential on PLB-985 cells. **A-C)** Normalized y-direction speeds (source is the top y-axis; normalized to the maximum speed of all samples) of whole populations in a collagen assay for various tested LAPAP attractants and concentrations. All samples are compared to control (medium) and normal fMLF (25 – 50 nM) concentrations. Lines represent a LOESS fit with a span of 0.1 and ribbons depict the 95 % CI. **A)** fMLF-Alkyne concentrations (1 – 25 nM). **B)** fMLF-K-FITC concentrations (25 – 50 nM). **C)** fMLF-PEG-FITC concentrations (25 – 50 nM).

4.1.1.3 Results

4.1.1.3.1 Chemotactic Potential of LAPAP Attractants

Considering the potential impact of ligand modifications on their affinity – and thus the chemotactic ability – our initial focus was on assessing the chemotactic efficacy of various fMLF-variants for LAPAP (figure 17). Three distinct variants were evaluated: one for indirect LAPAP (fMLF-Alkyne) and two for direct LAPAP (fMLF-K-FITC and fMLF-PEG-FITC). Our objective was to compare their chemotactic potential in collagen assays with the conventional fMLF.

Surprisingly, all three variants elicited the characteristic migratory burst toward the source, consistent with fMLF behavior, with the intensity increasing with their respective concentrations. However, like the normal fMLF, sustained migration was not observed. Despite these resemblances, these variants exhibited lower maximal burst speeds and shorter persistence periods.

Collectively, our collagen assays demonstrated that each variant possesses the capacity to induce chemotaxis in neutrophils.

4.1.1.3.2 Protocol Adjustment Screening for Neutrophils

In our efforts to adapt LAPAP for neutrophils, our initial focus was on assessing the precision of pattern formation. At this stage, no attractants were introduced, instead, dyes were employed to evaluate the accuracy of the patterning process. The approach began by utilizing a well-established technique, where the dye adaptor consisted of FAM (fluorescein) linked to alkyne, while the ligand adaptor included an azide and RGD-Cy5 to enable gradient visualization (figure 18 A). Upon examining uncoated coverslips, a clear trend emerged: as the duration of the patterning process increased, the intensity of the resulting patches also heightened. This trend indicates an amplification in the amount of patterning achieved, as demonstrated by the intensified brightness of the patches generated.

After confirming the effectiveness of the established protocol, an alternative click order was explored – in this case, the dye adaptor comprised FAM linked to azide, while the ligand adaptor consisted of alkyne and Atto-647-N (figure 18 B). Interestingly, altering the click order seemed to result in an inverse patterning: higher intensity led to fewer patterned LAPAP molecules. Intriguingly, even without

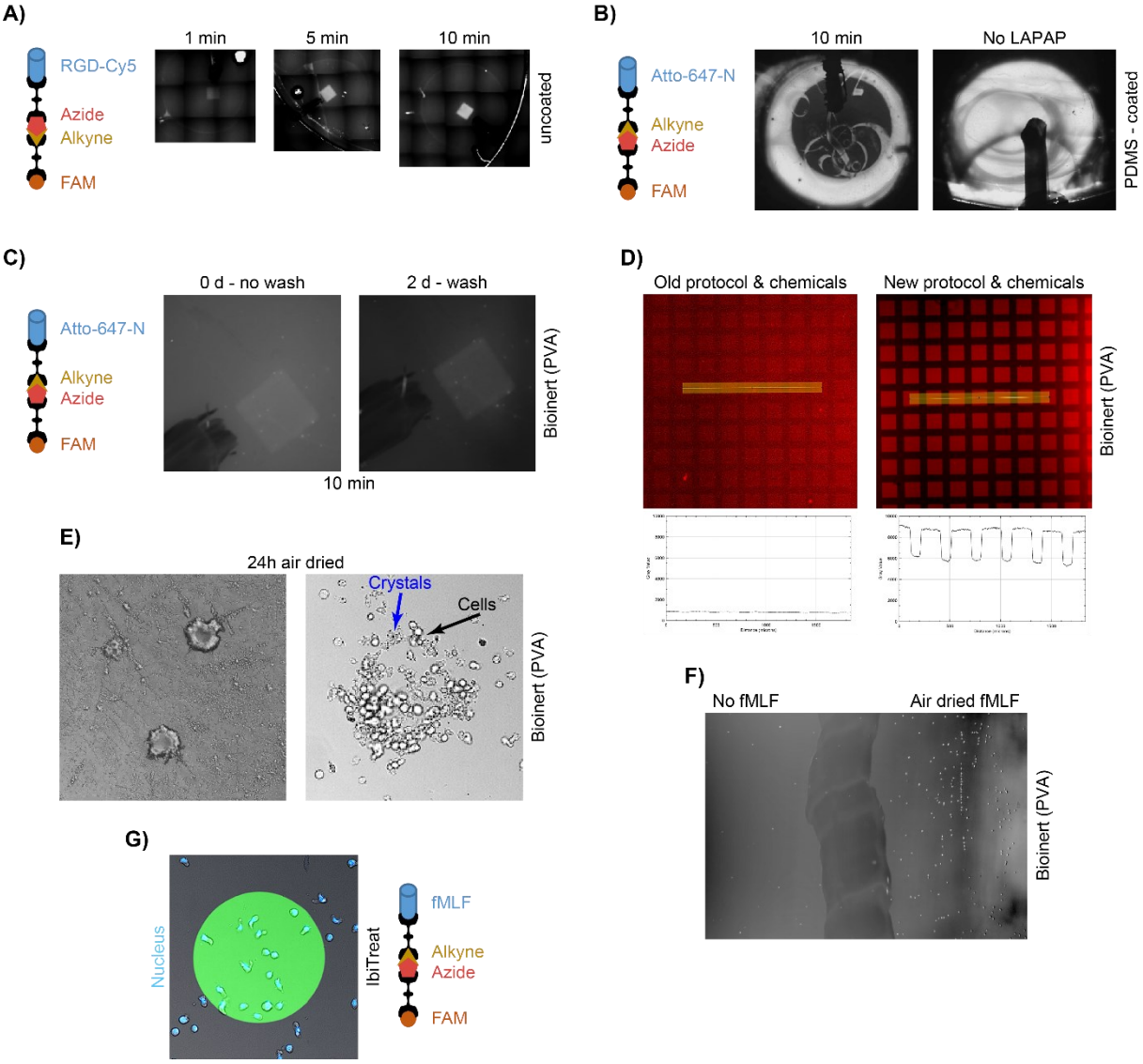


Figure 18: LAPAP protocol adjustments for neutrophil migration. **A)** LAPAP with the original protocol using an alkyne dye adaptor and FAM which crosslinks to a ligand adaptor with azide and RGD-Cy5 (left). LAPAP (single square) was performed on uncoated glass coverslips which were patterned for 1, 5, or 10 minutes. **B)** LAPAP with the modified protocol using an azide dye adaptor and FAM which crosslinks to a ligand adaptor with alkyne and Atto-647-N (left). LAPAP (single square) was performed on PDMS-coated glass coverslips which were either not patterned or patterned for 10 minutes. **C)** The effect of washing on the LAPAP background noise. LAPAP was done with the modified protocol using an azide dye adaptor and FAM which crosslinks to a ligand adaptor with alkyne and Atto-647-N (left). LAPAP (single square) was performed on Bioinert dishes which were patterned for 10 minutes and subsequently immediately imaged (mid) as well as two days after washing in PBS (right). **D)** Comparison of the starting protocol and old chemicals to a further adjusted protocol and new chemicals. LAPAP (multi-squares) was performed on Bioinert dishes with the azide dye adaptor and FAM which crosslinks to a ligand adaptor with alkyne and Atto-647-N. The old protocol & chemicals used an old lot and protocol of the “Click-it” kit whereas the new protocol & chemicals used a self-mad kit with chemicals from Jena Biosciences according to the protocol of Ibidi. The intensity profile of multiple patterned squares, and the empty space between them, was measured for both experiments. **E & F)** The effect of air drying on fMLF-alkyne and on neutrophils. **E)** A droplet of fMLF-Alkyne was air-dried for 24 h on a Bioinert dish and the crystal formation was imaged (left). The dish was re-wetted and dHL-60 cells were added to the dish. The agglomeration of cells (black arrow) on crystals (blue arrow) is shown (right). **F)** A droplet of fMLF-alkyne was air dried for 24 h on one half of a Bioinert dish, while the other half was left untreated. The dish was re-wetted and dHL-60 cells were added to the dish and a snapshot image was taken of both parts. **G)** The effect of a LAPAP fMLF patch on dHL-60 cells was observed. The newly adjusted LAPAP protocol was used to pattern multiple circles on an IbiTreat dish (left) with an azide dye adaptor and FAM which crosslinks to a ligand adaptor with fMLF-alkyne (right). The nucleus of cells (blue) was stained with NucBlue and FAM presence can be discerned (green).

performing the LAPAP process, the presence of dye was evident on the PDMS-coated coverslips. This observation suggested that PDMS might act as an absorbent, retaining some of the alkyne-Atto-647-N adaptor and hindering its removal during washing.

Despite encountering the inverse patterning issue, closer inspection of the patterned area revealed its presence, albeit with significant background noise (figure 18 C, left). Surprisingly, after two days of washing in PBS, the pattern's intensity remained relatively stable, while a substantial reduction in background noise was observed. This indicated that washing contributed to a notable improvement in the contrast between the pattern and its background (figure 18 C, right).

In the subsequent approach, the protocol and respective utilized reagents were attempted to be optimized. Initially, the same established procedure of previous lab members were followed, also employing an older lot of the click-it kit. Using the original protocols and chemicals, when working with the alkyne-Atto-647-N adaptor, the outcomes were not satisfactory, with a particularly low signal-to-noise ratio (figure 18 D, left).

Collaborating with experts from Ibidi, the protocol was revised by transitioning to a custom-made click-it reaction kit, integrating components from Jena Biosciences. The adjustments encompassed both the patterning process based on their in-house guidelines (i.e., using a 50 µL droplet for patterning instead of 15 µL; elevating FAM concentration from 360 µM to 400 - 1000 µM; reducing illumination from 10 minutes to 5 minutes, and prolonging washing durations with 10 minutes for each washing step) as well as adapting the click-it protocol (i.e., extending incubation time from 30 minutes to 60 minutes and incorporating more stringent washing steps). Implementing these changes had a significant impact on our results as the signal-to-noise ratio got a substantial enhancement, resulting in an approximate 9-fold increase (figure 18 D, right). Notably, whether employing the adjusted protocol with the old lot or with a new click-it kit lot, neither yielded outcomes as promising as those achieved with the refined protocol and the new set of chemicals (data not shown).

During this stage of protocol optimization, also the occurrence of precipitation was noticed for either of the adaptors during the LAPAP procedure (data not shown). Various solubilizing agents were explored (ethanol, DMSO, and DMF), but none were able to alleviate the precipitation issue. Also, different ratios of buffer to solubilizing agent were tested (6 % and 10 %) without achieving a solution.

The observed precipitation prompted us to investigate its effects on dHL-60 cells. To do so, a droplet of fMLF-alkyne was air-dried for 24 hours and subsequently introduced a dHL-60 culture to the dish (figure 18 E). Interestingly, the cells responded to the crystals by strongly adhering to them, resulting in cell clusters forming around the crystal locations. Furthermore, when we divided a dish into two sections – one untreated and the other with air-dried fMLF-alkyne – even in areas where crystals weren't directly visible, the presence of air-dried fMLF-alkyne led to significantly increased cell adhesion. This observation is particularly intriguing given that the plate used was a bioinert Ibidi plate coated with PVA, which is designed to minimize cell adhesion.

The ultimate objective of this project was to elicit a response from dHL-60 or dPLB-985 cells. While we successfully optimized the protocol to achieve robust and intense signals using dyes, this protocol was not yet directly tested on cells. As depicted in figure 18 G, a fMLF-alkyne patch was patterned, and dHL-60 cells were added to it. However, despite observing cell adhesion both on and around the patch, no distinctive cell behavior or cell aggregation was observed on the patch, when compared to the areas outside of it. We also collaborated with Ibidi, a company proficient in implementing LAPAP techniques for industrial and research applications, in our endeavor to

induce neutrophil cell migration using LAPAP. Unfortunately, despite various attempts and an array of explored optimization parameters (as indicated in table 3) a discernible response from differentiated cells was never observed. Irrespective of the protocol variations, click reagents, LAPAP methods, fMLF variants, gradient or uniform concentration patterns, cell types, or cell culture dishes which were employed, no cell response was achieved. Nevertheless, several behaviors were noted during our investigations:

1. fMLF patterning resulted in more adherent cells, also outside of patches.
2. Lower patterned concentrations promoted stronger adherence than higher ones.
3. Bioinert (PVA) surfaces normally prevented the adherence of cells.
4. IbiTreat (cell culture surface treatment) led to excessive adherence.
5. Patterned RGD, a cell adhesion peptide, did not enhance cell adherence.

	Variations	Outcome
Click chemistry		
- **Reagents**	1. Different lot numbers 2. Different vendors	Significant effect on pattern efficiency
- **Reaction order**	1. Azide → Alkyne 2. Alkyne → Azide	Alkyne → Azide seems to have better efficiency
Direct LAPAP	1. fMLF-K-FITC 2. fNLFNTK-FITC 3. fMLF-PEG-FITC	No effect
Substrate surface	1. Glass 2. Glass + PDMS 3. Glass + PVA 4. Glass + PEG 5. Glass + Fibronectin 6. Bioinert (ibidi) 7. IbiTreat (ibidi) 8. MatTek	Affects mostly cell adherence and to some extent patterning (PDMS e.g., adsorbs reagents)
Patterning	1. Intensity (0 – 100 %) 2. Duration (1 – 10 min)	Significant effect on pattern efficiency
Concentrations	1. Both adaptors 2. Direct LAPAP	Significant effect on pattern efficiency
Cell lines	1. PLB-985 2. HL-60	No effect
Solubilizing agents **(adaptors & direct LAPAP)**	1. DMSO 2. EtOH 3. DMF	No effect
Air drying LAPAP	1. Alkyne 2. Azide	Crystal formation → Neutrophils adhere

Table 3: LAPAP protocol adjustment parameters. A list of various parameters that were screened and varied to test for neutrophil reaction after patterning.

4.1.1.4 Discussion

When this project was started, LAPAP held immense potential as a tool for many concepts of this thesis. Its capability to enable precise control of gradient generation and uniform patches drove me to invest a substantial amount of time and effort in refining and optimizing existing protocols. Spanning a timeframe of three years, this optimization process entailed systematic alteration of nearly 30 parameters, yielding a substantial enhancement of the signal-to-noise ratio. This success translated into the successful patterning of dyes through both direct and indirect LAPAP methods.

However, despite achieving well-defined patterns of fMLF-LAPAP variants (the original FAM dye's presence could still be discerned to a certain extent, confirming the pattern's existence), including gradients and uniform concentration patches, we were unable to elicit any discernible response from dPLB-985 or dHL-60 cells. This couldn't be attributed to the chemotactic ineffectiveness of the fMLF-LAPAP variants, as their capacity to induce a chemotactic response in neutrophils was demonstrated when administered in soluble form. The observed differences in chemotactic behavior, particularly in terms of persistence and peak burst speed, within collagen assays as opposed to the original fMLF titration, can likely be attributed to modifications in the peptide's characteristics. Notably, fMLF, being a tripeptide, undergoes significant alterations when linked to a fluorophore and a linker. These alterations encompass changes in size, charge, and even chemical properties such as hydrophilicity. Collectively, these modifications can subtly affect the affinity of the peptide for FPR on neutrophils, thereby accounting for the observed discrepancies. Importantly, the introduction of click chemistry doesn't render the peptides inaccessible to neutrophils, as even the direct LAPAP fMLF variants failed to induce either chemotactic or haptotactic responses.

Of note, certain studies have effectively harnessed LAPAP to generate gradients targeted at neutrophils, resulting in observable responses from these cells. For instance, Roy et al. employed a direct fMLF variant (fNle-Leu-Phe-Nle-Tyr-Lys-FITC) in their investigation, utilizing an under-agarose setup on an untreated glass surface [128]. Intriguingly, we sought to replicate their approach using the same fMLF variant. However, our experiments did not yield the anticipated response from neutrophils. A clear distinction between our experimental conditions and those of Roy et al. resides in the experimental setup itself. While our approach involved an open system where cells were not constrained, their methodology entailed an under-agarose system, effectively compelling cells to interact with the patterns through the imposition of agarose confinement. This intriguing difference in experimental setup could potentially account for the divergent outcomes observed.

Collaborative experiments with experts at ibidi failed to elicit any responsive behavior from neutrophils, thus eliminating the likelihood of experimental errors or knowledge gaps as the primary cause. Intriguingly, our discussions with these experts revealed a consensus that a potential solution could involve compelling cells onto the patterns through methodologies such as under-agarose assays or confining microfluidic designs. Throughout our protocol optimization phase, we engaged in dialogues with experts and researchers who had prior experience with the system. These discussions, combined with our empirical observations, unveiled certain inherent limitations of the LAPAP approach.

The fundamental question arises as to the natural authenticity of a system that requires the imposition of cell interactions with a pattern, i.e., forcing cells onto a patch with confinement. If cells cannot inherently engage with the surface, is the system genuinely representative of natural physiological scenarios? Furthermore, it's important to consider that any cell reactions under these circumstances would inherently be

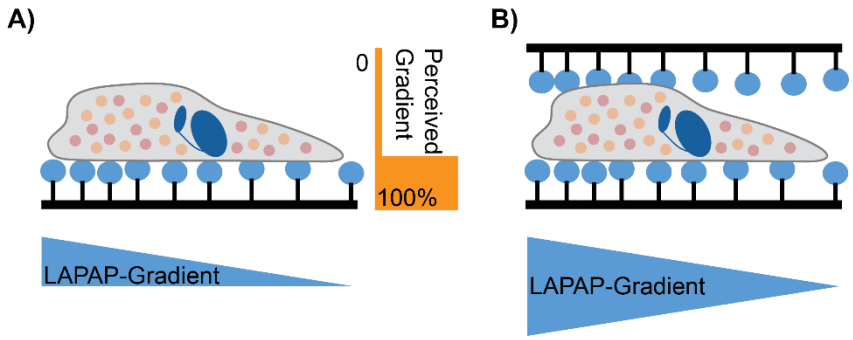


Figure 19: LAPAP conceptual problems and potential solution. **A)** In all 2D migration assays utilizing LAPAP gradients, two gradients become evident. The primary gradient emerges from the patterned LAPAP (blue gradient), while a substantially steeper gradient originates from the z-axis. Since 2D LAPAP exclusively patterns the substrate surface, a distinct binary “gradient” exists in the z-plane (orange gradient). **B)** A strategy to address this gradient ambiguity is to employ LAPAP in a 3D context. This can be achieved through the utilization of confining microfluidic devices or collagen assays, effectively circumventing the gradient-related challenges along the z-axis.

haptotactic rather than true chemotactic responses. Both variations of LAPAP involve covalent tethering of the attractant to the surface, in stark contrast to the soluble chemotactic agents that cells typically encounter. That cells commonly seem to endocytose soluble attractants could pose challenges in the context of a covalently bound surface attractant, hampering the engulfing process [64]. Empirical insights from past lab members suggest that patterns which are traversed by cells exhibit minimal reduction in intensity. However, when cells stay on a patch, the signal diminishes, hinting at a mechanism wherein cells might eventually disengage the attractant, given sufficient time. Furthermore, the intricate dynamics of receptor trafficking on the plasma membrane cannot be overlooked. The question arises whether a ligand covalently tethered to the surface might impede or alter this crucial trafficking process. In a broader context, the utilization of covalently bound ligands appears to introduce substantial modifications to the physiological context. Another notable observation from our colleagues' experience is the presence of stark contrast in behaviors between the haptotactic LAPAP-induced responses and those triggered by soluble attractants. This discrepancy raises the possibility that the observed reactions might be artifacts rather than genuine manifestations of natural cellular responses. It's noteworthy that many researchers have shifted away from the LAPAP approach in their investigations, while ibidi indicated a more promising avenue for LAPAP, particularly in the context of adherent cells and applications like cancer research, rather than focusing on chemotaxis or haptotaxis studies.

A significant conceptual challenge posed by LAPAP lies in the emergence of two distinct gradients when employed in 2D patterning. While the primary gradient stems from the LAPAP patterning process itself, a secondary and notably steeper gradient emerges in the z-axis (figure 19 A). As the 2D LAPAP technique exclusively targets the substrate surface, receptors on a cell are only engaged within the contact region with the surface. Consequently, receptors situated in the upper and middle regions of the cell remain unengaged, resulting in a discernible "binary" gradient along the z-direction. This underscores that the most pronounced gradient does not align with the LAPAP pattern but rather originates from the top to the bottom of the cell. This phenomenon could explain the observations of former group members who noted cells adopting a more rounded morphology on patterns, suggesting a tendency to “dig” into the patterns rather than migrate along them. To counteract this challenge, we thought of employing LAPAP within 3D environments, such as collagen matrices or cell-derived

matrices. Alternatively, we considered utilizing 2.5D assays, such as microfluidic devices that confine cells. This approach would allow LAPAP patterns to be applied both to the substrate and to the PDMS ceiling. However, even in such setups, the central region of a cell might lack any signal, introducing an artificial aspect to the gradients, with the most substantial gradients being directed toward the top and bottom of the cells. Nonetheless, employing LAPAP in 3D or 2.5D assays would represent a more viable approach than purely 2D LAPAP assays.

Among the notable alternative strategies to LAPAP, microfluidic devices stand out, offering the capacity to engineer a diverse range of gradients and uniform concentrations. However, the implementation of microfluidic systems introduces heightened complexity in both design and manipulation. Furthermore, these systems do not readily permit instantaneous gradient switches due to inherent dead volume within the setup. Rapid adjustments to gradients can result in a pronounced flow that possesses the potential to wash off cells. While mechanisms to counteract excessive flow do exist, they inherently necessitate a compromise by slowing down gradient modifications.

Despite thorough optimization efforts and expert consultations, we were unable to consistently observe chemotactic responses. Concerns regarding anomalous cell behavior, covalent binding implications, and practical constraints led to the realization that the potential challenges and intricacies associated with the LAPAP method in the context of leukocyte migration outweighed its anticipated advantages. Consequently, our work on this project was concluded in 2019.

4.1.2 To Make Them Move – Chemotaxis in Immortalized SCF-HoxB8 Neutrophils

4.1.2.1 Summary

In initial *in vitro* studies, SCF-HoxB8 cells displayed neutrophil effector functions but exhibited limited migratory capabilities [129–131]. However, these cells demonstrated the ability to migrate *in vivo* [132]. To address this limitation, we adjusted the differentiation protocol for SCF-HoxB8 cells that would render them responsive to chemotactic stimuli in diverse migratory assays. Through the optimization of various differentiation parameters, such as the availability and concentration of cytokines and the timing of their administration, we successfully generated migratory primary murine neutrophils. These differentiated neutrophils demonstrated the ability to effectively follow chemoattractant cues in various environments, including collagen matrices and microfluidic devices.

In summary, the addition of GM-CSF (10 %) and G-CSF (20 ng/mL) on day 0 not only significantly increased the surface levels of Ly-6G, a marker for murine neutrophils, but also enhanced the migratory capabilities of neutrophil SCF-HoxB8 cells. Moreover, unlike human neutrophils or neutrophil-like cells (e.g., PLB-985), SCF-HoxB8 cells exhibited more pronounced reactions to much higher concentrations of fMLF (10 µM compared to 5 nM). These findings suggest that SCF-HoxB8 cells can be a valuable tool for studying murine neutrophil migration *in vitro*.

4.1.2.2 Introduction

In biological research, selecting the appropriate model system is of crucial importance as it forms the foundation for addressing specific scientific questions. While cancer cell lines are widely used, primary cells often provide more relevant and reliable data, as they have not undergone extensive mutations that can alter their behavior or other cellular properties. However, working with primary cells comes with its own challenges. The availability of primary cells can be limited, especially when working with human donors. Additionally, ethical, and legal considerations may not only prevent genetic modifications from being performed directly on donors but also raise concerns about the potential unnecessary euthanasia of animal models. For example, in the case of studying neutrophils, I find it ethically problematic to euthanize mice frequently to obtain cells for *in vitro* experiments, while human neutrophils can be obtained through simple blood donations, providing a vast and diverse source of cells. However, working with human neutrophils has its challenges, such as donor-to-donor variation, which can be both advantageous for robust results and complex to account for in experimental design. Moreover, genetic modifications of human neutrophils are challenging due to their short lifespan *in vitro* (~ 13 h for murine and up to 5 days for human *in vivo*) and delicate handling requirements [76,133].

One approach to combine the advantages of primary cells and cell lines is the use of immortalized primary cells. This involves genetically modifying primary precursor cells to enable their long-term proliferation while retaining the ability to differentiate into various primary effector cells. In a study by Wang et al., murine myeloid (i.e., cells from the bone marrow) cells from the bone marrow were immortalized using a retroviral vector carrying the conditional HoxB8 gene, which promotes cell proliferation while blocking differentiation [131]. The HoxB8 expression is controlled by an estrogen promoter, allowing differentiation into different lineages once estrogen is removed from the culture. The differentiation potential includes neutrophils, macrophages, and dendritic cells, and is dependent on specific culture conditions and how the respective cell line was immortalized. Previous studies have shown that differentiated neutrophils are genetically and functionally similar to primary neutrophils, and while some studies looked at their ability to migrate *in vivo*, at the time of this project there were limited

studies on their *in vitro* migration capabilities [134,135]. Interestingly, HoxB8 cells of the dendritic cell lineage are commonly used – also in our lab – in migratory studies *in vivo* as well as *in vitro* [136] In this study, we aim to optimize the migratory abilities of SCF-HoxB8 cells by adapting the published differentiation protocol.

It is important to note that this project utilized a screening approach, and thus, only a limited number of replicates were performed. The primary focus was to identify a rough starting point for optimizations.

4.1.2.3 Results

4.1.2.3.1 Generation and Differentiation Efficiency and Handling

To generate an immortalized cell line specific to the neutrophil lineage, the process was initiated by pre-stimulating murine bone marrow cells with stem cell factor (SCF), interleukin-3 (IL-3), and interleukin-6 (IL-6). Subsequently, these cells were further cultured in a medium containing granulocyte-macrophage colony-stimulating factor (GM-CSF) and SCF to promote the growth and expansion of precursors for the neutrophil lineage. The optimization of differentiation involved altering various parameters and time points from the original protocol, as depicted in figure 20 A.

The initial published differentiation protocol involved the simple removal of estrogen from the medium and culturing of the cells for four days to achieve effective differentiation. However, despite observing cells with a characteristic lobed nucleus, there was only a marginal increase in the expression of the Ly-6G surface marker, which is a distinctive marker for murine neutrophils (see figure 20 B and C “control”) [137,138]. Following discussions with David Sykes, one of the original co-authors, we decided to incorporate GM-CSF, granulocyte-colony stimulating factor (G-CSF), and lipopolysaccharide (LPS) into the culture. This modification aimed to optimize both cell migration capabilities and the expression of Ly-6G. To achieve this, the concentrations and timing of these molecules during the cell culture process were adjusted.

Upon adding G-CSF to the cell culture, a significant increase in cell proliferation was observed. Furthermore, the expression of Ly-6G in SCF-HoxB8 cells was enhanced compared to the original differentiation protocol. Surprisingly, doubling the concentration of G-CSF had only a limited effect on the expression, and adding G-CSF on day 2 resulted in lower expression compared to its addition on day 0.

The presence of GM-CSF in combination with G-CSF had the most significant impact on Ly-6G expression. When GM-CSF was added to the medium, SCF-HoxB8 cells exhibited approximately double the expression of Ly-6G compared to G-CSF alone. However, for this effect to occur, GM-CSF needed to be present from day 0 onwards, otherwise, the enhancement in expression was lost, and cells showed similar levels as with G-CSF alone. Interestingly, in combination with GM-CSF, it appears that doubling the concentration of G-CSF or adding it at a later time point might further increase the overall expression. It is important to note that no experiments were performed with only GM-CSF added (without G-CSF), so much of the expression increase may be attributed to GM-CSF alone.

Throughout all experiments, we made additional observations regarding the handling and characteristics of SCF-HoxB8 cells. Undifferentiated cells exhibited a consistent round shape, but significant morphological changes were observed upon differentiation (figure 20 D). Differentiated cells displayed distinct polarization, featuring both a lamellipodium and a uropod. Notably, both differentiated and undifferentiated SCF-HoxB8 cells exhibited significantly increased proliferation rates, with doubling times higher than those of the DC HoxB8 cells. Initially, using the same seeding conditions for both cell types, the neutrophils rapidly overgrew the dishes during differentiation, leading to an adjusted seeding protocol, reducing cell seeding. Upon initiation of

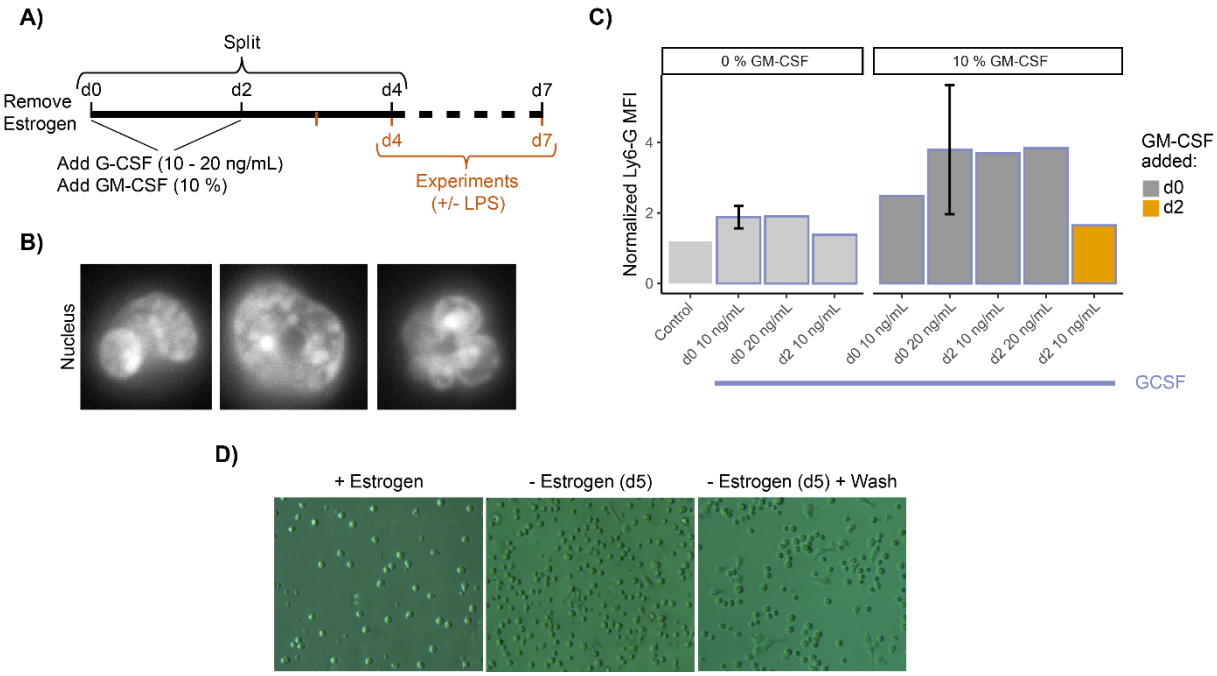


Figure 20: Optimization of differentiation efficiency and handling of immortalized SCF-HoxB8 neutrophils. **A)** Timeline of SCF-HoxB8 culturing. On day 0 (d0) estrogen was removed and cells were split on days 2 and 4. From day 4 to a maximum of day 7, differentiated cells were used for experiments. Optimization was performed by adding G-CSF and GM-CSF during day 0 or day 2 to the cultures in various concentrations or adding LPS before experiments. **B)** Nuclear staining (NucBlue) of five day differentiated cells. The images were taken from the same culture, showing the different stages of differentiation within one culture. These images were taken from the same culture, providing a visual representation of the various stages of differentiation within a single culture. As murine neutrophils differentiate, their nuclear shape evolves from a roundish form to an elongated one, progressing to a doughnut-shaped appearance, and ultimately becoming lobed and segmented. **C)** Normalized median fluorescence intensity (MFI) of Ly-6G for various optimization approaches. The MFI values were normalized to stained undifferentiated cells in each staining. During the optimization process, the concentrations of GM-CSF and G-CSF were adjusted, and the timing of their addition to the culture was also varied. Most samples were performed only once, and replicates were only included in samples where an error bar, representing the standard deviation, is visible in the data. **D)** Microscopy images of cell cultures of undifferentiated (+ Estrogen) and differentiated cells (- Estrogen). The images highlight the morphological changes in the cells, as well as their adhesion to surfaces. In the "- Estrogen + Wash" sample, extensive washing was performed to remove any remaining cells from the dish.

differentiation, two distinct subpopulations of cells emerged - cells that remained in suspension and cells that adhered firmly to the surface. Even extensive washing failed to remove these adherent cells, requiring the use of a cell scraper to detach them (figure 20 D).

4.1.2.3.2 Migratory capabilities

When examining the migration of SCF-HoxB8 cells under different culture conditions, we observed that during collagen assays, most undifferentiated cells experienced cell death within a few hours of the experiment (figure 21 A). Furthermore, in collagen assays, only a very small fraction of undifferentiated cells (approximately 1 %) exhibited migratory capabilities, whereas all differentiated cells displayed random migratory behavior (figure 21 B).

During the differentiation process, some cells already exhibited migratory behavior by day 3, although the majority began migrating around day 4 (figure 21 C). We conducted tests up to day 7, and at this stage, most cells were still displaying migratory

activity. Generally, it appears that the longer the differentiation process, the higher the proportion of migratory cells obtained. There seems to be a slight trend suggesting that cells become more migratory as they undergo longer differentiation, as day 7 cells showed increased migratory behavior compared to earlier stages.

The addition of LPS to the cultures either 2 hours or 24 hours before the experiment did not appear to significantly affect the chemotactic ability of the cells. However, it was observed that fewer cells could be harvested from the dishes after LPS treatment, suggesting that the cells might have either died or attached to the surface following the LPS treatment (data not shown).

The absence of G-CSF in the culture made it challenging to obtain enough cells for collagen assays. Notably, when observing collagen videos with G-CSF alone, it was evident that cells became slower over time, unresponsive, and eventually died after a few hours. However, when GM-CSF was included in the culture, cells seemed to become more responsive, and only a few cells died during the imaging process. The addition of GM-CSF appeared to enhance the viability and responsiveness of the cells in the collagen assays (figure 21 D). Incorporating G-CSF and GM-CSF from day 0 onward had a significantly more pronounced impact on migration compared to introducing these factors on day 2.

Unfortunately, initial experiments yielded inconclusive results for two primary reasons. Firstly, the approach employed here was essentially a screening methodology, which involved testing numerous parameters simultaneously (such as varying quantities of LPS, G-CSF, GM-CSF, and the timing of their addition, along with different concentrations of fMLF, CXCL1, CXCL12, and CCL3, as well as the duration of cell differentiation). This approach generated multivariate outcomes where several parameters were examined only once in each experimental configuration. The primary objective was to cast a wide net and identify a relatively favorable cell migration scenario, from which one could then proceed for further optimizations. Secondly, our observations were initially limited to discerning random migration and overall migration behavior (e.g., migration duration, migratory switch, early cell death, etc.). This was the reason as initially no sustained migration was detected toward fMLF (up to 3 µM), CXCL1 (up to 100 ng/mL), CXCL12 (up to 100 ng/mL), or CCL3, whether administered alone or in combination, and at varying concentrations. It appeared that the cells responded transiently to these stimuli, briefly moving toward the source, and subsequently adopting a swifter pace while migrating randomly. Generally, the presence of a chemokine appeared to enhance cell motility in terms of cell speed and range of random migration. Only when the concentrations were increased (10 – 100 µM for fMLF and 500 – 1000 ng/mL for CXCL1) marginally prolonged chemotaxis was observed (figure 21 E & F). However, this movement toward the source was not sustained and even less persistent than that of human neutrophils. Overall, when compared to human neutrophils (both primary and PLB-985), the responsiveness to the tested attractants was relatively modest in terms of speed, directionality, and persistence.

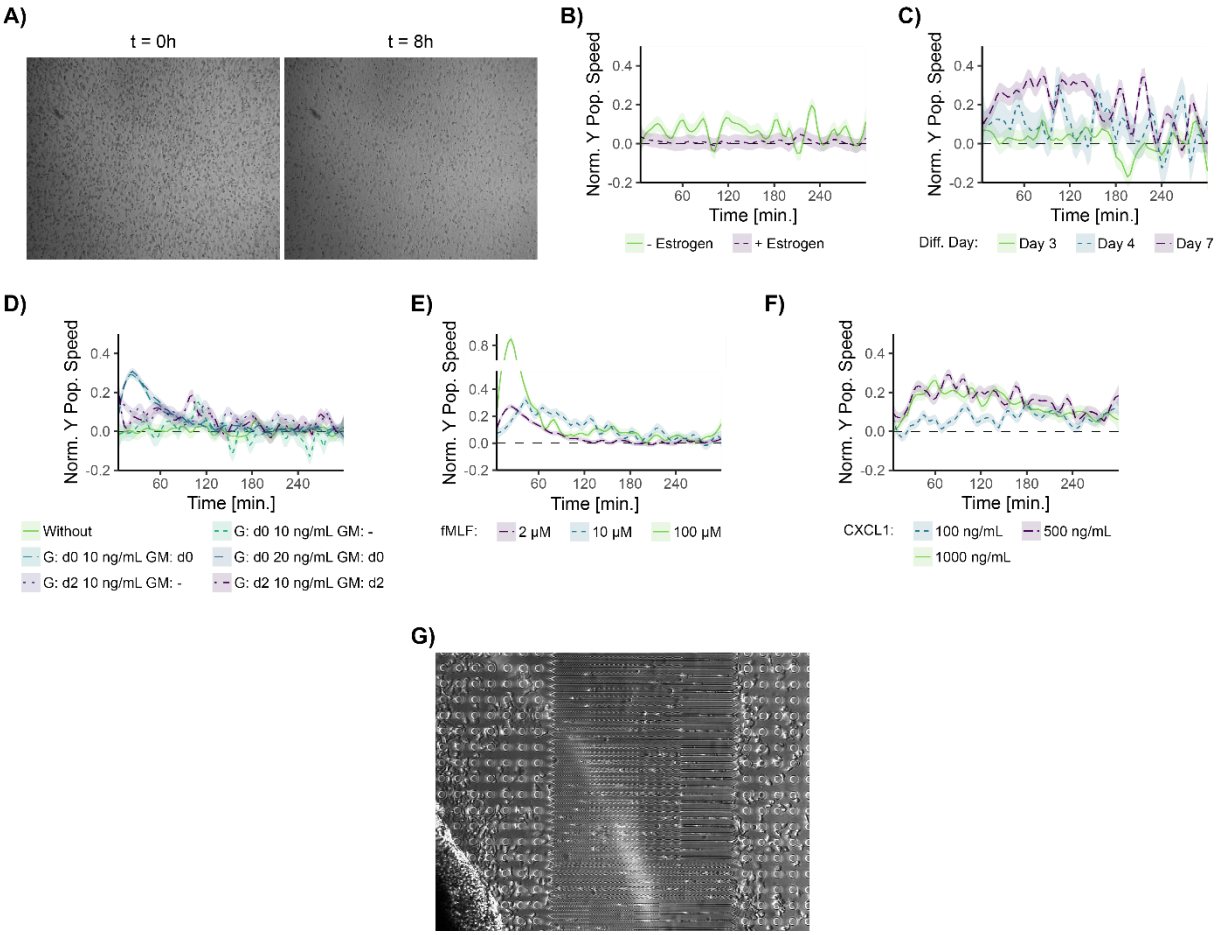


Figure 21: Migratory capabilities of differentiated SCF-HoxB8 cells. **A)** Brightfield image of immotile and undifferentiated SCF-HoxB8 in collagen at the beginning (0 h) and the end (8 h) of the experiment. **B-F)** Normalized y-direction speeds (source is the top y-axis; normalized to the maximum speed of all samples) of whole populations in a collagen assay with various tested parameters. Lines represent a LOESS fit with a span of 0.1 and ribbons depict the 95 % CI. **B)** Comparison of differentiated (+ Estrogen) and undifferentiated (- Estrogen) cells. Both samples had a 24 h pre-incubation with LPS and no G-CSF and GM-CSF were present. The + estrogen sample was differentiated for 7 days. A gradient with 3 µM fMLF was present. **C)** Effect of differentiation day (days 3, 4, and 7) on migratory capabilities. All samples had a 24 h pre-incubation with LPS and all samples had 10 ng/mL G-CSF from day 0 or day 3 (day 3 sample) onwards. A gradient with 2.5 µM (day 4 sample) or 3 µM fMLF was present. **D)** Influence of G-CSF (G) and GM-CSF (GM) concentration (10 % for GM-CSF, 10 or 20 ng/mL for G-CSF) and addition timing (d 0 or d 2) on migration. The without sample had no G-CSF or GM-CSF added. No LPS pre-treatment was performed and a gradient with 2.5 µM fMLF was present. Cells were differentiated for 4 days. **E)** Concentration effect of fMLF on migration. No LPS pre-treatment was performed, and G-CSF (20 ng/mL) and GM-CSF (10 %) were present from day 0. Cells were differentiated for 4 days. **F)** Concentration effect of CXCL1 on migration. No LPS pre-treatment was performed, and G-CSF (20 ng/mL) and GM-CSF (10 %) were present from day 2. Cells were differentiated for 4 days. **G)** A snapshot of SCF-HoxB8 cells in a microfluidic device after 3 h in a gradient of 10 µM fMLF.

In addition to collagen assays, we also conducted successful migration tests of SCF-HoxB8 cells in microfluidic devices and cell-derived matrices (figure 21 G). Notably, while PLB-985 cells exhibited chemotactic responsiveness in microfluidic setups for extended durations (6 hours or more), differentiated SCF-HoxB8 cells maintained this persistence for an estimated period of only around 3 hours.

4.1.2.4 Discussion

The primary objective of this project was to establish an immortalized primary cell line that held immense potential for being highly valuable not only for this thesis

research but also for other researchers in our laboratory. The prospect of having access to primary cells at any time, coupled with the ability to genetically manipulate them, promised to yield substantial benefits if our project turned out to be successful.

During the period when we started working on this project (2017/2018), there were limited studies available that explored the migratory behavior of differentiated SCF-HoxB8 cells. Existing papers often relied on transwell migration assays, which were not ideal for studying active migratory behavior, or *in vivo* experiments where the host body provided the necessary cytokine environment for proper differentiation. At that time, we could not find any study using SCF-HoxB8 cells for *in vitro* migration experiments, making this project a unique and intriguing opportunity. We aimed to avoid the challenges of obtaining ethical approval for human blood donations to work with primary human neutrophils or the potential genetic issues associated with the PLB-985 cell line and the lack of some essential neutrophil functions (e.g., granules). By establishing an immortalized primary cell line, we aimed to combine the best aspects of primary cells and a cell line, allowing the use of primary cells with constant proliferation and differentiation on demand, making it a valuable tool for the research of cell migration.

Despite being primarily a screening effort with many experiments yielding inconclusive results due to the initial unknown factors (e.g., which chemokine at which optimal concentrations, GM-CSF and G-CSF concentrations, timing of additions, and the potential inclusion of LPS), some significant findings can already be drawn from this study.

Adding GM-CSF and G-CSF on day 0 of differentiation appears to significantly enhance both the Ly-6G expression and migratory capabilities of the cells. It's worth noting that studies have indicated that higher levels of Ly-6G expression are associated with mature neutrophils that exhibit increased effector functions compared to cells with lower expression levels [139,140].

The addition of LPS to the cultures did not show any significant effect, except for a decrease in the number of harvested cells for the experiments. This could be attributed to two possible reasons: first, LPS might induce apoptosis in the cells, leading to a reduction in cell numbers; second, LPS could activate the cells, causing them to adhere to the surface of the culture dishes or centrifugation tubes, making it challenging to harvest them for experiments.

In chemotaxis experiments, responses to high concentrations of fMLF (10 µM onwards) and CXCL1 (500 ng/mL onwards) were observed. However, the concentration range for these chemokines was not fully titrated, leaving room for optimization. Furthermore, other chemokines like CXCL12 and CCL3 were initially tested but not fully titrated, and attractants like formylated tetra- or pentapeptides were not tested, which may have a better affinity to the murine FPR. Further investigations will be needed to explore the full potential of these chemotactic agents.

The presence of cells that strongly attach to the dish surface after differentiation may indicate a mixed population of macrophages and monocytes, as both cell types are known to adhere to plastic surfaces [141,142]. Although HoxB8 cells can be differentiated into monocytes, macrophages, dendritic cells, and neutrophils, the SCF outgrowth after transduction should predominantly select cells of the neutrophil lineage. However, it should be noted that the original publication demonstrated that the addition of GM-CSF to the medium, even after SCF outgrowth, can lead to the emergence of a macrophage subpopulation [131]. This subpopulation can even become predominant, reaching 100% of the cells after 10 days of culture. Nevertheless, even without the addition of GM-CSF and G-CSF, strongly attached cells were observed on plastic surfaces, suggesting that either monocyte and macrophage progenitors are still present in the

established SCF-HoxB8 culture or that certain neutrophils possess a more adhesive phenotype.

Starting from late 2018 onwards, several publications have been released, examining the migratory behavior of SCF-HoxB8 cells *in vitro*. These studies employed various assays, including 2D chemotaxis assays in Zigmond and Dunn chambers, as well as collagen assays. Interestingly, all of these studies incorporated the use of either G-CSF (10-20 ng/mL) or GM-CSF (exact concentration not mentioned) alone, and one study combined INF-γ (10 ng/ml) with TNF-α (0.1 ng/ml) on day 4 of the culture [143–145]. These findings support the notion that the initial optimization procedures conducted in our study were headed in the right direction, as other research groups have independently arrived at similar conclusions.

The recent publications, along with our analysis of SCF-HoxB8 cells in collagen assays and microfluidic devices, demonstrate that these cells exhibit migratory capabilities under various test conditions. This underscores the potential of SCF-HoxB8 cells as a valuable tool for studying the migration of primary murine neutrophils.

In summary, for optimal differentiation, we would recommend using a G-CSF concentration of 20 ng/mL in combination with 10 % GM-CSF on day 0. There may be additional benefits in adding LPS, INF-γ, or TNF-α to the culture before experimentation, but this would need to be tested and verified. It's important to note that the addition of GM-CSF may also lead to the differentiation of eosinophils and macrophages. However, after 6 days, their combined percentage should be less than 20%, and since macrophages tend to adhere to surfaces, they can be easily separated by collecting the cells in the supernatant.

Ultimately, we decided not to pursue further experiments with SCF-HoxB8 cells for the Ph.D. project, as their migratory capacities were found to be lower than those of the PLB-985 cells. This choice was based on the need for a cell line with more robust migratory capabilities to better address the specific research questions of the study.

4.1.3 Discontinued Projects and Negative Results

This section is devoted to the plethora of ideas and experiments that were conducted with the hopeful anticipation of yielding remarkable outcomes. However, these endeavors ultimately found no suitable place elsewhere within this thesis.

1. Exploring Collagen Assays: Part I

We performed an experimental trial involving live bacteria, specifically *Escherichia coli* (gram-negative) and *Bacillus subtilis* (gram-positive), in conjunction with various neutrophils, as well as both mature and immature dendritic cells. The primary objective of this trial was to evaluate the capacity of leukocytes to capture these bacteria. Regrettably, the results were discouraging as the bacteria's exceptional speed rendered them unattainable to the immune cells.

2. Exploring Collagen Assays: Part II

We conducted assays using bacterial culture supernatants (gram-negative and gram-positive) to assess their chemoattractant properties. Remarkably, the results demonstrated a significant affinity of all tested leukocytes (neutrophils, iDC and mDC) toward the bacterial supernatant, suggesting a potent chemotactic effect.

3. Cellular Resilience of Differentiated PLB-985 Cells

We were intrigued by the fate of PLB-985 cells after undergoing a week-long differentiation process, subsequent to the withdrawal of the differentiation agent, DMSO. Surprisingly, these cells displayed a remarkable resurgence, thriving and proliferating as if the differentiation process had not happened. This was in stark contrast to the expected non-proliferative state typically associated with post-differentiation cells. Intriguingly, this resurgence was accompanied by an altered cellular morphology, deviating from the conventional appearance observed prior to differentiation.

4. Optimizing Differentiation Methods for PLB-985 Cells

A multitude of methodologies is available for the optimization of PLB-985 cell differentiation. We performed experiments to compare the effectiveness of DMSO and ATRA, ultimately determining that DMSO outperformed ATRA across various parameters. These assessments included cell marker expression, migratory behavior, ease of handling, cost-efficiency, and the overall compatibility with the experimental setting.

In another experimental exploration, we assessed the impact of substituting FBS with Nutridoma-CS (proteome analysis had indicated an increased expression of FPR). This substitution led to slightly more proficient migratory cells. However, the promising results associated with Nutridoma-CS were somewhat dampened by its cost, exceeding 1,000 € for 100 mL.

5. Tackling COMSOL Gradient Modeling Challenges

A substantial investment of time and effort was dedicated to learning the intricacies of modeling attractant diffusion within collagen matrices and microfluidic systems using the COMSOL software. This was done to enhance our understanding of how gradients propagate within our experimental devices and to gain insights into what a cell would perceive at a specific point in time. Regrettably, the complexity and lack of user-friendliness of the software limited the insights we could extract from it.

6. Cells in Scientific Competition: "Dicty World Cell Race"

We entered the "World Cell Race," a global competition focusing on migratory cells' ability to navigate a predetermined maze as quickly as possible. The whole set

of our laboratory's cellular roster participated, including primary neutrophils, PLB-985 cells, and mature dendritic cells. However, our mature dendritic cells, which initially were our front-runners, proved to be unsuitable for the designated maze due to their size, resulting in underperformance and getting stuck in the maze. Regrettably, the event was cancelled, leaving us without comparative performance data for our cellular contenders against those from other research groups.

7. Initiating *in Vitro* Swarming Studies

To study if one can mimic swarming behavior of primary neutrophils *in vitro*, we employed differentiated SCF-HoxB8 cells within cell-derived matrices that retained fibroblasts. Using a UV-laser cutter, we initiated a systematic effort to ablate fibroblasts with the aim of observing *in vitro* swarming behavior of neutrophils due to the damaged fibroblasts. Despite our attempts, the anticipated swarming phenomenon did not manifest, even with increased cell ablation attempts.

8. Dendritic Cell’s CCR7 in PLB-985 Cells

Within the research of the Sixt Group, a specific project is prominent. Despite efforts by multiple researchers, CCR7-KO dendritic cells so far proved to be resistant to rescue through a CCR7 knock-in approach. While dendritic cells remained unresponsive to this intervention, an exploration was undertaken to determine whether genetic modifications of PLB-985 cells, involving the introduction of various CCR7 knock-in variants, could render them responsive to CCL19 for migration. Unfortunately, the genetically modified cells failed to exhibit any response to CCL19 cues, whether in the form of point or line sources, while they continued to exhibit migratory behavior in response to fMLF stimuli.

9. Microfluidic Investigations: Part I

A potential application of microfluidics involved the development of a device capable of precise gradient control. The concept was to generate line and point source gradients and maintain their stability over extended durations. Additionally, this device aimed to provide accurate regulation of gradient strength and various other gradient dynamics. Given the presence of multiple valves within the device, substantial effort was invested in optimizing its design. However, a recurring issue persisted – the unintended leakage of liquids into areas that should have been protected by the valves. This experience generated a valuable lesson: the path of least resistance does not invariably align with the intended trajectories of liquid flows. Remarkably, the liquids displayed a tendency to infiltrate our analysis zones, circumventing the designated flow channels. This served as a reminder that even within precisely designed systems, fluid dynamics can introduce unforeseen deviations.

10. Microfluidic Investigations: Part II

Another objective for microfluidics was to create a device capable of efficiently isolating neutrophils from a small blood droplet. This innovation had the potential to simplify the process of extracting neutrophils from human subjects using a straightforward pricking device. Initially, we were following existing publications that presented what appeared to be a straightforward separation of neutrophils based on their rolling motility or size. However, it soon became apparent that these papers omitted critical details. These devices required precision in every device dimension, along with precise calibration of pressure. Deviating from these requirements led to the absence of cell rolling, and subsequently to no separation of cells. Instead, cells were carried along by the buffer's flow and did not adhere for rolling.

11. Microfluidic Investigations: Part III

Within my repository, I maintain a collection of diverse microfluidic designs. These designs serve a range of purposes, including one specifically tailored for the capture of individual bacteria. This design were supposed to facilitate investigations into the interactions between these bacteria and hunting neutrophils. Moreover, this collection encompasses numerous designed devices containing valves, all engineered for precise gradient control. Regrettably, none of these designs progressed to the stage of production.

12. The Challenge of Optogenetic Control in Cell Motility

A modern tool in the field of cell motility is a potent optogenetic construct capable of directing cells toward a light stimulus. During this thesis, our efforts encompassed various cell types, including PLB and DC, and an array of distinct constructs (e.g., direct use of opsins or optogenetic mGluR6 constructs). However, no cell exhibited a response to a light stimulus under our experimental conditions. Nevertheless, I predominantly witnessed labeled cells actively avoiding light, also in the absence of optogenetic constructs, presumably to mitigate phototoxicity.

13. Exploring Electrode-Based Attractant Control

Given the presence of accomplished neuroscientists at ISTA, why not leverage their expertise to explore the potential of their injection electrode system for controlling the precise delivery of attractants over cells? Electrodes presented a means to confine attractants within their tips, pending a careful equilibrium between electric fields and attractant fumes. This concept offered the prospect of control over each attractant puff, including precise timing. For this project, we started designing experimental concepts as well as custom microscopes and electrode setups. Collaborative efforts with the Jösch lab yielded promising results during the initial experimentation phase, suggesting the potential of this approach. However, initiating an entirely new project during the fourth year of a Ph.D., while exciting, raised questions about practicality. Subsequently, this project was discontinued due to our prioritization of existing projects.

14. PLB-985 and HL-60 Adhesion Tests

In the context of the electrode experiment (see 13.), it was important for cells to adhere to surfaces to prevent being displaced by attractant fumes or slight fluid flow within the dishes. Given the importance of adherence in these experimental setups, we conducted a comparison between PLB-985 cells and their counterparts from the Diz-Muñoz lab, an adherence-selected subclone of HL-60 cells. While PLB-985 cells displayed superior migratory capabilities in collagen assays, they exhibited diminished adherence to surfaces, frequently resulting in their facile detachment in 2D assays. In contrast, HL-60 cells excelled in adherence. When incubated on coated surfaces, these cells adhered strongly, even resisting mild attempts to dislodge them (tilting and slight shaking). Nevertheless, while HL-60 cells had stronger adherence, they were not as efficient as PLB-985 cells in terms of migration.

15. Pre-processing and Analysis Automation

Motivated by a newfound fascination with coding languages such as FIJI macros, R, and Python, I started the automation of certain image analysis and data processing tasks. This initiative was driven by the interest to optimize workflows by eliminating repetitive tasks. Consequently, I developed straightforward yet effective pre-processing and analysis scripts, with the aim of improving not only my workflow but also facilitating the work of colleagues in the lab. However, despite the convenience and

efficiency offered by these scripts, their adoption remained limited. It appeared that, aside from a select few, the concept of automation did not resonate strongly. Even interactive analysis scripts tailored for specific lab members struggled to generate sustained interest. The journey from lines of code to tangible utility highlighted the intricate interplay between technological innovation and the human inclination for familiar routines.

16. Making fMLF-gradients visible: fMLF-K-EDA-Atto647N

To visualize fMLF gradients directly, we were searching for a fluorescent probe that combined brightness with photostability. As no such pre-generated variant existed, we ordered our own variant – fMLF-K-EDA-Atto647N (synthesized by Iris Biotech GmbH). With this dye, we aimed to visualize fMLF gradients within microfluidic devices or collagen assays and potentially wanted to study the trafficking of fMLF across cell surfaces and within their cellular domains. However, the obtained results were not promising. In collagen assays, the dye exhibited promising performance, albeit the gradual accumulation of the dye within cells led to their eventual cell death, possibly due to phototoxicity. Within microfluidic devices, the minuscule volumes posed a challenge, rendering the visualization of physiological concentration gradients impossible. Further exploration, involving confocal microscopy within collagen matrices, were performed to test if we can track fMLF across a cell's surface or within. While we could observe fMLF-agglomeration at single cells, they quickly departed from the field of view, likely to avoid the risk of phototoxicity. In the context of standard collagen assays, concentration titration showed an interesting result. The curves of the biased y-directional speed resembled that of unlabeled fMLF, albeit with altered dynamics resembling the previously mentioned alternative fMLF variants (see figure 17).

17. The Interplay of Curvature and the Lamellipodia

When we encountered a physicist exploring how lamellipodia follow curvature to exhibit energy-efficient behavior, it reminded us of my initial microfluidic experiments. In those experiments, when no chemoattractant was present, neutrophils exhibited a continuous circling pattern around pillars, moving from one pillar to another. These observations laid the foundation for our collaboration as we conducted experiments utilizing inhibitors. The aim was to determine whether destabilizing the lamellipodium could disrupt this circling cell migration. However, our initial findings revealed that destabilizing the lamellipodium did not interrupt the circling migration. Only the introduction of a chemoattractant proved effective in halting this pattern of movement.

4.2 Collaborations

4.2.1 CCR7 acts as both a sensor and a sink for CCL19 to coordinate collective leukocyte migration

Although the processes of cell migration and response to gradients have been extensively studied, our knowledge about the formation, maintenance, and modulation of these gradients *in vivo* is still largely incomplete. While we have made significant progress in understanding how cells detect and navigate along chemical gradients, there are many unanswered questions regarding the precise mechanisms by which gradients are established and regulated within living systems. In this study, we aim to address this gap by integrating experimental data with computational models to investigate the role of self-generating gradients in murine dendritic cells (DC). Specifically, we focus on the interaction between CCR7, a chemokine receptor, and its ligand CCL19, which induces chemotaxis in DC. By examining this system, we aim to gain insights into the dynamics and regulation of gradient formation in DC migration.

Our study revealed a dual role of CCR7, serving both as a sensory receptor for CCL19 and as a sink receptor capable of modifying local CCL19 concentrations. Notably, we observed that CCR7 can dynamically shape chemokine concentration fields, enabling the creation of gradients even within uniform concentrations, allowing for directional cell migration after the gradient formation. This unique function of CCR7 facilitates long-range migration of DC and allows for the adaptation of collective migration in response to the local gradient environment. Also, this ability to modulate the CCL19 gradient has implications for the migration of other co-migrating cells, such as T cells.

My contributions to the study involved conducting experiments using the neutrophil-like cells HL-60 and PLB-985 in complex 3D gradient fields, to compare the behavior of these cells to that of DC. By examining the responses and migratory patterns of these neutrophil-like cells in the presence of gradients, we aimed to gain insights into the similarities and differences between DC and neutrophils in their gradient sensing and migration capabilities.

While DC exhibit a sustained high directional speed toward the gradient source for extended periods of time, albeit a slower acceleration phase, neutrophil-like cells demonstrate a rapid acceleration toward the source but struggle to maintain responsiveness to the chemotactic cues over longer durations (figure 22). This indicates that while DC can effectively utilize the CCR7 receptor both as a detector and as a sink to modulate gradient fields, neutrophils may have limited or reduced ability to utilize their FPR1 as a sink, in addition to its canonical signaling pathway.

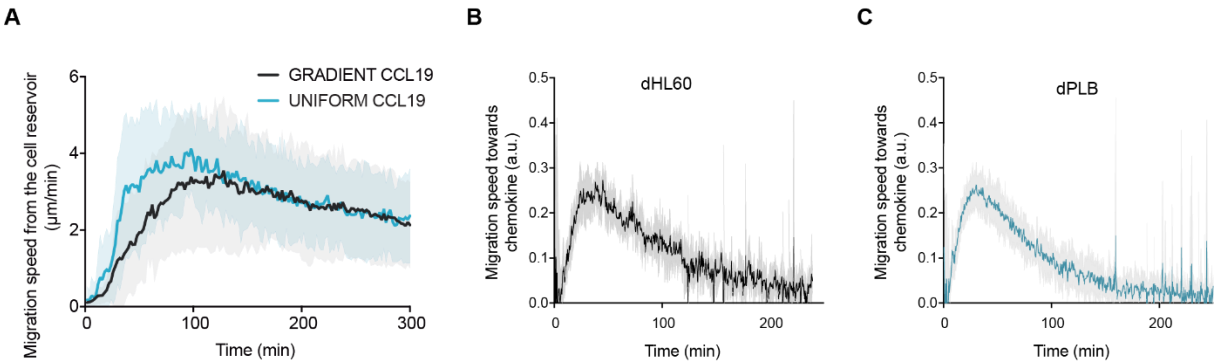


Figure 22: Dendritic cells migrate persistently and CCR7 dependent also in uniform CCL19 field. **A)** Mean migration speed of DCs from the cell source during first 5h with a gradient or uniform CCL19 (n = 5 from 3 independent experiments, mean +/- SD). **B & C)** Mean migration speed of neutrophil-like dHL60 and dPLB cells toward 25 nM fMLF in 3D collagen setup over time (mean+/-SD, 5 independent experiments). Figure adapted from original.

4.2.2 Sensing their plasma membrane curvature allows migrating cells to circumvent obstacles

The adaptive properties of the plasma membrane are crucial for many physiological functions like cell migration, where the membrane is pushed outwards, or endocytosis, where parts of the plasma membrane are engulfed inwards. Besides these properties, the role of membrane deformation in facilitating efficient migration within complex tissue environments remains elusive. In this study, we employ a comprehensive approach combining experimental data and computational models to explore whether the curvature sensing BAR protein Snx33 assists migrating cells in adapting their shape characteristics to the local environment, thereby facilitating obstacle avoidance, and promoting effective migration.

Our investigation revealed that Snx33 is enriched at regions characterized by inward plasma membrane curvature, where it exerts a local inhibitory effect on actin polymerization, thereby establishing a functional connection between membrane curvature and the cytoskeleton. This coupling induces a mechanochemical instability that gives rise to protrusive patterns at the leading edge of migrating cells. Consequently, regions displaying inward curvature experience reduced propulsive forces while promoting spontaneous changes in protrusion dynamics. Leveraging these curvature-sensing mechanisms, cells can effectively navigate complex tissue environments by evading barriers and efficiently avoiding obstacles throughout their migration.

As part of my contribution, I introduced microfluidic devices and performed some of the microfluidic experiments. The microfluidic devices served as an essential tool for studying various aspects of the research, allowing for precise control and manipulation of the geometric environment. By incorporating microfluidics into the study, we aimed to gain valuable insights into the specific dynamics and role of Snx33 during cell migration under specific geometrical conditions.

We employed two distinct microfluidic devices in our study. The first contained decision points, where cells encountered constrictions of varying sizes (2, 3, 4, and 5 µm), while the second device consisted of straight channels with a single constriction that cells had to migrate through. To investigate the role of Snx33, we compared the behavior of WT HL-60 cells and Snx33 KO cells in both device types. Interestingly, we observed that KO cells exhibited significantly longer passing times when migrating through the branching decision points, whereas they were faster than WT cells when traversing channels with or without a single constriction (see figure 23 A, B, C, and E). Notably, there was no significant difference between WT and KO cells in selecting the path of least resistance (i.e., the larger pore size) in assays with decision points (see figure 23 D). Collectively, these findings suggest that the loss of Snx33 renders cells less effective in navigating branching points while enhancing their speed during migration.

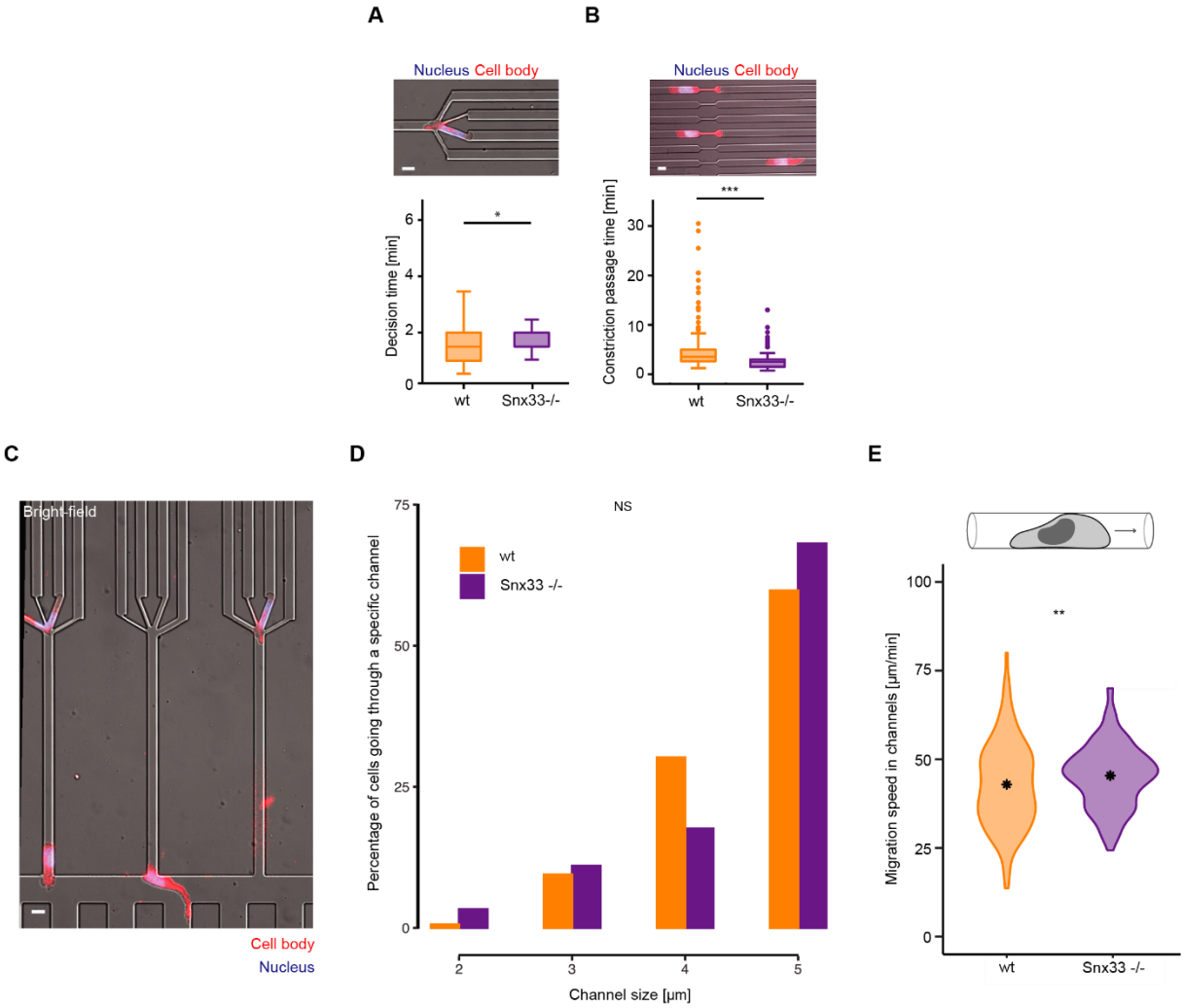


Figure 23: Loss of the curvature-sensing protein Snx33 impacts adaptive motility. **A)** Decision channel passage time (n=159 for wt, n=91 for Snx33-/-) in cells. **B)** Constriction passage time (n=234 for wt, n=158 for Snx33-/-) in cells. **C)** Overlay of bright-field, nuclei and cell body images of cells migrating in PDMS-based devices with a decision point. **D)** Frequency of wt and Snx33-/- cells choosing a channel of a certain size (n = 159 for wt, n = 91 for Snx33-/-). **E)** Migration speed in straight channels (n=235 for wt, n=169 for Snx33-/-). Data from 3 independent biological replicates. Scale bar = 10 µm. $p<0.001$ (***), $p<0.01$ (**), $p<0.05$ (*). Figure adapted from original.

4.2.3 Plan your trip before you leave: The neutrophils' search-and-run journey

In this spotlight, we summarized the findings of Georgantzoglou et al., where they utilized *in vivo* models to study the temporal response of neutrophils to an acute gradient.[73] Their work revealed a search-and-run strategy for neutrophils after they encountered a new gradient. Initially, after recruitment into the tissue, neutrophils exhibit random migration, lacking any long-term polarization. However, upon encountering a new gradient, such as at a wound site, neutrophils transition into a search phase characterized by the enrichment of actin in the leading edge. This enrichment leads to a deceleration of the cell and a subsequent turning motion toward the gradient source. Once turned, the cell enters the run phase where it accelerates toward the gradient source, showing a fast backward flow of actin and a persistent migration upwards the gradient. Throughout these phases, the contractility, actin flow, and actin concentration at the leading edge undergo dynamic changes that influence the cell's speed and migratory persistence. These findings highlight the intricate interplay between cellular processes and gradient sensing in neutrophil migration (see figure 24 for a visual representation of the observed behavior).

My contribution included the creation of the figure, illustrating the key finding of the study, as well as writing the accompanying figure legend. Additionally, I assisted in writing the spotlight article.

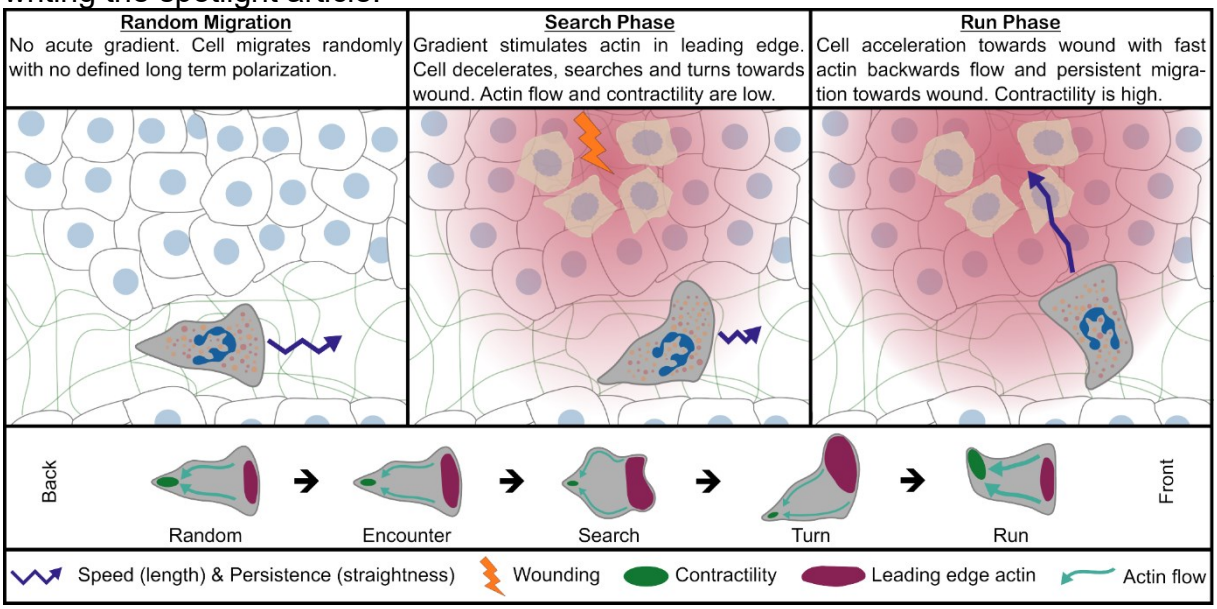


Figure 24: Model for neutrophil search-and-run strategy *in vivo*. After neutrophils are recruited into tissue, they migrate randomly. Once they encounter an acute gradient, they slow down and actin is enriched at the cell front to expand the leading edge, while cell contractility and actin flow are low. The dynamic expansion of the leading edge helps neutrophils to sense the direction of the gradient, leading to a biased turn into the direction of the wound and ending the search phase. At the onset of the run phase, contractility is increased, leading to a high retrograde actin flow, which results in rapid cell movement. The contractility creates an inertia effect on cell polarity, locking the cell into a forward movement toward the source with high directional persistence.

4.2.4 Cellular locomotion using environmental topography

The migratory ability of eukaryotic cells relies on the coordination between their intracellular cytoskeletal forces and the external environment, primarily facilitated by adhesion receptors. Among these receptors, the integrin family plays a prominent role, and their knockout leads to cells with diminished adhesive forces. Interestingly, leukocytes with knocked-out integrins still demonstrate rapid migration in 3D environments despite having significantly reduced levels of adhesion receptors [146]. In our study, we observed that even in the absence of transmembrane force coupling numerous leukocytes can migrate forward within microfluidic environments, depending on the surrounding surface topography. This is achieved by coupling the actin retrograde flow to the surrounding topographical features. This unique mechanism allows leukocytes to navigate and migrate in a controlled and directed manner, showcasing their adaptability in complex microenvironments. These findings provide valuable insights into the migratory capabilities of leukocytes and their ability to overcome challenges during their migration.

My contribution to this project focused on working with neutrophil-like PLB-985 cells as a comparison to other leukocytes utilized in the study. I adjusted the existing experimental setup for the PLB-985 cells, performed the experiments, and conducted the subsequent data analysis. This comparative approach allowed us to draw meaningful conclusions and insights regarding the migratory characteristics and dynamics of various leukocyte populations.

To investigate how cells transmit internal forces outwardly, we developed a microfluidic chip that provided a controlled environment for cellular movement. The chip featured multiple changing serrated zones and a smooth part at the end. The arrangement of these zones was based on the distance between each of the serrated subunits (6, 12, and 24 µm), resulting in varying degrees of surface roughness (see figure 25 A). This design allowed us to assess the impact of surface topography on cell behavior in the presence or absence of adhesive forces. Control PLB cells were able to traverse between all zones and pass through the smooth channel quickly and without any problem (see figure 25 B). However, when integrin activity was blocked by removing cations via EDTA, cells became trapped in zones with smoother surface topographies (see figure 25 C). Importantly, these observations were not limited to PLB cells but were also observed for T cells and DC (data not shown). These findings highlight the importance of force transmission in leukocytes and suggest that surface topography plays a crucial role in enabling their migration, even in the absence of integrin-mediated adhesion.

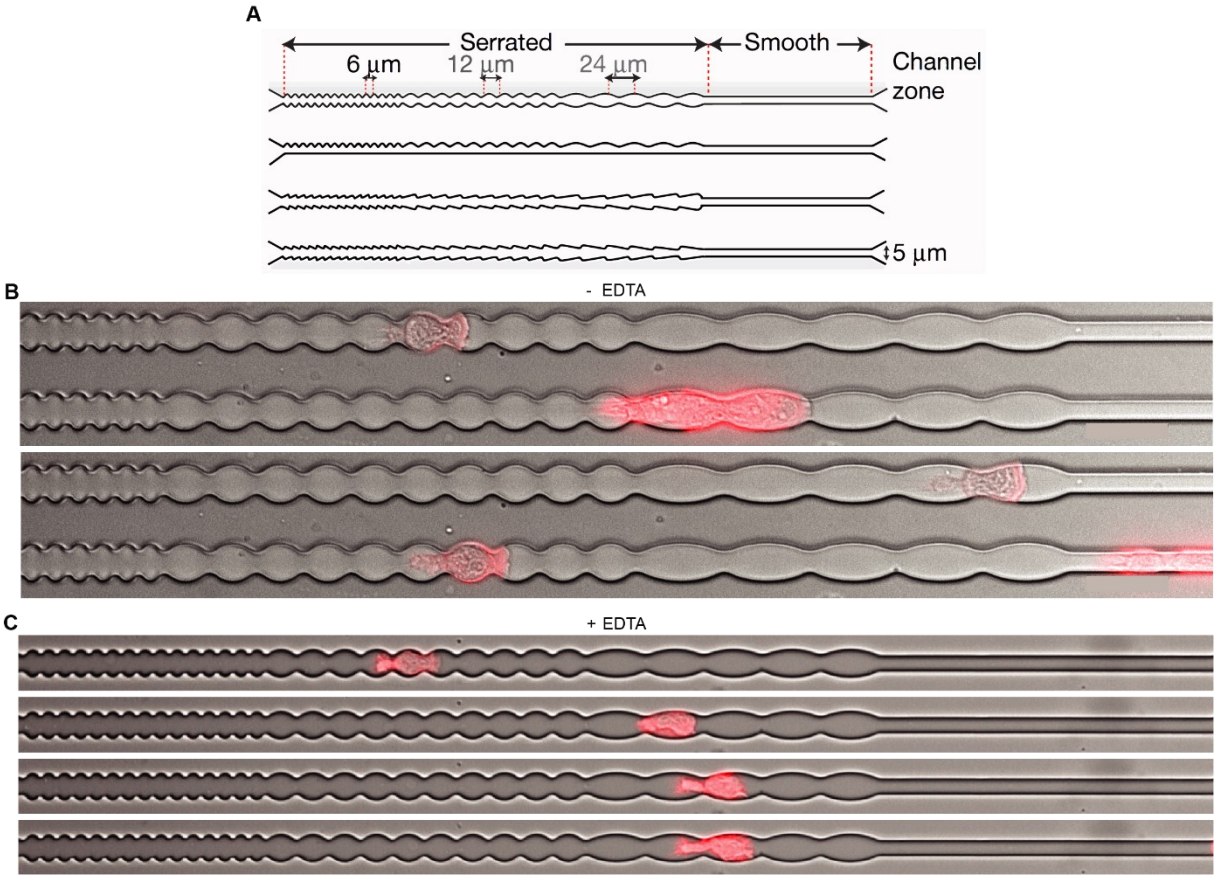


Figure 25: Force transmission of PLB-985 in varying microfluidic geometries. **A)** The channel design that was used in B & C. **B)** & **C)** Snapshots of 10 s intervals of Lifeact-mCherry-expressing cells migrating from left to right within the microfluidic chip without EDTA (B; control; two time points) or with EDTA, lacking integrin activity (EDTA depletes cations which are needed for integrin activity; C, four time points). Lifeact (red signal) labels actin structures. The figure was created by using snapshots of the original movie.

4.2.5 Nuclear Positioning Facilitates Amoeboid Migration Along the Path of Least Resistance

The nucleus, being the largest organelle in eukaryotic cells, serves the crucial role of protecting the genetic code. To ensure its integrity, the nucleus must maintain rigidity to prevent DNA damage but also needs to maintain a degree of flexibility so it can adapt to the surrounding cellular environment. During cell migration, various challenges arise, such as the need to navigate through small pores or pass through dense cell layers. While slower migrating cells can deform or dissolve tissue to facilitate their passage, faster migrating immune cells face a bottleneck when encountering pores that are significantly smaller than their nucleus. Although cells have the ability to squeeze and deform the nucleus, this process is time-consuming and can potentially slow down cells to avoid DNA damage. Interestingly, certain immune cells, like neutrophils, possess lobed nuclei, which are believed to aid them in traversing constrictions faster and more efficiently due to the reduced diameter of the nucleus. While migrating in 2D, where cells typically do not encounter pores or constrictions, most amoeboid cells position their nucleus at the rear of the cell. However, during 3D migration, the nucleus is positioned at the front, indicating its role as a mechanical gauge for cell migration when cells encounter obstacles.

In this study, we investigated whether fast-migrating immune cells utilize their nucleus as a mechanical gauge to detect the largest pore sizes in their path. We aimed to determine if positioning the nucleus strategically closer to the leading edge enables cells to navigate through narrow spaces more efficiently, thereby potentially reducing the need for time-consuming nucleus deformations.

In this work, my contribution involved working with primary human neutrophils. This encompassed obtaining ethical approval, purifying, and staining the cells, designing the experimental setup specifically for neutrophils, and providing assistance during the experiments. The experiments and analysis were primarily conducted by Jörg Renkawitz.

We utilized microfluidic devices with decision points featuring constrictions of different sizes (2, 3, 4, and 5 µm) to investigate cell behavior. We found that migrating dendritic cells (DC) preferred larger pore sizes not only during random migration but also when following chemotactic cues (see figure 26 A). This trend of favoring bigger pore sizes was even more pronounced during chemotaxis. Interestingly, we also observed similar behavior in primary murine T cells, murine T cell hybridoma cells (LMR 7.5), and primary human neutrophils, where these cells also exhibited a preference for larger pore sizes during chemotaxis (see figure 26 B). When examining the nucleus of DC, we noted that its positioning coincided with the final nuclear passage through the pores. Additionally, we saw that the nucleus underwent significant deformation and initially protruded into multiple pores before passage (see figure 26 C & D). Comparing the nuclear dynamics of DC with neutrophils revealed that the lobed nuclei of neutrophils entered multiple pores simultaneously (see figure 26 E – G), suggesting that the lobed structure of the neutrophil nucleus facilitates entry into constrictions. These findings suggest that multiple fast-migrating immune cells utilize their nucleus as a mechanical gauge to identify the path of least resistance.

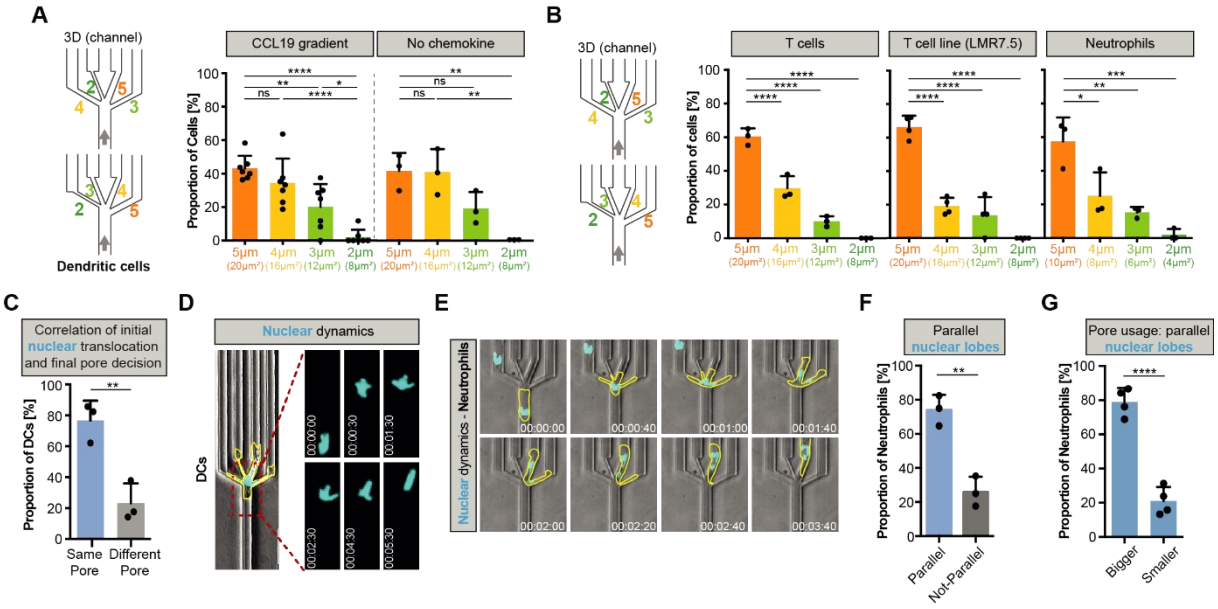


Figure 26: Nuclear positioning enables cells to take the path of least resistance. **A)** Quantification of pore-size preference of DCs treated as in f, with (left; 7 experiments, 119 cells; one-way ANOVA with Tukey's test; ****P < 0.0001, **P = 0.0029, *P = 0.0225) or without (right; 3 experiments, 81 cells; one-way ANOVA with Tukey's test; **P = 0.0049) a CCL19 chemokine gradient. Pooled data from two devices with differently ordered sequences of pore size (2, 3, 4, and 5 µm or 4, 2, 5, and 3 µm, respectively). **B)** Migration of T cells, LMR7.5 hybridoma T cells and neutrophils in microchannels through a decision point of four differently sized pores of 2-, 3-, 4- and 5-µm wide (T cells, LMR7.5, 4-µm height; neutrophils, 2-µm height), and quantification of pore-size preference along a chemokine gradient (T cells (CCL19): 3 experiments, 68 cells; LMR7.5: 3 experiments, 40 cells; neutrophils (fMLF): 3 experiments, 46 cells; one-way ANOVA with Tukey's test; ****P < 0.0001, ***P = 0.0007, **P = 0.0043, *P = 0.0193). Pooled data from two devices with differently ordered sequences of pore size (2, 3, 4, and 5 µm or 4, 2, 5, and 3 µm, respectively). Data in g and h are mean ± s.d. Time is indicated as h:min.s. **C)** Correlation of initial nuclear translocation and final pore decision (3 experiments, 61 cells; unpaired t-test, **P = 0.0068). **D)** Nuclear protrusion dynamics (Hoechst stain) during DC pore-size decision (cell outline in yellow, time indicated; representative of five experiments). **E)** Nuclear lobe dynamics (Hoechst stain) during neutrophil pore-size decision (cell outlines in yellow, time indicated; representative of three experiments). **F)** Quantification of parallel nuclear lobes into different pores during neutrophil pore-size decision (3 experiments, 46 cells; unpaired t-test, **P = 0.0027). **G)** Pore-size selection by parallel nuclear lobes (4 experiments, 71 cells; unpaired t-test, ****P < 0.0001). Figure adapted from original.

5 Materials and Methods

5.1 Cell Culture

All cells were grown and maintained at 37 °C in a humidified incubator with 5 % CO_2 and routinely tested for mycoplasma contamination.

Neutrophil-like PLB-985 & HL-60. Cells were obtained from the DSMZ (PLB-985, ACC 139) or were a gift from the Alba Diz-Muñoz (HL-60). In brief, cells were maintained in P10 medium, consisting of RPMI 1640 supplemented with 10 % FBS, 20 mM HEPES, and 1% GlutaMAX (all Gibco, Thermo Fisher Scientific). For differentiation, PLB cells were kept for 6 days in P10 containing 1.25 % DMSO (cell culture grade; Sigma-Aldrich), while on day 3 the medium was replaced by fresh DMSO containing P10. Differentiation status was validated using flow cytometry (CD11b, REAfinity, Miltenyi Biotec). Before experimentation, differentiated cells were washed three times to remove residual DMSO.

Human primary neutrophils. Cells were isolated from healthy donors (in accordance with relevant national guidelines and regulations, and informed consent of healthy volunteers: GS1-EK-4/543-2018) using EasySep Direct Human Pan-Granulocyte Isolation Kit (Stemcell). The purity and non-activated status of PMNs were validated using flow cytometry (FSC, SSC, CD11b, CD14, CD45, CD62L, CD66b, CD235a; all REAfinity, Miltenyi Biotec). For short-term storage or staining, PMNs were kept in Hank's balanced salt solution without phenol red (Gibco), supplemented with 0.6 % human serum albumin (Sigma) and 1 % glutamine (Gibco), with gentle agitation in a ventilated tube in a humidified incubator. For experiments, neutrophils were resuspended in RPMI without phenol red, supplemented with 0.6 % human serum albumin, 20 mM HEPES (Gibco), and 1 % glutamine.

Immortalized primary murine neutrophil progenitors (SCF-HoxB8 cells). Immortalized murine hematopoietic progenitor cell lines were generated by retroviral delivery of an estrogen-regulated form of HoxB8 as described elsewhere [131]. Briefly, bone marrow of a 6–12-wk-old C57Bl/6 mouse was isolated and pre-stimulated for 48 h with 1 % stem cell factor (SCF; supernatant from hybridoma culture), 10 ng/ml IL-3 (PeproTech) and 20 ng/ml IL-6 (eBioscience). A Ficoll-Paque density gradient centrifugation was used to enrich the number of progenitors and cells were subsequently retrovirally transduced with an estrogen-regulated form of the HoxB8 transcription factor. Selection and outgrowing of SCF-HoxB8 cells were achieved by culturing cells in RC10 medium consisting of RPMI 1640 supplemented with 10 % FBS, 1 % GlutaMAX, 10 U/mL Penicillin, 10 µg/mL Streptomycin, 50 mM mercaptoethanol (all Gibco, Thermo Fisher Scientific), 1 µM β-estradiol (Sigma), 10 % granulocyte-macrophage colony-stimulating factor (GM-CSF) and 1 % SCF (both supernatant from hybridoma cultures). Cells were also maintained and propagated in RC10 medium. For differentiation, cells were washed to remove β-estradiol and subsequently kept in RSD10 medium, which is similar to RC10 medium but SCF from hybridoma supernatant was exchanged for 20 ng/mL SCF (Biolegend). Additionally, various concentrations of GM-CSF (10 – 20 %) and granulocyte colony-stimulating factor (G-CSF; 10 – 20 µg/µL; PeproTech) were supplemented to RSD10 at different time points to test for differentiation efficiency. Cells were differentiated for a maximum of 6 days while the medium was replaced on days 2 and 4. Differentiation status was validated using flow cytometry (Ly-6G, REAfinity, Miltenyi Biotec)

5.2 Flow Cytometry

Staining. 0.2 – 1 x 10^6 cells were stained according to the manufacturer's protocol in flow cytometry buffer (FCB, 1× PBS, 1% BSA, and 2 mM EDTA). Briefly, cells were pelleted and resuspended in FCB with the recommended concentration of the respective antibodies: CD11b, CD14, CD45, CD62L, CD66b, CD235a (for primary neutrophils, all human REAfinity, Miltenyi Biotec), CD11b (for PLB-985, human REAfinity, Miltenyi Biotec) or Ly-6G (for SCF-HoxB8, murine REAfinity, Miltenyi Biotec). Samples were incubated for 10 minutes at 4 °C, washed twice with FCB, and immediately analyzed via flow cytometry. All samples contained an isotype control, an unstained autofluorescence sample, and in the case of multicolor staining, the respective compensation controls according to the manufacturer's protocol (MACS Comp Bead Kit, Miltenyi Biotec). Of note, due to the usage of REAfinity antibodies, a FcR block was unnecessary as these recombinant antibodies have mutated Fc regions which prevent them from binding to FcR receptors. Additionally, all REAfinity antibodies belong to an universal IgG1 isotype, requiring only one isotype control.

Flow cytometry. Flow cytometry analysis was performed on a FACS CANTO II flow cytometer (BD Biosciences). For multicolor staining, a compensation matrix was created using compensation controls. For samples, forward scatter (FSC-A) and side scatter (SSC-A) were used to gate on live cells. Unstained samples (i.e., autofluorescence) were used to adjust laser intensities and subsequently, the forward scatter (FSC-A and FSC-H) was used for singlet/doublet discrimination. The remaining signals were used for the analysis.

Flow cytometry analysis. The gates from the flow cytometry were controlled and adjusted if needed. The median fluorescence intensity of each sample was extracted and normalized to a stained control group (e.g., undifferentiated cells).

5.3 3D Collagen Migration Assay

Collagen assembly. Custom-made migration chambers were assembled by using a plastic dish with a 17-mm hole at the center, which was covered by coverslips on both sides of the hole. A 3D collagen scaffold (final concentration of 1.7 mg/ml) was obtained by mixing bovine collagen (PureCol, Advanced BioMatrix) in 1x Eagle's minimum essential medium and 0.4 % sodium bicarbonate (both Sigma-Aldrich), with 1.5 × 10^5 cells in P10 at a 2:1 ratio. After casting the collagen mix in the homemade migration chambers, gels were allowed to polymerize for at least 1 h at 37 °C, 5 % CO_2.

Gradient collagen migration. Gels were either overlaid with 100 µl of P10 alone, an attractant solution in P10, or an attractant-filled cut-off GELoader tip (Eppendorf) was stuck into the collagen gel. If not mentioned otherwise, fMLF (Sigma-Aldrich) was used as an attractant and diluted in P10. For experiments with a fluorescent proxy, the respective Atto dye (carboxy Atto-488 and carboxy Atto-655, ATTO-TEC) were added to the solution to meet the same concentration as the attractant. In some cases, the overlaid medium control was spiked with the same Atto dyes, as the 5 nM fMLF attractant sample. If a microscope without CO_2 and humidity control was used, chambers were sealed with paraffin (Sigma) before starting imaging. Migration was observed by time-lapse video microscopy.

Uniform collagen migration. For the uniform collagen migration assay the homemade migration chambers were built without the top coverslip to allow a rapid submersion of the collagen. Additionally, to enable firm adhesion of collagen to the glass surface, coverslips were first washed with nitric acid and then coated with 0.2 % gelatin. It was subsequently crosslinked with 1 % glutaraldehyde and quenched by using 1 M

glycine. Polymerized gels were fully submerged rapidly with 5 mL P10 or an attractant solution in P10. Migration was observed by time-lapse video microscopy.

5.4 Under Agarose Assay

Under agarose assembly. To create migration chambers, paraffin was used to attach a 17 mm plastic ring to a plastic dish with a 14 mm hole at the center, which was covered by a coverslip at the bottom. 4 % Ultra-Pure Agarose (Invitrogen) was dissolved in nuclease-free water (Gibco) and subsequently mixed with phenol-free RPMI-1640 supplemented in a 1:3 ratio with 20 % FBS and 1× Hanks' buffered salt solution at pH 7.3 (all Gibco, Thermo Fisher Scientific). A total volume of 400 µl agarose mix was cast into each migration chamber.

Gradient under agarose migration. After polymerization, a 2-mm hole was punched into the center of the agarose pad, and a long rectangular block was punched out slightly above the center. Residual liquid within the holes was aspirated and the outer parts of the dish were filled with PBS followed by 30 min equilibration in an incubator (37 °C and 5 % CO_2). Subsequently, the central hole was used to load the cell suspension and the rectangular hole was used to load the respective concentration of fMLF (Sigma-Aldrich) to generate a soluble gradient. Migration was observed by time-lapse video microscopy.

Uniform under agarose migration. Before casting the agarose for the assays with a uniform concentration, a highly concentrated fMLF concentration was mixed with an agarose aliquot to achieve the desired concentration. After polymerization, a 2-mm hole was punched into the center of the agarose pad, and residual liquid was removed. The cell suspension, prepared in the same concentration as the corresponding under agarose assay, was then loaded into the central hole.

5.5 Microfluidics

Microfluidic device fabrication. Pillar patterns were generated by a Python script (by Saren Tasciyan) in SVG format. Device and photomask designs were completed in layers for each height using Inkscape (v1). SVG files were converted to AutoCAD DXF R14 files and subsequently to Gerber files (LinkCAD). Designs were printed on chrome photomask at a resolution of 1 µm (JD Photo Data & Photo Tools). For high-resolution structures, wafers were first coated with a sub-micrometer layer of SU-8 as a sticky substrate for later SU-8 structures. We used GM-1040 SU-8 photoresist (Gersteltec) at 5,000 rpm for 2 min with flood UV exposure. The feature layer was then applied with SU8-2005 (Microchem). According to the datasheet, a UV-absorbing glass plate and higher exposure were used to make sharp features. PL-360-LP from Omega Optical and 550 mJ/cm2 with an EVG mercury lamp-based mask aligner gave good results in the 3–9 µm thickness range. The thick (25 µm) loading channels were made with Microchem SU8-3025 using the EVG mask aligner according to the Microchem datasheet without the PL-360-LP plate. The master wafers underwent vapor silanization for 1 h with (1H, 1H, 2H, 2H-perfluorooctyl) trichlorosilane. The results were single hydrophobic master wafers containing several aligned layers. Polydimethylsiloxane (PDMS) devices were made with Sylgard 184 Elastomer Kit (Dow Corning) using a ratio of 10:1. The PDMS was mixed in a Thinky mixing machine and then poured on the wafer in a 3D printed tray and further degassed several times in a vacuum chamber. The devices were baked at 80°C overnight. The hardened devices were peeled off the mold and cut into single devices using a razor blade. Holes were punched with a skin biopsy puncture tools (2 mm) for the loading holes, and pressure-sensitive tape was used to remove debris. Glass coverslips were sonicated for 5 min in 100 % ethanol followed by 100 % isopropanol and blown dry. Devices were bonded to the glass slides

by oxygen plasma and then sealed together at 85°C for 1 h to create a permanent bond.

Microfluidic migration assay. Microfluidic devices and P10 medium (without phenol red) were pre-incubated overnight in an incubator (37 °C and 5 % CO_2) to equilibrate CO_2. A final concentration of 50 µM ascorbic acid was achieved by adding it to the pre-incubated medium, which was then used for all subsequent steps. On experimentation day, devices were first plasma cleaned and then primed with P10 medium and kept in an incubator for at least 1h (37 °C and 5 % CO_2). For the visualization of cell nuclei, cells were pre-incubated for at least 20 min. with NucBlue (Invitrogen), followed by washing twice. Before loading microfluidic devices, they were primed again to account for depleted proteins that bound to the device surfaces due to plasma cleaning. All subsequent loading and removal steps were performed using GELoader tips (Eppendorf) to allow for proper aspiration and loading. After re-priming, 6 µL of medium from attractant holes was aspirated, and then 2 µL of a concentrated fMLF solution was added to achieve a final concentration of ~ 50 µM of fMLF. The attractant solution also contained 25 µM of carboxy Atto-655 (ATTO-TEC) to visualize the gradient. After the attractant was loaded, 6 µL of medium from cell holes was aspirated, and then 2 µL of a concentrated cell solution was added to either load 10,000 or 50,000 cells. Microfluidic devices were then loaded onto the microscope where they were incubated for at least 30 min. before imaging was started. Migration was observed by time-lapse video microscopy.

5.6 Laser-Assisted Adsorption by Photobleaching (LAPAP)

LAPAP Reagents. fMet-Leu-Phe-PEG11-N3 (fMLF-azide) and fMet-Leu-Phe-PEG11-PRA (fMLF-alkyne) were synthesized by Iris Biotech GmbH, fAsn-Leu-Phe-Asn-Thr-K-FITC was bought from Invitrogen, fMet-Leu-Phe-GGGGGGK-K(FITC)-NH2 (fMLF-K-FITC) and fMet-Leu-Phe-PEG-(FITC)-NH2 (fMLF-PEG-FITC) were synthesized by AnaSpec. FAM-alkyne and FAM-azide were purchased from Lumiprobe or Jena Bioscience, GRGDS-HF555-azide was synthesized by Eurogentec, and Atto-647N-alkyne was obtained from ATTO-TEC GmbH. The Click-it kit was purchased from Thermo while the click-reaction kit was a gift by ibidi GmbH, containing chemicals from Jena Bioscience.

Surface immobilization. The projector-based photo patterning technique was implemented using an LCD projector integrated into a microscope setup. The procedure involved the substitution of the light source in a conventional LCD overhead projector (Panasonic PT AE6000E with a contrast ratio of 297±1:1) with a 470 nm LED source (Thorlabs model M470L3). The projection lens was removed, and the projected image was directed through a relay lens (Thorlabs AC508-100-A-ML, focal length of 100 mm) into the rear port of an inverted routine microscope (Leica microscope). To achieve this, a 50/50 beam splitter (Thorlabs BSW10R) was employed to guide half of the incident light through the chosen objective to the surface of the substrate. The reflection of the projected pattern from the substrate-air interface was captured by a digital camera (Prosilica). Precise alignment between the projected image and the microscope's focal plane was achieved by adjusting the projector while the microscope was focused on the substrate surface. Custom software utilizing MATLAB and MicroManager was employed to generate and project patterns, as well as controlling LED illumination.

Before pattern exposure, the substrate was thoroughly cleaned and, if needed, coated with either PDMS or Polyvinyl alcohol (PVA). 15 µL – 50 µL FAM-alkyne, FAM-azide, or fMLF-FITC were added to the substrate and the microscope focus was subsequently adjusted to bring a projected target pattern into focus precisely at the surface of the substrate. Patterning was then performed with variable intensities and patterning

times. The substrate was subsequently washed four times for at least 10 min. and if needed the subsequent click-chemistry partner was added (GRGDS-HF555-azide, Atto-647N-alkyne, or fMLF-azide) and incubated for 30 – 60 min. The click reaction was carried out following the instructions provided in either the Click-it kit manual or the ibidi manual. In the case of ibidi, the process involved initially mixing BTTAA with CuSO4, followed by the addition of Na3PO4 buffer along with Vitamin C and the appropriate click partner. The substrate was again washed four times before adding cell suspension and/or imaging.

5.7 Imaging and Microscopy

All migration assays were conducted under controlled temperature (37 °C) and CO2 (5 %) conditions. For collagen and microfluidic assays, the humidity was also regulated (~80 %). However, under agarose assays were performed without humidity control, although a water reservoir was placed around them to maintain hydration.

Collagen assays, microfluidic devices with proxy dye, and LAPAP. Cell migration was recorded with either an inverted wide-field Nikon Eclipse or a Nikon Ti2E microscope. The Nikon Eclipse was used with a 10×/0.3 PH1 air objective, equipped with a Lumencor light source (390 nm, 475 nm, 542/575 nm) and an incubation chamber, heated stage, and CO_2 mixer (Ibidi). The Nikon Ti2E was used with a 10x/0.3 DIC (differential interference contrast) and a 20x/0.75 DIC PFS air objectives, equipped with a Lumencor light source (390 nm, 438 nm, 475 nm, 513 nm, 549 nm, 575 nm, and 632 nm) and an incubation chamber, heated stage, and CO_2 mixer (Ibidi). For the collagen assays, after each microscopy session, an image of the respective chroma slides (GFP and far-red) was taken with the same parameters as during the live cell imaging.

Under agarose and collagen assays without proxy dye. Time-lapse acquisition was performed using inverted routine microscopes (Leica) equipped with either bright-field or DIC imaging. The microscopes were equipped with phase alternating line cameras (Prosilica) and controlled by either SVS-Visitek software (Seefeld) or a custom-made software (by Robert Hausschild, Institute of Science and Technology Austria). Imaging was conducted using 4×/0.1, 10×/0.22, or 20×/0.3 objectives.

Nuclear visualization. Microscopy was performed with an inverted Axioobserver (Zeiss, Germany) microscope using a 60X/1.46NA oil objective with optovar 1X. A TIRF 488/561-nm laser (Visitron systems, Germany) was used to record a z-stack of stained nuclei.

Cell culture microscopy. Cell cultures were controlled with an inverted routine microscope (Leica) equipped with either bright-field or DIC imaging. Images were taken with a connected camera (Leica).

5.8 Image and Data Analysis

For image analysis Cellpose[147], Fiji[148], and the Trackmate plugin[149] were used for tracking of cells in collagen assays. Imaris (Bitplane) was used for the analysis of microfluidic tracks. Data analysis scripts were created using R (V 4.1.3) or Python (V 3.8.16).

Collagen tracking. Movies were first flat field corrected by subtracting the median of a dark image of each proxy value. Images of chroma slides were normalized and the proxy values of collagen movies were divided by the obtained normalized values. Movies were subsequently stabilized by using the “Correct 3D drift” plugin in FIJI and the median projection was subtracted. Cells in the resulting movie were segmented using Cellpose, where a custom model was created by training the model on PLB cells in collagen. Tracking was done via Trackmate in a semi-automatic fashion, using segmented and brightfield data, to ensure that the same single cell is tracked throughout

the movie. In general, only moving cells were tracked and movies were separated into visual quadrants to track roughly an equal number of cells in each quadrant throughout all movies.

Collagen cell track data extraction script. Using a custom script (by Christoph Sommer, Institute of Science and Technology Austria), the trajectories of each cell were utilized to extract the proxy intensity values around each cell location at each time point. In addition, the script also calculated various migratory parameters based on the cell trajectories and the respective proxy values. Briefly, the script first smoothed the pixel intensity field of each proxy with a small Gaussian blur ($\sigma = 5$). Second, to obtain an estimate of cell orientations, a spline interpolation was performed on cell trajectories to define the cell front and back at each time point. The process of interpolation applied some smoothing to the cell tracks, resulting in slight alterations to the x and y coordinates of all the tracks. The orientation of the cells, along with the smoothed x/y coordinates, was employed to extract proxy values from three distinct regions: the center of the cell and regions located in front and behind the cell. These regions were determined based on a specified distance (e.g., 9 µm) from the cell center, allowing for a comprehensive analysis of the local gradient in different areas surrounding the cell. For the extraction of the proxy value, a single pixel was used as the reference point. However, thanks to the application of Gaussian smoothing, the extracted value accounted for the influence of neighboring pixels and effectively captured the surrounding local environment. Besides extracting proxy intensity values, the script also calculated the angle deviation to the source and the directional change between two consecutive time points. The calculation of these directional parameters involved using the cell orientation. For the deviation to the source, the origin of line sources was set at a y-coordinate of 0, whereas for point sources, the coordinates of the respective pipette tips were used as the origin. In addition, using the respective smoothed trajectories and source location (i.e., $y = 0$ for line sources and pipette tip for point sources), the script further computed several other parameters: speed (both raw speed and interpolated values), acceleration, displacement toward the source, and the change in displacement toward the source.

Collagen-aligned maxima script. A custom script (by Christoph Sommer, Institute of Science and Technology Austria) was used to extract aligned maximal gradient proxy values in relation to the given source in each movie. In simpler terms, this method positioned hypothetical cells throughout the entire collagen space at each time point. These hypothetical cells were always perfectly aligned with the gradient source and were used to extract a gradient profile on a cellular level using a similar approach as described in the "Collagen cell track data extraction script" method. This allowed for the comparison of cell-level gradient profiles of real cell trajectories and of theoretically perfectly aligned cells. Briefly, the script first smoothed the pixel intensity field of each proxy with a small Gaussian blur ($\sigma = 5$). For line sources, the source orientation axis was defined as $y = 0$. Along a perpendicular line to the source axis, the difference between two pixels at a defined length (e.g., 18 µm) was extracted for each pixel of a movie. For point sources, a polar transformation was applied in relation to the entire pipette, considering the position, length, and angle of the pipette within the collagen. Areas that were perpendicular to the pipette axis were excluded from the analysis by applying a mask. The tip of the pipette served as the origin of the polar coordinate system. Along a line starting from this origin, the difference between two pixels at a defined length (e.g., 18 µm) was calculated for each non-masked pixel of a movie. For both source types, the obtained values were then divided by the proxy value of half the distance (e.g., 9 µm), to obtain a normalized gradient value. Subsequently, the script averaged the obtained values based on the distance from the source as well as time.

Of note, when values at boundaries were to be extracted, they were excluded from the analysis without replacement.

Collagen data analysis script. Data from the extraction script and the aligned maxima script were imported into R where they were further processed. Cell tracks were additionally filtered to remove non-responsive cells as well as cells that stopped migrating early on. To remove cells that stopped migrating early on, we calculated the sum of x and y displacement over all time points, and tracks were removed that had less than 35 µm displacement in both. To remove non-responsive cells, we calculated the absolute median displacement toward the source over all time points and removed cells that had a lower value than 0.001. These values were validated by looking at the removed and remaining trajectories. Subsequently, several parameters were further computed, as can be seen below. Of note, all parameters were calculated for each cell individually and only averaged for the specific groups (e.g., Point) later.

- Amount of **finisher cells** was calculated by defining a finishing area of 250 µm before (line) or around (point) the given source. Cells that entered the area once were considered "finishers". Cells that were in the finishing zone from the start were excluded.
- **Straightness** was calculated according to the formula:
$$\frac{Eucledian\ distance}{Total\ travveled\ distance};$$
the Euclidian distance was defined as the length of a straight path between the first and last location of a cell in a movie.
- **Chemotactic index** was calculated according to the following formula:
$$\frac{Total\ displacement\ towards\ source}{Total\ travveled\ distance};$$
- **Δc values** were calculated using the formula:
$$\frac{c_{Front} - c_{Back}}{c_{Center}};$$
c represents the concentration of the proxy at the indicated region.
- To **identify minima and maxima** in the speed time series, a custom function that analyzed the data based on a threshold value (= 1) was used. This function compared each point in the time series with shifted versions of itself to determine whether it corresponded to a minimum, maximum, or neither. The threshold value could be utilized to exclude or ignore data points within a certain range around the tested time point.
- The speed **oscillation amplitude change** was calculated as a factor that measured how much the speed changed at a given minimum compared to the previous maximum, or between two randomly sampled time points. The formula used for the calculation was as follows:
$$\frac{speed_{max} - speed_{min}}{speed_{max}};$$
- To determine the **oscillation frequency** of speed, the time intervals between subsequent extrema of the same type (minima, maxima, or random points) were calculated.
- **Velocity autocorrelation function** (VACF) was calculated by first computing the velocity vector at each time point of a track. Subsequently, the velocity vector was transformed into the unit vector by dividing by its magnitude to reduce the influence of speed oscillations on the VACF. Now the VACF was calculated by computing the scalar product of these unit vectors according to the following formula:
$$VACF(t) = (1/N) * \Sigma[Vi(0) \cdot Vi(t)];$$

where VACF(t) represents the autocorrelation function at time t, N is the total number of data points, $V_i(0)$ is the velocity at the initial time, and $V_i(t)$ is the velocity at time t. VACF values were normalized by dividing the obtained averaged VACF values by the VACF value of lag 0 (i.e., the correlation of a value with itself). In simpler terms, for each time lag (the time difference between the two velocities), you multiply the corresponding velocities together and average these products over all possible pairs of time intervals. This gives you the correlation between velocities at different time lags. For the calculations, we used a maximum lag of 100 time points, i.e., one time point was correlated with up to 100-time points before.

- To extract the **VACF persistence time**, the VACF curve was split into two regions – the initial exponential decay and the following linear decay. To automatically identify the splitting point, the first occurring minima was used. The values of the initial decay were log-transformed (natural logarithm) whereas values of the linear decay were not transformed. Subsequently, a linear fit was performed on both regions to extract the slope. Using the following formula, the persistence time of each region and sample was calculated:

$$|\frac{1}{slope} * 0.5|;$$

- For **speed binning** (i.e., grouping a range of values into a discrete, smaller number of "bins") the range between the 2 % and 98 % speed quantile was used to fit 10 equal distanced bin center points. Of note, the quantile values were calculated based on all data points throughout all experiments. Hence, every experimental setup (i.e., control, line-5nM, line-20nM, and point) shared the same bins. The distance between the bin center points was then halved, and the range of each bin was defined as:

$$bin\ range = \ bin\ center\ \pm \frac{bin\ distance}{2};$$

  Subsequently, the median value of each bin was calculated for each experimental setup. This method allowed for equal-sized bins across all existing values and reincluded parts of the excluded quantile range (i.e., 2 % top and low).
- For **directional change binning** (i.e., grouping of values into a discrete, smaller number of "bins") the top 5 % and lowest 5 % directional change values were removed for plotting purposes (*of note, they were not excluded for calculating statistics*). The remaining values were used to fit nine quantile centers (≙ bin center) between the 2 % and 98 % quantiles (i.e., 2 %, 14 %, 26 %, 38 %, 50 %, 62 %, 74 %, 86 %, and 98 % quantiles). Of note, the quantile values and the subsequent bins were calculated based on data points only within each experimental setup (i.e., control, line-5nM, line-20nM, and point). Hence, every bin was unique to each experimental setup. The distance between the bin center points was then halved, and the range of each bin was defined as:

$$bin\ range = \ bin\ center\ \pm \frac{bin\ distance}{2};$$

  Subsequently, the median value of each bin was calculated for each experimental setup. This method allowed fitting an equal number of cells into each bin within each experimental setup and reincluded parts of the excluded quantile range (i.e., 2 % top and low).
- To determine the **turning probability of more than 45 degrees** for high and low-concentration experiencing cells, the following calculations were computed. The 25 % and 75 % quantiles of gradient values at speed minima were computed to define cells that had a “high” gradient experience (> 75 %) or a “low” gradient exposure (< 25 %). Subsequently, we defined that if any of the

directional change values around the corresponding minima (-1 to +1 time points) was larger than 45 degrees, it counted as a turn. For each experimental setup (i.e., control, line-5nM, line-20nM, and point), and each experienced gradient exposure type (low and high) the proportions of cells turning more than 45 degrees around a speed minima were calculated and averaged.

Collagen-biased population speed. The average population migration speed toward the source was determined with a custom-made plugin (by Robert Hauschild, Institute of Science and Technology Austria). In brief, images were background corrected and particle filtering was used to discard objects other than cells. To calculate the y-directed migration speed of the cell population over time, the lateral displacement of each frame was determined, optimizing its overlap with the previous frame. This displacement was then divided by the time interval between the frames. The resulting value represents the rate at which the cell population migrates along the y-axis (vertical direction) over time.

Collagen-biased single cell speed. The travelled distance of a single cell specifically toward the source between two consecutive frames was divided by the framerate to obtain a measure for the biased single cell speed.

Microfluidic tracking. Movies were first stabilized by using the “Correct 3D drift” plugin in FIJI and subsequently, movies were rotated to ensure a straight alignment of the pillars. Tracking was done automatically with Imaris spot detection of the stained nuclei. Briefly, only cells within the microfluidic maze's designated analysis zone were tracked. Cell nuclei were detected using an estimated diameter of 18 µm, and spots needed to have a quality above 60 to be considered. To ensure accurate tracking, spots within a track were allowed to move a maximum distance of 45 µm, with a maximum gap of 1 frame for tracks. Tracks were then filtered based on a minimum displacement requirement of the analysis zone length minus 100 µm. For example, in a device with an analysis zone length of 700 µm, cells needed to travel at least 600 µm to be included in the final analysis. Obtained tracks were exported as .csv files.

*Microfluidic mask generation. S*tabilized and rotated movies (see microfluidic tracking) were loaded into ilastik for pixel classification [150]. Based on the brightfield signal of the movies, ilastik was used to generate probability maps of the microfluidic maze pillars. Obtained probability maps were then loaded into Fiji where they were thresholded and corrected using binary operations as well as manual interventions.

Microfluidic path analysis. In combination with microfluidic masks, tracks were analyzed using a custom Python script. Briefly, using a convolution algorithm, decision areas within the microfluidic mask were automatically established, and zones before and after the analysis area were manually included to define the starting and finishing areas of each maze. Each area could be differentiated into one of two groups: efficiency-related or efficiency-unrelated. In efficiency-unrelated areas, cells could only move left or right, with no impact on efficiency except if a cell moved backward. For the efficiency-related areas, cells could either choose to go on straight, therefore making an inefficient decision or make a turn toward the finishing area. Hence, to follow an optimal path, each cell would need to move toward the finishing area at least every second decision area. The obtained maps of decision areas were overlaid with the respective tracks of cells and the algorithm determined which decision a cell made in each decision area. The algorithm started with the assumption that a cell would make all decisions correctly (i.e., moving toward the finishing line). It then measured how many decision areas it took for the cell to make a substantial move toward the finishing line. If this move required more than two, a penalty was assigned. This approach allowed the algorithm to evaluate the efficiency of each cell. In simple terms, the cell

trajectory determined which decision areas a cell entered overall (e.g., 10). As every second encountered decision area was efficiency unrelated, half of the entered areas counted for the “turning efficiency” (e.g., 5). This efficiency of cells was subsequently measured by computing how many of the entered decision areas it took to make the correct turn toward the finishing area (e.g., 2 out of 5 a cell took the wrong turn, which leads to an efficiency of 60 %).

Microfluidic gradient extraction. A custom-made script was developed (by Christoph Sommer, Institute of Science and Technology Austria) which utilized the generated microfluidic masks (see methods: *microfluidic mask generation)* and single-cell tracks. The mask ensured that proxy extraction avoided pillar areas. Cell trajectories were used to extract the proxy value at every time point and at user-defined distances (usually 12 µm) along the cell trajectory to indicate the values at the front and back of the cell. The script calculated averaged values over a radial area at each location, applying a Gaussian blur ($\sigma = 5$) for smoothing. The obtained values were then processed in R by calculating a linear fit and extracting the slope for each time point. These slopes served as a measure of the gradient around each cell at every time point.

5.9 Statistics and Data Visualization

Statistics were created using R (V 4.1.3), while plots were created with R and Adobe Illustrator.

Data from independent experiments were pooled and appropriate controls were performed for all independent replicates. Replicates were controlled and only included if experimental parameters were identical. Statistics were calculated using the appropriate statistical tests. Before adequate parametric or metric tests were chosen, samples were checked via Q-Q plots for residuals and the normality of data distribution was tested via the Shapiro-Wilk test of normality.

Lower and upper hinges in all boxplots represent the 25^{th} and 75^{th} percentile, respectively. The upper whisker extends from the hinge to the largest value, but no further than 1.5 * IQR while the lower whisker extends from the hinge to the smallest value, but no lower than 1.5 * IQR of the hinge. Data that lie outside the whiskers are plotted as black dots. Black lines within the boxplot represent the median while grey dots represent mean values.

6 References

1. Rimer, J., Cohen, I. R. & Friedman, N. Do all creatures possess an acquired immune system of some sort? *BioEssays* **36**, 273–281 (2014).
2. Cooper, M. D. & Herrin, B. R. How did our complex immune system evolve? *Nat. Rev. Immunol. 2010 101* **10**, 2–3 (2010).
3. Hurst, T. P. & Magiorkinis, G. Editorial: The Past and the Future of Human Immunity Under Viral Evolutionary Pressure. *Front. Immunol.* **10**, 2340 (2019).
4. Murphy, K. & Weaver, C. *Janeway's Immunobiology, 9th Revised edition*. *Immunity* vol. 546 (Garland Science, 2016).
5. Rich, R. R. The human immune response. *Clin. Immunol. Princ. Pract. Fourth Ed.* 3–15 (2013) doi:10.1016/B978-0-7234-3691-1.00025-8.
6. Alberts, B. *et al. Molecular Biology of the Cell 6e*. *Garland Science* vol. 6 (2014).
7. Scapini, P. & Cassatella, M. A. Social networking of human neutrophils within the immune system. *Blood* vol. 124 710–719 (2014).
8. Nathan, C. Neutrophils and immunity: challenges and opportunities. *Nat. Rev. Immunol.* **6**, 173–182 (2006).
9. Mócsai, A. Diverse novel functions of neutrophils in immunity, inflammation, and beyond. *J. Exp. Med.* **210**, 1283–1299 (2013).
10. Yousefi, S. & Simon, H.-U. NETosis - Does It Really Represent Nature's "Suicide Bomber"? *Front. Immunol.* **7**, 328 (2016).
11. Mantovani, A., Cassatella, M. A., Costantini, C. & Jaillon, S. Neutrophils in the activation and regulation of innate and adaptive immunity. *Nat. Rev. Immunol.* **11**, 519–531 (2011).
12. Schwartzberg, L. S. Neutropenia: Etiology and Pathogenesis. *Clin. Cornerstone* **8**, S5–S11 (2006).
13. Newburger, P. E. & Dale, D. C. Evaluation and management of patients with isolated neutropenia. *Semin. Hematol.* **50**, 198–206 (2013).
14. Iking-Konert, C. *et al.* Transdifferentiation of polymorphonuclear neutrophils: acquisition of CD83 and other functional characteristics of dendritic cells. *J. Mol. Med. (Berl).* **79**, 464–474 (2001).
15. Jones, C. N. *et al.* Spontaneous neutrophil migration patterns during sepsis after major burns. *PLoS One* **9**, (2014).
16. Vicente-Manzanares, M. & Horwitz, A. R. Cell migration: An overview. in *Methods in Molecular Biology* vol. 769 1–24 (2011).
17. Luster, A. D., Alon, R. & von Andrian, U. H. Immune cell migration in inflammation: present and future therapeutic targets. *Nat. Immunol.* **6**, 1182–1190 (2005).
18. Masopust, D. & Schenkel, J. M. The integration of T cell migration, differentiation and function. *Nat. Rev. Immunol.* **13**, 309–320 (2013).
19. Martin, T. A., Ye, L., Sanders, A. J., Lane, J. & Jiang, W. G. *Cancer Invasion and Metastasis: Molecular and Cellular Perspective*. *Metastatic Cancer: Clinical and Biological Perspectives* (2013). doi:101607626.
20. Douglas, R. G., Amino, R., Sinnis, P. & Frischknecht, F. Active migration and passive transport of malaria parasites. *Trends Parasitol.* **31**, 357–362 (2015).
21. Ribet, D. & Cossart, P. How bacterial pathogens colonize their hosts and invade deeper tissues. *Microbes Infect.* **17**, 173–183 (2015).
22. Kearns, D. B. A field guide to bacterial swarming motility. *Nat. Rev. Microbiol.* **8**, 634–44 (2010).
23. Wu, J. shun *et al.* Plasticity of cancer cell invasion: Patterns and mechanisms. *Transl. Oncol.* **14**, (2021).

24. Kunwar, P. S., Siekhaus, D. E. & Lehmann, R. In Vivo Migration: A Germ Cell Perspective. *https://doi.org/10.1146/annurev.cellbio.22.010305.103337* **22**, 237–265 (2006).
25. Lämmermann, T. *et al.* Rapid leukocyte migration by integrin-independent flowing and squeezing. *Nature* **453**, 51–55 (2008).
26. Panková, K., Rösel, D., Novotný, M. & Brábek, J. The molecular mechanisms of transition between mesenchymal and amoeboid invasiveness in tumor cells. *Cell. Mol. Life Sci.* **67**, 63–71 (2010).
27. Fortunato, I. C. & Sunyer, R. The Forces behind Directed Cell Migration. *Biophys. 2022, Vol. 2, Pages 548-563* **2**, 548–563 (2022).
28. Iglesias, P. A. & Devreotes, P. N. Navigating through models of chemotaxis. *Current Opinion in Cell Biology* vol. 20 35–40 (2008).
29. Schwarz, J. & Sixt, M. Quantitative Analysis of Dendritic Cell Haptotaxis. in *Methods in Enzymology* vol. 570 567–581 (Academic Press, 2016).
30. Majumdar, R., Sixt, M. & Parent, C. A. New paradigms in the establishment and maintenance of gradients during directed cell migration. *Curr. Opin. Cell Biol.* **30**, 33–40 (2014).
31. Prentice-Mott, H. V *et al.* Biased migration of confined neutrophil-like cells in asymmetric hydraulic environments. *Proc. Natl. Acad. Sci. U. S. A.* **110**, 21006–11 (2013).
32. Becker, E. L. Stimulated neutrophil locomotion. Chemokinesis and chemotaxis. *Arch. Pathol. Lab. Med.* **101**, 509–513 (1977).
33. Wilkinson, P. C. How do leucocytes perceive chemical gradients? *FEMS Microbiol. Immunol.* **2**, 303–311 (1990).
34. Schwarz, J. *et al.* A microfluidic device for measuring cell migration towards substrate-bound and soluble chemokine gradients. *Sci. Rep.* **6**, 36440 (2016).
35. Aizel, K. *et al.* A tuneable microfluidic system for long duration chemotaxis experiments in a 3D collagen matrix. *Lab Chip* (2017) doi:10.1039/C7LC00649G.
36. Cai, D. & Montell, D. J. Diverse and dynamic sources and sinks in gradient formation and directed migration. *Curr. Opin. Cell Biol.* **30**, 91–98 (2014).
37. Aukland, K. & Nicolaysen, G. Interstitial fluid volume: local regulatory mechanisms. *Physiol. Rev.* **61**, 556–643 (1981).
38. Netti, P. A., Berk, D. A., Swartz, M. A., Grodzinsky, A. J. & Jain, R. K. Role of Extracellular Matrix Assembly in Interstitial Transport in Solid Tumors 1. *CANCER Res.* **60**, 2497–2503 (2000).
39. Tweedy, L., Knecht, D. A., Mackay, G. M. & Insall, R. H. Self-Generated Chemoattractant Gradients: Attractant Depletion Extends the Range and Robustness of Chemotaxis. *PLoS Biol.* **14**, (2016).
40. Alanko, J. *et al.* Sinking the way: a dual role for CCR7 in collective leukocyte migration. *bioRxiv* 2022.02.22.481445 (2022) doi:10.1101/2022.02.22.481445.
41. Afonso, P. V. *et al.* LTB4 Is a Signal-Relay Molecule during Neutrophil Chemotaxis. *Dev. Cell* **22**, 1079–1091 (2012).
42. Reichman-Fried, M., Minina, S. & Raz, E. Autonomous modes of behavior in primordial germ cell migration. *Dev. Cell* **6**, 589–596 (2004).
43. Sz. Tamás, B. Vámosi, B. Roux, B. E. 'Inflamapping' with GEM-LTB4: Live visualization of LTB4 gradients with a novel fluorescent biosensor. in *Neutrophil 2022* 30 (2022).
44. Alberts, B. *et al. Molecular Biology of the Cell*. *4th Edition, New York* (2002).
45. Pollard, T. D. Actin and actin-binding proteins. *Cold Spring Harb. Perspect. Biol.* **8**, (2016).

46. Li, H. & Yang, Z. RHO Gtpases and the Actin Cytoskeleton. *Actin A Dyn. Framew. Mult. Plant Cell Funct.* 301–321 (2000) doi:10.1007/978-94-015-9460-8_17.
47. Etienne-Manneville, S. & Hall, A. Rho GTPases in cell biology. *Nature* **420**, 629–635 (2002).
48. Pollard, T. D. & Cooper, J. A. Actin, a central player in cell shape and movement. *Science* **326**, 1208–1212 (2009).
49. Mattila, P. K. & Lappalainen, P. Filopodia: molecular architecture and cellular functions. *Nat. Rev. Mol. Cell Biol. 2008 96* **9**, 446–454 (2008).
50. Bravo-Cordero, J. J., Magalhaes, M. A. O., Eddy, R. J., Hodgson, L. & Condeelis, J. Functions of cofilin in cell locomotion and invasion. *Nat. Rev. Mol. Cell Biol.* **14**, 405–417 (2013).
51. Legate, K. R., Wickström, S. A. & Fässler, R. Genetic and cell biological analysis of integrin outside-in signaling. *Genes Dev.* **23**, 397–418 (2009).
52. Ridley, A. J. *et al.* Cell Migration: Integrating Signals from Front to Back. *Science (80-.).* **302**, 1704–1709 (2003).
53. Bagorda, A. & Parent, C. A. Eukaryotic chemotaxis at a glance. *J. Cell Sci.* **121**, 2621–2624 (2008).
54. Ramaekers, F. C. S. & Bosman, F. T. The cytoskeleton and disease. *J. Pathol.* **204**, 351–354 (2004).
55. Rappel, W. J. & Edelstein-Keshet, L. Mechanisms of cell polarization. *Curr. Opin. Syst. Biol.* **3**, 43–53 (2017).
56. Mastrogiovanni, M., Di Bartolo, V. & Alcover, A. Cell polarity regulators, multifunctional organizers of lymphocyte activation and function. *Biomed. J.* **45**, 299–309 (2022).
57. Iijima, M., Huang, Y. E. & Devreotes, P. Temporal and spatial regulation of chemotaxis. *Dev. Cell* **3**, 469–478 (2002).
58. Hadjitheodorou, A. *et al.* Directional reorientation of migrating neutrophils is limited by suppression of receptor input signaling at the cell rear through myosin II activity. *Nat. Commun.* **12**, (2021).
59. Hanlon, C. D. & Andrew, D. J. Outside-in signaling - A brief review of GPCR signaling with a focus on the Drosophila GPCR family. *J. Cell Sci.* **128**, 3533–3542 (2015).
60. Artemenko, Y., Lampert, T. J. & Devreotes, P. N. Moving towards a paradigm: common mechanisms of chemotactic signaling in Dictyostelium and mammalian leukocytes. *Cell. Mol. Life Sci.* **71**, 3711–3747 (2014).
61. Islam, L. N., Nabi, A. & Nurun, H. M. Endotoxins of enteric pathogens modulate the functions of human neutrophils and lymphocytes. *J. Biochem. Mol. Biol.* **36**, 565–571 (2003).
62. Magalhaes, A. C., Dunn, H. & Ferguson, S. S. G. Regulation of GPCR activity, trafficking and localization by GPCR-interacting proteins. *Br. J. Pharmacol.* **165**, 1717 (2012).
63. Sleno, R. & Hébert, T. E. The Dynamics of GPCR Oligomerization and Their Functional Consequences. *Int. Rev. Cell Mol. Biol.* **338**, 141–171 (2018).
64. Subramanian, B. C., Moissoglu, K. & Parent, C. A. The LTB4-BLT1 axis regulates the polarized trafficking of chemoattractant GPCRs during neutrophil chemotaxis. *J. Cell Sci.* **131**, jcs.217422 (2018).
65. Innocenti, M. New insights into the formation and the function of lamellipodia and ruffles in mesenchymal cell migration. *Cell Adh. Migr.* **12**, 401 (2018).
66. Zhen Tan, R. & Chiam, K.-H. A computational model for how cells choose temporal or spatial sensing during chemotaxis. *PLOS Comput. Biol.* **14**,

e1005966 (2018).
67. Hegemann, B. & Peter, M. Local sampling paints a global picture: Local concentration measurements sense direction in complex chemical gradients. *BioEssays* vol. 39 1600134 (2017).
68. Petrie Aronin, C. E. *et al.* Migrating Myeloid Cells Sense Temporal Dynamics of Chemoattractant Concentrations. *Immunity* **47**, 862-874.e3 (2017).
69. Merlini, L. *et al.* Local Pheromone Release from Dynamic Polarity Sites Underlies Cell-Cell Pairing during Yeast Mating. *Curr. Biol.* **26**, 1117–1125 (2016).
70. Nandan, A., Das, A., Lott, R. & Koseska, A. Cells use molecular working memory to navigate inchanging chemoattractant fields. *Elife* **11**, (2022).
71. van Haastert, P. J. M. Short- and long-term memory of moving amoeboid cells. *PLoS One* **16**, e0246345 (2021).
72. Prentice-Mott, H. V. *et al.* Directional memory arises from long-lived cytoskeletal asymmetries in polarized chemotactic cells. *Proc. Natl. Acad. Sci. U. S. A.* **113**, 1267–1272 (2016).
73. Georgantzoglou, A., Poplimont, H., Walker, H. A., Lämmermann, T. & Sarris, M. A two-step search and run response to gradients shapes leukocyte navigation in vivo. *J. Cell Biol.* **221**, (2022).
74. Endres, R. G. & Wingreen, N. S. Accuracy of direct gradient sensing by cell-surface receptors. *Prog. Biophys. Mol. Biol.* **100**, 33–39 (2009).
75. Devreotes, P. & Janetopoulos, C. Eukaryotic chemotaxis: Distinctions between directional sensing and polarization. *Journal of Biological Chemistry* vol. 278 20445–20448 (2003).
76. Kolaczkowska, E. & Kubes, P. Neutrophil recruitment and function in health and inflammation. *Nat. Rev. Immunol.* **13**, 159–175 (2013).
77. Afonso, P. V *et al.* LTB 4 Is a Signal-Relay Molecule during Neutrophil Chemotaxis. (2012) doi:10.1016/j.devcel.2012.02.003.
78. Eyles, J. L., Roberts, A. W., Metcalf, D. & Wicks, I. P. Granulocyte colony-stimulating factor and neutrophils—forgotten mediators of inflammatory disease. *Nat. Clin. Pract. Rheumatol.* **2**, 500–510 (2006).
79. Ricklin, D., Hajishengallis, G., Yang, K. & Lambris, J. D. Complement: a key system for immune surveillance and homeostasis. *Nat. Immunol.* **11**, 785–97 (2010).
80. Francis, E. A. & Heinrich, V. Quantifying the Sensitivity of Human Immune Cells to Chemoattractant. *Biophys. J.* **112**, 834–837 (2017).
81. Futosi, K., Fodor, S. & Mócsai, A. Neutrophil cell surface receptors and their intracellular signal transduction pathways. *Int. Immunopharmacol.* **17**, 638–650 (2013).
82. DiStasi, M. R. & Ley, K. Opening the flood-gates: how neutrophil-endothelial interactions regulate permeability. *Trends Immunol.* **30**, 547–556 (2009).
83. Langer, H. F. & Chavakis, T. Leukocyte - Endothelial interactions in inflammation. *J. Cell. Mol. Med.* **13**, 1211–1220 (2009).
84. Park, S. A. & Hyun, Y.-M. M. Neutrophil Extravasation Cascade: What Can We Learn from Two-photon Intravital Imaging? *Immune Netw* **16**, 317–321 (2016).
85. Byrne, M. B. *et al.* Oscillatory behavior of neutrophils under opposing chemoattractant gradients supports a winner-take-all mechanism. *PLoS One* **9**, (2014).
86. Zhelev, D. V, Alteraifi, A. M. & Chodniewicz, D. Controlled Pseudopod Extension of Human Neutrophils Stimulated with Different Chemoattractants. *Biophys. J.* **87**, 688–695 (2004).

87. Heit, B. *et al.* PTEN functions to 'prioritize' chemotactic cues and prevent 'distraction' in migrating neutrophils. *Nat. Immunol.* **9**, 743–52 (2008).
88. Heit, B., Liu, L., Colarusso, P., Puri, K. D. & Kubes, P. PI3K accelerates, but is not required for, neutrophil chemotaxis to fMLP. *J. Cell Sci.* **121**, 205–214 (2008).
89. Heit, B., Tavener, S., Raharjo, E. & Kubes, P. An intracellular signaling hierarchy determines direction of migration in opposing chemotactic gradients. *J. Cell Biol.* **159**, 91–102 (2002).
90. Foxman, E. F., Campbell, J. J. & Butcher, E. C. Multistep navigation and the combinatorial control of leukocyte chemotaxis. *J. Cell Biol.* **139**, 1349–1360 (1997).
91. Heinrich, V., Simpson, W. D. & Francis, E. A. Analytical prediction of the spatiotemporal distribution of chemoattractants around their source: Theory and application to complement-mediated chemotaxis. *Front. Immunol.* **8**, (2017).
92. Mankovich, A. R., Lee, C. Y. & Heinrich, V. Differential Effects of Serum Heat Treatment on Chemotaxis and Phagocytosis by Human Neutrophils. *PLoS One* **8**, (2013).
93. Dahl, M. V & Lindroos, W. E. Leukocyte Chemotaxis Under Agarose: Manipulations of Serum and Plasma Before Incorporation Into Agarose Can Influence Cell Movement 1. *J. Immunol. Methods* **29**, 301–310 (1979).
94. Melly, M. A., Thomison, J. B. & Rogers, D. E. Fate of staphylococci within human leukocytes. *J. Exp. Med.* **112**, 1121–30 (1960).
95. Schwarz, J. *et al.* Dendritic Cells Interpret Haptotactic Chemokine Gradients in a Manner Governed by Signal-to-Noise Ratio and Dependent on GRK6. *Curr. Biol.* **27**, 1314–1325 (2017).
96. Southgate, E. L. *et al.* Identification of Formyl Peptides from Listeria monocytogenes and Staphylococcus aureus as Potent Chemoattractants for Mouse Neutrophils. *J. Immunol.* **181**, 1429–1437 (2008).
97. Liu, X. *et al.* Bidirectional regulation of neutrophil migration by mitogen-activated protein kinases. *Nat. Immunol.* **13**, 457–464 (2012).
98. Rincón, E., Rocha-Gregg, B. L. & Collins, S. R. A map of gene expression in neutrophil-like cell lines. *BMC Genomics* **19**, 573 (2018).
99. Yuli, I. & Snyderman, R. Extensive hydrolysis of N-formyl-L-methionyl-L-leucyl-L-[3H] phenylalanine by human polymorphonuclear leukocytes. A potential mechanism for modulation of the chemoattractant signal. *J. Biol. Chem.* **261**, 4902–4908 (1986).
100. Wang, X., Hossain, M., Bogoslowski, A., Kubes, P. & Irimia, D. Left , Right , Left , Right : Chemotaxing Neutrophils Enter Alternative Branches at Capillary Bifurcations Left , Right , Left , Right : Chemotaxing Neutrophils Enter Alternative Branches at Capillary Bifurcations.
101. Afonso, P. V. *et al.* LTB4 Is a Signal-Relay Molecule during Neutrophil Chemotaxis. *Dev. Cell* **22**, 1079–1091 (2012).
102. Levine, H. & Rappel, W.-J. The physics of eukaryotic chemotaxis. *Phys. Today* **66**, 24–30 (2013).
103. Herzmark, P. *et al.* Bound attractant at the leading vs. the trailing edge determines chemotactic prowess. *Proc. Natl. Acad. Sci. U. S. A.* **104**, 13349–13354 (2007).
104. Brown, D. a & Berg, H. C. Temporal stimulation of chemotaxis in Escherichia coli. *Proc. Natl. Acad. Sci. U. S. A.* **71**, 1388–1392 (1974).
105. Krembel, A., Colin, R. & Sourjik, V. Importance of Multiple Methylation Sites in Escherichia coli Chemotaxis. *PLoS One* **10**, (2015).
106. Klamser, P. P. *et al.* Impact of Variable Speed on Collective Movement of Animal

Groups. (2021).
107. Bretschneider, T. *et al.* The Three-Dimensional Dynamics of Actin Waves, a Model of Cytoskeletal Self-Organization. *Biophys. J.* **96**, 2888 (2009).
108. Hons, M. *et al.* Chemokines and integrins independently tune actin flow and substrate friction during intranodal migration of T cells. *Nat. Immunol. 2018 196* **19**, 606–616 (2018).
109. Riedl, M., Merrin, J., Sixt, M. & Hof, B. Synchronization in collectively moving inanimate and living active matter. *bioRxiv* 2022.10.06.511128 (2022) doi:10.1101/2022.10.06.511128.
110. Beta, C., Edelstein-Keshet, L., Gov, N. & Yochelis, A. From actin waves to mechanism and back: How theory aids biological understanding. *Elife* **12**, (2023).
111. Inagaki, N. & Katsuno, H. Actin Waves: Origin of Cell Polarization and Migration? *Trends Cell Biol.* **27**, 515–526 (2017).
112. Weiner, O. D., Marganski, W. A., Wu, L. F., Altschuler, S. J. & Kirschner, M. W. An Actin-Based Wave Generator Organizes Cell Motility. *PLoS Biol.* **5**, 2053–2063 (2007).
113. Berg, H. C. & Purcell, E. M. Physics of chemoreception. *Biophys. J.* **20**, 193–219 (1977).
114. Fischer, T., Hayn, A. & Mierke, C. T. Fast and reliable advanced two-step pore-size analysis of biomimetic 3D extracellular matrix scaffolds. *Sci. Rep.* **9**, (2019).
115. Renkawitz, J. *et al.* Nuclear positioning facilitates amoeboid migration along the path of least resistance. *Nature* 1 (2019) doi:10.1038/s41586-019-1087-5.
116. Skoge, M. *et al.* A worldwide competition to compare the speed and chemotactic accuracy of neutrophil-like cells. *PLoS One* **11**, 1–19 (2016).
117. Shellard, A. & Mayor, R. Rules of collective migration: from the wildebeest to the neural crest. *Philos. Trans. R. Soc. B* **375**, (2020).
118. Debets, V. E., Janssen, L. M. C. & Storm, C. Enhanced persistence and collective migration in cooperatively aligning cell clusters. *Biophys. J.* **120**, 1483 (2021).
119. Wang, X., Hossain, M., Bogoslowski, A., Kubes, P. & Irimia, D. Chemotaxing neutrophils enter alternate branches at capillary bifurcations. *Nat. Commun. 2020 111* **11**, 1–12 (2020).
120. BOYDEN, S. The chemotactic effect of mixtures of antibody and antigen on polymorphonuclear leucocytes. *J. Exp. Med.* **115**, 453–466 (1962).
121. Zigmond, S. H. Ability of polymorphonuclear leukocytes to orient in gradients of chemotactic factors. *J. Cell Biol.* **75**, 606–616 (1977).
122. Wu, H., Huang, B. & Zare, R. N. Generation of complex, static solution gradients in microfluidic channels. *J. Am. Chem. Soc.* **128**, 4194–4195 (2006).
123. Ricoult, S. G., Kennedy, T. E. & Juncker, D. Substrate-bound protein gradients to study haptotaxis. *Front. Bioeng. Biotechnol.* **3**, (2015).
124. Azioune, A., Storch, M., Bornens, M., Théry, M. & Piel, M. Simple and rapid process for single cell micro-patterning. *Lab Chip* **9**, 1640–1642 (2009).
125. Whitesides, G. M., Ostuni, E., Takayama, S., Jiang, X. & Ingber, D. E. Soft lithography in biology and biochemistry. *Annu. Rev. Biomed. Eng.* **3**, 335–373 (2001).
126. Bélisle, J. M., Correia, J. P., Wiseman, P. W., Kennedy, T. E. & Costantino, S. Patterning protein concentration using laser-assisted adsorption by photobleaching, LAPAP. *Lab Chip* **8**, 2164–2167 (2008).
127. Rostovtsev, V. V., Green, L. G., Fokin, V. V. & Sharpless, K. B. A stepwise huisgen cycloaddition process: Copper(I)-catalyzed regioselective ‘ligation’ of

azides and terminal alkynes. *Angew. Chemie - Int. Ed.* **41**, 2596–2599 (2002).
128. Roy, J., Mazzaferri, J., Filep, J. G. & Costantino, S. A haptotaxis assay for neutrophils using optical patterning and a high-content approach. *Sci. Rep.* **7**, 1–13 (2017).
129. Liebermann, D. A. & Hoffman, B. Myeloid progenitors on demand. *Nat. Methods* **3**, 248–9 (2006).
130. Redecke, V. *et al.* Hematopoietic progenitor cell lines with myeloid and lymphoid potential. *Nat. Methods* **10**, 795–803 (2013).
131. Wang, G. G. *et al.* Quantitative production of macrophages or neutrophils ex vivo using conditional Hoxb8. *Nat. Methods* **3**, 287–293 (2006).
132. Cohen, J. T. *et al.* Engraftment, Fate, and Function of HoxB8-Conditional Neutrophil Progenitors in the Unconditioned Murine Host. *Front. Cell Dev. Biol.* **10**, 840894 (2022).
133. Pillay, J. *et al.* In vivo labeling with 2H2O reveals a human neutrophil lifespan of 5.4 days. *Blood* **116**, 625–627 (2010).
134. Faller, S. *et al.* Hydrogen sulfide limits neutrophil transmigration, inflammation, and oxidative burst in lipopolysaccharide-induced acute lung injury. *Sci. Reports 2018 81* **8**, 1–10 (2018).
135. Gran, S. *et al.* Imaging, myeloid precursor immortalization, and genome editing for defining mechanisms of leukocyte recruitment in vivo. *Theranostics* **8**, 2407–2423 (2018).
136. Leithner, A. *et al.* Fast and efficient genetic engineering of hematopoietic precursor cells for the study of dendritic cell migration. *Eur. J. Immunol.* **48**, 1074–1077 (2018).
137. Pillay, J., Tak, T., Kamp, V. M. & Koenderman, L. Immune suppression by neutrophils and granulocytic myeloid-derived suppressor cells: similarities and differences. *Cell. Mol. Life Sci.* **70**, 3813–3827 (2013).
138. Fleming, T., Fleming, M. L. & Malek, T. Selective expression of Ly-6G on myeloid lineage cells in mouse bone marrow. RB6-8C5 mAb to granulocyte-differentiation antigen (Gr-1) detects members of the Ly-6 family. *J. Immunol.* **151**, 2399–2408 (1993).
139. Mackey, J. B. G. *et al.* Maturation, developmental site, and pathology dictate murine neutrophil function. *bioRxiv* 2021.07.21.453108 (2021) doi:10.1101/2021.07.21.453108.
140. Scapini, P. & Cassatella, M. A. Location in the spleen dictates the function of murine neutrophils. *J. Exp. Med.* **214**, 1207–1209 (2017).
141. Kelley, J. L., Rozek, M. M., Suenram, C. A. & Schwartz, C. J. Activation of human blood monocytes by adherence to tissue culture plastic surfaces. *Exp. Mol. Pathol.* **46**, 266–278 (1987).
142. De Sole, P. *et al.* Effect of adherence to plastic on peripheral blood monocyte and alveolar macrophage chemiluminescence. *J. Biolumin. Chemilumin.* **8**, 153–158 (1993).
143. Zehrer, A. *et al.* A Fundamental Role of Myh9 for Neutrophil Migration in Innate Immunity. *J. Immunol.* **201**, 1748–1764 (2018).
144. Chu, J. Y., McCormick, B., Mazelyte, G., Michael, M. & Vermeren, S. HoxB8 neutrophils replicate Fcγ receptor and integrin-induced neutrophil signaling and functions. *J. Leukoc. Biol.* **105**, 93 (2019).
145. Saul, S., Castelbou, C., Fickentscher, C. & Demaurex, N. Signaling and functional competency of neutrophils derived from bone-marrow cells expressing the ER-HOXB8 oncoprotein. *J. Leukoc. Biol.* **106**, 1101–1115 (2019).
146. Lämmermann, T. & Sixt, M. Mechanical modes of 'amoeboid' cell migration.

Curr. Opin. Cell Biol. **21**, 636–644 (2009).
147. Stringer, C., Wang, T., Michaelos, M. & Pachitariu, M. Cellpose: a generalist algorithm for cellular segmentation. *Nat. Methods 2020 181* **18**, 100–106 (2020).
148. Schindelin, J. *et al.* Fiji: an open-source platform for biological-image analysis. *Nat. Methods 2012 97* **9**, 676–682 (2012).
149. Tinevez, J. Y. *et al.* TrackMate: An open and extensible platform for single-particle tracking. *Methods* **115**, 80–90 (2017).
150. Berg, S. *et al.* ilastik: interactive machine learning for (bio)image analysis. *Nat. Methods 2019 1612* **16**, 1226–1232 (2019).

7 Appendix

7.1 Collaboration References

The original publications are reproduced with permission or within the reuse policy of the copyright owners.

7.1.1 Sensing their plasma membrane curvature allows migrating cells to circumvent obstacles

Pre-print in *bioRxiv (2021)*. https://doi.org/10.1101/2021.03.26.437199
Accepted to be published in *Nature Communications (2023)*

bioRxiv preprint doi: https://doi.org/10.1101/2021.03.26.437199; this version posted October 28, 2021. The copyright holder for this preprint (which was not certified by peer review) is the author/funder, who has granted bioRxiv a license to display the preprint in perpetuity. It is made available under aCC-BY-NC-ND 4.0 International license.

Sensing their plasma membrane curvature allows migrating cells to circumvent obstacles

Ewa Sitarska[1,§], Silvia Dias Almeida[1,‡], Marianne Sandvold Beckwith[1], Julian Stopp[2], Yannick Schwab[1], Michael Sixt[2], Anna Kreshuk[1], Anna Erzberger[1,*] and Alba Diz-Muñoz[1,*]

Addresses

[1] Cell Biology and Biophysics Unit, European Molecular Biology Laboratory, 69117 Heidelberg, Germany.

[2] Institute of Science and Technology Austria, 3400 Klosterneuburg, Austria.

[§] Collaboration for joint PhD degree between EMBL and Heidelberg University, Faculty of Biosciences.

[‡] Current address: Division of Medical Image Computing, German Cancer Research Center (DKFZ), 69120 Heidelberg, Germany.

* Correspondence: diz@embl.de and erzberge@embl.de

Abstract

Cell migration is a hallmark out-of-equilibrium process in biology. In addition to persistent self-propelled motion, many cells display remarkable adaptive behaviors when they navigate complex environments within the body. Combining theory and experiments, we identify a curvature-sensing mechanism underlying obstacle avoidance in immune-like cells. The genetic perturbation of this machinery leads to a reduced capacity to evade obstructions combined with faster and more persistent cell migration in obstacle-free environments. We propose that the active polymerization of the actin cytoskeleton at the advancing edge of migrating cells is locally inhibited by the curvature-sensitive BAR protein Snx33 in regions with inward plasma membrane curvature. This coupling between actin and membrane dynamics leads to a mechanochemical instability that generates complex protrusive patterns at the cellular front. Adaptive motility thus arises from two simultaneous curvature-dependent effects, i) the specific reduction of propulsion in regions where external objects deform the plasma membrane and ii) the intrinsic patterning capacity due to the membrane-actin coupling that promotes spontaneous changes in the cell's protrusions. Our results show how cells utilize actin- and plasma membrane biophysics to sense their environment, allowing them to adaptively decide if they should move ahead or turn away. On the basis of our findings, we propose that the natural diversity of BAR proteins may allow cells to tune their curvature sensing machinery to match the shape characteristics in their environment.

bioRxiv preprint doi: https://doi.org/10.1101/2021.03.26.437199; this version posted October 28, 2021. The copyright holder for this preprint (which was not certified by peer review) is the author/funder, who has granted bioRxiv a license to display the preprint in perpetuity. It is made available under aCC-BY-NC-ND 4.0 International license.

Main text:

The self-propelled motion of cells underlies many developmental, physiological, and pathological processes[1-3]. Former investigations revealed the rich physics of persistent cellular propulsion, clarifying for example how the non-equilibrium properties of a polar actin network can generate a steadily advancing leading edge[4-8]. In addition to persistent motion, migrating cells display remarkable adaptive behaviors. Cells within the body efficiently circumvent obstacles[9,10] to navigate complex and dynamic environments[11] but the physical basis of motility adaptation is not well understood. These adaptive behaviors are particularly important for cell types that encounter highly variable environments, such as immune cells and disseminating tumor cells. During migration, the outmost boundary of the cell – the plasma membrane – is deformed by the changing microenvironment. Thus, cells might decode their membrane curvature to decide if they should move ahead or turn away. Many migrating cells indeed express a variety of curvature-sensing proteins, which can directly interact with both the plasma membrane and the subjacent actin cytoskeleton[12]. Here we investigate the role of curvature sensing in adaptive motility.

The family of BAR domain-containing proteins could facilitate membrane curvature sensing. These proteins form crescent shaped membrane-binding dimers that can sense and generate curvature[12-14], and are known to interact with regulators of the actin cytoskeleton through several auxiliary domains[12,15]. We identified candidates from this large protein family by measuring their expression profile in immune-like HL-60 cells before and after terminal differentiation, where they undergo substantial changes in gene expression and initiate rapid migration, resembling what occurs in the bone marrow *in vivo*[16] (**Fig. 1a, b, Supplementary Fig. 1a**). The BAR domain protein Snx33 was 16-fold over-expressed in the curvature-rich state (**Supplementary Fig. 1b**). Based on its structure, Snx33 likely prefers comparatively small, positive (inward) curvatures (**Fig. 1c**, **Supplementary Fig. 2a-d**)[12]. We imaged its subcellular localization by confocal microscopy after fluorescent tagging and found that Snx33 is enriched in distinct membrane ruffles at the leading edge of these cells (**Fig. 1d, e**).

To address the role of curvature sensing in adaptive migration, we generated cells lacking Snx33 (Snx33-/-) using CRISPR/Cas9 genome editing (**Supplementary Fig. 3a, b**), and first assessed cell-scale migratory behavior. We positioned the cells in microfluidic devices[17,18] where they migrated through channels with branching points with multiple differently sized pores. Snx33-/- cells required significantly more time than their wild-type counterparts to navigate these decision-points and find the path of least resistance (**Fig. 1f**, **Supplementary Fig. 4a, b**). However, in decision-free channels with or without a single constriction, Snx33-/- cells migrated faster than their wildtype counterparts (**Fig. 1g**, **Supplementary Fig. 4c**). Next, we quantified unconfined migration on planar substrates. We trained and used machine learning-based algorithms in ilastik[19] to analyze movies of cells imaged by total internal reflection fluorescence microscopy (TIRFM) (**Fig. 1h**, see Methods for details). Similar as in decision-free channels, Snx33-/- cells migrated faster than wildtype cells (**Fig. 1i**). Moreover, while the motility of Snx33-/- cells was more persistent, wild-type cells were more prone to perform large spontaneous turns (**Fig. 1j**). Thus, the loss of Snx33 appears to render cells less effective in navigating a branching point, while more persistent in a decision-free environment, suggesting they have improved propulsion but lack the ability to adapt when faced with an inert obstacle.

Propulsion in immune-like cells depends on the active polymerization of actin at the leading edge of the cell[20,21]. Given that cell shape reflects changes in actin-rich protrusions[22], we performed a quantitative and unbiased comparison of selected cell morphometric parameters, i.e., cell spreading, cell eccentricity and leading edge characteristics during decision-free migration on a planar substrate. As immune cells radically change their morphology in short periods of time, we averaged time-lapse movies to capture their dynamics. Snx33-/- cells spread to a larger extent, showed a more elongated morphology and bigger leading edge (**Fig. 2a-f, Supplementary Fig. 5a-e**); migration phenotypes that

bioRxiv preprint doi: https://doi.org/10.1101/2021.03.26.437199; this version posted October 28, 2021. The copyright holder for this preprint (which was not certified by peer review) is the author/funder, who has granted bioRxiv a license to display the preprint in perpetuity. It is made available under aCC-BY-NC-ND 4.0 International license.

were independent of cell adhesion to the substrate (**Supplementary Fig. 5f-h**). Moreover, we measured the static tether pulling force of the plasma membrane with atomic force microscopy, and observed an increase from 61.58 pN for wildtype to 75.25 pN in Snx33-/- cells (which corresponds with an increase in membrane tension from 177.87 to 265.62 uN/m; see Methods for details; **Supplementary Fig. 6a, b**). Expressing fluorescently-tagged Snx33 reversed these changes in the morphology and mechanics of the leading edge thereby proving the specificity of the observed phenotypes (**Supplementary Fig. 5b, c and Supplementary Fig. 6b, c and d**). Notably, these phenotypes were not a consequence of defective differentiation, as the neutrophil differentiation marker CD11b was unperturbed in Snx33-/- cells (**Supplementary Fig. 6e**). Altogether, the observation that Snx33-/- cells have larger actin protrusions and higher membrane tension during decision-free migration indicates that deficient curvature sensing triggers an increase in actin polymerization at the leading edge even in the absence of obstacles.

These findings suggest that Snx33 mediates an intrinsic coupling between actin organization and membrane curvature. Such feedback effects have been proposed to trigger mechanochemical instabilities[23,24] indicative of an intrinsic patterning capacity. Motile cells often feature wave-like patterns of actin activity and plasma membrane ruffles at their leading edge[20,21,25] as observed by scanning electron microscopy (SEM) and polarized total internal reflection fluorescence microscopy (p-TIRFM), (**Fig. 2g, h and Supplementary Fig. 7a, b**). To link the dynamic membrane-actin patterns to the putative curvature-sensing function of Snx33, we analyzed the mechanochemical instability arising from a corresponding coupling between actin-dependent force generation and membrane curvature with a minimal set of equations and parameters (**Fig. 2i-k and Supplementary Note**). We considered a Helfrich membrane with a bending rigidity κ and surface tension γ [26,27] subject to an active pressure field due to actin polymerization. For the simplified case of a 1D pattern on a periodic domain x, we obtain the following equation for the membrane curvature C

$$\left(\lambda^2 \frac{\partial^2}{\partial x^2} - 1\right) C = -\frac{f_A}{\gamma} A, \qquad 1$$

in which $\lambda = \sqrt{\kappa/\gamma}$ is the membrane persistence length, A is the concentration field of a generic activator of actin polymerization, and f_A is the force per activator molecule. The activator concentration is taken to evolve according to a reaction-diffusion equation, in which we consider self-activation of A [20] on a timescale τ_A and a curvature-dependent regulatory term $r_C(C)$

$$\tau_A \frac{\partial}{\partial t} A = A + r_C(C) + \lambda_A^2 \frac{\partial^2}{\partial x^2} A, \qquad 2$$

in which $\lambda_A = \sqrt{\tau_A D}$ is a reaction-diffusion length scale with diffusion coefficient D. For regulation in the regime of small curvatures, the second reaction term can be truncated beyond linear order and written as $r_C(C) = \xi \gamma / f_A \, C$ with a dimensionless coupling constant ξ. Linear stability analysis of Eqs. 1-2 then yields the dispersion relation for the growth rate $\omega(k)$ of the perturbation mode with wavenumber k

$$\omega(k) = \frac{1}{\tau_A}\left(1 - k^2\lambda_A^2 + \frac{\xi}{1 + k^2\lambda^2}\right). \qquad 3$$

The parameter region in which spontaneous patterning occurs (where $\omega_{Max} > 0$ with $k_{Max} > 0$) is shown in **Fig. 2j.** Spontaneous patterns emerge in this system only when there is a *negative* coupling between curvature and actin activity, such that actin polymerization decreases in regions of inward (positive) plasma membrane curvature (**Fig. 2g, h and i**), distinct from previously considered scenarios with curved activators[28-30]. Thus, we find that the local down-regulation of actin polymerization in regions with positive membrane curvature can generate mechanochemical patterns at the leading edge of migrating cells (**Fig. 2g, h and Supplementary Fig. 7a, b**).

bioRxiv preprint doi: https://doi.org/10.1101/2021.03.26.437199; this version posted October 28, 2021. The copyright holder for this preprint (which was not certified by peer review) is the author/funder, who has granted bioRxiv a license to display the preprint in perpetuity. It is made available under aCC-BY-NC-ND 4.0 International license.

This theoretical result agrees with the likely binding preference of Snx33 to membrane regions with small positive curvatures (**Supplementary Fig. 2a-d**) and is compatible with the observation that actin polymerization appears increased in Snx33-/- cells **(Fig. 2d, e, Supplementary Fig. 5c, Supplementary Fig. 6b).** But how does Snx33 inhibit actin polymerization? Several BAR domain proteins, including Snx33, directly bind and regulate the activity of actin nucleator promoting factors from the WASP family[12,31]. WAVE2 is the main member of this family in neutrophils and earned its name because it localizes in a wave pattern during cell migration[20]. What regulates WAVE2 binding to the membrane, and whether and how that determines ruffle topography remains poorly understood[32]. Our analysis of the mechanochemical feedback between membrane curvature and an actin activator such as WAVE2 (Eqs. 1-2) suggests that the dominant wavelength of the pattern should increase in response to a decrease in the magnitude of the curvature coupling coefficient ξ (**Fig. 3a**). To test this prediction, we imaged WAVE2 patterns in Snx33-/- and wild-type cells during migration by TIRFM (**Fig. 3b-d**). Snx33-/- cells showed an increase in both the length and the width of WAVE2 patches (**Fig. 3e, Supplementary Fig. 7c, d**). A mechanochemical curvature coupling would furthermore imply that the change in WAVE2 patch morphology should accompany a longer wavelength of the curved ruffles on the plasma membrane (**Fig. 3a**). To test this, we quantified the effective ruffle wavelength from SEM images and indeed observed a significantly less tight arrangement of ruffles for Snx33-/- cells when compared with their wild-type counterparts (**Fig. 3f, g, Supplementary Fig. 7e, f**). Notably, to date, only very drastic WAVE2 patch phenotypes have been reported (complete abrogation or increase in number), which lead to a severely disrupted morphology and capacity to migrate[33,34]. The milder perturbation introduced by the genetic disruption of curvature sensing by Snx33 allowed the identification of the key molecular circuit that couples the active mechanics of the actin network with the biophysics of the membrane to generate complex patterns at the leading edge of migrating cells.

This intrinsic patterning capacity can facilitate adaptive motility by reducing persistence and promoting the random evasive maneuvers we observed (**Fig 1j**). But the particular form of Snx33-mediated membrane-actin coupling suggests an additional more direct effect, in which propulsion is reduced specifically where the presence of an obstacle in the path of the cell is likely, i.e. where external indentations generate an increased fraction of regions with positive curvature. To gain further insights into the object-avoidance response of Snx33-deficient cells, we devised a reductionistic assay to investigate how cells steer away from a cellular obstacle, a common phenomenon to many cell types also known as contact inhibition of locomotion (CIL)[20,35]. We seeded a higher density of cells and imaged their 2D migration in the presence of cell-cell interactions by TIRFM. Snx33-/- cells collided more often and formed larger cell-cell contacts compared to wild-type cells (**Fig. 4a, b)**. To gain molecular insight into the role of Snx33 in CIL, we simultaneously live-imaged the WAVE2 complex and Snx33 at the leading edge of freely moving cells. While both proteins largely colocalized in most of the cell, they were anticorrelated in the highly negatively (outward) curved leading edge (**Supplementary Fig. 8a, b**). Here, Snx33 levels decreased while WAVE2 accumulated (**Supplementary Fig. 8c, d**), consistent with Snx33 binding positive curvature and restricting WAVE2 to negatively curved areas. Moreover, when cells collided, Snx33 localized to the cell contact area that is largely devoid of outward curvature, where subsequently WAVE2 disappeared and relocated to contact free zones of the plasma membrane. This resulted in cell repolarization by formation of a new leading edge (**Fig. 4c, d**)**.** To assess whether the dysfunctional CIL response in Snx33-/- cells is indeed due to impaired WAVE2 inhibition at the contact area, we followed WAVE2 localization before and after collision in Snx33-/- cells. In contrast to wildtype cells, Snx33-/- cells indeed failed to remove WAVE2 from the contact site (**Fig. 4e, Supplementary Fig. 8e**)**.** Altogether, we show a key role for membrane topography and the curvature sensing protein Snx33 in regulating actin polymerization during CIL. Specifically, Snx33 restricts WAVE to negatively curved areas and thus leads to cell repolarization towards a contact free zone upon collision with an obstacle.

bioRxiv preprint doi: https://doi.org/10.1101/2021.03.26.437199; this version posted October 28, 2021. The copyright holder for this preprint (which was not certified by peer review) is the author/funder, who has granted bioRxiv a license to display the preprint in perpetuity. It is made available under aCC-BY-NC-ND 4.0 International license.

Object avoidance is key not only for the migration of immune and cancer cells in complex tissue environments, but also fundamental during embryogenesis and collective migration *in vivo*[36]. Combining theory, genetic perturbations, microscopy and microfluidics we identified a local mechanochemical circuit underlying adaptive motility in immune-like cells. We show that by coupling plasma membrane curvature with WAVE2-driven actin polymerization, the curvature sensing protein Snx33 facilitates adaptive motility in two distinct and complementary ways. On the one hand, the mechanochemical feedback between actin and curvature results in an intrinsic patterning capacity which destabilizes the leading edge and reduces migration persistence. The ability to spontaneously reorient and explore the microenvironment with dynamic protrusions in and of itself contributes to more efficient navigation in crowded contexts[17,33,37-40]. On the other hand, while a diverse range of feedback mechanisms can conceivably lead to shape instabilities[41-44], Snx33 implements the coupling between membrane curvature and actin activity in a way that is uniquely suited to aid obstacle avoidance. Locally reducing propulsion in regions of inward curvature specifically steers the cell away from the direction in which the presence of an obstacle on the outside is most likely. Thus, Snx33 and WAVE2 form a non-genetic adaptive circuit that decodes the cell's local membrane topography and induces a response to decide if it should move ahead or turn away.

The machinery we identified morphologically solves the object avoidance problem by exploiting the physics of the materials it is made of, specifically the biophysics of the plasma membrane and the active properties of the subjacent actin network. Given these findings and the diversity of BAR domain proteins present in cells, it is conceivable that on long timescales, cells tune their expression levels to match the curvature statistics of their microenvironment, implying that a cell's curvature-sensing machinery may itself constitute a structural prediction of its surroundings.

bioRxiv preprint doi: https://doi.org/10.1101/2021.03.26.437199; this version posted October 28, 2021. The copyright holder for this preprint (which was not certified by peer review) is the author/funder, who has granted bioRxiv a license to display the preprint in perpetuity. It is made available under aCC-BY-NC-ND 4.0 International license.

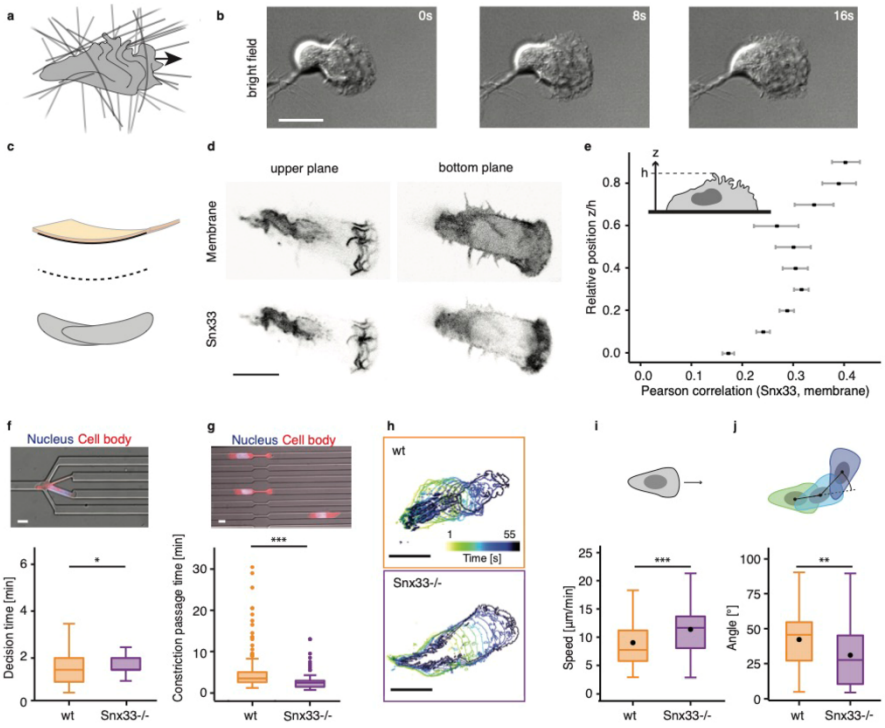


Figure 1: The curvature-sensing protein Snx33 is enriched in membrane waves and its loss impacts adaptive motility. a) The leading edge of migrating cells is characterized by intricate curvature patterns. Arrow indicates the direction of cell movement. **b)** Time-lapse bright-field imaging shows migrating immune-like differentiated HL-60 cells. **c)** The schematic illustrates the predicted binding preference for inward (positive) membrane curvature of Snx33, a BAR protein with one of the highest fold change during migration. **d)** Fluorescently-tagged Snx33 and membrane marker in upper and lower z-planes in a cell. **e)** Pearson correlation coefficient of fluorescently-tagged Snx33 and membrane marker at different heights acquired by confocal microscopy. n=10. Error bars denote standard error of the mean. **f)** Decision channel passage time (n=159 for wt, n=91 for Snx33-/-) in cells. **g)** Constriction passage time (n=234 for wt, n=158 for Snx33-/-) in cells. **h)** Cell body displacement over time in wt and Snx33-/- cells. **i)** Cell speed in wt and Snx33-/- cells and **j)** distribution of angles at which cells turn during migration. n=82 (wt), n=78 (Snx33-/-). Data from 3 independent biological replicates. Statistics: t-test or non-parametric Mann-Whitney-U-test. Scale bars = 10 µm. $p<0.001$ (***), $p<0.01$ (**), $p<0.05$ (*).

bioRxiv preprint doi: https://doi.org/10.1101/2021.03.26.437199; this version posted October 28, 2021. The copyright holder for this preprint (which was not certified by peer review) is the author/funder, who has granted bioRxiv a license to display the preprint in perpetuity. It is made available under aCC-BY-NC-ND 4.0 International license.

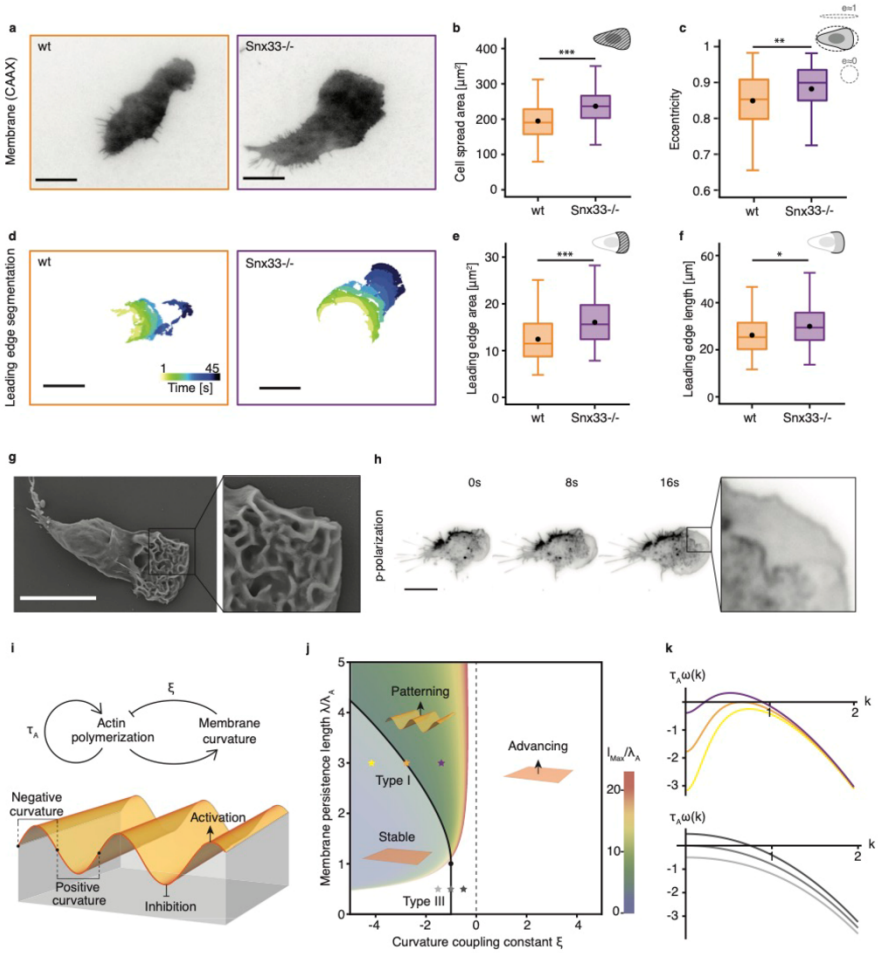


Figure 2: Genetic perturbation of Snx33-dependent curvature sensing alters cell and leading-edge morphology and may impact actin organization. a) TIRFM images of a wildtype and a Snx33-/- cell. **b)** Cell spread area and **c)** eccentricity differ between wildtype and Snx33-/- cells during movement. **d)** Leading-edge segmentation of a wildtype and a Snx33-/- cell. **e)** Leading-edge area and **f)** length differ between wildtype and Snx33-/- cells. n=82 (wt), n=78 (Snx33-/-). **g)** Scanning electron microscopy (SEM) image of a wildtype cell with zoom-in at the leading-edge. **h)** Time-lapse p-polarization of p-TIRFM imaging reveals dynamic membrane waves at the leading-edge. **i,j)** Negative coupling between membrane curvature and actin activity leads to spontaneous patterning. The transition from decaying to growing patterns corresponds to a type-I instability at the critical curvature coupling constant $\xi_1^* = -\left(\left(\lambda_A^2 + \lambda^2\right)/(2\lambda_\Lambda\lambda)\right)^2$ for membrane persistence lengths $\lambda > \lambda_\Lambda$. Color scale denotes the wavelength with the highest growth rate l_{Max}. **k**) Dispersion relations near the critical coupling constants for $\lambda > \lambda_A$ (type-I) and $\lambda < \lambda_A$ (type-III) at the positions marked in **j**). Statistics: t-test or non-parametric Mann-Whitney-U-test. Scale bars = 10 µm. p<0.001 (***), p<0.01 (**), p<0.05 (*).

bioRxiv preprint doi: https://doi.org/10.1101/2021.03.26.437199; this version posted October 28, 2021. The copyright holder for this preprint (which was not certified by peer review) is the author/funder, who has granted bioRxiv a license to display the preprint in perpetuity. It is made available under aCC-BY-NC-ND 4.0 International license.

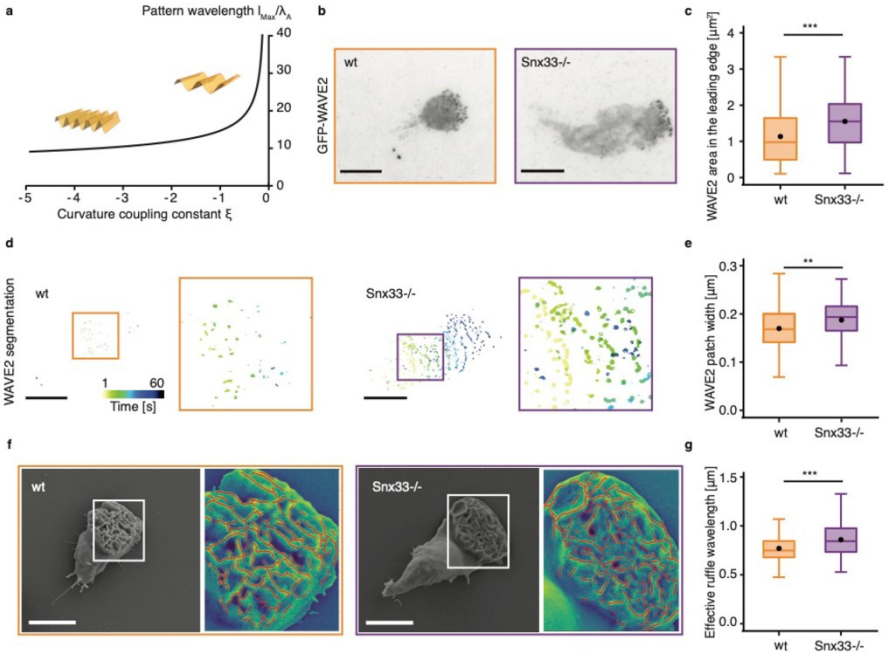


Figure 3: Disruption of curvature sensing alters actin activator patterns and membrane ruffles. a) Our theoretical calculation predicts that the dominant wavelength l_{Max} of the mechanochemical pattern should increase as the magnitude of the curvature coupling ξ decreases (here shown for $\lambda/\lambda_A = 4$). **b)** TIRFM images of a wildtype and Snx33-/- cell show the distribution of the actin activator WAVE2. **c)** The total area occupied by WAVE2 patches in the leading edge increases upon perturbation of Snx33. **d)** Segmentation of dynamic WAVE2 patches in a wildtype and Snx33-/- cell. **e)** The width of WAVE2 patches increases upon perturbation of Snx33. n=82 (wt), n=78 (Snx33-/-). **f)** SEM images with ruffle segmentations (red) show the leading edges of a wildtype and Snx33-/- cells from the 50th percentile of the distribution shown in panel g). **g)** The effective ruffle wavelength increases upon perturbation of Snx33. n=175 (wt), n=170 (Snx33-/-). Statistics: t-test or nonparametric Mann-Whitney-U-test. Scale bars = 10 µm. p<0.001 (***), p<0.01 (**), p<0.05 (*).

bioRxiv preprint doi: https://doi.org/10.1101/2021.03.26.437199; this version posted October 28, 2021. The copyright holder for this preprint (which was not certified by peer review) is the author/funder, who has granted bioRxiv a license to display the preprint in perpetuity. It is made available under aCC-BY-NC-ND 4.0 International license.

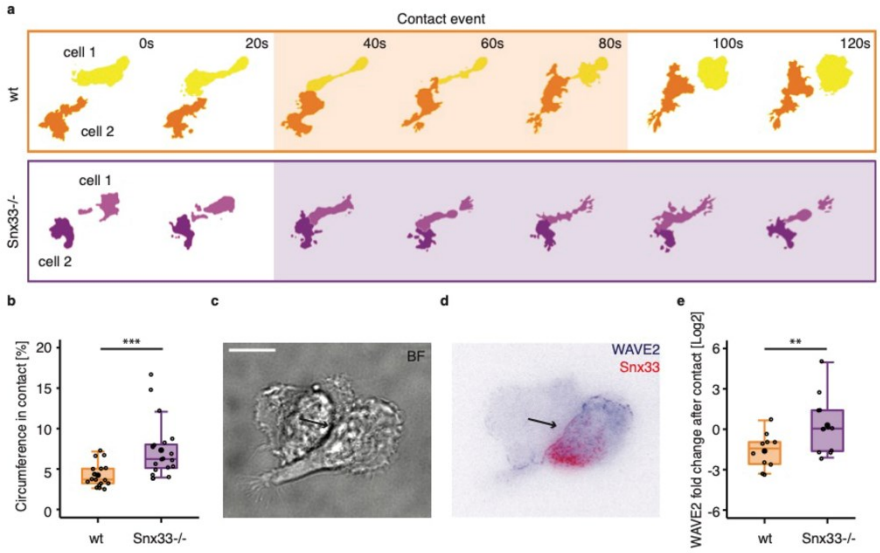
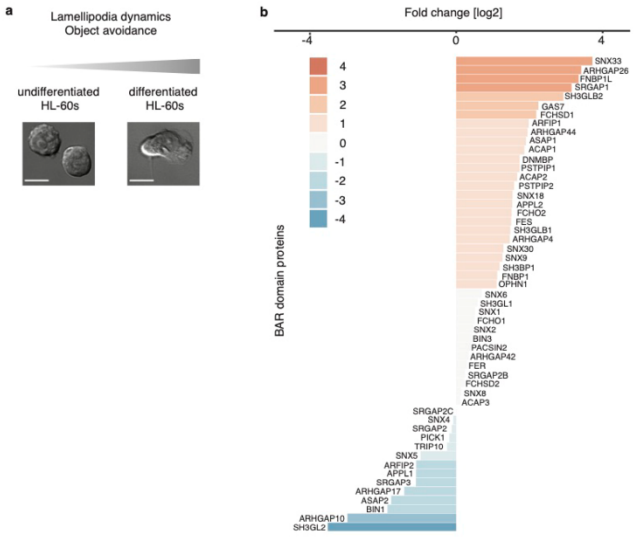
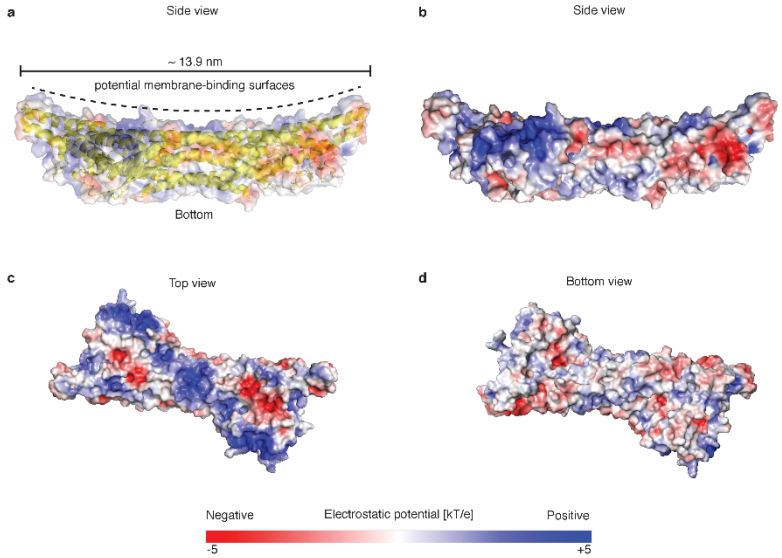


Figure 4: Snx33 regulates contact avoidance by locally inhibiting the WAVE2 complex. a) Segmentation of a contact event between two wildtype (upper panel) and two Snx33-/- (lower panel) cells. Shaded area highlights the duration of contact. **b)** Percentage of cell circumference in contact with another cell in wildtype (n=18) and Snx33-/- (n=20) cells. **c)** Bright-field and **d)** TIRFM imaging of a cell-cell contact in wildtype cells with fluorescently-tagged Snx33 and a component of WAVE2. Arrow is pointing towards cell-cell contact. **e)** WAVE2 fold change after cell-cell contact in wildtype (n=9) and Snx33-/- (n=10) cells. Statistics: t-test or non-parametric Mann-Whitney-U-test. Scale bars = 10 µm. p<0.001 (***), p<0.01 (**), p<0.05 (*).

bioRxiv preprint doi: https://doi.org/10.1101/2021.03.26.437199; this version posted October 28, 2021. The copyright holder for this preprint (which was not certified by peer review) is the author/funder, who has granted bioRxiv a license to display the preprint in perpetuity. It is made available under aCC-BY-NC-ND 4.0 International license.

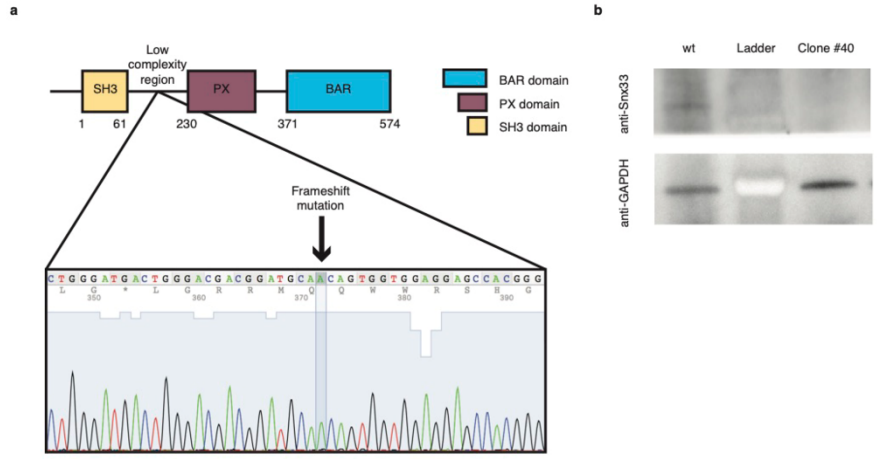


Supplementary Figure 1: HL60 differentiation in vitro and fold change in expression of BAR domain proteins. a) Schematic illustrating changes in HL-60 cells during its differentiation. **b)** Over-expressed (orange) and under-expressed (blue) BAR domain genes between undifferentiated (non-migratory) and differentiated (migratory) HL-60 cells. Scale bars = 10 µm.

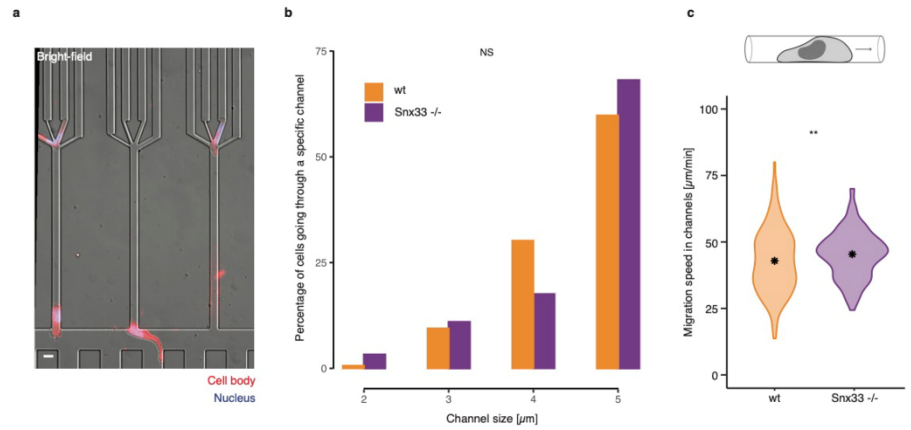


Supplementary Figure 2: Structure of Snx33 membrane binding unit (PX-BAR) strongly suggests binding to inward (positive) membrane curvature. a) Structure of PX-BAR domains of Snx33 (4AKV) together with electrostatic surface representation (side view). Dotted line indicates the potential membrane-binding surfaces, while solid line shows overall dimensions of the dimer. **b-d)** Electrostatic surface representation of 4AKV side view **(b)**, top view **(c)** and bottom view **(d)**. Visualizations were created in PyMOL (The PyMOL Molecular Graphics System, Version 2.4.2 Schrödinger, LLC).

bioRxiv preprint doi: https://doi.org/10.1101/2021.03.26.437199; this version posted October 28, 2021. The copyright holder for this preprint (which was not certified by peer review) is the author/funder, who has granted bioRxiv a license to display the preprint in perpetuity. It is made available under aCC-BY-NC-ND 4.0 International license.

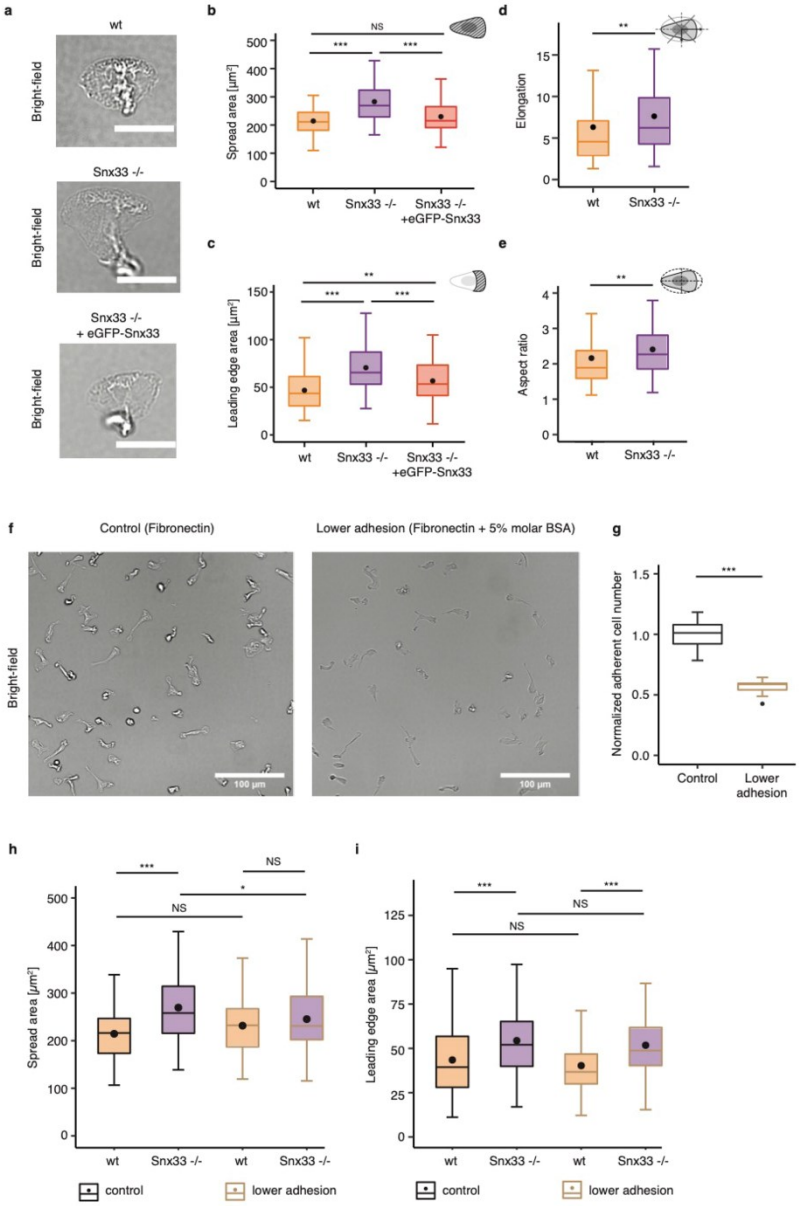


Supplementary Figure 3: Snx33 knockout cell line validation. a) Snx33 clone sequencing confirming a frameshift mutation. **b)** Snx33 and GAPDH Western blots of wt cells and Snx33-/- clone.



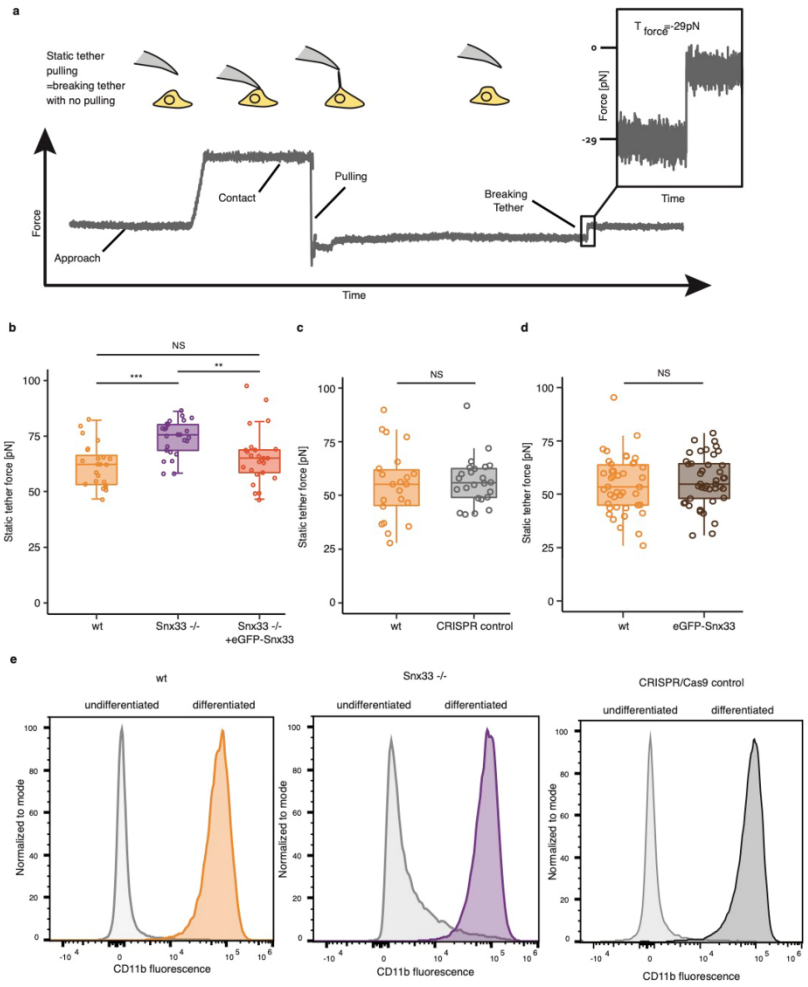
Supplementary Figure 4: Snx33 knockout cells are faster and choose the path of the least resistance. a) Overlay of bright-field, nuclei and cell body images of cells migrating in PDMS-based devices with a decision point. **b)** Frequency of wt and Snx33-/- cells choosing a channel of a certain size (n = 159 for wt, n = 91 for Snx33-/-). **c)** Migration speed in straight channels (n=235 for wt, n=169 for Snx33-/-). Data from 3 independent biological replicates. Scale bar = 10 μm. p<0.001 (***), p<0.01 (**), p<0.05 (*).

bioRxiv preprint doi: https://doi.org/10.1101/2021.03.26.437199; this version posted October 28, 2021. The copyright holder for this preprint (which was not certified by peer review) is the author/funder, who has granted bioRxiv a license to display the preprint in perpetuity. It is made available under aCC-BY-NC-ND 4.0 International license.



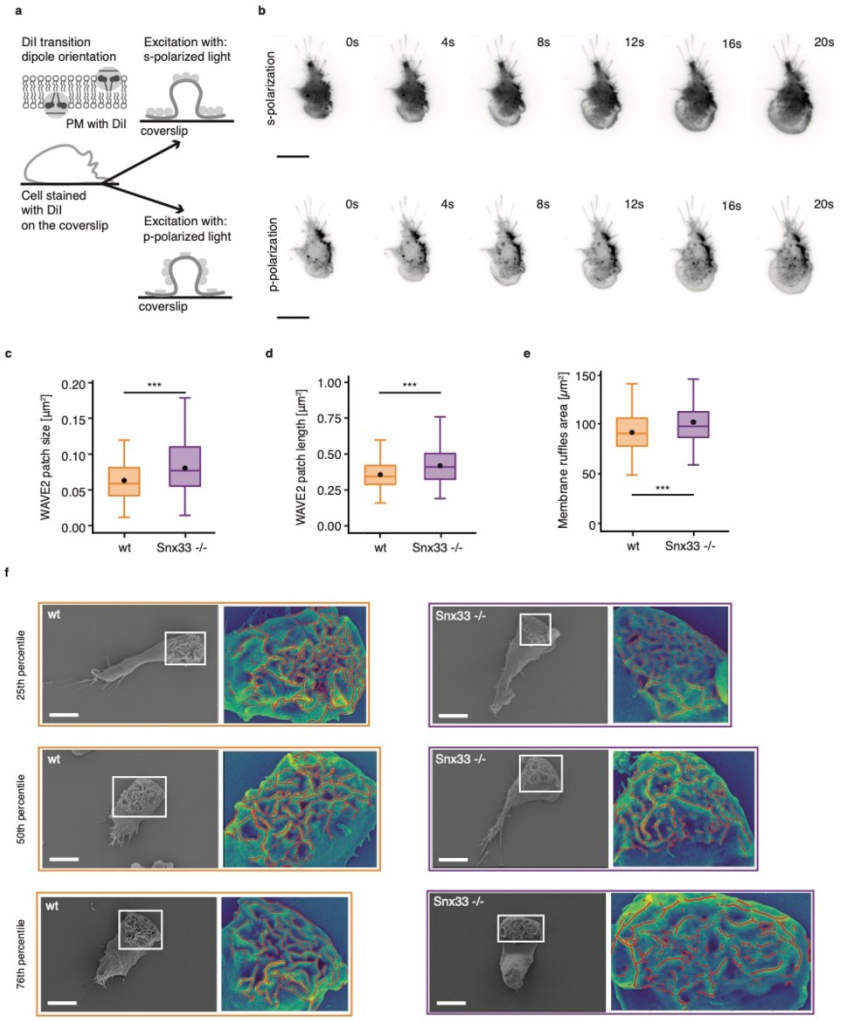
Supplementary Figure 5: Cell and leading-edge morphology in Snx33 knockout and wt cells. a) Example images of bright-field of wild type, Snx33-/- and Snx33-/- with eGFP-tagged Snx33 cells. Quantification of **b)** cell spread and **c)** leading edge area. Data from 3 independent experiments. n= 67 (wt), n=73 (Snx33-/-), n=67 (Snx33-/- +GFP-Snx33) **d)** Quantification of cell elongation and **e)** aspect ratio from TIRFM images. n=82 (wt), n=78 (Snx33-/-). **f)** Example bright-field images of wt cells on control (fibronectin only) and lower adhesion substrate (fibronectin with 5% molar BSA). **g)** Adhesion-dependent cell number quantification. Data from two independent experiments. Quantification of **h)** cell and **i)** leading edge area. n = 82 (wt), n = 102 (Snx33-/-); Lower adhesion: n= 53 (wt), n = 72 (Snx33-/-). Statistics: t-test and Mann-Whitney-U- Test. Scale bars = 10 µm. p<0.001 (***), p<0.01 (**), p<0.05 (*).

bioRxiv preprint doi: https://doi.org/10.1101/2021.03.26.437199; this version posted October 28, 2021. The copyright holder for this preprint (which was not certified by peer review) is the author/funder, who has granted bioRxiv a license to display the preprint in perpetuity. It is made available under aCC-BY-NC-ND 4.0 International license.



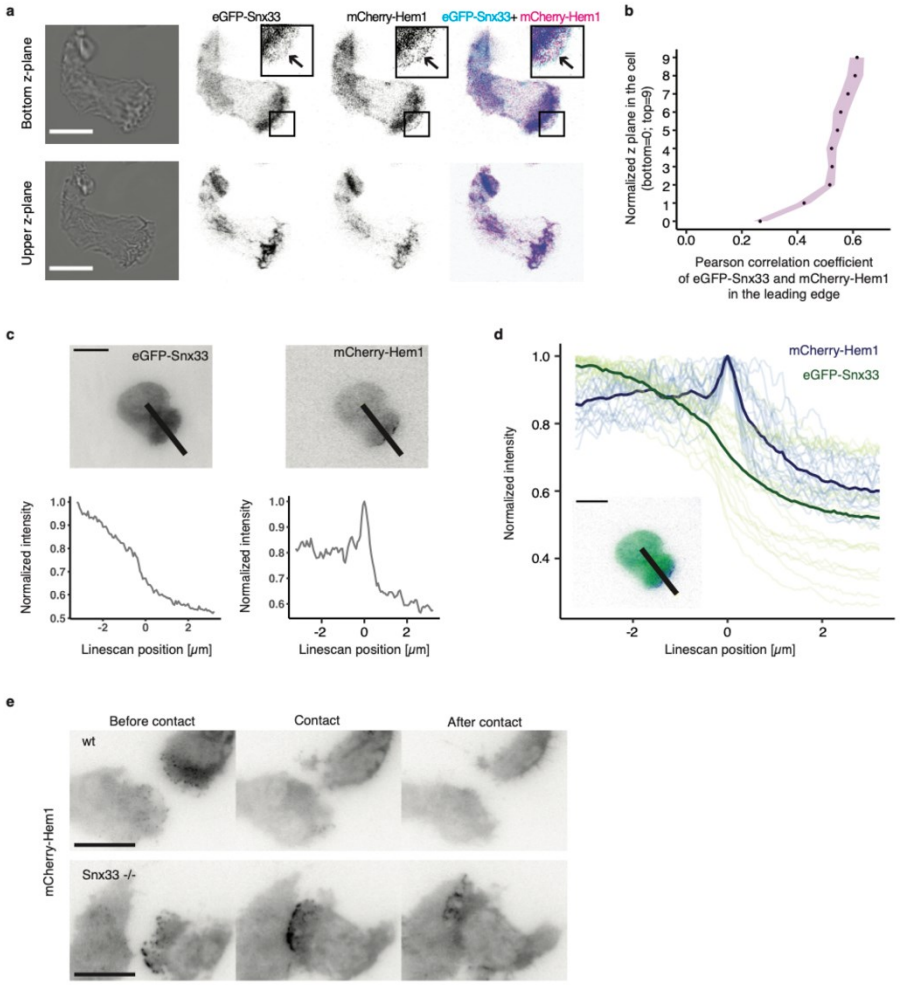
Supplementary Figure 6: Snx33 knockout increases apparent membrane tension. a) Schematic of static tether pulling experiments. **b)** Mean static tether force of wt (n = 24), Snx33-/- (n = 26) and Snx33-/- with overexpressed eGFP-Snx33 (n = 25) from 3 independent experiments. **c)** Mean static tether force of wt (n = 27) and CRISPR control (n = 28) cells from 4 independent experiments. **d)** Mean static tether force of wt (n = 42) and eGFP-Snx33 over-expressed (n = 42) cells from 6 independent experiments. Overexpression of Snx33-GFP on the wt background did not decrease the tether force, suggesting that a gain of function is not sufficient to alter the leading edge or its effects on membrane mechanics. **e)** Representative histograms of CD11b intensity of wild-type, Snx33-/- and CRISPR/Cas9 control of HL-60 cells before and after 5 days of differentiation. Statistics: t-test and Mann-Whitney-U-test. p<0.001 (***), p<0.01 (**), p<0.05 (*).

bioRxiv preprint doi: https://doi.org/10.1101/2021.03.26.437199; this version posted October 28, 2021. The copyright holder for this preprint (which was not certified by peer review) is the author/funder, who has granted bioRxiv a license to display the preprint in perpetuity. It is made available under aCC-BY-NC-ND 4.0 International license.



Supplementary Figure 7: Membrane topography imaged by pTIRFM. WAVE2 pattern size and ruffle wavelength increases in Snx33-/- cells. a) Schematic illustrating the principles of pTIRFM imaging using carbocyanine dyes *(DiI)*. **b)** Time lapse pTIRFM imaging of a cell using s-polarization (upper panel) and p-polarization (lower panel). Quantification of **c)** WAVE2 patch size and **d)** length in wt and Snx33-/- cells imaged by TIRFM. n=82 (wt), n=78 (Snx33-/-). **e)** Quantification of membrane ruffles area in wt and Snx33-/- cells imaged by SEM. n=175 (wt), n=170 (Snx33-/-). **f)** SEM images (25th, 50th and 76th percentile) with zoom-in of the overlay of the leading-edge and ruffle segmentation (red) for wt and Snx33-/- cells. Statistics: t-test or nonparametric Mann-Whitney-U-test. Scale bars = 10 µm. p<0.001 (***), p<0.01 (**), p<0.05 (*).

bioRxiv preprint doi: https://doi.org/10.1101/2021.03.26.437199; this version posted October 28, 2021. The copyright holder for this preprint (which was not certified by peer review) is the author/funder, who has granted bioRxiv a license to display the preprint in perpetuity. It is made available under aCC-BY-NC-ND 4.0 International license.



Supplementary Figure 8: Snx33 is excluded from the protruding edge. a) Bright-field and confocal images of a cell, Snx33 and WAVE2 in the bottom and upper z-planes. Arrows indicate the most protruding edge at the cell bottom. **b)** Pearson correlation of Snx33 and WAVE2 in normalized z-planes in the leading edge. n=10. Purple regions denote standard error of the mean. **c)** Exemplary images of fluorescently-tagged Snx33 and WAVE2 and line scans through the leading edge in cells using TIRFM. **d)** Snx33 and WAVE2 normalized intensity at the protrusion edge. **e)** TIRFM images of WAVE2 signal before, during and after the contact event in wt and Snx33-/- cells. Scale bar= 10 μm.

bioRxiv preprint doi: https://doi.org/10.1101/2021.03.26.437199; this version posted October 28, 2021. The copyright holder for this preprint (which was not certified by peer review) is the author/funder, who has granted bioRxiv a license to display the preprint in perpetuity. It is made available under aCC-BY-NC-ND 4.0 International license.

Acknowledgements

We thank Jan Ellenberg for critical feedback on the manuscript, Nir Gov and Ulrich Schwarz for fruitful discussions, and the Life Science Editors for editing assistance. The plasmid with hSnx33 was a kind gift from Duanqing Pei. We thank Brian Graziano for providing protocols, reagents and key advice to generate CRISPR knockout HL-60 cells. We thank Jakub Czuchnowski for advice on image analysis. We thank the EMBL flow cytometry core facility, the EMBL advanced light microscopy facility and the EMBL genomics core facility for support and advice. We thank the EMBL genome biology computational support (and specially Charles Girardot and Jelle Scholtalbers) for critical assistance during RNAseq analysis. We acknowledge the financial support of the European Molecular Biology Laboratory (EMBL) to A.D-M., Y.S. and A.E., the EMBL Interdisciplinary Postdocs (EIPOD) fellowship under Marie Sklodowska-Curie Actions COFUND to M.S.B., the BEST program funding by FCT (SFRH/BEST/150300/2019) to S.D.A. and the Joachim Herz Stiftung Add-on Fellowship for Interdisciplinary Science to E.S.

Author Contributions

A.D.M., and E.S conceived the project and designed the experiments. E.S., M.B. and J.S., performed the experiments with EM advice from Y.S and microfluidic support from M.S.. E.S. and S.D.A. analyzed the data with support from A.E. and A.K.. A.E. performed the theoretical analysis. A.D.M., E.S and A.E wrote the manuscript. All authors contributed to the interpretation of the data, read and approved the final manuscript.

References

1. Friedl, P. & Alexander, S. Cancer Invasion and the Microenvironment: Plasticity and Reciprocity. *Cell* **147,** 992–1009 (2011).
2. Reig, G., Pulgar, E. & Concha, M. L. Cell migration: from tissue culture to embryos. *Development* **141,** 1999–2013 (2014).
3. Svitkina, T. The Actin Cytoskeleton and Actin-Based Motility. *Cold Spring Harb Perspect Biol* **10,** a018267–21 (2018).
4. Theriot, J. A. & Mitchison, T. J. Actin microfilament dynamics in locomoting cells. *Nature* **352,** 126–131 (1991).
5. Mogilner, A. & Oster, G. Cell motility driven by actin polymerization. *Biophysical Journal* **71,** 3030–3045 (1996).
6. Juelicher, F., Kruse, K., Prost, J., reports, J. J. P.2007. Active behavior of the cytoskeleton. *Elsevier* doi:10.1016/j.physrep.2007.02.018
7. Keren, K. *et al.* Mechanism of shape determination in motile cells. *Nature* **453,** 475–480 (2008).
8. Hawkins, R. J. *et al.* Pushing off the walls: a mechanism of cell motility in confinement. *Phys. Rev. Lett.* **102,** 058103 (2009).
9. Stoitzner, P., Stössel, H., Romani, N. & Pfaller, K. A Close-Up View of Migrating Langerhans Cells in the Skin. *Journal of Investigative Dermatology* **118,** 117–125 (2002).
10. Weigelin, B., Bakker, G.-J. & Friedl, P. Intravital third harmonic generation microscopy of collective melanoma cell invasion: Principles of interface guidance and microvesicle dynamics. *Intravital* **1,** 32–43 (2012).
11. Sarris, M. & Sixt, M. Navigating in tissue mazes: chemoattractant interpretation in complex environments. *Current Opinion in Cell Biology* **36,** 93–102 (2015).
12. Carman, P. J. & Dominguez, R. BAR domain proteins-a linkage between cellular membranes, signaling pathways, and the actin cytoskeleton. *Biophys Rev* **10,** 1587–1604 (2018).
13. McMahon, H. T. & Gallop, J. L. Membrane curvature and mechanisms of dynamic cell membrane remodelling. *Nature* **438,** 590–596 (2005).
14. Simunovic, M., Voth, G. A., Callan-Jones, A. & Bassereau, P. When Physics Takes Over: BAR Proteins and Membrane Curvature. *Trends in Cell Biology* **25,** 780–792 (2015).
15. de Kreuk, B.-J. & Hordijk, P. L. Control of Rho GTPase function by BAR-domains. *Small GTPases* **3,** 45–52 (2014).
16. Hoogendijk, A. J. *et al.* Dynamic Transcriptome-Proteome Correlation Networks Reveal Human Myeloid Differentiation and Neutrophil-Specific Programming. *Cell Reports* **29,** 2505–2519.e4 (2019).
17. Renkawitz, J. X. R. *et al.* Nuclear positioning facilitates amoeboid migration along the path of least resistance. *Nature* 1–29 (2019). doi:10.1038/s41586-019-1087-5
18. Yamada, K. M. & Sixt, M. Mechanisms of 3D cell migration. *Nat Rev Mol Cell Biol* 1–15 (2019). doi:10.1038/s41580-019-0172-9
19. Berg, S. *et al.* ilastik: interactive machine learning for (bio)image analysis. *Nat Meth* **16,** 1226–1232 (2019).

bioRxiv preprint doi: https://doi.org/10.1101/2021.03.26.437199; this version posted October 28, 2021. The copyright holder for this preprint (which was not certified by peer review) is the author/funder, who has granted bioRxiv a license to display the preprint in perpetuity. It is made available under aCC-BY-NC-ND 4.0 International license.

20. Weiner, O. D., Marganski, W. A., Wu, L. F., Altschuler, S. J. & Kirschner, M. W. An actin-based wave generator organizes cell motility. *PLoS Biol* **5,** e221 (2007).
21. Graziano, B. R. *et al.* A module for Rac temporal signal integration revealed with optogenetics. *J Cell Biol* **216,** 2515–2531 (2017).
22. Lacayo, C. I. *et al.* Emergence of large-scale cell morphology and movement from local actin filament growth dynamics. *PLoS Biol* **5,** e233 (2007).
23. Ramaswamy, S., Toner, J. & Prost, J. Nonequilibrium fluctuations, traveling waves, and instabilities in active membranes. *Phys. Rev. Lett.* **84,** 3494–3497 (2000).
24. Gov, N. S. Guided by curvature: shaping cells by coupling curved membrane proteins and cytoskeletal forces. *Philos Trans R Soc Lond B Biol Sci* **373,** (2018).
25. Fritz-Laylin, L. K. *et al.* Actin-based protrusions of migrating neutrophils are intrinsically lamellar and facilitate direction changes. *Elife* **6,** 437 (2017).
26. Helfrich, W. Elastic properties of lipid bilayers: theory and possible experiments. *Z Naturforsch C* **28,** 693–703 (1973).
27. Deserno, M. Fluid lipid membranes: from differential geometry to curvature stresses. *Chem Phys Lipids* **185,** 11–45 (2015).
28. Gov, N. S. & Gopinathan, A. Dynamics of Membranes Driven by Actin Polymerization. *Biophysical Journal* **90,** 454–469 (2006).
29. Peleg, B., Disanza, A., Scita, G. & Gov, N. Propagating cell-membrane waves driven by curved activators of actin polymerization. *PLoS ONE* **6,** e18635 (2011).
30. Sadhu, R. K. & Gov, N. S. Modelling cellular spreading and emergence of motility in the presence of curved membrane proteins and active cytoskeleton forces. *arXiv.org* **physics.bio-ph,** 2021.01.02.425086 (2021).
31. Zhang, J., Zhang, X., Guo, Y., Xu, L. & Pei, D. Sorting nexin 33 induces mammalian cell micronucleated phenotype and actin polymerization by interacting with Wiskott-Aldrich syndrome protein. *Journal of Biological Chemistry* **284,** 21659–21669 (2009).
32. Inagaki1, N. & Katsuno, H. Actin Waves: Origin of Cell Polarization and Migration? *Trends in Cell Biology* **27,** 515–526 (2017).
33. Diz-Muñoz, A. *et al.* Membrane Tension Acts Through PLD2 and mTORC2 to Limit Actin Network Assembly During Neutrophil Migration. *PLoS Biol* **14,** e1002474–30 (2016).
34. Graziano, B. R. *et al.* Cell confinement reveals a branched-actin independent circuit for neutrophil polarity. *PLoS Biol* **17,** e3000457 (2019).
35. Roycroft, A. & Mayor, R. Molecular basis of contact inhibition of locomotion. *Cellular and Molecular Life Sciences* **73,** 1119–1130 (2015).
36. Stramer, B. & Mayor, R. Mechanisms and in vivo functions of contact inhibition of locomotion. *Nat Rev Mol Cell Biol* **18,** 43–55 (2016).
37. Driscoll, M. K. *et al.* Cell shape dynamics: from waves to migration. *PLoS Comput Biol* **8,** e1002392 (2012).
38. Leithner, A. *et al.* Diversified actin protrusions promote environmental exploration but are dispensable for locomotion of leukocytes. *Nature Cell Biology* **18,** 1253–1259 (2016).
39. Stankevicins, L. *et al.* Deterministic actin waves as generators of cell polarization cues. *Proceedings of the National Academy of Sciences* **117,** 826–835 (2020).
40. Begemann, I. *et al.* Mechanochemical self-organization determines search pattern in migratory cells. *Nat Phys* 1–13 (2020). doi:10.1038/s41567-019-0505-9
41. Kumar, P. B. S. & Rao, M. Shape Instabilities in the Dynamics of a Two-Component Fluid Membrane. *Phys. Rev. Lett.* **80,** 2489 (1998).
42. Sens, P. Dynamics of nonequilibrium membrane bud formation. *Phys. Rev. Lett.* **93,** 108103 (2004).
43. Mietke, A., Jülicher, F. & Sbalzarini, I. F. Self-organized shape dynamics of active surfaces. *Proc. Natl. Acad. Sci. U.S.A.* **116,** 29–34 (2019).
44. Ruske, L. J. & Yeomans, J. M. Morphology of Active Deformable 3D Droplets. *Physical Review X* **11,** 021001 (2021).

bioRxiv preprint doi: https://doi.org/10.1101/2021.03.26.437199; this version posted October 28, 2021. The copyright holder for this preprint (which was not certified by peer review) is the author/funder, who has granted bioRxiv a license to display the preprint in perpetuity. It is made available under aCC-BY-NC-ND 4.0 International license.

Methods

Cell culture

HL-60 cells were grown in RPMI 1640 media with 10% heat-inactivated FBS (#10500-064, Gibco) and 1% Penicillin-Streptomycin (#15140-122, Gibco) in a humidified incubator at 37°C with 5% CO_2. Cells were differentiated by adding 1.5% DMSO (#D2438, Sigma Aldrich) and used after 5 days. Each independently-differentiated batch was treated as a biological replicate. For starvation, cells were kept for 1 hour in FBS-free RPMI 1640 media with 0.3% fatty acid free BSA (#A7030-10G, Sigma Aldrich). For imaging or fixation, differentiated HL-60 (dHL-60) cells were plated on fibronectin-coated (0.01mg/ml, #356008, Corning) glass-bottom dishes (#627860, Greiner bio-one) and allowed to adhere for 10 minutes in growth media. Next, cells were washed and stimulated with 10 nM fMLP (#F3506-5MG, Sigma Aldrich). For lowering adhesion, the coating was supplemented with 5% molar BSA (#A7030-10G, Sigma Aldrich). To generate stable cell lines with GFP-Snx33, mCherry-Hem1 (component of the WAVE2 complex, referred to as WAVE2) and mCherry-CAAX lentiviral transduction was used as described previously[33]. Cells were sorted on a BD FACS Aria™ at EMBL Flow Cytometry Core Facility.

Generation of knockout cell line by CRISPR/Cas9

CRISPR/Cas9 generation in HL-60 cells was performed as described previously[34]. Cloning of the target guide sequence to target *Snx33* was performed as previously described[45,46] (Forward: *CACCGctgggacgacGGATGCACAG*; Reverse: *aaacCTGTGCATCCgtcgtcccagC*). Cells expressing BFP-tagged Cas9 were single-cell sorted in 96-well plate on BD FACS Aria™ Fusion at EMBL Flow Cytometry Core Facility. Single-cell clones were verified by genomic DNA amplification by Touchdown PCR[47] and sequencing, followed by Western blot of selected clonal lines.

Western blot

For immunodetection of Snx33 and GAPDH, $6x10^6$-$1.2x10^7$ HL-60 cells were lysed in RIPA Lysis and Extraction buffer (#89900, Thermo ScientificTM) according to manufacturer's instruction with supplementation of the protease inhibitors (#4693159001, Roche). Samples were denatured with 4xLaemmli buffer (#161- 0747, BioRad) containing 10% β-mercaptoethanol (#m6250, Sigma Aldrich) at 95° for 5 min. After SDS-PAGE and transfer, PVDF membrane with transferred proteins was blocked in 5% BSA in TBST and incubated over-night with 1:1000 dilution of anti-Snx33 (#orb331346, Biorbyt) or 1:80 000 dilution of anti-GAPDH (#NB300-221, Novus Biologicals). The blot was developed with secondary antibodies at 1:10 000 dilution of Donkey-Anti-Rabbit-HRP (711-035-152, Jackson Immuno Research) or Goat-Anti-Mouse-HRP (115-035-062, Jackson ImmunoResearch).

CD11b staining of HL-60 cells

After starvation, $1x10^5$ of undifferentiated and differentiated HL-60 cells were stained with Anti-Hu CD11b Alexa Fluor® 488 antibody solution (#A4-681-T100, Exbio). Fluorescence was measured on a Cytek® Aurora (Cytek) at the EMBL Flow Cytometry Core Facility and further analyzed and plotted using FlowJo.

RNA sequencing

Total RNA samples obtained from 3 biological replicates were purified using RNeasy Mini Kit (#74104, Qiagen) according the manufacturer instructions with a DNase digestion step (#79254, Qiagen). To ensure high quality, samples were analyzed on an Agilent 2100 Bioanalyzer (Agilent Technologies). RNA sequencing was performed on an Illumina NextSeq 500 platform as NextSeqHigh-75 SE at the EMBL genomics core facility. For sequence alignment the hg19 reference genome was used. Differential expression analysis was performed with a custom-made Galaxy pipeline using a DESeq2 package.

Imaging

TIRFM images of live cells were acquired on a Nikon Ti Eclipse inverted microscope with a TIRF objective CFI Plan Apo Lambda 100x Oil (#MRD01905, Nikon) and sCMOS camera controlled by NIS-Elements (Nikon). Sample drift was reduced using an autofocus system (Perfect Focus, Nikon) for time lapse imaging.

Confocal images of fixed cells were obtained with a silicone objective UPLSAPO 60X S (NA 1.3; WD 0.3 mm) on an Olympus FV3000 inverted microscope at EMBL advanced light microscopy facility.

bioRxiv preprint doi: https://doi.org/10.1101/2021.03.26.437199; this version posted October 28, 2021. The copyright holder for this preprint (which was not certified by peer review) is the author/funder, who has granted bioRxiv a license to display the preprint in perpetuity. It is made available under aCC-BY-NC-ND 4.0 International license.

Epifluorescent and bright-field imaging of fixed cells was performed using a 40x objective (#MRD00405, Nikon), the SOLA SE II and 100W halogen lamps (Nikon) using appropriate filter sets.

Polarized TIRFM (pTIRFM) modality was implemented based on previous work[48-53]. For imaging, dHL-60 cells were stained before plating with carbocyanine dye DiI (#D3911, ThermoFisher Scientific).

Fixation and F-actin staining

Migrating dHL-60 cells were fixed by adding fixation buffer (2x) to growth media (1:1 v/v) and incubated at 4°C for 1 hour. Fixation buffer (1x) contains 3.7% paraformaldehyde (#28908, Thermo Scientific), 1x intracellular buffer (140 mM KCL, 1 mM $MgCl_2$, 2 mM EGTA, 20 mM HEPES, pH 7.5), 320 mM sucrose (#S0389-500G, Sigma Aldrich) and 0.2% BSA (#A7030-10G, Sigma Aldrich). Cells were washed and stored in dPBS. For permeabilization and staining, cells were re-suspended in intracellular buffer (1x) containing 0.2% of Triton X-100 (#T8787, Sigma Aldrich). If applicable, phalloidin coupled with TRITC (#P1951, Sigma Aldrich) was added at this step. After washing with dPBS, cells were stored at 4°C in the dark or used immediately for imaging.

Theoretical calculations

Calculations for Fig. 2j and Fig. 3a were performed in Wolfram Mathematica v12.1.1.0. For the details of the derivations please see the **Supplementary Note**.

Cell migration assays in PDMS-based devices

PDMS-based microfluidic devices were prepared as previously described[17,54,55]. The devices used for migration of dHL-60 cells had heights of 2.8 µm and 3.13 µm for channels with decision point and channels with constriction, respectively. The decision channels had constrictions of 2, 3, 4 and 5 µm in two arrangements. The channels with single constrictions were 2 µm. To visualize nuclei and cell body, Hoechst 33342 (#62249, Thermo Fisher Scientific) and TAMRA (Invitrogen) were added before the introduction of cells into the PDMS device. Cell migration towards chemoattractant (fMLP) was imaged on an inverted wide-field Nikon Eclipse microscope using 20x/0.5 PH1 air objective, equipped with a Lumencor light source (390 nm, 475 nm, 542/575 nm), an incubation chamber and the heated stage with CO_2. The acquired data were analyzed using ImageJ software and manually curated. Only single cells that moved through the entire channel were considered for analysis. All the parameters were quantified based on the nuclei signal.

Tether extrusion using atomic force spectroscopy

Apparent membrane tension was measured by extruding plasma membrane tethers. For measurements, Olympus BioLevers (k = 60 pN/nm) from Bruker were mounted on a CellHesion 200 AFM (Bruker), which is integrated into an Eclipse Ti inverted light microscope (Nikon). Cantilevers were calibrated using the thermal noise method and coated with 2.5 mg/ml Concanavalin A (#C5275, Sigma Aldrich). Prior to the measurements, cantilevers were rinsed in dPBS. For tether measurement, the cantilever was position over the cell, preferably over the leading edge. Measurements parameters for static tether pulling experiments were as followed: approach velocity was set to 1 µm/s, contact force to 100–300 pN, contact time to 5–10 s, and retraction speed to 10 µm/s. After a 10 µm tether was pulled, the cantilever position was held constant until it broke, but no longer than 30 s. In every experimental repetition the conditions' order was randomized. For every cell at least 3 different tether measurements were taken.

The data analysis was performed using the JPK Data Processing Software. For assessing the magnitude of membrane tension based on tether force measurements, the following formula was used[33]:

$$T = \frac{F_0^2}{8B\pi^2}$$

where F_0 is the tether force measured by the AFM and B is the bending rigidity of the plasma membrane, which we assume to be invariable between different experimental conditions (2.7×10^{-19} Nm based on previous measurements[56,57]).

bioRxiv preprint doi: https://doi.org/10.1101/2021.03.26.437199; this version posted October 28, 2021. The copyright holder for this preprint (which was not certified by peer review) is the author/funder, who has granted bioRxiv a license to display the preprint in perpetuity. It is made available under aCC-BY-NC-ND 4.0 International license.

Image analysis

For confocal images, only the z-planes that contained the top 80% intensity of mCherry-CAAX (membrane marker) were considered based on line scans covering the entire resliced maximum intensity z projection. A channel of interest (ChoF1) was used for mask generation based on automatic Otsu segmentation. A custom-made ImageJ script allowed to calculate the Pearson correlation coefficient (PCC) for every z-plane of ChoF1 with ChoF2 based on the mask of ChoF1 using the in-built Coloc2 ImageJ plugin. Z-slices were assigned to 10 bins and the mean with standard error of the mean for every bin was calculated.

For epifluorescence images, single cells were manually selected using the ImageJ software. To segment the cell body, the contrast of bright-field images was enhanced using the equalize histogram function followed by a canny edge detection, a semi-manual closing of the obtained edges and filling the holes. To segment the leading edge, a similar strategy was used with semi-manual selection of the region with the enriched edges after the canny edge detection with higher values step. Based on the segmentation, a custom Python script was used for measurements. Eccentricity was calculated by ellipse fitting and further division of ellipse foci distance by major axis length.

For analysis of migrating cells imaged by TIRFM, a segmentation of the cell mask (based on mCherry-CAAX signal) and of the WAVE2 mask (based on eGFP-Hem1 signal) were acquired using the machine learning-based ilastik software[19]. Further image analysis was achieved using an in-house built program implemented in Python. The angle at which cells are moving was calculated based on the center of mass for 3 consecutive frames. The leading edge was defined as the difference between two consecutive frames where at least one pixel of WAVE2 mask is present per cluster. Leading edge length was defined as a number of pixels in the outside perimeter of the leading edge. For the analysis of cell-cell contacts the same segmentation strategy was used to segment individual cells. Cell-cell contact was defined as the perimeters' intersection of both cells.

For membrane topography analysis of SEM data, the leading edge area with ruffles was manually segmented on median filtered images. Next, ridges were detected within the segmented regions using the Meijering filter[58]. Ridges were later segmented using automatic Otsu thresholding and skeletonized using a custom Python script. Inversion of the number of pixels within the skeletonization per leading edge area corresponds to the effective the ruffle wavelength.

For analysis of signal enrichment at the cell edge based on TIRFM images, data on fluorescent intensity along the line of equal width and length were extracted from both channels of interest (eGFP-Snx33, mCherry-Hem1) using ImageJ. Data were aligned according to the highest fluorescence intensity of mCherry-Hem1 and normalized. Normalized mean intensity was calculated in both channels of interest for every point along the line scan and plotted using R.

Scanning electron microscopy

After 30 min of 10 nM fMLP stimulation, cells were fixed in 2,5% GA (#16220, EMS) in 0,1M PHEM buffer by adding 37°C double strength fixative (5% GA in 0,1M PHEM) directly 1:1 to the cell medium. After 10 minutes incubation, the fixative was replaced by fresh single strength fixative and cells were further fixed at room temperature for 1h. After fixation, cells were washed 2 times in 0,1M PHEM and 2 times in 0,1M cacodylate buffer. Next, they were postfixed for 2h on ice in freshly prepared and filtered 1% OsO_4 (#19190, EMS) and 0,8% potassium ferrocyanide ($K_4[Fe(CN)_6]*3H_2O$, #4984, Merck) in 0,1M cacodylate buffer. After postfixation, the cells were washed 4 times in H_2O, and left at 4°C until further processing.

Next, cells were treated with freshly prepared and filtered 1% tannic acid (TA, CAS#1401-55-4, EMS) in water using a Pelco BioWave microwave for seven 1-minute cycles alternating between 150 W and 0 W power. Steady temperature was set to 23°C and vacuum to on for all steps. After TA treatment, cells were washed 2x in H_2O on the bench and 2x in H_2O in the microwave for 40 s per step at 250 W power. Cells were then treated with 1% UA (#77870, Serva) in H_2O using the same microwave program as for TA. After washing once in H_2O and twice in 25% EtOH, cells were dehydrated in a graded series of ethanol (25% - 50% - 75% - 90% - 100% - 100%) using a microwave program with step length of 40 s and 250 W power, with a steady temperature at 4°C and without vacuum. Finally, the cells were infiltrated with a graded series of Hexamethyldisilizane (HMDS, CAS# 999-97-3, Sigma Aldrich) in ethanol (25% - 50% - 75% - 100% - 100%) using a microwave program with 6 steps of 1 minute each, with a power of 150 W for step 1, 3, 4 and 6, and 0 W for steps 2 and 5. After the final 100% HMDS infiltration, all HMDS was removed, and coverslips were left to dry overnight. Silica gel with moisture indicator (Merck) was added in 4 empty wells (corners) in the 24-well plate to remove excess humidity.

bioRxiv preprint doi: https://doi.org/10.1101/2021.03.26.437199; this version posted October 28, 2021. The copyright holder for this preprint (which was not certified by peer review) is the author/funder, who has granted bioRxiv a license to display the preprint in perpetuity. It is made available under aCC-BY-NC-ND 4.0 International license.

After drying, coverslips were mounted in aluminum stubs (Agar Scientific G301F) using carbon tape, and sputter coated with a layer of gold for 180 s at 30 mA current using a Quorum sputter coater model Q150RS.

Imaging was performed on a Zeiss Crossbean 540 microscope, using 5 kV acceleration voltage and 700 pA current for the electron beam, with a working distance of 5 mm. A secondary electron detector (SESI) was used for signal detection, and all images were acquired with a pixel size of 28,9 nm/pixel.

Statistical analysis

Statistical analyses were performed using R, while data visualization by both R and Adobe Illustrator®. Normality of data distribution was tested by Shapiro-Wilk test. Two-tailed t-test was used for normal distribution. Otherwise, a non-parametric Mann-Whitney-U-test was used, if not indicated differently. In all box-plots, the lower and upper hinges correspond to the first and third quartiles (the 25th and 75th percentiles). The upper whisker extends from the hinge to the largest value, but no further than 1.5*IQR (distance between the first and third quartiles). The lower whisker extends from the hinge to the smallest value, but no lower than 1.5*IQR of the hinge. Data beyond the end of the whiskers are plotted as black dots. Black line and dot correspond to the median and mean, respectively.

45. Shalem, O. *et al.* Genome-scale CRISPR-Cas9 knockout screening in human cells. *Science* **343,** 84–87 (2014).
46. Sanjana, N. E., Shalem, O. & Zhang, F. Improved vectors and genome-wide libraries for CRISPR screening. *Nat Meth* 1–2 (2014). doi:10.1038/nmeth.3047
47. Koch, B. *et al.* Generation and validation of homozygous fluorescent knock-in cells using CRISPR–Cas9 genome editing. *Nature Publishing Group* **13,** 1465–1487 (2018).
48. Axelrod, D. Evanescent Excitation and Emission in Fluorescence Microscopy. *Biophysical Journal* **104,** 1401–1409 (2013).
49. Anantharam, A., Onoa, B., Edwards, R. H., Holz, R. W. & Axelrod, D. Localized topological changes of the plasma membrane upon exocytosis visualized by polarized TIRFM. *J Cell Biol* **188,** 415–428 (2010).
50. Oreopoulos, J., Epand, R. F., Epand, R. M. & Yip, C. M. Peptide-Induced Domain Formation in Supported Lipid Bilayers: Direct Evidence by Combined Atomic Force and Polarized Total Internal Reflection Fluorescence Microscopy. *Biophysical Journal* **98,** 815–823 (2010).
51. Oreopoulos, J. & Yip, C. M. Combined scanning probe and total internal reflection fluorescence microscopy. *Methods* **46,** 2–10 (2008).
52. Sund, S. E., Swanson, J. A. & Axelrod, D. Cell membrane orientation visualized by polarized total internal reflection fluorescence. *Biophysical Journal* **77,** 2266–2283 (1999).
53. Axelrod, D. *Chapter 7 - Total Internal Reflection Fluorescence Microscopy. Biophysical Tools for Biologists, Volume Two: In Vivo Techniques* **89,** 169–221 (Elsevier Inc., 2008).
54. Renkawitz, J., Reversat, A., Leithner, A., Merrin, J. & Sixt, M. *Micro-engineered 'pillar forests' to study cell migration in complex but controlled 3D environments. Biophysical Tools for Biologists, Volume Two: In Vivo Techniques* **147,** 79–91 (Elsevier Inc., 2018).
55. Kopf, A. *et al.* Microtubules control cellular shape and coherence in amoeboid migrating cells. *J Cell Biol* **219,** 193–24 (2020).
56. Sens, P. & Plastino, J. Membrane tension and cytoskeleton organization in cell motility. *J Phys Condens Matter* **27,** 273103 (2015).
57. Hochmuth, F. M., Shao, J. Y., Dai, J. & Sheetz, M. P. Deformation and flow of membrane into tethers extracted from neuronal growth cones. *Biophysical Journal* **70,** 358–369 (1996).
58. Meijering, E. *et al.* Design and validation of a tool for neurite tracing and analysis in fluorescence microscopy images. *Cytometry A* **58,** 167–176 (2004).

Supplementary Note: Curvature-dependent mechanochemical patterning

Many migrating cells exhibit characteristic patterns of actin activity and membrane curvature at their front [1]. These have been studied in the past by considering the complex interplay of various actin-regulatory molecules [7, 8]. Interactions with the curvature of the plasma membrane have also been investigated, in particular the effect of curvature-sensing and inducing proteins that promote the polymerization of actin [4, 5, 9–11]. In immune-like HL-60 cells, the BAR domain containing protein Snx33 is upregulated during migration. Based on its structure, Snx33 is likely to bind membrane regions with weak inward curvatures, and we find that disrupting Snx33 impacts the cell-scale organization of the actin cytoskeleton. We investigate here a putative role of Snx33 on the patterning capacity of the leading edge. We consider a minimal set of equations to describe the dynamics of membrane curvature coupled to the concentration field of an activator of actin polymerization. We analyze the mechanochemical instabilities present in the system, and delineate the parameter region in which spontaneous patterning can occur.

1 Main equations

In the following, we derive the coupled system of equations consisting of a curvature-dependent reaction-diffusion equation for an activator of actin polymerization, and the equation for the curvature of the membrane.

1.1 Activator equation

We consider the concentration field A of a generic activator of actin such as WAVE2. Because actin protrusions at the cell front are often thin structures with a dense meshwork and an average filament orientation towards the leading edge [13], we neglect variations of A across the thickness of the protrusion and assume that diffusive transport of actin regulatory molecules occurs predominantly in the direction of average filament alignment x. We consider self-activation of A with a characteristic time constant τ_A and introduce the curvature-dependent regulatory term $r_\mathrm{C}(C)$. From the continuity equation for the surface concentration of activator molecules, we then obtain the following partial differential equation

$$\tau_\mathrm{A}\frac{\partial}{\partial t}A(x,t) = A(x,t) + r_\mathrm{C}(C(x,t)) + \lambda_\mathrm{A}^2\frac{\partial^2}{\partial x^2}A(x,t), \tag{1}$$

in which $\lambda_\mathrm{A} = \sqrt{\tau_\mathrm{A} D}$ denotes a reaction-diffusion length scale, with D the diffusion coefficient along the cell migration axis x.

1.2 Curvature equation

The curvature C depends on the mechanical properties of the plasma membrane. We consider a Helfrich membrane without spontaneous curvature with a bending rigidity κ and surface tension γ [2, 6]. In the weak bending approximation and with periodic boundary conditions, the conservation of momentum leads to the following equation for the curvature profile along x [3, 12]

$$\kappa\frac{\partial^2}{\partial x^2}C(x,t) - \gamma C(x,t) = P, \tag{2}$$

in which $P = P_\mathrm{ext} - P_\mathrm{int}$ denotes the pressure difference between the outside and the inside of the cell. We assume that actin polymerization generates an active pressure field which acts on the membrane from within the cell that depends on $A(x,t)$, and we neglect any pressure difference in the absence of activator molecules. With this term and introducing the membrane persistence length $\lambda = \sqrt{\kappa/\gamma}$, Eq. 2 reads

$$\lambda^2\frac{\partial^2}{\partial x^2}C(x,t) - C(x,t) = -\frac{f_\mathrm{A}}{\gamma}A(x,t), \tag{3}$$

in which we denote with f_A the force per activator molecule.

2 Regulation in the limit of small curvatures

Generally, the shape of the regulatory function $r_C(C)$ is unknown and depends on the properties of the curvature-sensing proteins involved. The shape of the dominant BAR protein in our experimental system suggests that curvature sensing is relevant in the regime of small curvatures $C(x,t) = \delta C(x,t)$ (**Supplementary Fig. 2**). Assuming differentiability of r_C with respect to C, we may write a general expansion of the form

$$r_C(C) = r_C(0) + \left.\frac{\mathrm{d}r_C}{\mathrm{d}C}\right|_{C=0} \delta C + \mathcal{O}(\delta C^2). \tag{4}$$

The magnitude of the linear coefficient depends on the activity of curvature-dependent regulatory proteins. In the following, we assume that no curvature regulation takes place for a completely flat membrane sheet, i.e. $r_C(0) = 0$.

3 Patterning regime

We now explore the consequences of curvature-regulatory coupling between membrane shape and actin activity by analyzing the stability of the steady state $C = 0$ and $A = 0$, in which the membrane is flat and no actin activity is present. Introducing rescaled variables and the normalized curvature coupling coefficient

$$a = \frac{A f_A \lambda}{\gamma}, \qquad c = \lambda C; \qquad \xi = \left.\frac{\mathrm{d}r_C}{\mathrm{d}C}\right|_{C=0} \frac{f_A}{\gamma}, \tag{5}$$

we may write Eqs. 1 and 3 in dimensionless form as

$$\tau_A \partial_t a = a + \xi c + \lambda_A^2 \partial_x^2 a, \tag{6}$$

$$\left(\lambda^2 \partial_x^2 - 1\right) c = -a. \tag{7}$$

A small perturbation away from the uniform steady state can be written as

$$\delta a = \delta a_0 \exp(\omega t + \mathrm{i}kx), \qquad \delta c = \delta c_0 \exp(\omega t + \mathrm{i}kx), \tag{8}$$

in which k is the perturbation wavenumber and ω the corresponding growth rate. Substituting Eq. 8 into Eqs. 6 and 7 and keeping terms to linear order in the perturbation, we obtain the dispersion relation

$$\omega(k) = \frac{1}{\tau_A}\left(1 - k^2\lambda_A^2 + \frac{\xi}{1 + k^2\lambda^2}\right). \tag{9}$$

The stability diagram as a function of the length scale ratio $\lambda/\lambda_{\mathrm{A}}$ and the curvature coupling constant ξ is shown in **Fig. 2j**. For positive coupling, the growth rate is positive and maximal at $k = 0$, describing a uniformly advancing flat sheet in the linearized system. For $\xi < 0$, there is a region in which spontaneous patterning occurs, i.e. where $\omega(k_{\mathrm{Max}}) > 0$ with $k_{\mathrm{Max}} > 0$. Two types of instabilities are present in the system. For $\lambda < \lambda_{\mathrm{A}}$, stable and unstable regions are separated by a type-III instability at the critical parameter value $\xi^*_{\mathrm{III}} = -1$, with timescale τ_{A} and coherence length $\sqrt{\lambda_{\mathrm{A}}^2 - \lambda^2}$. For $\lambda > \lambda_A$, the transition between stable and unstable regions corresponds to a type-I instability, and the critical line is given by

$$\xi^*_{\mathrm{I}} = -\left(\frac{\lambda_{\mathrm{A}}^2 + \lambda^2}{2\lambda_{\mathrm{A}}\lambda}\right)^2. \tag{10}$$

Here, the characteristic timescale is $\tau_{\mathrm{A}} 2\lambda^2/(\lambda^2+\lambda_{\mathrm{A}}^2)$ and the coherence length is $2\lambda\lambda_{\mathrm{A}}/(\lambda^2 + \lambda_{\mathrm{A}}^2)\sqrt{2(\lambda^2 - \lambda_{\mathrm{A}}^2)}$. The pattern wavelength at the maximum is given by

$$l_{\mathrm{Max}} = \frac{2\pi\lambda}{\sqrt{-\mathrm{i}\sqrt{\xi}\frac{\lambda}{\lambda_{\mathrm{A}}} - 1}} \tag{11}$$

and shown in **Fig. 3a**. Thus, negative curvature feedback can lead to the spontaneous formation of patterns. The wavelength of the fastest-growing mode increases when the magnitude of the curvature coupling constant ξ decreases.

We note that by coupling the Snx33-mediated feedback circuit to a second positive feedback loop, for example driven by a second polymerization-promoting curvature sensing protein species as considered here [5], one may recover dynamical behaviors such as traveling waves, which are observed in migrating cells.

References

[1] Allard, J. and Mogilner, A. (2013). Traveling waves in actin dynamics and cell motility. *Current Opinion in Cell Biology*, 25(1):107–115.

[2] Brown, F. L. (2008). Elastic modeling of biomembranes and lipid bilayers. *Annual Review of Physical Chemistry*, 59:685–712.

[3] Deserno, M. (2015). Fluid lipid membranes: From differential geometry to curvature stresses. *Chemistry and Physics of Lipids*, 185:11–45.

[4] Gov, N. S. (2018). Guided by curvature: Shaping cells by coupling curved membrane proteins and cytoskeletal forces. *Philosophical Transactions of the Royal Society B: Biological Sciences*, 373(1747).

[5] Gov, N. S. and Gopinathan, A. (2006). Dynamics of membranes driven by actin polymerization. *Biophysical Journal*, 90(2):454–469.

[6] Helfrich, W. (1973). Elastic Properties of Lipid Bilayers: Theory and Possible Experiments. *Zeitschrift fur Naturforschung - Section C Journal of Biosciences*, 28(11-12):693–703.

[7] Inagaki, N. and Katsuno, H. (2017). Actin Waves: Origin of Cell Polarization and Migration? *Trends in Cell Biology*, 27(7):515–526.

[8] Mata, M. A., Dutot, M., Edelstein-Keshet, L., and Holmes, W. R. (2013). A model for intracellular actin waves explored by nonlinear local perturbation analysis. *Journal of Theoretical Biology*, 334:149–161.

[9] Naoz, M. and Gov, N. S. (2020). Cell-Substrate Patterns Driven by Curvature-Sensitive Actin Polymerization: Waves and Podosomes. *Cells*, 9(3).

[10] Peleg, B., Disanza, A., Scita, G., and Gov, N. S. (2011). Propagating cell-membrane waves driven by curved activators of actin polymerization. *PLoS ONE*, 6(4):1–11.

[11] Sadhu, R. K., Penič, S., Iglič, A., and Gov, N. S. (2021). Modelling cellular spreading and emergence of motility in the presence of curved membrane proteins and active cytoskeleton forces. *European Physical Journal Plus*, 136(5).

[12] Schneider, J. A. (2016). The interplay of cell membrane and cytoskeleton Dissertation. (August 1985).

[13] Svitkina, T. M. (2020). Actin Cell Cortex: Structure and Molecular Organization. *Trends in Cell Biology*, 30(7):556–565.

7.1.2 CCR7 acts as both a sensor and a sink for CCL19 to coordinate collective leukocyte migration

Originally published in *Nat. Immunol. (2023)*. https://doi.org/10.1126/sciimmunol.adc9584

SCIENCE IMMUNOLOGY | RESEARCH ARTICLE



DENDRITIC CELLS

CCR7 acts as both a sensor and a sink for CCL19 to coordinate collective leukocyte migration

Jonna Alanko[1,2]*, Mehmet Can Uçar[1], Nikola Canigova[1], Julian Stopp[1], Jan Schwarz[1,3], Jack Merrin[1], Edouard Hannezo[1]*, Michael Sixt[1]*

Copyright © 2023 The Authors, some rights reserved; exclusive licensee American Association for the Advancement of Science. No claim to original U.S. Government Works

Immune responses rely on the rapid and coordinated migration of leukocytes. Whereas it is well established that single-cell migration is often guided by gradients of chemokines and other chemoattractants, it remains poorly understood how these gradients are generated, maintained, and modulated. By combining experimental data with theory on leukocyte chemotaxis guided by the G protein–coupled receptor (GPCR) CCR7, we demonstrate that in addition to its role as the sensory receptor that steers migration, CCR7 also acts as a generator and a modulator of chemotactic gradients. Upon exposure to the CCR7 ligand CCL19, dendritic cells (DCs) effectively internalize the receptor and ligand as part of the canonical GPCR desensitization response. We show that CCR7 internalization also acts as an effective sink for the chemoattractant, dynamically shaping the spatiotemporal distribution of the chemokine. This mechanism drives complex collective migration patterns, enabling DCs to create or sharpen chemotactic gradients. We further show that these self-generated gradients can sustain the long-range guidance of DCs, adapt collective migration patterns to the size and geometry of the environment, and provide a guidance cue for other comigrating cells. Such a dual role of CCR7 as a GPCR that both senses and consumes its ligand can thus provide a novel mode of cellular self-organization.

Downloaded from https://www.science.org on September 07, 2023

INTRODUCTION

How cells navigate through tissues is one of the fundamental questions in biology, with great relevance in areas such as immunology, development, and cancer metastasis. Leukocytes in particular need to be recruited within short time frames because immunological threats arise at unpredictable sites in the body. Moreover, adaptive immunity is generated in lymphatic organs, which are usually remote from the primary site of infection, requiring long-range cellular trafficking (*1*). A key concept derived from in vitro studies of cultured cells is chemotaxis, where cells migrate toward increasing concentrations of externally established, supposedly defined distributions of chemotactic cues (*2*, *3*). In a metazoan setting, the relationship between chemoattractant distribution and cellular response is poorly understood. This is mainly because the spatiotemporal distribution of soluble chemotactic cues is challenging to measure in vivo, and the mechanisms that determine how gradients are generated and maintained in complex dynamic tissues require further exploration (*4*, *5*).

The majority of chemotactic cues are sensed by G protein–coupled receptors (GPCRs), which respond to a wide range of exogenous and endogenous ligands. The most diversified group of chemotactic proteins in animals is the chemokine system, which comprises around 50 ligands that bind to around 20 receptors (*6*). Chemokines are the main orchestrators of leukocyte trafficking, and they act by triggering extravasation from the bloodstream, as well as determining the interstitial positioning and the directional guidance of inflammatory cells within tissues (*7*). Chemokines also guide cells during developmental processes like germ cell and neural crest migration, neurogenesis and vasculogenesis, and organ development (*3*, *8*–*10*).

Chemokine receptors signal predominantly via Gαi protein signaling. Whereas this specifies the directional response of the cell, ligand binding also leads to receptor internalization, which desensitizes the cell toward ongoing ligand exposure. Desensitization can terminate the migratory response of the cell whenever the local chemokine concentration exceeds a threshold (*2*, *11*). Alternatively, receptor internalization followed by recycling effectively cleans receptors from ligands and might thereby allow cells to adapt to broader ranges of concentrations, e.g., when moving through gradients (*2*, *12*).

The few established experimental paradigms where functional chemokine gradients have been substantiated in animals mostly involve source-sink systems, where the chemokine is secreted by one cell type and consumed by another so that a spatial gradient arises between source and sink (*8*, *13*). This gradient is then sensed by a third migratory cell type. The functional unit forming a chemokine sink is a cell type that expresses a so-called decoy or scavenger receptor. Whereas decoy GPCRs lost the capacity to activate G proteins, they effectively internalize ligands (*8*).

A variant of such source-sink models is self-generated chemokine gradients that have been demonstrated to drive the collective migration of cell clusters in the lateral line of the developing zebrafish. Here, cells positioned at the leading edge of this traveling primordial organ express a sensory receptor that guides collective migration in an initially homogenous field of the chemokine CXCL12 (*14*–*17*). Cells at the trailing edge of the cell cluster express a decoy receptor for CXCL12 and thereby establish the gradient. Furthermore, in some cancer cells and *Dictyostelium* amoeba, single cells carry cell surface enzymes that create self-generated gradients by degrading guidance cues and thereby organize collective locomotion (*18*–*20*).

[1]Institute of Science and Technology Austria (ISTA), Klosterneuburg, Austria. [2]MediCity and InFLAMES Research Flagship Center, University of Turku, Turku, Finland. [3]Ibidi GmbH, Gräfelfing, Germany.
*Corresponding author. Email: jonna.alanko@utu.fi (J.A.); edouard.hannezo@ist.ac.at (E.H.); michael.sixt@ist.ac.at (M.S.)

Here, we use the paradigm of CCR7-mediated chemotaxis to investigate leukocyte migration in different chemokine fields. CCR7 is one of the most prominent GPCRs in the adaptive immune system and is particularly critical for dendritic cells (DCs), professional antigen-presenting cells whose migration after pathogen encounter from peripheral tissues to draining lymph nodes relies on CCR7 and its two chemokine ligands, CCL19 and CCL21 (*21*–*24*). Using CCL19 as a model of soluble chemoattractant, we show that chemokine sensing and internalization by a signaling GPCR also affect ligand distribution, thereby allowing a single receptor to both self-generate and sense gradients that guide collective leukocyte migration.

RESULTS

Dendritic cells exhibit persistent CCR7-dependent migration in a uniform CCL19 field

As a model for leukocyte chemotaxis, we used CCR7-guided migration of mature DCs. Upon exposure to pathogenic threats, these cells rely on CCR7 to navigate from peripheral tissues toward the center of draining lymph nodes (*25*). This process can be faithfully mimicked in vitro by incorporating DCs into three-dimensional (3D) collagen gels overlaid with a medium containing the soluble CCR7 ligand CCL19 (Fig. 1A). The cells migrated directionally toward the chemokine diffusing from the overlaid compartment into the collagen gel (Fig. 1B) and showed a continuous increase in speed and persistence that lasted for hours and spanned millimeter distances (Fig. 1B; fig. S1, A and B; and movie S1). When we measured how the chemoattractant gradient evolved over time using 10-kDa fluorescein isothiocyanate (FITC)–dextran as a molecular proxy of comparable size, we found that the gradient gradually changed from a steep near-exponential distribution toward a flat, almost linear shape within 1 to 2 hours (fig. S2A). Although this might suggest that DCs migrate more efficiently in response to flat and linear gradients (fig. S2B), this seemed unlikely based on previous findings that the chemotactic prowess of DCs is higher in exponential than in linear gradients (*26*). Furthermore, immature DCs (*27*) and other leukocytes such as neutrophil-like cells showed a very transient migratory response when exposed to chemoattractants in the same experimental setup (figs. S1, A and B, and S2C and movies S2 and S3). This response pattern was in line with the established model where cells can only effectively sense a gradient when the chemoattractant concentration is in the range of the K_d [dissociation constant (binding affinity)] of the receptor and when the concentration difference of the ligand across the cell body (Δc) is sufficiently high to allow for spatial discrimination (*28*, *29*). This, together with the long-recognized notion that the activity range of diffusion-based gradients of morphogens is very unlikely to reach the millimeter range (*13*), led us to consider the option that DCs might modulate and re-shape the chemokine gradient as they migrate.

To test whether DCs shape gradients of their own chemoattractant, we used a system that enables us to control the spatial distribution of both cells and chemokine. We set up under agarose assays where DCs migrate in a confined space from a cell reservoir in response to different chemokine distributions (Fig. 1C). In the absence of chemokine, only a few cells showed persistent migration, whereas cells effectively and persistently moved toward an externally imposed gradient of CCL19 over a 5-hour imaging period (Fig. 1D). Similar numbers of DCs left the reservoir when CCL19 was distributed uniformly. Both speed and directional persistence were even increased compared with cells migrating in an imposed gradient, and cells in uniform concentration migrated persistently beyond the 3-mm range (Fig. 1, F to H, and movies S4 and S5). CCR7-knockout (KO) cells barely left the reservoir, behaving similarly to cells in the absence of chemokine (Fig. 1, D and E). When small numbers of labeled CCR7-KO DCs were spiked into a population of wild-type (WT) DCs, the behavior of CCR7-KO DCs was not rescued (Fig. 1I and movie S6), demonstrating that no secondary, CCR7-independent, guidance cue steered collective migration. These data strongly suggest that DCs create a CCR7-dependent gradient while they migrate, presumably by locally inactivating the chemokine.

DCs create local CCL19 gradients by CCR7-mediated chemokine uptake

It was previously shown that DCs could proteolytically process the second CCR7 ligand CCL21, but this was not the case for CCL19 (*30*). Because CCR7 is rapidly endocytosed upon binding to CCL19 (fig. S2D), we next investigated whether CCR7 internalization could lead to chemokine consumption and the formation of potential gradients. When we visualized DCs upon exposure to labeled CCL19, we observed efficient uptake of CCL19, which accumulated in small endosomal structures preferentially at the trailing edge of the cells and occasionally colocalizing with patches of actin (Fig. 2A). Cells absorbed increasing amounts of CCL19 over time, and this was strictly CCR7 dependent, excluding the role of any unknown scavenger receptors in these cells (Fig. 2B). CCL19 uptake could also be detected as chemokine depletion from the medium with WT but not with CCR7-KO DCs, with ~10% decrease occurring during the first hour (Fig. 2C). To test whether this depletion was quantitatively sufficient to support possible gradient-generating activity, we developed an under agarose assay with two competing chemokine sources: one contained CCL19 only and the other CCL19 mixed with "sink" DCs (Fig. 2D). We then monitored the migration of small numbers of "sensor" DCs located between both chemokine sources. When CCR7-KO DCs were used as sinks, sensor cells migrated equally toward both sources. When WT DCs were used as sinks, sensor cells migrated almost exclusively toward the cell-free source, suggesting that the endocytic capacity of WT cells was sufficient to deplete CCL19 in functionally relevant quantities (Fig. 2D).

We next returned to the physiologically more relevant 3D collagen assays and tested whether the sustained long-range migration of DCs toward CCL19 gradients might be caused by their gradient-amplifying activity. We embedded DCs in collagen gels containing uniform CCL19 and overlaid the gels with a medium containing no DCs but varying concentrations of CCL19 (Fig. 2E, fig. S2, E and F, and movie S7). As expected, DCs migrated toward the overlaid chemokine source whenever the concentration was higher than the uniform level surrounding them. Cells overlaid with equal, or even lower, levels of CCL19 than the uniform CCL19 concentration in the gel persistently migrated toward the overlaid chemokine source. This demonstrates that even when sparsely distributed in fibrillar 3D environments, DCs lower the environmental chemokine concentration sufficiently to collectively sustain their own chemotactic migration.

Downloaded from https://www.science.org on September 07, 2023

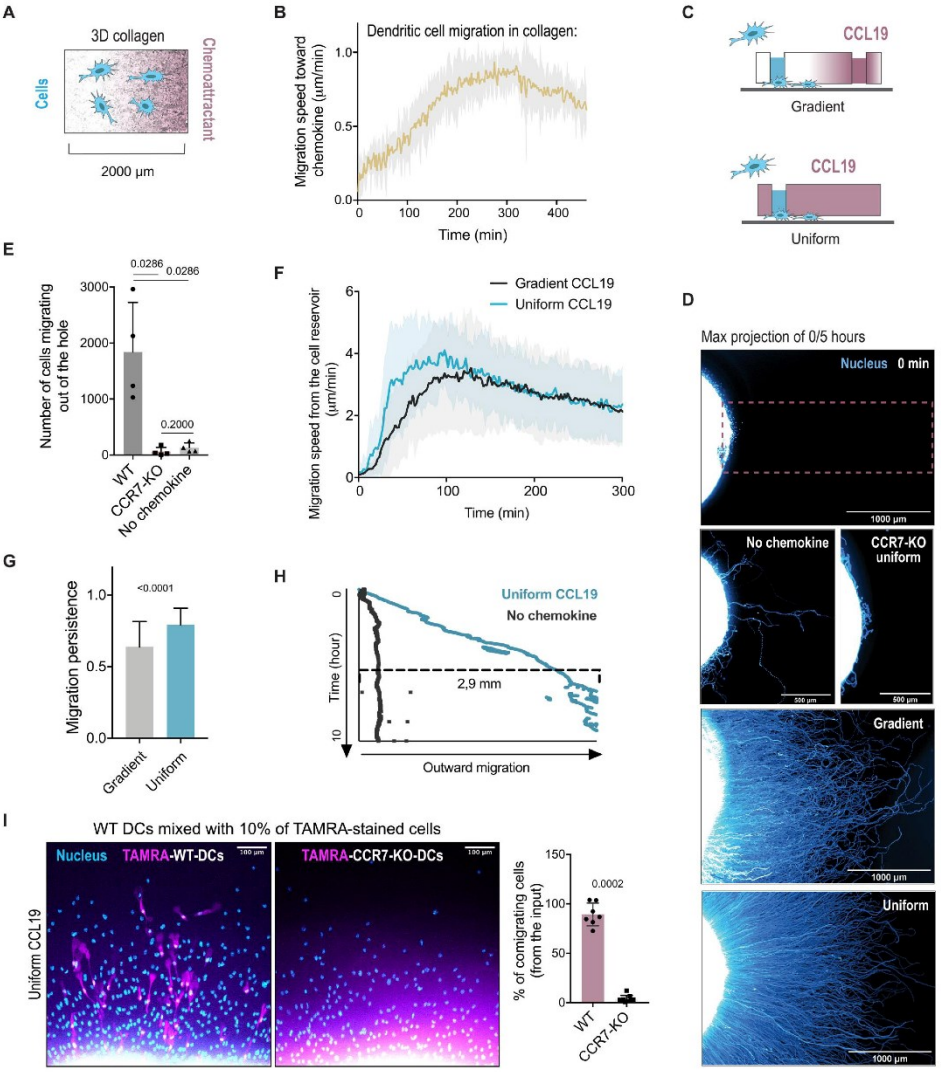


Fig. 1. Dendritic cell collectives exhibit CCR7-dependent persistent migration in a uniform CCL19 field. (**A**) Schematic of 3D collagen assay with embedded cells and diffusible chemoattractant on one side. (**B**) Speed of mature DCs migrating in collagen toward CCL19 source at the population level for the first 7.5 hours ($n = 6$ from four independent experiments, means ± SD). (**C**) Schematic of agarose assay, in which cells migrate from a reservoir under an agarose gel either toward a CCL19 reservoir or in a uniform CCL19 field, where the same amount of CCL19 (18 ng) is mixed with the agarose. (**D**) Maximum projection of nuclear stain of WT or CCR7-KO DCs migrating out of the cell reservoir hole to under agarose for 0 min or 5 hours ± CCL19 in an imposed gradient or uniform chemokine concentration. The dashed rectangular box indicates the area used for quantifications in (**E**) to (**G**). (E) The number of cells migrating out of the cell reservoir under agarose ± uniform CCL19 ($n = 4$ from three independent experiments, means ± SD, Mann-Whitney test). (F) Mean migration speed of DCs from the cell source during the first 5 hours with a gradient or uniform CCL19 ($n = 5$ from three independent experiments, means ± SD). (G) Migration persistence of single cells in the under agarose assay with uniform or gradient CCL19 [n (gradient) = 435 cells, n (uniform) = 1246 cells, means ± SD, Mann-Whitney test]. (**H**) Kymograph showing the progress of the leading edge of migrating DC population in ±uniform CCL19 during the first 10 hours (representative of ≥3 independent experiments). (**I**) Snapshots (80-min time point) of TAMRA-stained WT or CCR7-KO DCs comigrating with WT DCs under agarose with uniform CCL19 for 10 hours. The graph shows the percentage of TAMRA-stained cells that migrate together with the group of WT cells (means ± SD, $n = 7$ to 9 from three independent experiments, Mann-Whitney test).

Downloaded from https://www.science.org on September 07, 2023

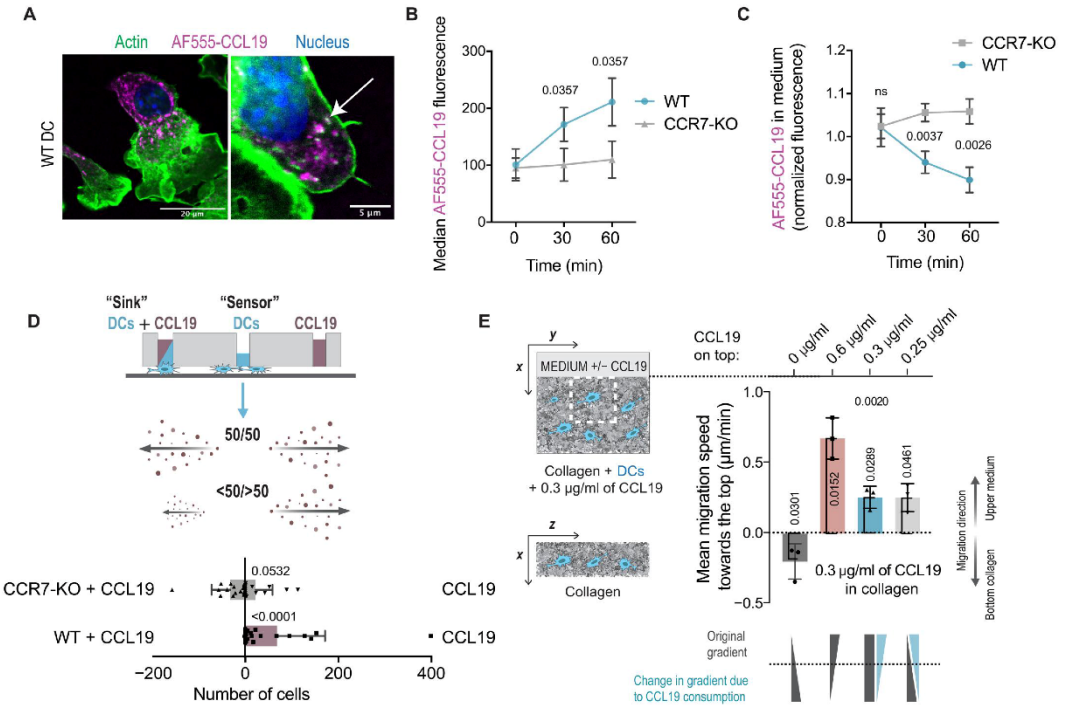


Fig. 2. Dendritic cells create local CCL19 gradients by CCR7-mediated chemokine uptake. (**A**) DCs incubated with AF555-labeled CCL19 under agarose for 2 to 3 hours, fixed and stained for nucleus (DAPI) and actin (phalloidin). The arrow points to an intracellular AF555-CCL19 vesicle-like structure positive for actin (representative images from 22 cells from three independent experiments). (**B**) Median AF555 fluorescence in WT and CCR7-KO DCs after incubation with AF555-CCL19–containing medium for 0, 30, or 60 min (n = 3 to 5 independent experiments, means ± SD, Mann-Whitney test). (**C**) Normalized AF555 fluorescence left in the AF555-CCL19–containing medium after incubation with WT or CCR7-KO DCs for 0, 30, or 60 min (n = 3 independent experiments, values normalized to the sum of all data points in an experiment, means ± SD, unpaired t test). (**D**) Top: Schematic of "sink-sensor" under agarose setup to detect the ability of sink cells to deplete CCL19 from the medium by tracking the migration direction of the middle sensor cells. Bottom: Quantification of the number of sensor cells migrating to the left or right with WT or CCR7-KO DCs as the sink cells (n = 15 or 16 from three independent experiments, means ± SD, Mann-Whitney test). (**E**) Left: Schematic of the 3D collagen setup, in which CCL19 (0.3 µg/ml) is uniformly mixed with collagen and DCs, and a medium containing different concentrations of CCL19 is placed on top. The white dashed line box represents the detection field. Right: Quantification of the mean migration speed of DCs toward the upper compartment containing CCL19 (0, 0.6, 0.3, or 0.25 µg/ml) during the first 8 hours (n = 3 independent experiments, means ± SD, values normalized to the sum of the experiment, Kruskal-Wallis multiple comparison test, and one sample t test showing the difference to 0 in vertical).

DC-generated CCL19 gradients are dependent on Lfc-mediated CCR7 endocytosis

To challenge our hypothesis of internalization-mediated chemokine consumption, we aimed to impair CCR7 endocytosis without altering its CCL19 sensing capacity and thus migration in gradients of CCL19. For receptors undergoing ligand-triggered endocytosis, ligand sensing and receptor internalization are often interconnected, but moderate reduction of receptor endocytosis should still allow migration in gradients before all the receptors get saturated. CCR7 endocytosis was previously shown to be blocked with the dynamin inhibitor Dynasore (*31*). However, Dynasore reduced DC migration also in gradients of CCL19 (fig. S3A), which was in line with previously demonstrated effects on other surface receptors such as integrins (*32*). In search for other targets mediating CCR7 internalization, we investigated Lfc, a Rho guanine nucleotide exchange factor. Lfc was recently shown to accumulate at the trailing edge of migrating DCs (*33*), where the internalized CCL19 was also localized (Fig. 2A). Moreover, the human homolog of Lfc (GEF-H1/ARHGEF2) has previously been linked to vesicle trafficking (*34*, *35*) and actin comet formation on endosomes (*36*). We found that Lfc-KO DCs showed reduced CCL19-triggered CCR7 endocytosis (Fig. 3A) and consequently decreased CCL19 uptake (Fig. 3B). When migrating under agarose toward externally imposed gradients of CCL19, directional persistence of Lfc-KO DCs was unimpaired, indicating that the sensing function of CCR7 was intact and no general migration defects were caused by the Lfc deficiency under our assay conditions (Fig. 3, C and D). In contrast, Lfc-KO DC migration in uniform CCL19 concentration

Downloaded from https://www.science.org on September 07, 2023

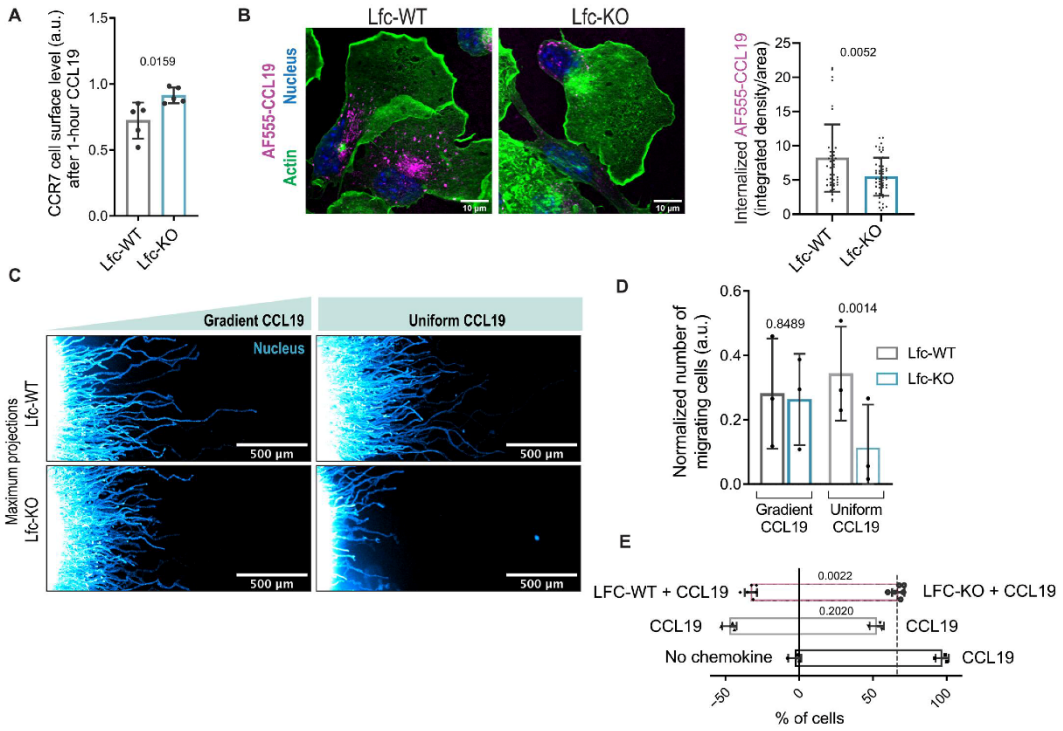


Fig. 3. CCR7 endocytosis and CCL19 uptake are dependent on Lfc. (**A**) Antibody staining of CCR7 cell surface level in Lfc-WT and Lfc-KO DCs after 1-hour incubation with CCL19 (normalized to the corresponding 0 min control, $n = 5$ independent experiments, Mann-Whitney test). (**B**) Left: Representative images of Lfc-WT and Lfc-KO DCs incubated with AF555-CCL19 for 2 to 3 hours before fixing and staining for nucleus (DAPI) and actin (phalloidin). Right: Quantification of the AF555-CCL19 signal inside the Lfc-WT and Lfc-KO DCs. Samples were imaged with LSM880, and the integrated density of AF555-CCL19 was measured from the middle slice/area of the cell ($n = 47$ to 52 cells from three independent experiments, means ± SD, Mann-Whitney test). (**C**) Maximum projections of stained nuclei in Lfc-WT and Lfc-KO DCs migrating under agarose with gradient or uniform CCL19 for 10 hours (representative images of three independent experiments). (**D**) The number of migrating Lfc-WT and Lfc-KO DCs under agarose with gradient or uniform CCL19 (normalized to the sum of each experiment, means ± SD from three independent experiments, paired t test). (**E**) Quantification of the % of sensor DCs migrating to left or right in above described sink and sensor assay with ± CCL19 on each side or Lfc-WT and Lfc-KO DCs as competing sinks ($n = 3, 3, 6$ from three independent experiments, means ± SD, Mann-Whitney test).

was substantially reduced. To confirm that this was due to insufficient gradient-generating activity, we used Lfc-KO and WT cells as sink cells in the aforementioned setup. Lfc-WT and Lfc-KO cells as competing sinks led the sensor DCs to migrate preferentially toward the Lfc-KO sink, confirming that CCL19 gradients are generated by endocytosis (Fig. 3E).

A quantitative model of cell guidance by self-generated CCL19 gradients

To further challenge the idea that endocytosis-mediated depletion of soluble chemoattractant could quantitatively explain the migration behavior detected in our agarose assays, we developed particle-based simulations for cells migrating in an initially uniform chemokine field. We modeled individual cells as soft polar particles that perform a persistent random walk and can degrade chemokine molecules in their proximity. Locally self-generated chemokine gradients are in turn sensed by cells, causing them to reorient their polarity toward higher chemokine concentrations. Last, the cells experience an effective repulsive force by other neighboring cells, representing steric interactions (see Fig. 4A and fig. S3B, and data file S1: Theory notes 1 to 3 for the implementation of model assumptions and estimation of parameters). This set of rules provided a minimal model to link individual cell motility and cell-chemokine interactions to the collective behavior of immune cell migration. For a wide range of parameter values, we systematically observed that cells migrated collectively in a propagating front away from their source, as reported previously for bacterial chemotaxis (*37*, *38*), which robustly reproduced the experimentally obtained trajectories (Fig. 4B, top). The simulations accurately captured the cell density and velocity profiles obtained from the experimental data (Fig. 4C and fig. S3D), with velocities decaying over time because of flattening of the chemokine

Downloaded from https://www.science.org on September 07, 2023

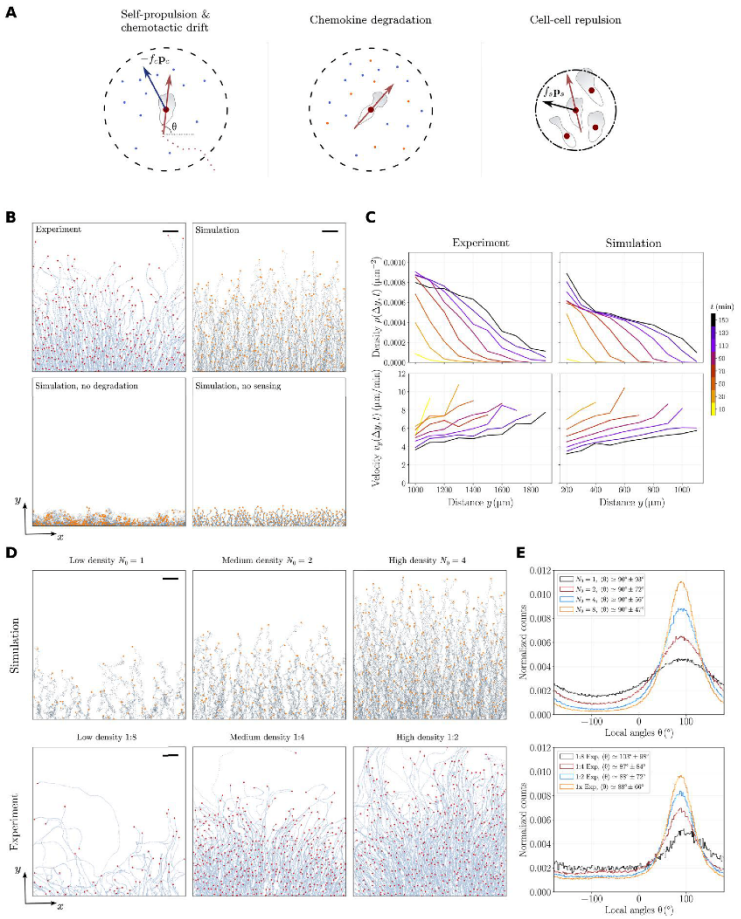


Fig. 4. Particle-based simulations reproduce the experimental migratory dynamics and predict that collective directional bias depends on cell density. (**A**) Schematics for the model assumptions used in the particle-based simulation setup. Left: Each cell is modeled as a self-propelled polar particle with polarity (red arrow) defined by its local angle θ with respect to the horizontal axis. In the presence of chemokine molecules (blue discs) within a neighborhood of radius R_c (dashed circular line) surrounding the center of mass of the cell, a net displacement "force" (blue arrow) controlled by the chemotactic strength f_c acts to reorient and displace the cell toward larger local chemokine concentrations. Middle: Upon displacement, the cell degrades a given percentage of sensed chemokine molecules from this neighborhood (orange discs). Right: Each cell additionally experiences a repulsive force (black arrow) from neighboring cells in a radius R_s (dash-dotted circular line), controlled by interaction strength f_s, which leads to a reorientation and displacement of the cell away from its neighbors. (**B**) Exemplary trajectories of DCs migrating in uniform CCL19 under agarose and in simulations (top) exhibit a qualitatively comparable bias away from the cell source. Bottom: Simulations of cells that cannot deplete or additionally cannot sense chemokine molecules, leading to impaired migration (trajectories are representative of four independent experiments and 50 simulations; scale bar, 100 μm in real experimental and rescaled simulation units). (**C**) Spatiotemporal dynamics of cell densities and velocities as a function of distance from the cell source *y*, obtained from under agarose assays (left) and simulations (right), showing good agreement. Cell densities (top) propagate as a wave away from the source, with velocities (bottom) globally decaying over time (color-coded), whereas cells at the population front show consistently larger velocities. (**D**) Exemplary trajectories of different densities of cells obtained from simulations (top) and under agarose assays (bottom). At a fixed propagation time, cells in higher-density populations migrate collectively over larger distances and exhibit a stronger directional bias. Densities are controlled by adjusting the cellular influx (number N_0 of cells added at fixed time intervals in simulations) and by different cell dilutions used in the experiments (denoted 1:2, 1:4, and 1:8; scale bar, 100 μm in real experimental and rescaled simulation units). Density and velocity profiles represent averaged values more than $n > 40{,}000$ cell trajectories from 50 simulations. (**E**) Directional bias of entire cell populations as obtained from the local angle (angle with respect to the horizontal axis) distributions of cellular trajectories in simulations (top) and experiments (bottom). Increasing the population density leads to narrower local angle distributions, with an average bias of $\theta \simeq +90°$ and comparable fluctuations in simulations and experiments. 1×, 1:2, 1:4, and 1:8 denote different cell dilutions ($n > 300$ cell trajectories from two independent experiments and $n > 3000$ trajectories from 20 simulations).

Downloaded from https://www.science.org on September 07, 2023

concentration and densities propagating as a wave away from the cell source in comparable time scales as in the experiments. Varying the chemokine depletion rate did not affect the overall shape of the chemokine gradient but minimally influenced the time to reach a certain chemokine concentration at a given distance (fig. S3E). Simulations additionally showed that cells in uniform attractant concentration are not able to migrate efficiently if either attractant depletion or sensing is compromised (Fig. 4B, bottom), in agreement with our CCR7-KO and Lfc-KO DC data.

Crucially, simulations also predicted that the directional bias depends strongly on the density of migrating cells, because denser populations migrated over longer distances and more persistently (Fig. 4D, top). We tested this experimentally with different amounts of DCs loaded into the cell reservoir and exposed to uniform CCL19 and found good qualitative agreement with the model prediction (Fig. 4D, bottom, and fig. S3C). An intuitive mechanism for this feature is that single cells without followers create gradients in any given direction, leading to persistent yet unbiased overall migration, whereas cells in a collectively migrating group are effectively guided from the back, where the local chemokine concentration remains low because of internalization by follower cells (*19*, *39*). As a result, cells at the population front face sharper gradients than those in the bulk, which lose their polarity over time as the local chemokine gradients become shallower. To probe the effect more quantitatively, we examined the angular distribution of migrating cells, with an angle close to +90° (−90°) indicating migration away from (toward) the cell source. We found that the angular distributions became markedly sharper with increasing cell density, with an approximately Gaussian shape having maxima centered around +90° and comparable SDs in experiments and simulations (Fig. 4E). Last, we found that the population front exhibited increased collective polarity, because group polarization, a metric quantifying the collective alignment of active polar particles (*40*), decreased over time as the population bulk advanced in the field of view (fig. S4, A and B). The observed cell density–dependent effects were not due to unknown relay factors secreted by the DCs because the process described here is exclusively CCR7 dependent (Fig. 1, D, E, and I), and the migration of CCL19-KO DCs was not impaired in uniform CCL19 field compared to WT-DC (fig. S4C). In addition, simulations of cells without chemotactic ability failed to reproduce the enhanced directional bias of denser cell populations, even with a large self-propulsion speed or strong repulsive cell-cell interactions (fig. S4D), emphasizing that our experimental results do not simply arise from the random persistent movement from a dense source of fast-migrating cells.

DC-generated CCL19 gradients allow cells to sense upcoming obstacles from a distance

The ability of *Dictyostelium* amoebae to self-generate chemoattractive gradients was recently shown to allow them to solve geometric mazes (*18*). To test the regulatory potential of CCR7 as a dual sensor and consumer of CCL19, we engineered a fork-like microfluidic device, where cells can choose between a closed channel and a channel leading to a big reservoir (Fig. 5A). In the presence of uniform CCL19, DCs selectively entered and moved through the channel leading to the reservoir (Fig. 5B). This was in line with our simulations, showing that chemokine depletion from the closed channel favored entry into the reservoir-connected channel, where attractive gradients could build up (Fig. 5B and fig. S5D). The level of fluorescently labeled CCL19 was detectably lower in the closed channel at the time the first cells in the device arrived at the decision point, supporting the view of cells reducing the chemokine concentration in the closed channel before entering it (fig. S5B). Chemokine concentration was also lower behind and higher in front of a moving DC cluster, whereas the level inside the cells increased over time (fig. S5, A and C). The selective entry into the open channel was strictly CCR7/CCL19 dependent because CCR7-KO DCs, which can neither create nor sense CCL19 gradients, barely entered the device and moved randomly into both channels at a low rate (Fig. 5, B and C, and movie S8). When Lfc-KO DCs were placed into the same device, only a few cells were able to reach the decision point (Fig. 5D and movie S9). Lowering the initial CCL19 concentration (0.5 μg/ml) allowed similar numbers of Lfc-KO and Lfc-WT cells to enter the device (Fig. 5D and movie S10). However, Lfc-KO cells made significantly more "mistakes" and migrated more often into the closed channel (Fig. 5E). These data were consistent with the reduced CCL19 uptake of Lfc-KO DCs and gradient generation capacity and together demonstrate that CCL19 sinking endows DCs with the ability to assess environmental features at a distance.

DC-generated CCL19 gradients enable DCs to guide comigrating T cells

Last, we asked whether CCR7-mediated self-generation of CCL19 gradients by DCs could affect the behavior of other cells. CCR7 guides pathogen-loaded DCs from inflamed peripheral tissues via lymphatic vessels into lymph nodes. T cells also use CCR7 to enter the lymph node, although they arrive via blood circulation and pass through lymph nodes not only upon inflammation but also as part of their homeostatic trafficking program. Once in the same area, both cell types swarm around each other and establish short physical contacts to scan their surface receptors, eventually resulting in the proliferation of antigen-specific T cells. However, whether and how DCs and T cells coordinate their local migratory response is not known. When we tested the response of either DCs or T cells to CCL19 under agarose, we found that T cells alone responded poorly to uniform CCL19 (Fig. 6A). Upon mixing with DCs, some T cells moved along with DCs via short-lived, CCR7-independent interactions, but in addition to this, a wave of T cells preceded the migrating DCs up to approximately 150 μm in a CCR7/CCL19-dependent manner (Fig. 6, B and E, and movie S11). This suggests that T cells could sense the CCL19 gradient that was generated by DCs but were unable or inefficient at generating their own gradient. The spatiotemporal structure of this coupled wave propagation could be recapitulated in our numerical simulations by modeling T cells as a population unable to consume CCL19 but that could migrate with faster velocities than DCs in response to the same gradient (Fig. 6, C and D). Notably, the DC-generated CCL19 gradient was superior in guiding T cells in front of DCs compared with an externally applied CCL19 gradient (Fig. 6A). Further experiments measuring the cell surface levels of CCR7 in DCs compared with activated WT and CCR7-KO T cells revealed that although the T cells clearly expressed CCR7 at their surface, as evident when compared with the CCR7-KO T cells, the level was significantly lower than in DCs (Fig. 6F). T cells also internalized significantly less Alexa Fluor 555 (AF555)–labeled CCL19 over time, although the normalized uptake rate in WT T cells was

Downloaded from https://www.science.org on September 07, 2023

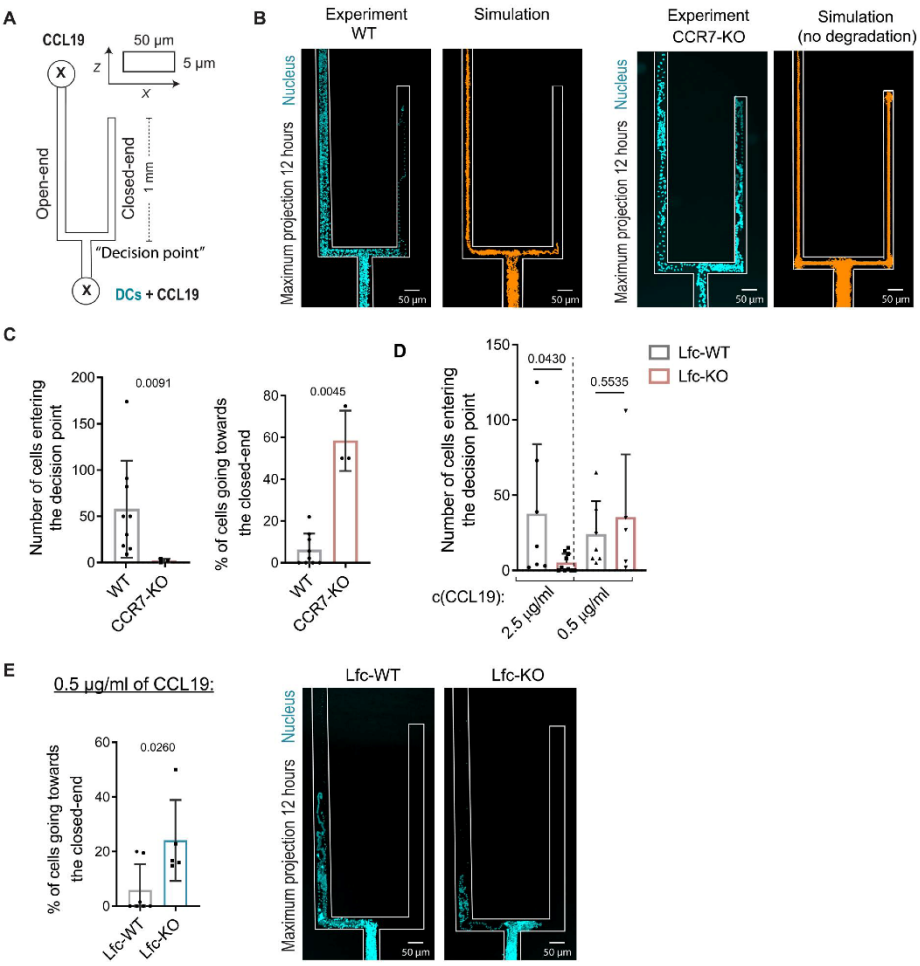


Fig. 5. DC-generated CCL19 gradients allow cells to avoid upcoming obstacles. (**A**) Schematic of the PDMS microfluidic device design with two inlets/reservoirs connected by a 50-µm-wide and 5-µm-high channel. The whole device is filled with uniform CCL19, and cells are added to the lower inlet. (**B**) WT and CCR7-KO DCs migrating for 12 hours in devices filled with uniform CCL19. Shown are maximum projections of nuclear stain and the corresponding cell migration trajectories obtained from simulations (representatives of WT: nine from three independent experiments; CCR7-KO: three from two independent experiments). (**C**) The number of WT and CCR7-KO DCs entering the decision point (the crossroad), and on the right, the % of WT and CCR7-KO DCs migrating toward the closed end of the PDMS device [means ± SD, *n*(WT) = 9 and *n*(CCR7-KO) = 3 from two independent experiments, Mann-Whitney test]. (**D**) The number of Lfc-WT and Lfc-KO DCs reaching the decision point in a microfluidic device with uniform CCL19 (0.5 or 2.5 µg/ml; means ± SD, $n \geq 5$ from three independent experiments, unpaired *t* test). (**E**) % of Lfc-WT and Lfc-KO DCs migrating for 12 hours toward the closed end with lower CCL19 concentration (0.5 µg/ml) and the representative maximum projections of nuclear stain (means ± SD, $n = 5$ to 7 from three independent experiments, unpaired *t* test).

Downloaded from https://www.science.org on September 07, 2023

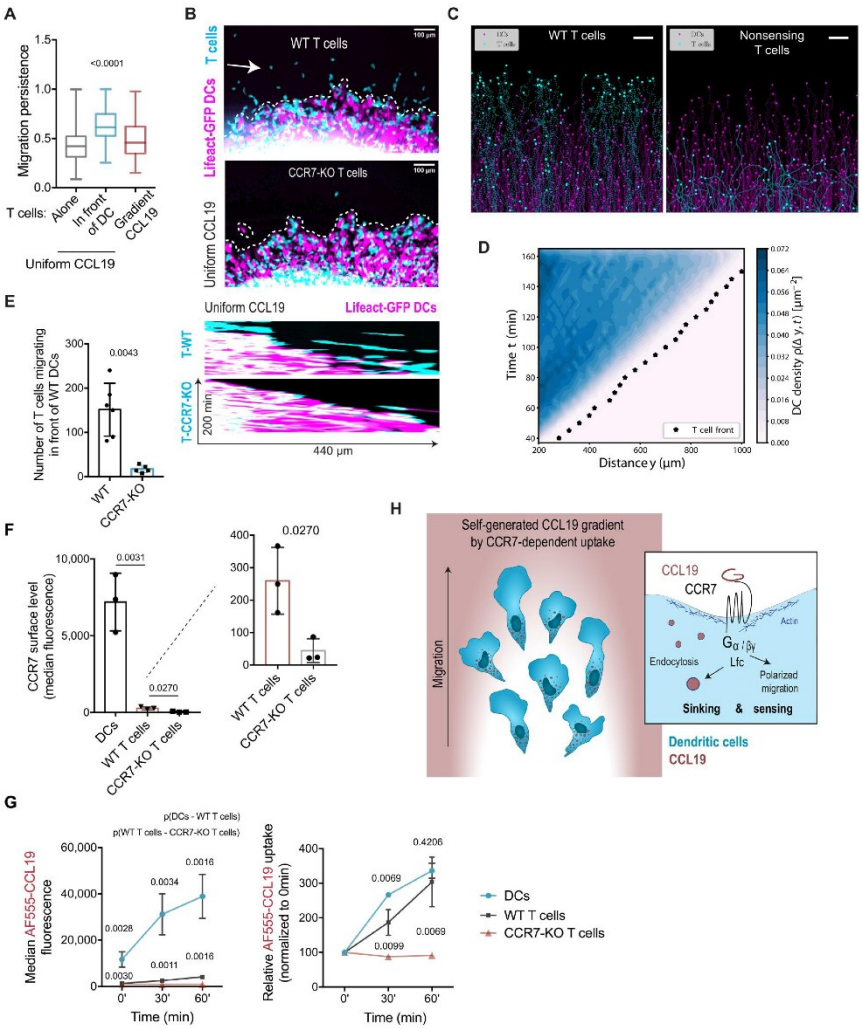


Fig. 6. DC-generated CCL19 gradients enable DCs to guide comigrating T cells. (**A**) Migration persistence of WT T cells migrating under agarose with uniform CCL19 either alone or in front of DCs, or alone with gradient CCL19 (n > 400 cells from three independent experiments, means ± SD, Kruskal-Wallis test). (**B**) Lifeact-GFP–expressing DCs (magenta) migrating together with TAMRA-stained WT or CCR7-KO T cells (cyan) under agarose with uniform CCL19. Top: representative snapshots with a white dashed line depicting the front line of DCs and an arrow pointing to an example T cell migrating in front of DCs (representatives of n = 5 or 6 from three independent experiments). Bottom: Corresponding kymographs showing the spatiotemporal density profiles for 200 min. (**C**) Trajectories of DCs (magenta) and T cells (cyan) obtained from simulations illustrating the accumulation of T cells ahead of the DC front (left). Inhibiting the chemical sensing of faster migrating T cells leads to a randomly migrating T cell population independently of the DC front (right). Scale bars, 100 µm in real experimental units and in rescaled simulation units. (**D**) Kymographs of DCs and T cells as obtained from the simulations. The color bar denotes the DC densities, and the star symbols represent the concentration maxima of T cells at different time points. Despite their larger chemotactic sensitivity, T cells preserve a characteristic length scale of ~150 µm in front of the DCs at all times (n > 16,000 cell trajectories from 20 simulations). (**E**) The number of T cells (WT or CCR7-KO) migrating in front of DCs (n = 5 or 6 from three independent experiments, means ± SD, Mann Whitney test). (**F**) CCR7 cell surface level in DCs and WT or CCR7-KO T cells (median fluorescence, n = 3 independent experiments, means ± SD, unpaired t test). (**G**) Uptake of AF555-CCL19 over time by DCs and WT or CCR7-KO T cells. Shown are median AF555 fluorescence (left) and the same dataset normalized to the corresponding 0-min time point (right) to illustrate the relative uptake rate (n = 3 or 4 from three independent experiments, means ± SD, unpaired t test). (**H**) Schematic of DC migration along self-generated CCL19 gradients. CCR7 has a dual role in chemokine sinking/depletion and sensing.

Downloaded from https://www.science.org on September 07, 2023

comparable to DCs (Fig. 6G). This suggests that the ability of cells to create chemokine gradients can also be determined by quantities and not solely by the nature of the receptor. Together, the above data demonstrate that DCs not only have the capacity to orchestrate their collective migration to lymph nodes but can also guide the migration of T cells, which on their own have limited capacity to modulate CCL19 distribution.

DISCUSSION

In this work, we demonstrate that CCR7 can act both as a sensor and a sink for CCL19 on the same cell and thereby orchestrate robust self-organizing patterns of collective cell migration (Fig. 6H). The dual function of CCR7 facilitates cross-communication between different cell types and, similar to the self-generated cAMP (cyclic adenosine 3′,5′-monophosphate) gradients in *Dictyostelium* amoebae (*18*), highly accurate navigation in geometrical mazes (movie S12).

Although CCR7 was shown to undergo endocytosis together with CCL19 upon ligation (*31*, *41*, *42*), the effect of this cell-scale chemokine uptake on locally shaping the chemokine field and thus influencing the migration of surrounding cells has not been recognized. However, some inflammatory chemokine receptors have been previously associated with chemokine scavenging in addition to their signaling function (*43*, *44*), suggesting that the phenomenon could have potentially wide-ranging physiological implications for immune cell communication. Recent work on the migration of mesodermal cells during zebrafish gastrulation further showed that an analogous mechanism shapes chemotactic gradients of a nonchemokine GPCR-ligand in early embryogenesis (*45*). The generality of this self-organizing mechanism raises the key question of the role of receptor desensitization in functionally adapting a cell to excessive ligand concentrations. At the single-cell level, internalization/recycling cleans the receptor from the ligand and thereby allows for new binding events so that the cell can locally adapt to the ambient ligand concentration. At the same time, internalization inevitably depletes the environment from ligands, which in turn leads to the population-wide adaptation of a cell collective to the ligand concentration. This previously unexplored effect could enable the cell collective to generate optimal concentration regimes where sensing of chemotactic gradients is effective because not all receptors are saturated.

Since the early observations in zebrafish (*15*, *17*), self-generated gradients have been increasingly recognized in different cellular contexts over the past years, and cells have been shown to form gradients of soluble attractants by different mechanisms, such as special scavenger receptors or enzymatic degradation (*15*, *17*, *19*, *39*). In contrast to CCL19, the other CCR7 ligand CCL21 has a long and highly charged C-terminal tail by which the chemokine gets immobilized to glycosaminoglycans in the extracellular matrix. This tail can be enzymatically cleaved by DC-bound cell surface proteases (*46*, *47*), whereas full-length CCL21 was shown to trigger less endocytosis compared with CCL19 (*41*). If and how DCs are able to create gradients of CCL21 is an interesting question for future investigations.

Because the generation and maintenance of long-range gradients of guidance cues in vivo are far from trivial, the ability of DCs to collectively create and sense chemokine gradients for efficient migration might ensure their robust function in changing chemokine environments. Collective cell migration is a well-known phenomenon in processes such as morphogenesis, wound healing, and tissue renewal (*48*). Although mature DCs were generally thought to migrate individually, it had previously been noticed that the percentage of DCs successfully reaching the draining lymph node increased nonlinearly with the number of DCs starting to migrate in the periphery (*49*). Moreover, immune cell density is extremely high in lymph nodes, leaving ample opportunity for local regulation of CCL19 concentration by CCR7-mediated scavenging (*21*). Recently, it was found that in zebrafish, a lower-jawed organism without well-organized lymph nodes, T cells migrated collectively in a CCR7-dependent manner in the special tessellated lymphoid network to facilitate whole-body surveillance (*50*). Although in our experiment, T cells were not able to migrate efficiently by themselves in a uniform CCL19 field, it is possible that self-generated chemokine gradients could contribute to collective T cell migration in such settings.

Evolutionarily, gradient-generating chemokine decoy receptors that lost G protein signaling but retained internalization capacity might be the specialized derivative of the dual function we describe here. After this initial discovery of DC-generated chemokine gradients orchestrating their own collective locomotion as well as that of T cells, future studies would be crucial to shed light on the significance of self-generated chemokine gradients in other types of immune cells.

MATERIALS AND METHODS

Study design

The objective of this study was to investigate the ability of DCs to migrate persistently over long distances even in uniform CCL19 chemokine and to determine the underlying mechanism and the consequences of DC-generated CCL19 gradients. For this, we used cells differentiated from conditionally immortalized Hoxb8 precursor cells or from mice and studied their migration characteristics in different in vitro setups (under agarose, collagen, and microfluidic devices) by live cell microscopy imaging together with flow cytometric analysis, confocal imaging, and mathematical modeling. Unless noted in the figure legend, experiments were performed at least three independent times, and data from multiple experiments were pooled. Investigators were not blinded to groups. Dead unmoving cells were excluded from the migration analysis, as well as clogged or leaky microfluidic channels with detectable unspecific fluid flow. Otherwise, no data were excluded. Details of the theoretical model based on particle-based simulations are described in the data file S1.

Mice

All C57BL/6J mice used in this study were bred and maintained in the animal facility at the Institute of Science and Technology Austria in accordance with the institute's ethics commission and Austrian law for animal experimentation. Permission for all experimental procedures was granted and approved by the Austrian Federal Ministry of Education, Science and Research (identification code: BMWF-66.018/0005-II/ 3b/2012). Both female and male mice were equally used for cell isolations.

Downloaded from https://www.science.org on September 07, 2023

Chemokines

Purified recombinant mouse CCL19 (R&D Systems, 440-M3-025) was used throughout the study. The AF555-CCL19 was prepared with the Alexa Fluor 555 Microscale Protein Labeling Kit (Invitrogen, A30007) according to the manufacturer's instructions. For the final elution, Zeba Spin Desalting Columns (7K MWCO; Thermo Fisher Scientific, 89882) were used, and the final protein concentration was measured with NanoDrop using unlabeled CCL19 as a control.

Cell culture

All cells were grown and maintained at +37°C in a humidified incubator with 5% CO_2.

Dendritic cells (Hoxb8 and bone marrow–derived)

DCs were differentiated either from conditionally immortalized hematopoietic progenitor cells [Hoxb8; described previously (*51*, *52*)] or from the bone marrow of 6- to 11-week-old female or male C57BL/6J mice. Bone marrow from Lfc-WT (+/+) and Lfc-KO (−/−) 129 mice was a gift from K.-D. Fischer (*33*). CCL19-KO (−/−) DCs were generated from the bone marrow of C57BL/6J KO mice. Immortalized hematopoietic precursor cells were generated from WT, CCR7-KO (−/−), or Lifeact-GFP C57BL/6J mouse bone marrow by retroviral delivery of an estrogen-regulated form of Hoxb8. Blasticidin-selected cells were maintained in basic "R10" medium consisting of RPMI 1640 medium (Gibco, 21875-034) with 10% heat-inactivated fetal bovine serum (FBS) (Gibco, 10270-106), penicillin (100 U/ml)/streptomycin (100 μg/ml) (Gibco, 15140-122), and 50 μM β-mercaptoethanol (Gibco, 31350-010) supplemented with 5% supernatant of an Flt3L-producing cell line and 1 μM estrogen (Sigma-Aldrich, E2758). Differentiation from Hoxb8 precursor cells was induced by estrogen washout. DCs were differentiated by culturing 2×10^6 bone marrow cells or 4×10^5 to 5×10^5 Hoxb8 cells in R10 supplemented with 10 or 20% of house-generated granulocyte-macrophage colony-stimulating factor (GM-CSF) hybridoma supernatant for 9 days [detailed protocol in (*52*)]. After this, nonadherent cells were collected, and DC maturation was induced by overnight incubation with lipopolysaccharide (LPS, 200 ng/ml) from *Escherichia coli* 0127:B8 (Sigma-Aldrich, L4516). DC differentiation and maturation were confirmed for each cell batch with flow cytometry and antibodies against CD11c (CD11c-APC, clone N418, Invitrogen, 17-0114-82, RRID:AB_469346) and major histocompatibility complex class II (MHC II-eFluor450, M5/114.15.2, Invitrogen, 48-5321-82, RRID:AB_1272204) as previously described (*52*). Before every experiment, DCs were washed and allowed to recover at least for 1 hour in R10.

T cells

T cells were isolated from the spleens of female or male C57BL/6J mice with EasySep Mouse T cell Isolation Kit (STEMCELL Technologies, 19851) according to the manufacturer's instructions. Isolated T cells were then activated by plating the cells on cell-culture wells coated overnight with antibodies (1 μg/ml) against CD3e and CD28 (Invitrogen, 16-0031-82, RRID:AB_468847 and 16-0281-82, RRID:AB_468921) for 2 days in R10 medium supplemented with interleukin-2 (IL-2) (10 ng/ml; 402-ML-020, R&D Systems). After this, activated T cells were collected and expanded in IL-2 containing R10.

Neutrophil-like cells

Neutrophil-like HL-60 (a gift from A. Diz-Muñoz) and PLB-985 cells (from DSMZ, ACC 139) were maintained in RPMI 1640 (Gibco, 21875-034) supplemented with 10% FBS (Gibco, 10270-106) and 20 mM Hepes (Sigma-Aldrich, H0887-100ML). For differentiation, cells were kept for 6 days in a medium containing 1.25% dimethyl sulfoxide (DMSO) (cell-culture grade; Sigma-Aldrich), and the differentiation status was validated using flow cytometry (CD11b-APC-Vio770, Miltenyi Biotec, 130-110-614, RRID:AB_2654674). Before experimentation, differentiated cells were washed three times to remove DMSO.

Migration assays

In collagen

A total of 3×10^5 DCs or 1.5×10^5 differentiated neutrophil-like cells were mixed with collagen I solution containing purified bovine collagen I (1.7 mg/ml; 5005, Advanced Biomatrix), 1× minimum essential medium (Gibco, 21430020), and 0.3% of sodium bicarbonate ($NaHCO_3$; Sigma-Aldrich, s8761) in R10 medium (total volume 300 μl). The collagen-cell mixture was then cast in the custom-made chamber, and collagen was allowed to polymerize for 45 min at 37°C before overlaying the gel with either recombinant mouse CCL19 (0.6 μg/ml) (for DCs, R&D Systems, 440-M3-025), 25 nM fMLP (for neutrophil-like cells, Sigma-Aldrich, F3506-5MG), or with 10-kDa FITC-dextran (Sigma-Aldrich, FD10S). In the case of FITC-dextran diffusion, the assay was done without collagen-embedded cells. The chamber was sealed with paraffin, and cell migration was recorded immediately with time-lapse video microscopy for 4 to 8 hours at 37°C, 5% CO_2 with 60-s intervals. The average migration speed of the entire cell population toward the chemokine source was determined with a custom-made ImageJ plugin (by R. Hauschild, Institute of Science and Technology Austria). Briefly, images were background-corrected, and particle filtering was used to discard objects other than cells. For each frame, the lateral displacement optimizing its overlap with the previous frame was determined and divided by the time interval between the frames, yielding the y-directed migration speed of the cell population over time. The respective script can be shared upon request. In the case of uniform CCL19, CCL19 (0.3 μg/ml) was mixed with collagen and DCs before polymerization, after which the gel was overlaid with different concentrations of CCL19. Single-cell migration characteristics were analyzed by tracking the individual cells with TrackMate.

Under agarose

Four hundred microliters of agarose mix containing 1% UltraPure Agarose (Invitrogen, 16500100) in phenol-free R10 medium supplemented with 1× Hanks' balanced salt solution (pH 7.3; Sigma-Aldrich, H1387) and 10% FBS was poured on custom-made chambers with a diameter of 17 mm and allowed to polymerize for 35 min. In the case of gradient chemokine, two holes (diameter, 2 mm) were punched 1 cm apart into the agarose for 0.5 to 1 μl of pelleted cells and for 17.5 ng of CCL19 in phenol-free R10 (Gibco, 11835030) for a chemokine source. For uniform chemokine concentration, 17.5 ng of CCL19 was mixed with the agarose mix before polymerization, and only one hole was punched into the agarose. Cells were stained with NucBlue (Invitrogen, R37605) for 15 min at 37°C and washed once with R10 before injecting into the agarose hole. Cell migration was recorded with an inverted Nikon Ti wide-field fluorescent microscope at 37°C with 5% CO_2 for 6 to 12

Downloaded from https://www.science.org on September 07, 2023

hours with 1-min intervals and 4× or 10× objective. For comigration studies, some of the cells were stained with 10 μM of TAMRA SE [5-(and-6)-carboxytetramethylrhodamine, succinimidyl ester; Invitrogen, C1171] for 10 min at room temperature (RT), washed with R10, and allowed to recover for 30 min before use. For dynamin inhibition, DCs were treated with 100 μM Dynasore (Sigma-Aldrich, D7693) or an equal volume of DMSO for 1 hour before migration under agarose supplemented with Dynasore/DMSO.

In the above-described setup, a thin layer of chemokine-containing medium covers the space between the glass surface and the agarose layer and is left at the bottom of the punched hole, where the pelleted cells are pipetted. Therefore, no initial chemokine gradient should be formed between the cell source and the agarose. However, to exclude a potential chemokine gradient still being formed with uniform CCL19 in this setup, we initially compared cell migration when DCs were placed into the hole as a 1-μl pellet or in 7 μl of a medium containing the same CCL19 concentration as the agarose. This volume fills the hole in agarose completely. Because cells were migrating out of the hole equally well in both cases (movie S13), we performed all other under agarose experiments in this paper with 0.5 to 1 μl of pelleted cells.

For the "sink and sensor" setup, three 1.5-mm holes 5 mm apart were punched into the agarose. Pelleted DCs (2.5 μl) were mixed with 10 ng of CCL19 in colorless R10 with a total volume of 4 μl and injected into one of the edge holes. For chemokine-only controls, CCL19 (10 ng/4 μl) in colorless R10 was used. A total of 15,000 NucBlue stained DCs in 4 μl of colorless R10 were injected into the middle hole as the sensor cells and the migration of these cells were recorded with a fluorescent microscope. In the case of Lfc-WT and Lfc-KO DCs, cells were incubated with the chemokine mix [CCL19 (10 ng/4 μl) in colorless R10] at 37°C for 3 hours before injection into the agarose hole.

T cell migration together with DCs

T cells were stained with TAMRA (Invitrogen) for 10 min at RT, washed with R10, and allowed to recover for 30 min before use. Both Lifeact-GFP DCs and T cells were also stained with NucBlue. An equal number of both cell types were mixed and pipetted into a 2-mm hole in agarose. The gel was prepared otherwise as above but with 0.75% of UltraPure Agarose (Invitrogen, 16500100). Cells were imaged with an inverted Nikon Ti widefield fluorescent microscope at 37°C with 5% CO_2 for 3 hours with 1-min interval and 10× objective. To quantify T cell migration in front of DCs, the Lifeact-GFP–expressing DCs were selected by filtering (variance 30) and thresholding, and this selection was used to clear out T cells interacting with DCs from the T cell/555 channel, thereby leading to a movie showing only T cells migrating in front of DCs, which was then used for tracking with TrackMate.

Image analysis and statistics

Fiji was used for all image processing and analysis in this work, and all graphs and statistical analyses were done with GraphPad Prism. The number of independent biological replicates and experiments used for the graphs as well as used statistical tests are described in figure legends. For most results, means ± SD were used.

Quantification of cell migration

Cell migration was quantified using TrackMate plugin for automated cell tracking (*53*) with carefully adjusted parameters and filtering to exclude unmoving dead cells and bad tracks. The same parameters were used consistently in different conditions to obtain comparable results. The NucBlue channel (405) was used for the tracking. The cell reservoir was cleared from the time-lapse images by appropriate filtering and thresholding before tracking. The kymograph showing the progress of the leading edge of the migrating DC population (Fig. 1H) was created using variance filtering, thresholding, and finding the edge followed by reslicing to obtain a kymograph.

Quantification of internalized AF555-CCL19 from immunofluorescence images

The integrated density of AF555-CCL19 inside the cells was measured from the middle slice by manually drawing a selection based on the actin staining. For the quantification, the measured integrated density was normalized to the corresponding cell area.

Quantification of DC length

The mean length of a migrating DC under agarose (used for the model) was measured manually from bright-field images.

Immunofluorescence

DCs were allowed to migrate under agarose with uniform AF555-CCL19 for 2 to 3 hours before fixing with prewarmed (37°C) 4% paraformaldehyde (PFA; Science Services, e15714) for 15 min at RT. The agarose layer was removed, PFA was washed away 3× with PBS, and cells were stained with 4′,6-diamidino-2-phenylindole (DAPI) and Alexa Fluor 488 phalloidin (A12379, Invitrogen) for 1 hour at RT, followed by 3× PBS wash and mounting with ProLong Gold Antifade Mountant (Invitrogen, P36930). Samples were imaged with Zeiss LSM880 upright or inverted microscopes with Plan-Apochromat 40×/numerical aperture (NA) 1.2 water or 40×/NA 1.4 oil objective.

Uptake of AF555-CCL19

A total of 300,000 cells were incubated with 100 ng of AF555-CCL19 in 100 μl of colorless R10 for 0, 30, or 60 min at 37°C. Cells were then transferred on ice, and the AF555 fluorescence in cells was measured with a FACSCanto II flow cytometer (BD Biosciences). Cells without any AF555-CCL19 were used as a negative control, and this value was subtracted from the rest. To measure the level of AF555-CCL19 in the medium, 600,000 DCs were incubated with 11 ng of AF555-CCL19 in 100 μl of colorless R10 for 0, 30, or 60 min at 37°C, after which the samples were centrifuged (300*g*, 5 min) and the AF555 fluorescence of the supernatants was measured with BioTek Synergy H1 plate reader. Colorless R10 medium was used as a negative control. The measured fluorescence values were normalized to the sum of the corresponding experiment.

Flow cytometry to measure CCR7 cell surface level

A total of 300,000 to 400,000 cells were incubated with different concentrations of CCL19 in 100 μl of R10 for different time points at 37°C in a 96-well plate, after which cells were fixed by adding an equal volume of 4% PFA on ice for 15 min. Cells were washed 2× with PBS and stored in fluorescence-activated cell sorting (FACS) buffer (2 mM EDTA and 1% BSA in PBS) at 4°C or washed with FACS buffer and immediately stained. Cells were incubated first with α-CD16/CD32 (5 μg/ml) (eBioscience, 14-0161-85, RRID:AB_467134) in FACS buffer for 10 min at RT to block Fc receptors. Cell surface CCR7 was stained by incubating the cells with 1:300 of mCCR7-PE antibody (eBioscience, 4B12,

Downloaded from https://www.science.org on September 07, 2023

12-1971-82, RRID:AB_465905) in FACS buffer containing the FC block for 1 hour at RT, after which cells were washed 3× with FACS buffer before measuring the median phycoerythrin signal with a FACSCanto II flow cytometer (BD Biosciences).

Simulation

Details of the particle-based model, simulation settings for comparison with the under agarose assays, microfluidic device experiments, and heterogeneous cell populations, as well as parameter values used in simulations can be found in data file S1.

Microfabricated devices

The microfluidic design was drawn in CorelDraw 2019, converted to Gerber format with LinkCad, and printed on a 5-inch chrome photomask (JD Photo Data). The 5-μm-high master wafer was made by ultraviolet photolithography using SU-8 TF 6005 photoresist (Kayaku Advanced Materials) and characterized with a profilometer. The master wafer was then vapor-treated with 1*H*,1*H*,2*H*,2*H*-perfluorooctyl-trichlorosilane for 1 hour. Polydimethylsiloxane (PDMS) devices were made with SYLGARD 184 Elastomer Kit (Dow Corning) using a ratio of 10:1. Mixed PMDS was poured on the wafer, degassed in a vacuum chamber, and baked overnight at 80°C. The hardened PDMS layer was then peeled off, cut into single devices, and through-holes of 2-mm diameter were punched out. Last, the devices were bonded onto ethanol-washed coverslips by oxygen plasma followed by sealing at 85°C for 15 min to make the bond permanent. The finished PDMS device with 50 × 5-μm channels was filled and preincubated with R10 overnight at 37°C, after which the device reservoirs were emptied, and the whole device was filled with either CCL19 (2.5 μg/ml) or AF555-CCL19 (11 μg/ml) in colorless R10. The chemokine was allowed to equilibrate for a minimum of 3 hours before the addition of 0.5 to 1 μl of pelleted NucBlue stained DCs to the cell reservoir. Cells were imaged every 1 min with an inverted Nikon Ti wide-field fluorescent microscope at 37°C with 5% CO_2 for 12 hours and 4× objective. The number of cells migrating toward the open-end and closed-end was manually counted.

Supplementary Materials

This PDF file includes:
Figs. S1 to S5
References (*54*–*59*)

Other Supplementary Material for this manuscript includes the following:
Data files S1 and S2
Movies S1 to S13
MDAR Reproducibility Checklist

REFERENCES AND NOTES

1. U. H. von Andrian, T. R. Mempel, Homing and cellular traffic in lymph nodes. *Nat. Rev. Immunol.* **3**, 867–878 (2003).
2. T. Lämmermann, W. Kastenmüller, Concepts of GPCR-controlled navigation in the immune system. *Immunol. Rev.* **289**, 205–231 (2019).
3. A. Rot, U. H. von Andrian, Chemokines in innate and adaptive host defense: Basic chemokinese grammar for immune cells. *Annu. Rev. Immunol.* **22**, 891–928 (2004).
4. J. Wang, H. Knaut, Chemokine signaling in development and disease. *Development* **141**, 4199–4205 (2014).
5. J. Bussmann, E. Raz, Chemokine-guided cell migration and motility in zebrafish development. *EMBO J.* **34**, 1309–1318 (2015).
6. C. E. Hughes, R. J. B. Nibbs, A guide to chemokines and their receptors. *FEBS J.* **285**, 2944–2971 (2018).
7. T. A. Springer, Traffic signals for lymphocyte recirculation and leukocyte emigration: The multistep paradigm. *Cell* **76**, 301–314 (1994).
8. R. Majumdar, M. Sixt, C. A. Parent, New paradigms in the establishment and maintenance of gradients during directed cell migration. *Curr. Opin. Cell Biol.* **30**, 33–40 (2014).
9. A. Belmadani, P. B. Tran, D. Ren, S. Assimacopoulos, E. A. Grove, R. J. Miller, The chemokine stromal cell-derived factor-1 regulates the migration of sensory neuron progenitors. *J. Neurosci.* **25**, 3995–4003 (2005).
10. M. Doitsidou, M. Reichman-Fried, J. Stebler, M. Köprunner, J. Dörries, D. Meyer, C. V. Esguerra, T. Leung, E. Raz, Guidance of primordial germ cell migration by the chemokine SDF-1. *Cell* **111**, 647–659 (2002).
11. J. J. Rose, J. F. Foley, P. M. Murphy, S. Venkatesan, On the mechanism and significance of ligand-induced internalization of human neutrophil chemokine receptors CXCR1 and CXCR2. *J. Biol. Chem.* **279**, 24372–24386 (2004).
12. R. G. Endres, N. S. Wingreen, Accuracy of direct gradient sensing by single cells. *Proc. Natl. Acad. Sci. U.S.A.* **105**, 15749–15754 (2008).
13. F. Crick, Diffusion in embryogenesis. *Nature* **225**, 420–422 (1970).
14. S. Lau, A. Feitzinger, G. Venkiteswaran, J. Wang, S. W. Lewellis, C. A. Koplinski, F. C. Peterson, B. F. Volkman, M. Meier-Schellersheim, H. Knaut, A negative-feedback loop maintains optimal chemokine concentrations for directional cell migration. *Nat. Cell Biol.* **22**, 266–273 (2020).
15. G. Venkiteswaran, S. W. Lewellis, J. Wang, E. Reynolds, C. Nicholson, H. Knaut, Generation and dynamics of an endogenous, self-generated signaling gradient across a migrating tissue. *Cell* **155**, 674–687 (2013).
16. M. Wong, L. R. Newton, J. Hartmann, M. L. Hennrich, M. Wachsmuth, P. Ronchi, A. Guzmán-Herrera, Y. Schwab, A.-C. Gavin, D. Gilmour, Dynamic buffering of extracellular chemokine by a dedicated scavenger pathway enables robust adaptation during directed tissue migration. *Dev. Cell* **52**, 492–508.e10 (2020).
17. E. Donà, J. D. Barry, G. Valentin, C. Quirin, A. Khmelinskii, A. Kunze, S. Durdu, L. R. Newton, A. Fernandez-Minan, W. Huber, M. Knop, D. Gilmour, Directional tissue migration through a self-generated chemokine gradient. *Nature* **503**, 285–289 (2013).
18. L. Tweedy, P. A. Thomason, P. I. Paschke, K. Martin, L. M. Machesky, M. Zagnoni, R. H. Insall, Seeing around corners: Cells solve mazes and respond at a distance using attractant breakdown. *Science* **369**, eaay9792 (2020).
19. L. Tweedy, R. H. Insall, Self-generated gradients yield exceptionally robust steering cues. *Front. Cell Dev. Biol.* **8**, 133 (2020).
20. A. J. Muinonen-Martin, O. Susanto, Q. Zhang, E. Smethurst, W. J. Faller, D. M. Veltman, G. Kalna, C. Lindsay, D. C. Bennett, O. J. Sansom, R. Herd, R. Jones, L. M. Machesky, M. J. O. Wakelam, D. A. Knecht, R. H. Insall, Melanoma cells break down LPA to establish local gradients that drive chemotactic dispersal. *PLOS Biol.* **12**, e1001966 (2014).
21. R. Yoshida, T. Imai, K. Hieshima, J. Kusuda, M. Baba, M. Kitaura, M. Nishimura, M. Kakizaki, H. Nomiyama, O. Yoshie, Molecular cloning of a novel human CC chemokine EBI1-ligand chemokine that is a specific functional ligand for EBI1, CCR7. *J. Biol. Chem.* **272**, 13803–13809 (1997).
22. R. Yoshida, M. Nagira, M. Kitaura, N. Imagawa, T. Imai, O. Yoshie, Secondary lymphoid-tissue chemokine is a functional ligand for the CC chemokine receptor CCR7. *J. Biol. Chem.* **273**, 7118–7122 (1998).
23. M. Nagira, T. Imai, K. Hieshima, J. Kusuda, M. Ridanpää, S. Takagi, M. Nishimura, M. Kakizaki, H. Nomiyama, O. Yoshie, Molecular cloning of a novel human CC chemokine secondary lymphoid-tissue chemokine that is a potent chemoattractant for lymphocytes and mapped to chromosome 9p13. *J. Biol. Chem.* **272**, 19518–19524 (1997).
24. S. Yanagihara, E. Komura, J. Nagafune, H. Watarai, Y. Yamaguchi, EBI1/CCR7 is a new member of dendritic cell chemokine receptor that is up-regulated upon maturation. *J. Immunol.* **161**, 3096–3102 (1998).
25. M. L. Heuzé, P. Vargas, M. Chabaud, M. Le Berre, Y.-J. Liu, O. Collin, P. Solanes, R. Voituriez, M. Piel, A.-M. Lennon-Duménil, Migration of dendritic cells: Physical principles, molecular mechanisms, and functional implications. *Immunol. Rev.* **256**, 240–254 (2013).
26. J. Schwarz, V. Bierbaum, K. Vaahtomeri, R. Hauschild, M. Brown, I. de Vries, A. Leithner, A. Reversat, J. Merrin, T. Tarrant, T. Bollenbach, M. Sixt, Dendritic cells interpret haptotactic chemokine gradients in a manner governed by signal-to-noise ratio and dependent on GRK6. *Curr. Biol.* **27**, 1314–1325 (2017).
27. A. Leithner, A. Eichner, J. Müller, A. Reversat, M. Brown, J. Schwarz, J. Merrin, D. J. J. de Gorter, F. Schur, J. Bayerl, I. de Vries, S. Wieser, R. Hauschild, F. P. L. Lai, M. Moser, D. Kerjaschki, K. Rottner, J. V. Small, T. E. B. Stradal, M. Sixt, Diversified actin protrusions promote environmental exploration but are dispensable for locomotion of leukocytes. *Nat. Cell Biol.* **18**, 1253–1259 (2016).

Downloaded from https://www.science.org on September 07, 2023

28. S. H. Zigmond, Ability of polymorphonuclear leukocytes to orient in gradients of chemotactic factors. *J. Cell Biol.* **75**, 606–616 (1977).
29. P. Herzmark, K. Campbell, F. Wang, K. Wong, H. El-Samad, A. Groisman, H. R. Bourne, Bound attractant at the leading vs. the trailing edge determines chemotactic prowess. *Proc. Natl. Acad. Sci. U.S.A.* **104**, 13349–13354 (2007).
30. N. Lorenz, E. J. Loef, I. D. Kelch, D. J. Verdon, M. M. Black, M. J. Middleditch, D. R. Greenwood, E. S. Graham, A. E. Brooks, P. R. Dunbar, N. P. Birch, Plasmin and regulators of plasmin activity control the migratory capacity and adhesion of human T cells and dendritic cells by regulating cleavage of the chemokine CCL21. *Immunol. Cell Biol.* **94**, 955–963 (2016).
31. J. M. Laufer, M. A. Hauser, I. Kindinger, V. Purvanov, A. Pauli, D. F. Legler, Chemokine receptor CCR7 triggers an endomembrane signaling complex for spatial Rac activation. *Cell Rep.* **29**, 995–1009.e6 (2019).
32. F. J. Eppler, T. Quast, W. Kolanus, Dynamin2 controls Rap1 activation and integrin clustering in human T lymphocyte adhesion. *PLOS ONE* **12**, e0172443 (2017).
33. A. Kopf, J. Renkawitz, R. Hauschild, I. Girkontaite, K. Tedford, J. Merrin, O. Thorn-Seshold, D. Trauner, H. Häcker, K.-D. Fischer, E. Kiermaier, M. Sixt, Microtubules control cellular shape and coherence in amoeboid migrating cells. *J. Cell Biol.* **219**, e201907154 (2020).
34. R. Pathak, C. Dermardirossian, GEF-H1: Orchestrating the interplay between cytoskeleton and vesicle trafficking. *Small GTPases* **4**, 174–179 (2013).
35. J. Alanko, J. Ivaska, Endosomes: Emerging platforms for integrin-mediated FAK signalling. *Trends Cell Biol.* **26**, 391–398 (2016).
36. C. Arnette, K. Frye, I. Kaverina, Microtubule and actin interplay drive intracellular c-Src trafficking. *PLOS ONE* **11**, e0148996 (2016).
37. J. Cremer, T. Honda, Y. Tang, J. Wong-Ng, M. Vergassola, T. Hwa, Chemotaxis as a navigation strategy to boost range expansion. *Nature* **575**, 658–663 (2019).
38. X. Fu, S. Kato, J. Long, H. H. Mattingly, C. He, D. C. Vural, S. W. Zucker, T. Emonet, Spatial self-organization resolves conflicts between individuality and collective migration. *Nat. Commun.* **9**, 2177 (2018).
39. L. Tweedy, D. A. Knecht, G. M. Mackay, R. H. Insall, Self-generated chemoattractant gradients: Attractant depletion extends the range and robustness of chemotaxis. *PLoS Biol.* **14**, e1002404 (2016).
40. J. Jhawar, R. G. Morris, U. R. Amith-Kumar, M. Danny Raj, T. Rogers, H. Rajendran, V. Guttal, Noise-induced schooling of fish. *Nat. Phys.* **16**, 488–493 (2020).
41. G. Bardi, M. Lipp, M. Baggiolini, P. Loetscher, The T cell chemokine receptor CCR7 is internalized on stimulation with ELC, but not with SLC. *Eur. J. Immunol.* **31**, 3291–3297 (2001).
42. C. Otero, M. Groettrup, D. F. Legler, Opposite fate of endocytosed CCR7 and its ligands: Recycling versus degradation. *J. Immunol.* **177**, 2314–2323 (2006).
43. G. D'Amico, G. Frascaroli, G. Bianchi, P. Transidico, A. Doni, A. Vecchi, S. Sozzani, P. Allavena, A. Mantovani, Uncoupling of inflammatory chemokine receptors by IL-10: Generation of functional decoys. *Nat. Immunol.* **1**, 387–391 (2000).
44. S. Volpe, E. Cameroni, B. Moepps, S. Thelen, T. Apuzzo, M. Thelen, CCR2 acts as scavenger for CCL2 during monocyte chemotaxis. *PLOS ONE* **7**, e37208 (2012).
45. J. Stock, T. Kazmar, F. Schlumm, E. Hannezo, A. Pauli, A self-generated Toddler gradient guides mesodermal cell migration. *Sci. Adv.* **8**, eadd2488 (2022).
46. K. Schumann, T. Lämmermann, M. Bruckner, D. F. Legler, J. Polleux, J. P. Spatz, G. Schuler, R. Förster, M. B. Lutz, L. Sorokin, M. Sixt, Immobilized chemokine fields and soluble chemokine gradients cooperatively shape migration patterns of dendritic cells. *Immunity* **32**, 703–713 (2010).
47. J. Hirose, H. Kawashima, M. Swope Willis, T. A. Springer, H. Hasegawa, O. Yoshie, M. Miyasaka, Chondroitin sulfate B exerts its inhibitory effect on secondary lymphoid tissue chemokine (SLC) by binding to the C-terminus of SLC. *Biochim. Biophys. Acta* **1571**, 219–224 (2002).
48. R. Mayor, S. Etienne-Manneville, The front and rear of collective cell migration. *Nat. Rev. Mol. Cell Biol.* **17**, 97–109 (2016).
49. A. Martín-Fontecha, S. Sebastiani, U. E. Höpken, M. Uguccioni, M. Lipp, A. Lanzavecchia, F. Sallusto, Regulation of dendritic cell migration to the draining lymph node: Impact on T lymphocyte traffic and priming. *J. Exp. Med.* **198**, 615–621 (2003).
50. T. F. Robertson, Y. Hou, J. Schrope, S. Shen, J. Rindy, J.-D. Sauer, H. Q. Dinh, A. Huttenlocher, A tessellated lymphoid network provides whole-body T cell surveillance in zebrafish. *Proc. Natl. Acad. Sci. U.S.A.* **120**, e2301137120 (2023).
51. V. Redecke, R. Wu, J. Zhou, D. Finkelstein, V. Chaturvedi, A. A. High, H. Häcker, Hematopoietic progenitor cell lines with myeloid and lymphoid potential. *Nat. Methods* **10**, 795–803 (2013).
52. A. Leithner, J. Renkawitz, I. De Vries, R. Hauschild, H. Häcker, M. Sixt, Fast and efficient genetic engineering of hematopoietic precursor cells for the study of dendritic cell migration. *Eur. J. Immunol.* **48**, 1074–1077 (2018).
53. J.-Y. Tinevez, N. Perry, J. Schindelin, G. M. Hoopes, G. D. Reynolds, E. Laplantine, S. Y. Bednarek, S. L. Shorte, K. W. Eliceiri, TrackMate: An open and extensible platform for single-particle tracking. *Methods* **115**, 80–90 (2017).
54. H. Chaté, Dry aligning dilute active matter. *Annu. Rev. Condens. Matter Phys.* **11**, 189–212 (2020).
55. R. Alert, X. Trepat, Physical models of collective cell migration. *Annu. Rev. Condens. Matter Phys.* **11**, 77–101 (2020).
56. P. Maiuri, J.-F. Rupprecht, S. Wieser, V. Ruprecht, O. Bénichou, N. Carpi, M. Coppey, S. De Beco, N. Gov, C.-P. Heisenberg, C. Lage Crespo, F. Lautenschlaeger, M. Le Berre, A.-M. Lennon-Dumenil, M. Raab, H.-R. Thiam, M. Piel, M. Sixt, R. Voituriez, Actin flows mediate a universal coupling between cell speed and cell persistence. *Cell* **161**, 374–386 (2015).
57. M. Kang, C. A. Day, A. K. Kenworthy, E. DiBenedetto, Simplified equation to extract diffusion coefficients from confocal FRAP data. *Traffic* **13**, 1589–1600 (2012).
58. C. T. Veldkamp, E. Kiermaier, S. J. Gabel-Eissens, M. L. Gillitzer, D. R. Lippner, F. A. DiSilvio, C. J. Mueller, P. L. Wantuch, G. R. Chaffee, M. W. Famiglietti, D. M. Zgoba, A. A. Bailey, Y. Bah, S. J. Engebretson, D. R. Graupner, E. R. Lackner, V. D. LaRosa, T. Medeiros, M. L. Olson, A. J. Phillips, H. Pyles, A. M. Richard, S. J. Schoeller, B. Touzeau, L. G. Williams, M. Sixt, F. C. Peterson, Solution structure of CCL19 and identification of overlapping CCR7 and PSGL-1 binding sites. *Biochemistry* **54**, 4163–4166 (2015).
59. T. Vicsek, A. Czirók, E. Ben-Jacob, I. Cohen, O. Shochet, Novel type of phase transition in a system of self-driven particles. *Phys. Rev. Lett.* **75**, 1226–1229 (1995).

Acknowledgments: We thank I. de Vries and the Scientific Service Units (Life Sciences, Bioimaging, Nanofabrication, Preclinical and Miba Machine Shop) of the Institute of Science and Technology Austria for excellent support, as well as all the rotation students assisting in the laboratory work (B. Zens, H. Schön, and D. Babic). **Funding:** This work was supported by grants from the European Research Council under the European Union's Horizon 2020 research to M.S. (grant agreement no. 724373) and to E.H. (grant agreement no. 851288), and a grant by the Austrian Science Fund (DK Nanocell W1250-B20) to M.S. J.A. was supported by the Jenny and Antti Wihuri Foundation and Research Council of Finland's Flagship Programme InFLAMES (decision number: 357910). M.C.U. was supported by the European Union's Horizon 2020 research and innovation programme under the Marie Skłodowska-Curie grant agreement no. 754411. **Author contributions:** J.A. and M.S. conceived the experiments and wrote the manuscript together with E.H. and M.C.U. N.C. reviewed and corrected the manuscript. N.C. performed and analyzed the experiment with sink and sensor DCs, J. Stopp performed and analyzed the collagen migration assays with neutrophils, and J. Schwarz performed the FITC dextran diffusion experiment. All other experiments were performed and analyzed by J.A. The wafers for PDMS devices were designed and prepared by J.M. M.C.U. and E.H. developed the particle-based model. M.C.U performed the simulations and analyzed the simulation and experimental data. **Competing interests:** The authors declare that they have no competing interests. **Data and materials availability:** All data needed to evaluate the conclusions in the paper are present in the paper or the Supplementary Materials. Original videos will be made available on request due to the large file size. Raw trajectory data used to compare the simulations and experiments and a script to process and analyze the data are provided in a supplementary zip folder, published in Zenodo (https://doi.org/10.5281/zenodo.8133960). Custom-made Python codes to reproduce the findings from the particle-based simulations are available in a supplementary zip folder, published in Zenodo (https://doi.org/10.5281/zenodo.8133960).

Submitted 11 May 2022
Accepted 9 August 2023
Published 1 September 2023
10.1126/sciimmunol.adc9584

Downloaded from https://www.science.org on September 07, 2023

Science Immunology

CCR7 acts as both a sensor and a sink for CCL19 to coordinate collective leukocyte migration

Jonna Alanko, Mehmet Can Uçar, Nikola Canigova, Julian Stopp, Jan Schwarz, Jack Merrin, Edouard Hannezo, and Michael Sixt

Sci. Immunol., **8** (87), eadc9584.
DOI: 10.1126/sciimmunol.adc9584

View the article online
https://www.science.org/doi/10.1126/sciimmunol.adc9584
Permissions
https://www.science.org/help/reprints-and-permissions

Downloaded from https://www.science.org on September 07, 2023

Use of this article is subject to the Terms of service

Science Immunology (ISSN) is published by the American Association for the Advancement of Science. 1200 New York Avenue NW, Washington, DC 20005. The title *Science Immunology* is a registered trademark of AAAS.
Copyright © 2023 The Authors, some rights reserved; exclusive licensee American Association for the Advancement of Science. No claim to original U.S. Government Works

Science Immunology
AAAS

Supplementary Materials for

CCR7 acts as both a sensor and a sink for CCL19 to coordinate collective leukocyte migration

Jonna Alanko *et al.*

Corresponding author: Jonna Alanko, jonna.alanko@utu.fi; Edouard Hannezo, edouard.hannezo@ist.ac.at; Michael Sixt, michael.sixt@ist.ac.at

Sci. Immunol. **8**, eadc9584 (2023)
DOI: 10.1126/sciimmunol.adc9584

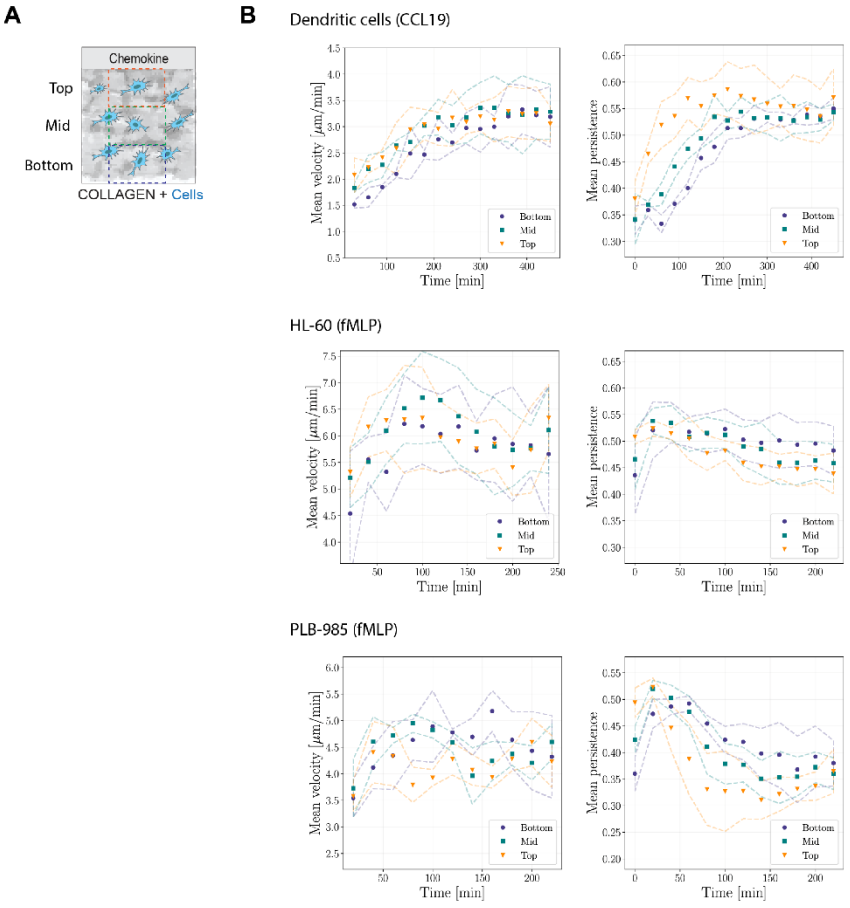
The PDF file includes:

Figs. S1 to S5
References (*54–59*)

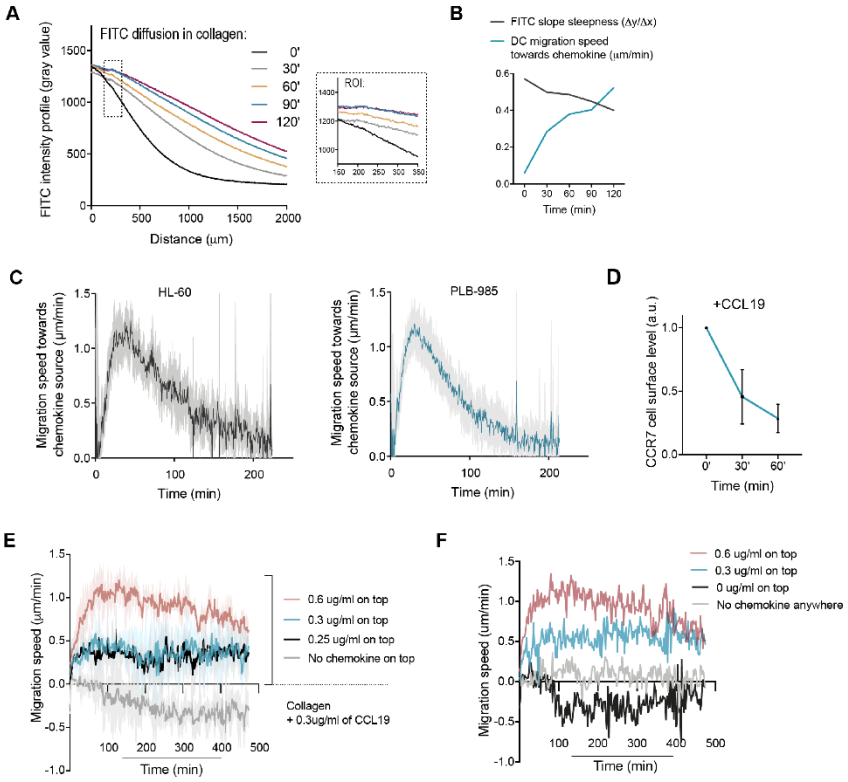
Other Supplementary Material for this manuscript includes the following:

Data files S1 and S2
Movies S1 to S13
MDAR Reproducibility Checklist

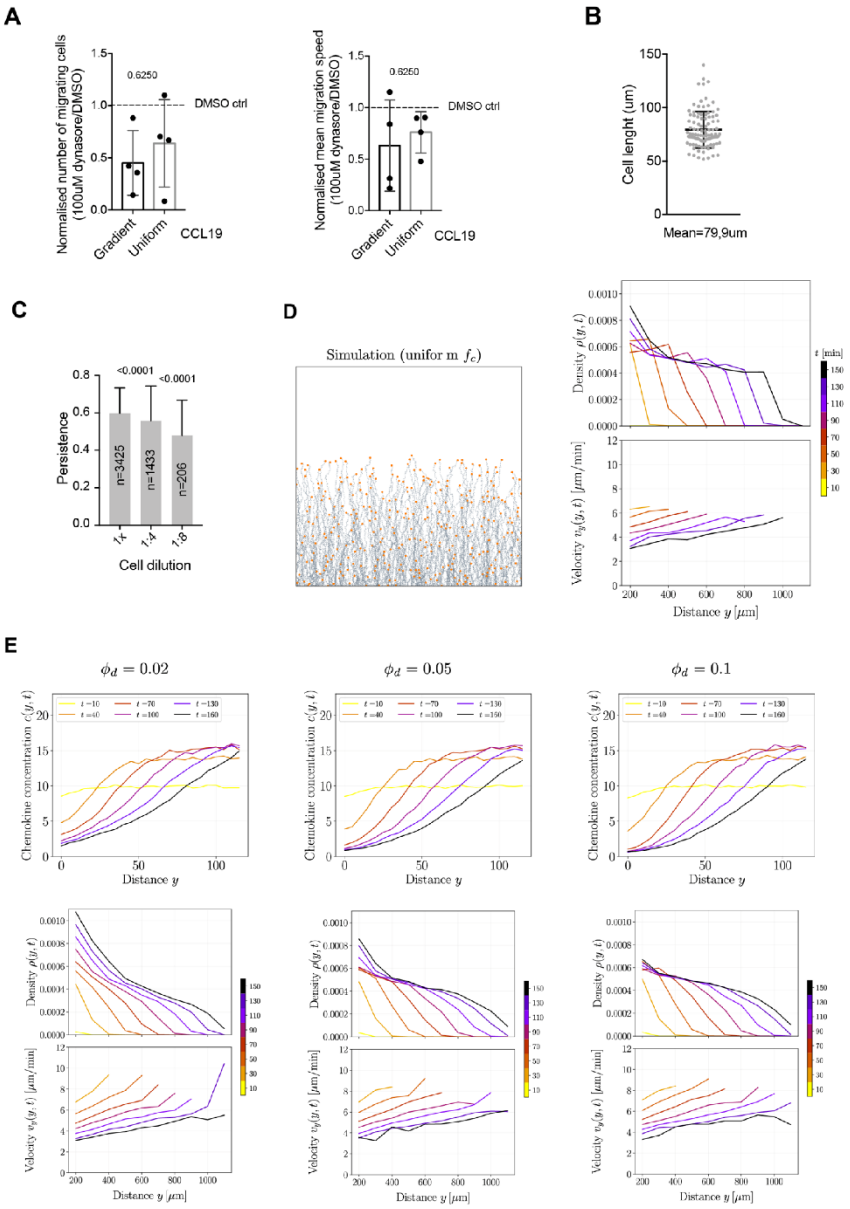
Supplementary figures



Supplementary Figure 1. A) Schematic of collagen assay with gradient chemokine. Cells are embedded into the collagen and the chemokine containing medium is added to the top. Single cell migration characteristics were analyzed at three different parts of the gel (top, middle, bottom). **B)** The mean velocity and migration persistence over time of DCs, HL-60s and PLB-985s migrating in CCL19 or fMLP gradient (n> 500 cells from 3 independent experiments). Plot markers indicate the mean values and the dashed lines represent means+/-SD.

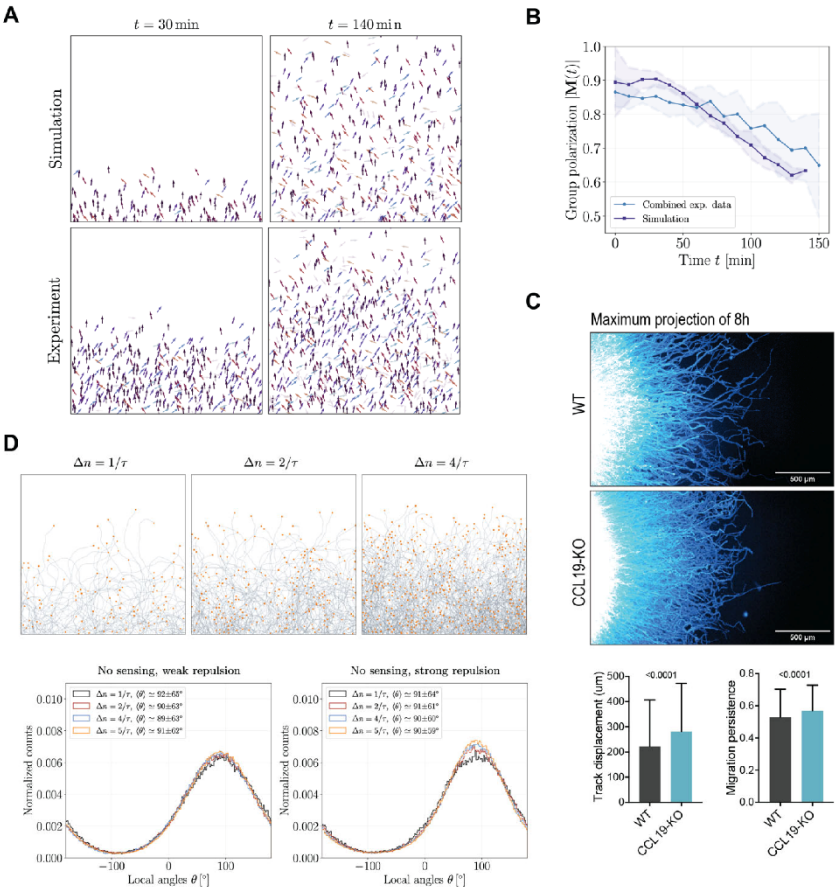


Supplementary Figure 2. A) Diffusion of 10kD FITC-dextran into 3D collagen over time. Shown are intensity profiles at different time points (0, 30, 60, 90 and 120min) in a 2000um region (similar to the cell assays) and a close up (ROI) from a shorter distance (representative of 2 independent experiments). **B)** A graph showing DC migration speed in 3D collagen (in Figure 1b) over the first 120min (um/min) and the slope steepness of FITC intensity profile. **C)** Migration speed of neutrophil-like HL-60 and PLB-985 cells towards 25nM fMLP in 3D collagen setup over time (mean+/-SD, 5-8 independent experiments). **D)** Antibody staining of CCR7 cell surface level in DCs incubated with 250ng/ml of CCL19 for 0, 30 or 60min (n=2-3 from 3 independent experiments, mean+/-SD). **E)** Corresponding curves for the bar plot shown in Figure 2e. The graph shows the mean migration speed of DCs in collagen with 0.3ug/ml CCL19 towards the upper compartment with different CCL19 concentration (n=3 independent experiments, mean+/-SD). **F)** Representative curves from one experiment showing also the mean migration speed of cells in case without any chemokine.

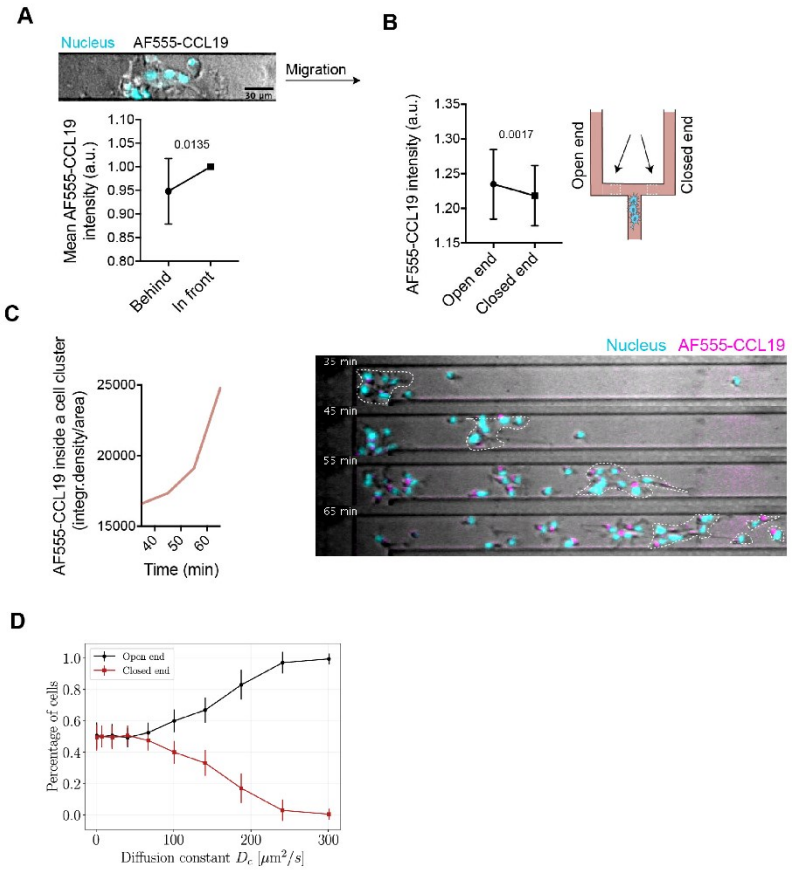


Supplementary Figure 3. A) DCs treated with 100μM of dynamin inhibitor (dynasore) or DMSO migrating under agarose with gradient or uniform CCL19. The number of migrating DCs (left panel) and

the mean migration speed (right panel) of the dynasore treated cells were quantified and normalized to the corresponding values of the DMSO treated cells (n=4 independent experiments, mean+/-SD, Wilcoxon matched-pairs signed rank test). **B)** Quantification of the average length of DC migrating under agarose with uniform CCL19 (n=381 cells from 4 exp, 3 independent experiments, mean+/-SD). **C)** Persistence of DCs (1x, 1:4 and 1:8 dilutions) migrating from a 2 mm hole under agarose with uniform CCL19 (n=3425, 1433, 206 cells from 3 independent experiments, mean+/-SD, Mann Whitney test). **D)** (Left) Exemplary cell trajectories obtained from simulations with a fixed value of chemotactic strength f_c uniformly assigned to all available cells. Although the spatio-temporal dynamics are qualitatively similar to the data, the trajectories exhibit a sharper density front than those of the experimental density profiles and with simulated densities observed in the case of varying f_c. (Right) Time evolution of cell densities (top) and velocities (bottom) for uniform f_c showing that densities propagate as a wave while reflecting the sharp density front, and velocities decay over time as in Fig.4C but do not capture the large velocity components for the outlier cells leading at the front (average, n>8000 cell trajectories from 10 simulations). **E)** Simulations demonstrating the effect of varying degree of chemokine depletion (2, 5 or 10%) by cells on chemokine gradient, cell density and velocity at different time points (average, n>16000 cell trajectories from 20 simulations).



Supplementary Figure 4. A) Representation of instantaneous cell polarities (arrows) at different time points from simulations (top) and experiments (bottom). Color-code on the arrows indicate the corresponding local angle values with black denoting θ=+90°. At large times (right panels) as the population has extensively migrated, we observe larger fraction of cells with polarities deviating from the vertical orientation pointing away from the source. **B)** Group polarization decays monotonically over time both in simulations and experimental data. Averages are taken from n=4 independent experiments and n=50 simulations where the shaded regions denote means+-SDs. **C)** Maximum projection of 8h imaging of nuclei of migrating WT and CCL19-KO DCs. The graphs below show the mean track displacement and migration persistence (mean+/-SD, n>3000 cells from 2 exp). **D)** Simulations testing the effect of inhibiting chemotactic sensing of cells for different population densities. (Top) Exemplary cell trajectories and (bottom) corresponding histograms of local angles as a proxy of cell polarity exhibit the absence of density dependence on the directional bias of the migrating cell population, even for increased cell-cell repulsion and higher self-propulsion speed than simulations of WT cells (n>3000 cell trajectories from 20 simulations).



Supplementary Figure 5. A) Example of a DC cluster migrating in microfluidic channel with uniform CCL19 (nuclei in cyan, AF555-CCL19 in white) and quantification of normalized mean intensity of AF555-CCL19 in microfluidic channel in front and behind of a migrating cell cluster (n=10 clusters from 4 samples, 2 independent experiments, mean+/-SD, Mann Whitney test). **B)** AF555-CCL19 intensity (normalized to the corresponding background value) in the microfluidic channel on the side of open-end and closed-end channels right before the decision of direction is made by the entering cell cluster, and a schematic illustrating the sites of measurements (while dashed line boxes) (n=8 measurements from 4 samples, 2 independent experiments, mean+/-SD, paired t-test). **C)** Quantification of the increasing AF555-CCL19 intensity (integrated density/area) inside a moving DC cluster over time in a microfluidic channel filled with uniform AF555-CCL19 and example snapshots. The white dashed line indicates the measured cell cluster. **D)** Predictions from particle-based simulations on the percentage of cells entering the open- (black) vs. the closed-end (red) channels as a function of the diffusion coefficient of the chemokine. The probability of cells entering the open-end channel increases monotonically with increasing chemokine diffusibility, where values of 100-200 um^2/s correspond to the experimentally relevant estimates (mean+/-SD, n>10000 cell trajectories from 50 simulations).

SM Movie legends

Movie 1. Matured DCs migrating towards CCL19 source (on top) in 3D collagen (25min/s, representative of 6 movies from 3 independent experiments).

Movie 2. PLB-985 cells migrating towards 25nM fMLP (on top) in 3D collagen (12.5min/s, rep of 5 independent experiments).

Movie 3. HL-60 cells migrating towards 25nM fMLP (on top) in 3D collagen (12.5min/s, rep of 5 independent experiments).

Movie 4. DCs migrating under agarose with gradient (left, CCL19 on the right side) or uniform (right) CCL19. Shown is nuclear stain in cyan (25min/s, rep of 5 movies from 3 independent experiments).

Movie 5. DCs migrating under agarose with uniform CCL19 over 10h period. Shown is brightfield and nuclear stain in magenta (representative of >5 movies from 3 independent experiments).

Movie 6. TAMRA-stained WT or CCR7-KO DCs (magenta) co-migrating with WT DCs under agarose with uniform CCL19. All cells are stained with nuclear stain (cyan) (15min/s, representative of 7,9 from 3 independent experiments).

Movie 7. DCs migrating in collagen with 0.3ugml CCL19 and different concentrations of CCL19 on top (see Figure 2e, representatives of 3 independent experiments).

Movie 8. WT (left) and CCR7-KO (right) DCs migrating in PDMS device with uniform CCL19 (cell reservoir at the bottom). Shown is a nuclear stain in cyan together with brightfield (10min/s, rep of 9 (WT) movies from 3 independent experiments, 3 (CCR7-KO) from 2 independent experiments).

Movie 9. Lfc-WT (left) and Lfc-KO (right) DCs migrating in PDMS device with 2.5 ug/ml of uniform CCL19 (cell reservoir at the bottom). Shown is brightfield and nuclear stain in cyan (representative of n ≥ 5 from 3 independent experiments).

Movie 10. Lfc-WT (left) and Lfc-KO (right) DCs migrating in PDMS device with 0.5 ug/ml of uniform CCL19 (cell reservoir at the bottom). Shown is brightfield and nuclear stain in cyan (representative of n ≥ 5 from 3 independent experiments).

Movie 11. Lifeact-GFP expressing DCs (cyan) migrating together with TAMRA-stained WT (left) or CCR7-KO (right) T cells (magenta) under agarose with uniform CCL19 (12min/s, representatives of 6,5 from 3 independent experiments).

Movie 12. DCs migrating in microfluidic device (channel 50um wide, 5um high) filled with uniform CCL19 (cell reservoir on the left). Shown is brightfield and nuclear stain in cyan, and the corresponding cell tracks at the bottom (representative of 2 independent experiments).

Movie 13. Control experiment to test the effect if DCs are added in the cell reservoir in under agarose assay with uniform CCL19 as a concentrated pellet (0.5-1ul) or as 7ul suspension with the same concentration of CCL19 (representatives of 3 independent experiments).

7.1.3 Plan your trip before you leave: The neutrophils' search-and-run journey

Originally published in *J Cell Biol. (2022)*. https://doi.org/10.1083/jcb.202206127

JCB Journal of Cell Biology

SPOTLIGHT

Plan your trip before you leave: The neutrophils' search-and-run journey

Julian Stopp and Michael Sixt

Reading, interpreting and crawling along gradients of chemotactic cues is one of the most complex questions in cell biology. In this issue, Georgantzoglou et al. (2022. *J. Cell. Biol.* https://doi.org/10.1083/jcb.202103207) use in vivo models to map the temporal sequence of how neutrophils respond to an acutely arising gradient of chemoattractant.

The ability to follow gradients of guidance cues is fundamental for almost all living systems, from the cellular to the organismal scale. There are distinctive strategies to sense molecule concentration differences of which prokaryotic chemotaxis is the best understood biological example. Bacteria interrupt phases of straight, flagella-driven swimming by tumbling phases where the bacterium randomly changes its direction. Tumbling is more likely to happen when the concentration of the guidance cue—usually a nutrient—has dropped compared to previous time-points. The resulting "biased random walk" leads the cell toward the higher concentration (1). In general, such a temporal strategy is effective for moving entities that are fast and small or if the gradient is shallow or fluctuating. With bigger cell size, slower migratory speed and steeper gradients, a spatial sensing strategy becomes an option. Eukaryotic cells do integrate spatial signals—they can effectively sense concentration changes across their surface. By polarizing their deformable cell body toward the higher concentration, they can crawl up-gradient. Spatial sensing has been established in many eukaryotic cells, most prominently in single celled amoeba of *Dictyostelium discoideum* but also in amoeboid animal leukocytes that share many of the signaling pathways established in *Dictyostelium* (2). While it is clear from controlled in vitro experiments that leukocytes can integrate spatial information, it is not well understood if and under which circumstances they use the temporal domain.

There are few studies where chemotactic gradients are sufficiently controlled to quantitatively address eukaryotic temporal gradient sensing. Some of them suggest that chemotaxis encompasses consecutive abrupt phases of motility and stagnation rather than a continuous phase and propose that the breaks between the motile and stationary states allow cells to adapt their receptors to the rising concentrations of the guidance cue (3, 4). While these works do not assess whether cells compare concentrations over time, they show that eukaryotic chemotaxis is not necessarily an uninterrupted process.

In their new study, Georgantzoglou et al. examine the chemotactic behavior of neutrophils in the living organism. They devised experiments where a chemotactic gradient can be abruptly induced in the tissue and the cytoskeletal response of the cells precisely monitored. Their data suggest that chemotaxis is a two-stage process which begins with a search phase where the cell samples its surrounding and continues with a run phase where it rushes toward the target (Fig. 1).

The authors used neutrophils in fins of zebrafish and ears of mice as back-to-back in vivo model systems. Using intravital microscopy they tracked the trajectories of endogenous or previously transferred neutrophils in response to an acutely administered laser-wound. Upon wounding, the cells transition from random migration to a directed, collective movement toward the site of damage, where the chemoattractant is released (5, 6). In a first set of experiments, they found that, once exposed to the gradient, neutrophils are faster whenever their path is pointing toward the wound (7). At the same time, neutrophils get more directionally persistent (i.e., they make less directional changes) the closer they are to the wound; thus, once they are on the right track, they speed up and go straight.

Georgantzoglou et al. next linked cellular behavior with cytoskeletal changes by using reporters of actin and myosin and cross-correlated cellular trajectories with cytoskeletal polarity and flow. Somewhat surprisingly, they found that low speed correlated with actin enrichment in the front and high speed with actin enrichment in the back. In turn, front actin enrichment correlated positively with ongoing directional changes, meaning that a cell with strong protrusive activity is slow and prone to turn. Fast and directionally persistent cells had their actin mainly at the back, the site where actomyosin contractility is high.

They then turned their attention to the phase immediately before and after wounding and found that the acute response of a randomly wandering neutrophil to an abruptly emerging gradient is to slow down and increase protrusive activity at the cell front. At the end of this hesitation time, which takes a few minutes, the neutrophil makes a turn toward the wound. Then, it polarizes the actin to the back and starts to accelerate toward the site of damage. This

ISTA, Institute of Science and Technology Austria, Klosterneuburg, Austria.

Correspondence to Michael Sixt: Sixt@ist.ac.at.

© 2022 Stopp and Sixt. This article is distributed under the terms of an Attribution–Noncommercial–Share Alike–No Mirror Sites license for the first six months after the publication date (see http://www.rupress.org/terms/). After six months it is available under a Creative Commons License (Attribution–Noncommercial–Share Alike 4.0 International license, as described at https://creativecommons.org/licenses/by-nc-sa/4.0/).

Check for updates

Downloaded from http://rupress.org/jcb/article-pdf/221/8/e202206127/1435863/jcb_202206127.pdf by Institute of Science and Technology Austria (ISTA) user on 14 December 2022

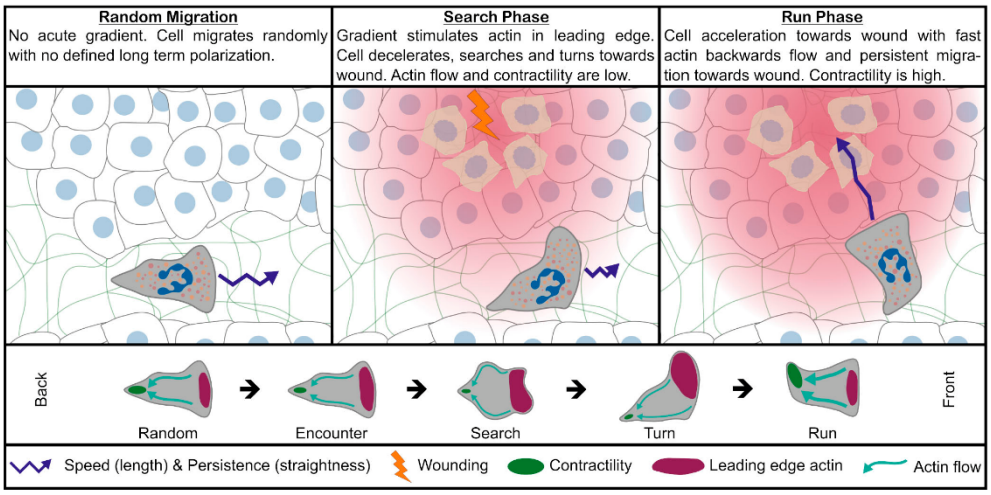


Figure 1. **Model for neutrophil search-and-run strategy in vivo.** After neutrophils are recruited into tissue, they migrate randomly. Once they encounter an acute gradient, they slow down and actin is enriched at the cell front to expand the leading edge, while cell contractility and actin flow are low. The dynamic expansion of the leading edge helps neutrophils to sense the direction of the gradient, leading to a biased turn into the direction of the wound and ending the search phase. At the onset of the run phase, contractility is increased, leading to a high retrograde actin flow, which results in rapid cell movement. The contractility creates an inertia effect on cell polarity, locking the cell into a forward movement toward the source with high directional persistence.

suggested a model where the initial response of a cell is to ramp up the formation of exploratory protrusion which sample for concentration differences. When reading out downstream signals (i.e., PIP3 as a marker for intracellular polarization) in cells where all actin dynamics were pharmacologically abolished with LatrunculinB, the authors found that successful polarization relied on shape changes. Hence, it is possible (but remains to be shown) that during the search phase, the cells do not only integrate spatial information, but also create a temporal domain by "sniffing around" in their immediate vicinity.

After the search phase, myosin II at the back of the cell became dominant and with it, actin relocalized to the trailing edge. When the authors dynamically imaged actomyosin, they saw a rapidly increasing flow directed from the front to the back. Actin flows are the mechanical force that, once coupled to the substrate by transmembrane receptors or shape-changes, drive the cell forward. Increased actin flow was in line with the cell trajectories, suggesting that after the search phase, neutrophils entered the run phase, where they head straight to the target. Blocking myosin activity with Blebbistatin led to extended search times and impaired run phases, confirming that polymerization-driven actin protrusions characterized the search phase, while contraction-driven actin flows were responsible for the run phase (Fig. 1).

From these data it seems plausible that during the transition from the search to the run phase, the cell consolidates all the information it previously collected and translates it into a well-defined front-back axis. How this works mechanistically remains to be shown. One possible scenario is that when myosin II ramps up its contractility and pulls all filaments toward the back-pole of the cell, this rectifies the cell along the axis where most actin has been polymerized during the search phase. Thus, the flow patterns of a retracting actin cortex might act as an integrator of the previously collected information.

Another open question is, how the search-and-run strategy translates in an environment, where the source of the gradient is either further away than a few cell body lengths or when other motile cells release the attractant themselves, as is often seen when cells migrate along cascades of relay factors. Sampling once and running straight toward these sources will not suffice here, as the cell will have to reorient along local anatomical obstacles and re-adjust its path along the changing gradient, respectively. One possible solution is that the search-and-run process might repeat itself, possibly in an oscillatory manner, similarly to what has been suggested in the germ cells and neurons (3, 4). To better understand the strategies that different cells use to navigate in complex environments we will need the combination of tractable in vivo models, as pioneered by the authors, and reconstituted in vitro models that allow to precisely manipulate and monitor both gradients and cellular responses.

Acknowledgments

The authors declare no competing financial interests.

References

1. Colin, R., et al. 2021. *FEMS Microbiol. Rev.* https://doi.org/10.1093/femsre/fuab038
2. Pal, D.S., et al. 2019. *Int. J. Dev. Biol.* https://doi.org/10.1387/ijdb.190265pd
3. Ming, G.L., et al. 2002. *Nature.* https://doi.org/10.1038/nature745
4. Minina, S., et al. 2007. *Curr. Biol.* https://doi.org/10.1016/j.cub.2007.05.073
5. Lämmermann, T., et al. 2013. *Nature.* https://doi.org/10.1038/nature12175
6. Poplimont, H., et al. 2020. *Curr. Biol.* https://doi.org/10.1016/j.cub.2020.05.030
7. Georgantzoglou, A., et al. 2022. *J. Cell Biol.* https://doi.org/10.1083/jcb.202103207

Downloaded from http://rupress.org/jcb/article-pdf/221/8/e202206127/1435863/jcb_202206127.pdf by Institute of Science and Technology Austria (ISTA) user on 14 December 2022

7.1.4 Cellular locomotion using environmental topography

Originally published in *Nature (2020)*. https://doi.org/10.1038/s41586-020-2283-z

Article

Cellular locomotion using environmental topography

https://doi.org/10.1038/s41586-020-2283-z

Received: 13 January 2018

Accepted: 9 March 2020

Published online: 13 May 2020

Check for updates

Anne Reversat[1,7]✉, Florian Gaertner[1], Jack Merrin[1], Julian Stopp[1], Saren Tasciyan[1], Juan Aguilera[1], Ingrid de Vries[1], Robert Hauschild[1], Miroslav Hons[1,2,8], Matthieu Piel[3,4], Andrew Callan-Jones[5], Raphael Voituriez[6] & Michael Sixt[1]✉

Eukaryotic cells migrate by coupling the intracellular force of the actin cytoskeleton to the environment. While force coupling is usually mediated by transmembrane adhesion receptors, especially those of the integrin family, amoeboid cells such as leukocytes can migrate extremely fast despite very low adhesive forces[1]. Here we show that leukocytes cannot only migrate under low adhesion but can also transmit forces in the complete absence of transmembrane force coupling. When confined within three-dimensional environments, they use the topographical features of the substrate to propel themselves. Here the retrograde flow of the actin cytoskeleton follows the texture of the substrate, creating retrograde shear forces that are sufficient to drive the cell body forwards. Notably, adhesion-dependent and adhesion-independent migration are not mutually exclusive, but rather are variants of the same principle of coupling retrograde actin flow to the environment and thus can potentially operate interchangeably and simultaneously. As adhesion-free migration is independent of the chemical composition of the environment, it renders cells completely autonomous in their locomotive behaviour.

Mechanistic understanding of cell motility started with Abercrombie's demonstration that particles placed on the dorsal surface of a cell undergo retrograde transport[2]. The authors concluded that cellular material is added to the front of the cell, feeding a rearwards flow, which couples to the substrate and thereby generates friction to drag the cell body forwards. Later studies showed that the added material is the growing polymer of F-actin and that F-actin retrograde flow couples via transmembrane adhesion receptors, mainly of the integrin family. Although this adhesion-dependent principle of motility turned out to be universal on two-dimensional (2D) surfaces, some cells can migrate in the absence of integrin-mediated adhesion when confined within a three-dimensional (3D) context[3,4]. This applies especially to the amoeboid (shape-changing) class of cells such as leukocytes[5]. Force transmission under these conditions is not understood, and alternative membrane-spanning molecules that mediate specific or even unspecific friction have been suggested[6,7]. Notably, in his seminal study, Abercrombie contemplated a second, qualitatively different, scenario: backward-moving waves of deformation might passively entangle with the applied particles (or a substrate) and propel the cell in a manner analogous to paddling and swimming[2].

To explore adhesion-independent locomotion, we initially investigated T lymphocytes. When these cells migrate within lymphatic organs, integrin depletion causes them to slow down by only 15%, meaning that they do employ integrins but retain a substantial capacity to transmit forces via other means[8,9]. We used a mouse T cell line, which migrates vigorously in 3D environments, such as in vitro-assembled collagen gels (Supplementary Video 1). To eliminate integrin-based force transmission, we deleted *Tln1*, which encodes talin 1, a cytosolic adaptor protein essential for integrin functionality[10] (Extended Data Fig. 1a–c). Talin-deficient (referred to here as 'talin KO') cells were completely unable to adhere to and migrate on 2D surfaces (Fig. 1a, b, Extended Data Fig. 1d, e). However, once incorporated into 3D collagen gels, their migratory characteristics were indistinguishable from wild-type cells (Fig. 1c, Extended Data Fig. 1f, Supplementary Video 1). In the following, we engineered artificial environments to dissect the geometrical transition between 2D surfaces and fibrillar environments, while keeping the chemical composition of the substrate unchanged. We first designed a microfluidic setup to confine leukocytes between two parallel surfaces separated by an adjustable space[11] ('2.5D'; Fig. 1d). While this setup supported efficient migration of wild-type cells, talin-KO cells were unable to translocate, although they showed morphological polarization (Fig. 1d, Extended Data Fig. 1g, Supplementary Video 2). When T cells expressing the actin reporter Lifeact-GFP were imaged with total internal reflection fluorescence (TIRF) microscopy, actin within the rapidly moving cell body remained static in relation to the adhesive substrate and flowed backwards in the cell frame of reference (Fig. 1e–g, Supplementary Video 3). Talin-KO cells on adhesive substrates or wild-type cells on passivated surfaces were immobile but showed similar actin dynamics in the cell frame of reference[8], meaning that actin slid backwards in relation to the substrate (Fig. 1e–g, Extended Data Figs. 1g–l, 2a–c, Supplementary Video 3). These findings demonstrate that, when placed on 2D substrates or when confined

[1]Institute of Science and Technology Austria (IST Austria), Klosterneuburg, Austria. [2]Institute of Scientific Instruments of the Czech Academy of Sciences, Brno, Czech Republic. [3]Institut Curie, PSL Research University, CNRS, UMR 144, Paris, France. [4]Institut Pierre-Gilles de Gennes, PSL Research University, Paris, France. [5]Laboratoire Matière et Systèmes Complexes, UMR 7057 CNRS, Université Paris Diderot, Paris, France. [6]Laboratoire de Physique Theorique de la Matière Condensée et Laboratoire Jean Perrin, CNRS/Université Pierre-et-Marie Curie, Paris, France. [7]Present address: Institute of Translational Medicine, Department of Cellular and Molecular Physiology, University of Liverpool, Liverpool, UK. [8]Present address: BIOCEV, First Faculty of Medicine, Charles University, Vestec, Czech Republic. ✉e-mail: anne.reversat@gmail.com; sixt@ist.ac.at

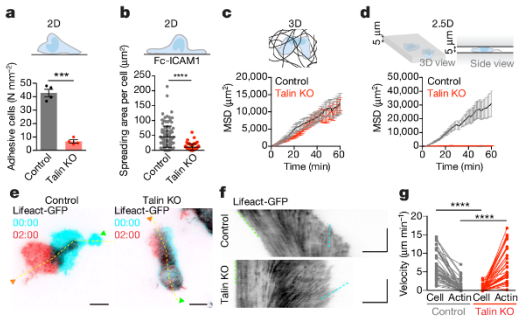


Fig. 1 | Adhesive and migratory properties of talin-KO T cells. a, The number of cells adhering to the 2D surface. Data are mean ± s.e.m. of four independent experiments; ***$P = 0.00076$, paired t-test. **b**, Surface area (μm^2) of cells spreading on Fc-ICAM1-coated glass. Control ($n = 139$) and talin-KO ($n = 81$) cells of three independent experiments are shown. Data are mean ± s.d.; ****$P < 0.0001$, Mann–Whitney U-test. **c**, Mean square displacement (MSD) of control ($n = 51$, in black) and talin-KO ($n = 52$, in red) cells migrating in 3D collagen gel from three independent experiments. Data are mean ± s.e.m.; $P = 0.2243$, Mann–Whitney U-test. **d**, MSD of control ($n = 290$, in black) and talin-KO ($n = 284$, in red) cells migrating in a 5-μm confiner from four independent experiments. Data are mean ± s.e.m.; $P < 0.0001$, Mann–Whitney U-test. **e**, Snapshots of TIRF microscopy of a control cell (left) and a talin-KO cell (right) expressing Lifeact-GFP under 5-μm confinement. Representative of three independent experiments. The green arrowheads mark the uropod and the orange arrowheads indicate the cell front. TIRF images in cyan are at $t = 0$ min and in red at $t = 2$ min. The yellow dashed line is used for the kymograph in **f**. Scale bars, 5 μm. Time is shown in min:s. **f**, Kymographs of a control cell and talin-KO cell under 5-μm confinement as shown in **e**. Cell velocity is indicated by the green dashed line, and actin retrograde flow is shown by the cyan dashed line. Horizontal scale bar, 5 μm; vertical scale bar, 1 min. **g**, Retrograde flow velocities for control ($n = 42$) and talin-KO ($n = 36$) cells from three independent experiments. ****$P < 0.0001$, Mann–Whitney U-test.

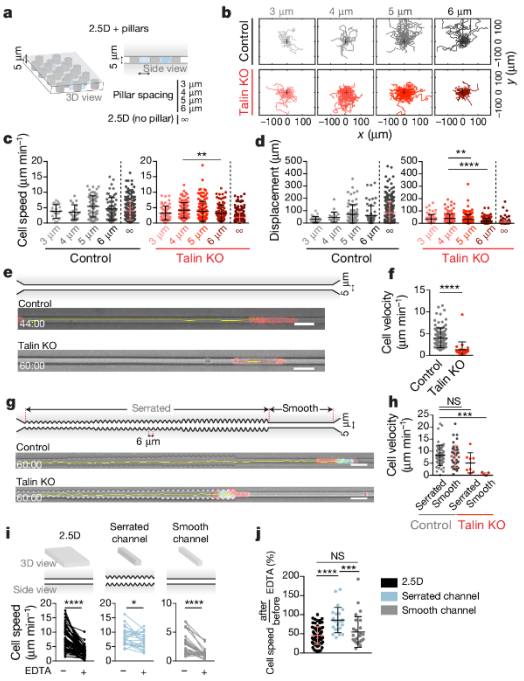


Fig. 2 | Migration of T cells in textured confinement. a, Experimental setup for **b**–**d**. **b**, Cell trajectories analysed in **c** and **d** during 1 h. The black crosses indicate the start of the individual tracks. **c**, **d**, Cell speed (**c**), mean ± s.d.; **$P = 0.0021$, otherwise not significant ($P > 0.9999$); and displacement (**d**), mean ± s.d.; **$P = 0.0089$ and ****$P < 0.0001$, otherwise not significant, Kruskal–Wallis test followed by post hoc Dunn's test. $n = 25$, 20, 75 and 61 for control cells in respective 3-μm, 4-μm, 5-μm and 6-μm zones. Data are from three independent experiments. $n = 64$, 115, 124 and 94 for talin-KO cells in respective 3-μm, 4-μm, 5-μm and 6-μm zones. Data are from six independent experiments. **e**, **f**, Migration in smooth channels. Data are from four independent experiments. In **e**, 5 × 5-μm smooth channels are shown. Top, scheme of the channel. Representative snapshots at $t = 44$ min of Lifeact-GFP-expressing control cells (middle) and at $t = 60$ min talin-KO cells (bottom) are displayed. Tracks are shown in yellow. Scale bars, 20 μm. In **f**, the cell velocity is shown. $n = 99$ for control cells, $n = 24$ for talin-KO cells. Data are mean ± s.d.; ****$P < 0.0001$, Mann–Whitney U-test. **g**, **h**, Migration in serrated channels. Data are from three (control) and four (KO) independent experiments. In **g**, the serrated topography with a 6-μm period in a 5 × 5-μm channel is shown. Top, scheme of the channel. A representative snapshot at $t = 60$ min of the Lifeact-GFP control cell (middle) and the talin-KO cell (bottom) is displayed. Tracks are shown in yellow. Scale bars, 20 μm. In **h**, the cell velocity in channels is shown. $n = 59$ (control serrated), 25 (control smooth), 8 (talin-KO serrated) and 5 (talin-KO smooth). Data are mean ± s.d.; ***$P = 0.0009$, Kruskal–Wallis test followed by post hoc Dunn's test. **i**, **j**, Cell speed before and after the addition of 10 mM EDTA. Data are from three independent experiments. 2.5D: $n = 73$ cells; serrated channel: $n = 23$; and smooth channel: $n = 27$. In **i**, the cell speed before (–) and after (+) the addition of EDTA in respective devices is shown. ****$P < 0.0001$ and *$P = 0.0167$, Wilcoxon matched-pairs signed-rank test. In **j**, the change in cell speed after versus before the addition of EDTA is shown. Data are mean ± s.d.; not significant (NS; $P > 0.9999$), ***$P = 0.0004$ and ****$P < 0.0001$, Kruskal–Wallis test followed by post hoc Dunn's tests.

between two surfaces, T cell locomotion depends on integrin-mediated force transmission[6,8,9,12] (see also Supplementary Discussion). This finding was in contrast to our collagen gel data and to the in vivo finding that T cells retain substantial migratory capacity following integrin depletion[8,9]. We reasoned that the major difference between confinement within a lymph node or within a fibrillar matrix and confinement between two planar surfaces is geometrical complexity. Hence, we introduced arrays of variably spaced pillars that intersected the two surfaces (Fig. 2a), thereby mimicking the geometry of a fibrillar gel while keeping the surface chemistry unchanged[13]. Between the pillars, the migratory capacity of talin-KO cells was restored (Fig. 2b–d, Extended Data Fig. 2d, e, Supplementary Video 4). While translocation velocities of wild-type cells were not affected by increased pillar spacings, the performance of talin-KO cells dropped in wider-spaced pillars, suggesting that tight contact with curved surfaces enables propulsion in the absence of integrins (Supplementary Video 4). We next turned to channels in which cells are fully enclosed by surfaces (Fig. 2e). Within smooth-walled 5 × 5-μm channels, control cells migrated persistently, while talin-KO cells were immobile (Fig. 2e, f, Supplementary Video 5). We next introduced surface texture as a serrated pattern with a 6-μm period and found that the migration of talin-KO cells was restored (Fig. 2g, h, Extended Data Fig. 2f, Supplementary Video 5). In channels that contained both smooth and serrated sectors, wild-type cells transited freely between the sectors. Following cation depletion with EDTA, which inactivates integrins (and several other cell-surface adhesion molecules), cells within smooth areas slowed down or stalled, while cells within serrated sectors kept migrating until they encountered a smooth area (Fig. 2i, j, Supplementary Video 6). The same principle was conserved when we tested dendritic cells and neutrophil granulocytes, two other types of amoeboid leukocytes. Notably, EDTA-treated

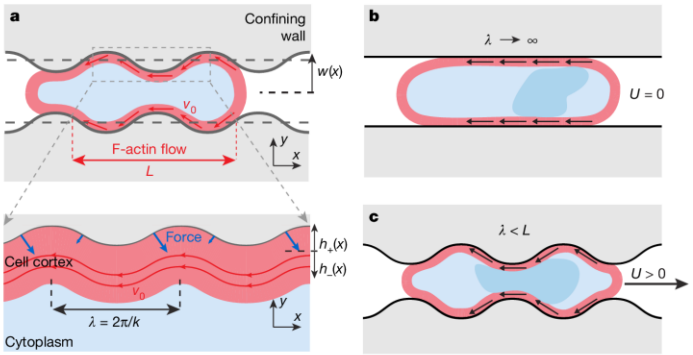


Fig. 3 | Physical model of adhesion-free cell migration in a complex environment. a, Scheme of the model: the channel has a varying wavy cross-section $w(x)$ and period $\lambda = 2\pi/k$. The cell contains cortical F-actin that presents a retrograde flow of length L, an average speed v_0 and is modelled as a viscous fluid layer of thickness $h(x)$. **b**, Scheme of a modelled cell in a smooth channel with an adhesion-free coupling of the actin cytoskeleton with the environment. The cell is polarized and has a high retrograde actin flow (black arrows) but cannot move forwards. **c**, Scheme of the modelled non-adhesive cell in a serrated channel. Cell propulsion is created by the shear stress in the actin cortex, which is caused by the bending of flow lines (black arrows) by the environmental topography. This induces a pressure gradient in the cortical F-actin mesh and thus non-vanishing normal forces onto the substrate. U, cell speed.

dendritic cells retained a weak locomotive capacity even in smooth channels (Extended Data Fig. 3a, b, Supplementary Video 7). This is in line with previous findings that, compared with T cells, dendritic cells have a higher capacity to transmit forces via unspecific transmembrane coupling[8,12,14]. These data demonstrate that force transmission of leukocytes follows a continuum of strategies. They can flexibly use integrin-mediated adhesion, unspecific transmembrane force coupling and, if both strategies fail due to the absence of suitable ligands, can efficiently utilize surface topography to transmit forces.

As a framework to understand topography-based locomotion, we propose a minimal model (Fig. 3a–c, Supplementary Text) in which actin is described as a viscous gel that travels from the leading to the trailing edge of the cell in the absence of any tangential friction force with the substrate. In serrated but not in smooth channels, this flow generates local shear stresses and thus a pressure gradient in the actin gel, which drives locomotion by imposing non-vanishing normal forces onto the substrate. Here the actin flow generated in the cell can couple to the environment when its topographical features are smaller than the flow scale of the actin cortex. To test this prediction, we varied the period of serrated topography from 6 to 12 to 24 µm. Serrated sectors were followed by smooth areas as an internal control (Fig. 4a). Wild-type T cells effectively traversed all (including smooth) channel designs, while talin-KO cells migrated in 6-µm and 12-µm period patterns but rarely in the 24-µm patterns (Fig. 4b–d, Extended Data Fig. 4a), in which the spacing exceeded the average length scale of cortical actin flow in a cell (Extended Data Fig. 4b). In channels with a successively increased serration period, continuous single-cell observation showed that, in qualitative agreement with model predictions, cells slowed from 6 to 12 µm, presented even slower and saltatory movement in the 24-µm stretches and were unable to enter the smooth channel (Fig. 4c, d, Supplementary Video 8). The model also predicts a linear dependence of the propulsion force on actin flow speed. Actin flow has two mechanical components: polymerization pushes filaments from the front to the back, while actomyosin contraction pulls at the back[12,15–17]. Accordingly, inhibition of myosin II slowed down but did not stall cells under adhesive conditions (Extended Data Fig. 5a–f). Following dual inhibition of adhesion and contractility, cells still performed better in the serrated than in the smooth channels (Extended Data Fig. 5d–f), suggesting a direct relation between actin flow speed and locomotive force, as predicted. Next, we quantitatively imaged the actin flow of talin-KO and EDTA-treated cells in textured channels and found an increase in the actin retrograde flow relative to the substrate whenever the cells slowed between the topographical features (Fig. 4e–g, Extended Data Fig. 5g, Supplementary Video 9). This suggests that, in analogy with the molecular clutch formed by transmembrane receptors, topographical features allow the coupling of retrograde actin flow to a substrate. Finally, we devised an entirely orthogonal approach, in which we placed primary mouse T lymphocytes on surfaces that were either passivated or coated with the integrin ligand intracellular adhesion molecule 1 (ICAM1) and overlaid them with a pad of agarose. As shown previously[8], cells migrated on ICAM1, but slipped and did not migrate on passivated substrate (Extended Data Fig. 6a–g). We then used passivated surfaces with engraved linear ridges to introduce anisotropic topography. We found that on these surfaces, migratory capacity was rescued and that cells predominantly migrated perpendicular but not parallel to the ridges (Extended Data Fig. 6a–g, Supplementary Video 10). Within the same cell, actin showed retrograde flow in relation to the substrate when the flow was aligned with the ridges, but not in orientation perpendicular to the ridges (Extended Data Fig. 7, Supplementary Video 10). Together, these data demonstrate that the cells slipped in an orientation along the ridges and coupled in an orientation perpendicular to the ridges.

In our experiments, we demonstrated topography-based force transmission by controlling the topography of the environment, meaning that we extrinsically imposed shape changes of the cell. To directly link this to the amoeboid (shape-changing) principle, we tested whether cells can autonomously generate appropriate deformations. Morphometric analysis of T cells showed that they have the intrinsic capacity to produce rearwards-propagating deformation waves (Extended Data Fig. 8a–e and previously published studies[18–23]) and that the travelling speed of these waves scaled with the speed of actin flow. Such deformation waves could intercalate with any textured environment and propel a cell as conjectured by Abercrombie[2].

Altogether, our findings demonstrate that cells can transmit forces by coupling the retrograde flow of actin to a geometrically irregular environment, and that this can happen in the complete absence of any transmembrane receptors that link the cytoskeleton to the substrate. Notably, force transmission by specific adhesion receptors, by unspecific friction and by shape change are not mutually exclusive mechanisms. Rather, they are variants of the same fundamental principle of coupling

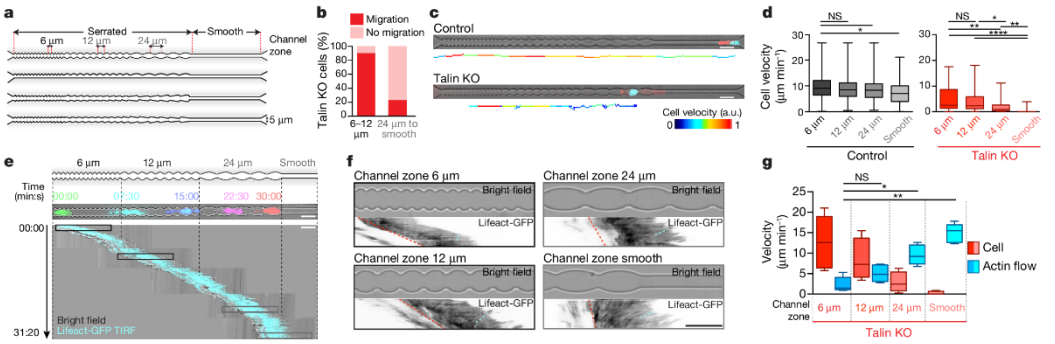


Fig. 4 | Force transmission of T cells in varying geometries. a, The channel design that is used in **b**–**g**. **b**, The proportion of talin-KO cells migrating in 6-µm and 12-µm zones ($n = 41$) and in the 24-µm zone and the smooth zone ($n = 22$). ****$P < 0.0001$, Fisher's exact test. **c**, Snapshots of control cells (top) and talin-KO cells in channels with a varying period. Lifeact-GFP is in red, and Hoechst is in cyan. Scale bars, 20 µm. Bottom, tracks are colour-coded for cell velocity. Data are representative of four and eight independent experiments, respectively. **d**, The velocity of control ($n = 88$) and talin-KO ($n = 79$) cells in zones with different periodicity. Data are representative of four and eight independent experiments, respectively. Control: *$P = 0.0234$; KO: *$P = 0.0188$, **$P = 0.0013$ (6 µm versus 24 µm) and **$P = 0.001$ (24 µm versus smooth), **$P < 0.0001$, otherwise NS, Kruskal–Wallis test followed by post hoc Dunn's test. **e**, TIRF microscopy of a Lifeact-GFP-expressing talin-KO cell moving from the 6-µm zone to the smooth zone. From top to bottom: scheme of the channel, colour-coded snapshots every 7.5 min and a kymograph of Lifeact-GFP (TIRF is shown in cyan and bright field is shown in grey). Scale bars, 20 µm. Representative of three independent experiments. **f**, Bright-field imaging of channel sectors and the corresponding kymograph of the Lifeact-GFP-expressing talin-KO cell shown in **e** during 50 s. The red dashed lines indicate cell displacement, and the cyan dashed lines indicate actin retrograde flow. Scale bar, 20 µm. **g**, Actin retrograde flow and cell velocities of talin-KO cells in different channel zones. Data are representative of four independent experiments. $n = 7$. *$P = 0.0423$ and **$P = 0.0036$, Kruskal–Wallis test followed by post hoc Dunn's test. Boxes in **d** and **g** extend from the 25th to the 75th percentile, with the middle line showing the median and the whiskers indicating the minimum to maximum values.

retrograde actin flow to the surrounding and can therefore operate alternately or even simultaneously. This endows amoeboid cells with enormous adaptability when migrating in heterogeneous environments.

Online content

Any methods, additional references, Nature Research reporting summaries, source data, extended data, supplementary information, acknowledgements, peer review information; details of author contributions and competing interests; and statements of data and code availability are available at https://doi.org/10.1038/s41586-020-2283-z.

1. Lämmermann, T. & Sixt, M. Mechanical modes of 'amoeboid' cell migration. *Curr. Opin. Cell Biol.* **21**, 636–644 (2009).
2. Abercrombie, M., Heaysman, J. E. & Pegrum, S. M. The locomotion of fibroblasts in culture. 3. Movements of particles on the dorsal surface of the leading lamella. *Exp. Cell Res.* **62**, 389–398 (1970).
3. Liu, Y.-J. J. et al. Confinement and low adhesion induce fast amoeboid migration of slow mesenchymal cells. *Cell* **160**, 659–672 (2015).
4. Friedl, P. & Wolf, K. Plasticity of cell migration: a multiscale tuning model. *J. Cell Biol.* **188**, 11–19 (2010).
5. Lämmermann, T. et al. Rapid leukocyte migration by integrin-independent flowing and squeezing. *Nature* **453**, 51–55 (2008).
6. Bergert, M. et al. Force transmission during adhesion-independent migration. *Nat. Cell Biol.* **17**, 524–529 (2015).
7. Schmidt, S. & Friedl, P. Interstitial cell migration: integrin-dependent and alternative adhesion mechanisms. *Cell Tissue Res.* **339**, 83–92 (2010).
8. Hons, M. et al. Chemokines and integrins independently tune actin flow and substrate friction during intranodal migration of T cells. *Nat. Immunol.* **19**, 606–616 (2018).
9. Woolf, E. et al. Lymph node chemokines promote sustained T lymphocyte motility without triggering stable integrin adhesiveness in the absence of shear forces. *Nat. Immunol.* **8**, 1076–1085 (2007).
10. Calderwood, D. A., Campbell, I. D. & Critchley, D. R. Talins and kindlins: partners in integrin-mediated adhesion. *Nat. Rev. Mol. Cell Biol.* **14**, 503–517 (2013).
11. Le Berre, M., Aubertin, J. & Piel, M. Fine control of nuclear confinement identifies a threshold deformation leading to lamina rupture and induction of specific genes. *Integr. Biol. (Camb.)* **4**, 1406–1414 (2012).
12. Renkawitz, J. et al. Adaptive force transmission in amoeboid cell migration. *Nat. Cell Biol.* **11**, 1438–1443 (2009).
13. Renkawitz, J., Reversat, A., Leithner, A., Merrin, J. & Sixt, M. Micro-engineered "pillar forests" to study cell migration in complex but controlled 3D environments. *Methods Cell Biol.* **147**, 79–91 (2018).
14. Vargas, P., Barbier, L., Sáez, P. J. & Piel, M. Mechanisms for fast cell migration in complex environments. *Curr. Opin. Cell Biol.* **48**, 72–78 (2017).
15. Medeiros, N. A., Burnette, D. T. & Forscher, P. Myosin II functions in actin-bundle turnover in neuronal growth cones. *Nat. Cell Biol.* **8**, 215–226 (2006).
16. Henson, J. H. et al. Two components of actin-based retrograde flow in sea urchin coelomocytes. *Mol. Biol. Cell* **10**, 4075–4090 (1999).
17. Cramer, L. P. Molecular mechanism of actin-dependent retrograde flow in lamellipodia of motile cells. *Front. Biosci.* **2**, d260–d270 (1997).
18. Driscoll, M. K. et al. Cell shape dynamics: from waves to migration. *PLoS Comput. Biol.* **8**, e1002392 (2012).
19. Howe, J. D., Barry, N. P. & Bretscher, M. S. How do amoebae swim and crawl? *PLoS One* **8**, e74382 (2013).
20. Bae, A. J. & Bodenschatz, E. On the swimming of *Dictyostelium* amoebae. *Proc. Natl Acad. Sci. USA* **107**, E165–E166 (2010).
21. Mandeville, J. T. H., Lawson, M. A. & Maxfield, F. R. Dynamic imaging of neutrophil migration in three dimensions: mechanical interactions between cells and matrix. *J. Leukoc. Biol.* **61**, 188–200 (1997).
22. Tozluoğlu, M. et al. Matrix geometry determines optimal cancer cell migration strategy and modulates response to interventions. *Nat. Cell Biol.* **15**, 751–762 (2013).
23. Jankowiak, G., Peurichard, D., Reversat, A., Schmeiser, C. & Sixt, M. Modelling adhesion-independent cell migration. *Math. Model. Methods Appl. Sci.* **30**, 513–537 (2020).

Publisher's note Springer Nature remains neutral with regard to jurisdictional claims in published maps and institutional affiliations.

© The Author(s), under exclusive licence to Springer Nature Limited 2020

Methods

Cell culture

Cells were grown and maintained in a humidified incubator at 37 °C and 5% CO_2. LMR7.5 T cell hybridomas, a gift from A. M. Lennon-Duménil (Institut Curie, Paris, France), were cultivated in R10 medium (RPMI 1640 supplemented with 10% FBS, 2 mM L-glutamine, 100 units/ml penicillin, 100 µg/ml streptomycin and 50 µM 2-mercaptoethanol; Gibco, Thermo Fisher Scientific). The Lifeact-GFP[24] parental T cell line was generated by nucleofection with an eGFP reporter construct (Kit V, Lonza). Alternatively, LMR T cells were infected with a plasmid encoding Lifeact-mCherry (pLenti6.3, Invitrogen, Thermo Fisher Scientific). LX-293 HEK cells (Clontech) were used for lentivirus production and maintained in D10 medium (DMEM with 2 mM L-glutamine, 10% FBS, and 100 units/ml penicillin and 100 µg/ml streptomycin; Gibco). All cell lines were mycoplasma-free and frequently tested. Neutrophil-like PLB-985 cells were obtained from the DSMZ (ACC 139). In brief, cells were maintained in RPMI 1640, supplemented with 10% FBS, 20 mM HEPES and 1% glutamine (all Gibco, Thermo Fisher Scientific). For differentiation, PLB cells were kept for 6 days in medium containing 1.25% DMSO (cell culture grade; Sigma-Aldrich). Differentiation status was validated using flow cytometry (CD11b, Miltenyi Biotec). Before experimentation, differentiated cells were washed three times to remove DMSO. Dendritic cells were differentiated from bone marrow that originated from 6–12-week-old male or female C57BL/6J mice[25]. Primary mouse T cells were obtained from peripheral lymph nodes and spleens[8] and homogenized with a 70-µm cell strainer. Untouched primary naive T cells were isolated from 6–12-week-old male C57BL/6J Lifeact-GFP mice with an EasySep Mouse T cell Isolation Kit according to the manufacturer's protocol (19851A, STEMCELL Technologies) and incubated overnight at 37 °C in 5% CO_2 in R10 medium.

Animals

Mice were bred and maintained at the local animal facility in accordance with the IST Austria ethics commission and the Austrian law. Permission was granted by the Austrian Federal Ministry of Science, Research and Economy (identification code: BMWF-66.018/0005-II/3b/2012).

Reporter and CRISPR–Cas9 cell line generation

CRISPR–Cas9 design and production. Single-guide RNAs (sgRNAs) were designed as described elsewhere[26]. In brief, sgRNAs were designed to induce the double-strand break in the first exons of the mouse gene encoding talin 1 (*Tln1*). Then sgRNAs were scored for high on-target effects (https://portals.broadinstitute.org/gpp/public/analysis-tools/sgrna-design) and low off-target effects (http://crispr.mit.edu). sgRNAs were cloned into the LentiCRISPRv1 vector (a gift from F. Zhang, Addgene plasmid no. 49535). Guide sequences: sgRNA-Scramble s(5′–3′) GCCGTGGCGCATGGGTAGCA; sgRNA-Talin1g1 s(5′–3′) ATAATGCCCTAC GAGCCGT (off-target score of 91); sgRNA-Talin1g2 s(5′–3′) CTCACT GTTTCCCCGGGTA (off-target score of 82); sgRNA-Talin1g3 s(5′–3′) GTCGAGGCTGGGCGACTGG (off-target score of 98).

Lentivirus production. Lentivirus production was performed as described previously[25]. In brief, LX-293 HEK cells (Clontech) were co-transfected with LentiCRISPRv1 or LentiCRISPRv2, packaging- psPAX2 (Addgene no. 12260) and pCMV-VSV-G envelope plasmids using Lipofectamine 2000 (Thermo Fisher Scientific) as recommended by the manufacturer, and cells were resuspended in R10 medium 1 day before transfection. Supernatant was collected after 72 h and stored at −80 °C.

CRISPR-based talin KO. Lifeact-eGFP LMR7.5 T cells were spin-infected at 1,500*g* for 1 h in the presence of the lentivirus-containing supernatant and 6 µg/ml Polybrene (Sigma-Aldrich). Spin infection was carried out in 12-well plates with 3×10^5 cells/ml per reaction plus 500 µl of undiluted virus. Three days after infection, cells were selected for stable virus insertion using 5 µg/ml puromycin (Gibco, Thermo Fisher Scientific) for 7 days and were subjected to western blotting. Cells were then cloned using fluorescence-activated cell sorting (FACS Aria III, BD Biosciences) and expanded in R10 medium containing puromycin (5 µg/ml).

T cell infection and selection. For infection of LMR7.5 T cells with the Lifeact-mCherry reporter construct, the same infection protocol was applied except cells were selected with 5 µg/ml blasticidin (Gibco, Thermo Fisher Scientific) and sorted for fluorescence.

Western blot

For immunodetection of talin and GAPDH proteins, 1×10^6 control and talin-KO cells were centrifuged and lysed in RIPA buffer (New England Biolabs) and the supernatant was denatured in 2× Laemmli buffer (161-0737, Bio-Rad,) at 95 °C for 5 min. Protein lysates were loaded on a 10% Tris-glycine gel (Invitrogen, Thermo Fisher Scientific), separated by SDS–PAGE and further transferred by electrophoresis to a polyvinylidene difluoride membrane (iBlot, Invitrogen, Thermo Fisher Scientific) according to the manufacturer's instructions, with a 9-min transfer time. Membranes were blocked in PBST-BSA 5% for 1 h and incubated with primary antibodies overnight at 4 °C. Antibodies to talin (mouse anti-pan-talin, clone 8d4; T3287, Sigma-Aldrich) and GAPDH (mouse, clone GA1R; ab125247, Abcam) were diluted 1:200 and 1:3,000 in PBST-BSA 1%, respectively. After washing with TBST, secondary antibody was applied for 1 h in PBST-BSA 5% at room temperature (goat anti-mouse IgG HRP conjugate, diluted 1:5,000; 170-6516, Bio-Rad). Protein detection was performed by enhanced chemiluminescence (ECL; Thermo Fisher Scientific) detection using a VersaDoc imaging system (Bio-Rad).

Adhesion assay

Control and talin-KO T cells (5×10^5) were plated in pre-warmed R10 medium in a 25-cm^2 culture flask (TPP, Sigma-Aldrich) and placed in a humidified incubator at 37 °C, 5% CO_2 for 24 h before observation. Cells were imaged with an inverted microscope at low magnification (DM IL Led and DFC450 digital camera, Leica Microsystems) and cells adhering to the bottom of the dish were counted manually.

Spreading assay

The 2D spreading assay was performed on glass coverslips (Menzel-Glaser no. 1, VWR) that were previously coated with 2 µg/ml of recombinant mouse ICAM-1/human Fc chimaera (796-IC, R&D Systems) overnight at 4 °C, and washed three times with PBS. Control (Lifeact-mCherry or Lifeact-GFP) and talin-KO (Lifeact-GFP or Lifeact-mCherry) T cells (0.2×10^6) were gently mixed in 200 µl R10 medium and allowed to settle on the coated dish for 60 min at 37 °C and 4.5% CO_2. Cell spreading was then imaged by simultaneous TIRF and epifluorescence microscopy.

Photolithography

Photolithography was performed as previously described[13,25,27,28] with the following adaptations.

Photomasks. Patterns were designed with Coreldraw X8 (Corel Corporation) exported to DXF, then converted to GERBER format with LinkCad. Chrome photomasks (100 mm or 125 mm; PhotoData/JD Photo-Tools) were used.

Confiners. The 3-µm confiner masters were produced by spin-coating SU8-GM1050 (Gersteltec) for 40 s at 3,000 rpm, pre-baking for 1 min at 120 °C, exposing to 35 mJ/cm^2 of UV, post-exposure baking for 5 min at 95 °C, developing in SU8 developer, and then hard-baking at 150 °C for 5 min. The 5-µm confiner master was produced by spin-coating SU8-2005 (Microchem) for 30 s at 3,000 rpm, pre-baking for 2 min at 95 °C, exposing to 105 mJ/cm^2 of UV, post-exposure baking for 3 min at 95 °C, developing in SU8 developer, and then hard-baking at 150 °C for 5 min.

EDTA device. A 4-μm high master was produced by spin-coating SU8-2005 for 30 s at 5,000 rpm, pre-baking for 2 min at 95 °C and UV exposure of 550 mJ/cm^2 through a PL-360-LP (Omega Optical) optical filter on an EVG mask aligner 610 (EVG Group). The wafer was post-exposure baked for 3 min at 95 °C, developed in SU8 developer and then hard-baked at 150 °C for 5 min. The optical filter was necessary for high-resolution features in SU8.

Multilayer devices. First, the 25-μm high control master was made by spin-coating SU8-3025 (Microchem) for 30 s at 3,000 rpm. The wafer was soft-baked for 15 min at 95 °C, then exposed to 200 mJ/cm^2 UV, then post-exposure baked at 95 °C for 5 min, then developed in SU8 developer. Second, the fluid-layer master was first fully coated with a submicron layer of GM1040-SU8 by spin-coating at 5,000 rpm for 2 min. The wafer was then baked at 95 °C for 5 min, exposed to 100 mJ/cm^2 UV, post-exposure baked at 95 °C for 30 min, and then developed in SU8 developer. The 5-μm fluid-layer features were made on top of the coated wafer by spin-coating SU-2005 for 30 s at 3,000 rpm, soft-baking for 2 min, UV exposure of 550 mJ/cm^2 through the optical filter, post-exposure baking for 3 min at 95 °C, and developing in SU8 developer. Third, the fluid-layer master was then prepared for the next layer by spin-coating HMDS at 3,000 rpm for 30 s and baking for 1 min at 126 °C. Scotch Magic tape (3M) was applied over the alignment marks. AZ-40XT-11D (MicroResist Technologies) was then coated at 3,000 rpm for 30 s. The Scotch tape was then peeled off to reveal the alignment marks. The wafer was then baked at 126 °C for 7 min, aligned and exposed to UV at 500 mJ/cm^2. After a post-exposure bake for 10 min at 120 °C, it was developed in 726 MIF for about 5–10 min. The features were then rounded to make parabolic channels at 130 °C for 2 min (centre height of 26.6 μm).

Silanization. Before applying PDMS, wafers were placed in a desiccator with 10 μl of Trichloro(1H,1H,2H,2H-perfluorooctyl)-silane (Sigma-Aldrich), a vacuum of 100 mbar was applied, and then the desiccator was sealed for 1 h. One permanent coating was sufficient for later uses.

PDMS device microfabrication

Microfabricated devices were generated as previously described[11,13,28], with 1:10 PDMS and degassed for 2 min at 2,000 rpm (mix) and for 2 min at 2,200 rpm (defoam) in a mixer/defoamer (ARE-250, Thinky) before use.

Confiner. PDMS (Sylgard 184, Ellsworth Adhesives) was gently poured onto the wafers, then 10-mm coverslips were activated by plasma cleaning for 2 min at medium intensity (Harrick Plasma Cleaner, pdc-002, Harrick Plasma) and pressed upside-down onto the PDMS-covered wafers. The wafer was baked on a hot plate at 95 °C for 15 min, and the 300-μm width micropillar-coated coverslip was gently removed from the wafer. A soft PDMS 10-mm diameter pillar (1:30) was poured into a homemade metal mould, degassed under vacuum and baked at 80 °C for 1 week.

EDTA device. Of 1:10 PDMS (Sylgard 184, Ellsworth Adhesives), 20–25 g was poured onto the wafer contained in an aluminium mould in a Petri dish, degassed in a vacuum desiccator and baked overnight at 80 °C. The devices were then diced with a razor blade and 2-mm entry and exit holes were punched (Harris Unicore biopsy puncher, Sigma-Aldrich). Following punching, they were cleaned with tape, sonicated in ethanol, blown dry and plasma-bonded to a coverslip.

Multilayer devices. PDMS (80 g; RTV615, Techsil) was used; 10 g of PDMS was put on the control layer and spin-coated (500 rpm for 15 s followed by 2,300 rpm for 60 s), and 70 g was applied on top of the flow layer in a tight aluminium mould and further degassed in a vacuum desiccator to pump out the remaining bubbles. Both layers were baked at 80 °C for 45 min, and the flow layer was removed from the mould, trimmed with a razor blade, and entry and exit holes were punched with a homemade arbor press. Debris from both the flow device and the control layer on its wafer were carefully removed with Scotch tape, the two layers were plasma-cleaned (2 min at medium intensity), aligned manually and bonded together. After overnight baking in 80 °C, the chip was removed from the wafer, the control layer entry holes were punched, and the chip was bonded to the glass coverslip by oxygen plasma and kept at 80 °C until further use. Before the experiments, all entry ports were connected with metal pins (NE-13-1003, New England Small Tube Corporation).

Migration assays

Before experiments, 2×10^5 T cells in 2 ml R10 medium were stained with Hoechst 33342 for 30 min (1 drop, NucBlue, R37605, Invitrogen, Thermo Fisher Scientific) when nucleus visualization was needed for cell tracking.

Collagen assay. A 3D collagen scaffold (final concentration of 1.7 mg/ml) was obtained by mixing bovine collagen (PureCol, Advanced BioMatrix) in 1× minimum essential medium Eagle and 0.4% sodium bicarbonate (both Sigma-Aldrich), with 3×10^5 cells in R10 medium at a 2:1 ratio[5,29]. After casting the mix in homemade migration chambers, gels were allowed to polymerize for 45 min at 37 °C, 5% CO_2. Migration was observed by time-lapse video microscopy.

Cell confiner assay. PDMS micropillars were placed on the soft pillar on a homemade magnetic glass lid. When indicated, dish and confiner were coated with 2 μg/ml of recombinant mouse ICAM-1/human Fc chimaera (796-IC, R&D Systems). The setup was placed in a dish containing R10 medium in a humidified incubator at 37 °C, 5% CO_2, 1 h before the experiments. Cells (5×10^4 in 5 μl R10 medium) were then pipetted onto the medium-freed micropillars and confined on a dish above a magnetic ring, and R10 medium was added back in the dish ready for imaging. For the myosin inhibition experiment, 50 μM para-nitroblebbistatin[30] was added to the medium (Optopharma).

Primary T cell confinement assay. To measure actin flow speed and cell curvatures, we used an agarose-confinement setup[8]. In brief, plasma-activated glass was overlaid with a 0.2 mg/ml solution of poly(L-lysine)-graft-PEG copolymer (PLL(20)-g[3.5]-PEG(2); SuSoS) at 4 °C overnight. To form a 0.5% agarose block with 10% FBS (and standard concentrations of other supplements), one part 2× HBSS buffer (Sigma) and two parts RPMI supplemented with twice the concentrations of all other supplements used in R10 medium were mixed together with one part 1% high-molecular-weight agarose (850152, Biozym Scientific GmbH) in water at 50 °C and subsequently cast onto the dish then allowed to solidify at room temperature. CCL19 (250-27B, Peprotech) was added to soluble agarose before casting. T cells were injected under the agarose block with a micropipette and incubated for 30 min at 37 °C under 5% CO_2 before imaging.

EDTA migration assay. T cells or PLB cells (5×10^4) were introduced into the 2-mm entry port of the microchamber, and the device was soaked in R10 medium. Cells were left to enter freely into the confinement and channel zone for 1 h and then imaged with a video microscope. After 1 h of imaging, chemical disruption of the cell adhesions was performed by removing R10 medium from the dish and adding R10 medium containing 10 mM EDTA (prepared from 0.5M stock; EDS-100G, Sigma-Aldrich) with or without 50 μM para-nitroblebbistatin[30] (Optopharma). Imaging was then resumed for 1 h. For dendritic cells, experiments were performed 1 day after overnight LPS activation (200 ng/ml; Sigma-Aldrich) with or without

2.5 µg/ml CCL19 (250-27B, Peprotech) added on the opposite hole of cell entry and with or without 30 mM EDTA[13].

Multilayered microfluidics: maze and microchannels migration assay. As talin-KO cells failed to freely enter the confinement zone, a homemade microfluidic setup was used to push the cells by applying a pressure differential to the inlet and outlet ports of the device. The microfluidics designs in Extended Data Fig. 2d were used, as well as separated chambers containing the four pillar mazes (identical to ref. [28] with four chambers). In brief, the core component of those devices is the flow layer with a 5-µm height pillar maze (Fig. 2a–d, Extended Data Fig. 2e) or channels (Figs. 2e–g, 4, Extended Data Figs. 2f, 4) with an exit, cell and medium entry ports and on one side and on the other side a sink channel connected to two or three exits. Flow and sink channels are rounded, 26 µm high. For a controlled flow of cells and fluids, all ports are equipped with independently controllable push-up PDMS membrane valves. In brief, the control channels are connected to solenoid valves (MH1, miniature, Festo) controlled with a MATLAB graphical user interface (MathWorks). First, the chip was mounted into the 37 °C, 5% CO_2 chamber of the microscope, and optimal closing pressures of 0.15–0.2 MPa of the water-filler PDMS membrane valves were determined for each chip; each valve was checked individually by microscopy. Second, the whole chip was saturated with a pre-warmed medium by applying a pressure of 0.04 MPa and incubated in R10 medium for 30 min. Cells were first loaded via the ports on one side, resulting in their distribution along the chamber, then slowly pushed with a pressure of <0.01 MPa from the medium port towards the confinement zone, and further pushed in the microchannels or micropillars maze. Finally, all valves were closed to ensure that no external pressure or flow was applied to the cells during imaging.

TIRF microfluidics: microchannels migration assay. For Fig. 4e–g, TIRF microscopy was not possible with the multilayered microfluidic devices, so devices with the flow layer only were generated. First, R10 medium was forced into the device with a vacuum desiccator, and then the chips were incubated in humidified 5% CO_2 at 37 °C for 2 h before the experiments. Experiments were performed on the microscope stage (humidified environment 5% CO_2 at 37 °C) and a low cell flow was delivered and stopped after talin-KO cell loading in the microchannel using a LA120 syringe pump (5 µl/h; Landgraf Laborsysteme).

Primary T cell confinement assay on nanoridges

T cells were confined under agarose as previously described with minor modifications[8]. In brief, plasma-activated coverslips with nanoridges (800 nm/800 nm/600 nm (groove/ridge/depth)) (ANFS-CS25-50, NanoSurface Biomedical) were passivated with a 1 mg/ml solution of poly(L-lysine)-graft-PEG copolymer (PLL(20)-g[3.5]-PEG(2), SuSoS) at 4 °C overnight. Flat control coverslips (FLAT-CS25-50, NanoSurface Biomedical) were either passivated as described above or coated with rhICAM1-Fc (2 µg/ml) (720-IC-050, R&D) to generate adhesive substrates. Next, 0.5% agarose was prepared by mixing A, 5 ml of 2× HBSS buffer (Sigma), and mixing B, 10 ml of serum-free RPMI supplemented with 20% BSA and twice the concentrations of all other supplements used in R10 medium (see above), and mixing C, 5 ml of 1% high-molecular-weight agarose (850152, Biozym Scientific GmbH) in PBS. Agarose solution (0.5%) was kept at 50 °C in a water bath before it was layered on top of the coated coverslips and allowed to solidify for 1 h at 4 °C. CCL19 (10 nM; 250-27B, Peprotech) was added to soluble agarose before casting. T cells were isolated from the spleen of wild-type and/or Lifeact-GFP mice (T cell isolation kit mouse; MACS, Miltenyi Biotec) and kept in R10 medium at 37 °C and 5% CO_2. Before imaging (30 min), 0.5 µl of highly concentrated T cells was injected under the agarose block.

Time-lapse video microscopy

Bright-field video of T cells for collagen assays (×10 objective), 3-µm high confiner assays and primary T cells migrating under agarose (×20 objective) were acquired by time-lapse acquisition (time interval of 20 s) using inverted cell culture microscopes (DM IL Led, Leica Microsystems) equipped with cameras (ECO415MVGE, SVS-Vistek) and custom-built climate chambers (5% CO_2, 37 °C, humidified). A 5-µm high confiner, EDTA and microfluidics assays were recorded every 30 s or 60 s at 2–6 multi-positions with NIS Elements software (Nikon Instruments). Experiments were performed with an inverted wide-field Nikon Eclipse Ti microscope in a humidified and heated chamber at 37 °C and 5% CO_2 (Ibidi Gas Mixer), equipped with a ×20/0.5 NA PH1 air objective, a Hamamatsu EMCCD C9100 camera and a Lumencor Spectra X light source (390 nm, 475 nm, 542/575 nm; Lumencor). TIRF microscopy was performed with a ×60/1.46 NA oil objective, optovar ×1 or ×1.6 in a humidified and heated chamber at 37 °C and 5% CO_2 using an inverted Axio Observer (Zeiss) microscope, a TIRF 488/561-nm laser (Visitron Systems) and an Evolve EMCCD camera (Photometrics) controlled by VisiView software (Visitron Systems). To visualize actin retrograde flow, assays were recorded every second for TIRF acquisition only (Fig. 1e–g, Supplementary Video 3 example 3) or every 2 s or 3 s when acquisition of both TIRF or wide-field fluorescence and bright field was necessary (Fig. 4e–g, Extended Data Figs. 4b, 5g, Supplementary Videos 3 (examples 1 and 2), 10). When cells migrated outside the field of view (Supplementary Video 10), they were manually followed via a joystick controller. For the primary T cell confinement assay on nanoridges (Extended Data Fig. 7), a video of actin flow (Lifeact-GFP) were recorded (2-s frame rate) on an inverted spinning-disc confocal microscope (Andor) using a ×100/1.4 NA objective and a 488-nm laser line in a custom-built climate chamber (37 °C under 5% CO_2). For the primary T cell flow analysis (Extended Data Fig. 8), inverted spinning-disc confocal microscopy was performed at 37 °C under 5% CO2 with an iMIC (TILL Photonics, FEI) instrument with a ×60/1.35 NA objective and a 488-nm laser line.

Image analysis

FIJI imaging processing software (https://fiji.sc/) was used for image and video microscopy analysis.

Spreading area. TIRF images of single cells were binarized after de-speckling and background subtraction, and the spreading area was measured using the Analyse Particles tool.

Cell size measurement. To measure cell size, fluorescent images of 3-µm-confined control (Lifeact-mCherry) and talin-KO (Lifeact-GFP) cells were binarized, and the single-cell spreading area and perimeter were measured using the Analyse Particles tool.

Manual tracking. A 1-h-long bright-field video of T cells in collagen and 3-µm high confiners were reduced to a 1-min and 2-min interval, respectively, and cells were tracked manually by using the 'Manual tracking' plugin provided by Fiji.

Automated tracking. For the 5-µm high confiner, pillar maze and EDTA assays, cell migration was analysed by nucleus tracking using TrackMate[31] (https://imagej.net/TrackMate). For the EDTA assay, tracks before and after EDTA treatment were analysed and the speed was extracted at the single-cell level in the different zones (2.5D confinement, smooth and serrated microchannels containing only one cell). For Fig. 4b, cell migration in the channel zones was regarded as efficient for velocities above 0.5 µm/min. The mean square displacement was calculated from the tracking files with a homemade script (MATLAB, MathWorks).

Actin flow versus cell velocity analysis. For Figs. 1e–g, 4e–g, Extended Data Figs. 1l, 4b, 5g, 8a, kymographs were generated along the cell trajectories, and both cell and actin velocities were extracted from those kymographs. To follow cells migrating in a channel with a high magnification (Fig. 4e–g, Supplementary Video 10), the channel was realigned with a homemade script (MATLAB, MathWorks).

Microchannel assay analysis. Cells going in both directions of the microchannels were analysed, and channels containing more than one cell were excluded. Kymographs were generated along the channel, and cell velocity was calculated for each cell in the different zones.

Actin flow in primary T cells confined on nanoridges. Actin flow vectors were measured by two methods: A, which was automatic particle tracking with TrackMate plugin (3.8.0) of FIJI[31] (ImageJ 1.52p, java 1.8.0), and B, which was optical flow analysis (using a custom MATLAB code). Only frames where optical flow analysis was confirming automatic particle tracking (deviation of <30°) were subjected to further analysis. To estimate vectors of forwards cell movement, cell contours were segmented with Ilastik[32], and cell displacement was measured by tracking the centroids. Angular distributions of actin flow vectors and angular distributions of cell forwards movement vectors were then analysed and plotted with respect to the orientation of nanoridges using a custom MATLAB code.

Curvature analysis. For Extended Data Fig. 8, we set up a homemade script that performs binarization of fluorescent images of Lifeact-GFP-expressing cells. The local curvature was calculated from a spline fit to the cell outline, and the cortical actin flow was quantified with optical flow analysis (MATLAB, MathWorks).

Statistical analysis

All statistical analyses were performed with GraphPad Prism (GraphPad Software). The normality test was performed, and the statistical strategy used accordingly (for example, non-parametric Mann–Whitney *U*-test and one-way ANOVA with Kruskal–Wallis test with post hoc Dunn's test) as indicated in Supplementary Table 1. For the box and whiskers graphs in Fig. 4d, g and Extended Data Figs. 2f, 4a, 4b, 5g, 6f, the box extends from the 25th to the 75th percentiles, with the middle line showing the median, and the whiskers indicating the minimum to maximum values. See Supplementary Table 1 for additional information.

Reporting summary

Further information on research design is available in the Nature Research Reporting Summary linked to this paper.

Data availability

Data that support the findings of this study are available within the Article and its Supplementary Information. Source data for Figs. 1, 2, 4 and Extended Data Figs. 1–8 are provided with the paper. Original videos will be made available on reasonable request due to the large file size.

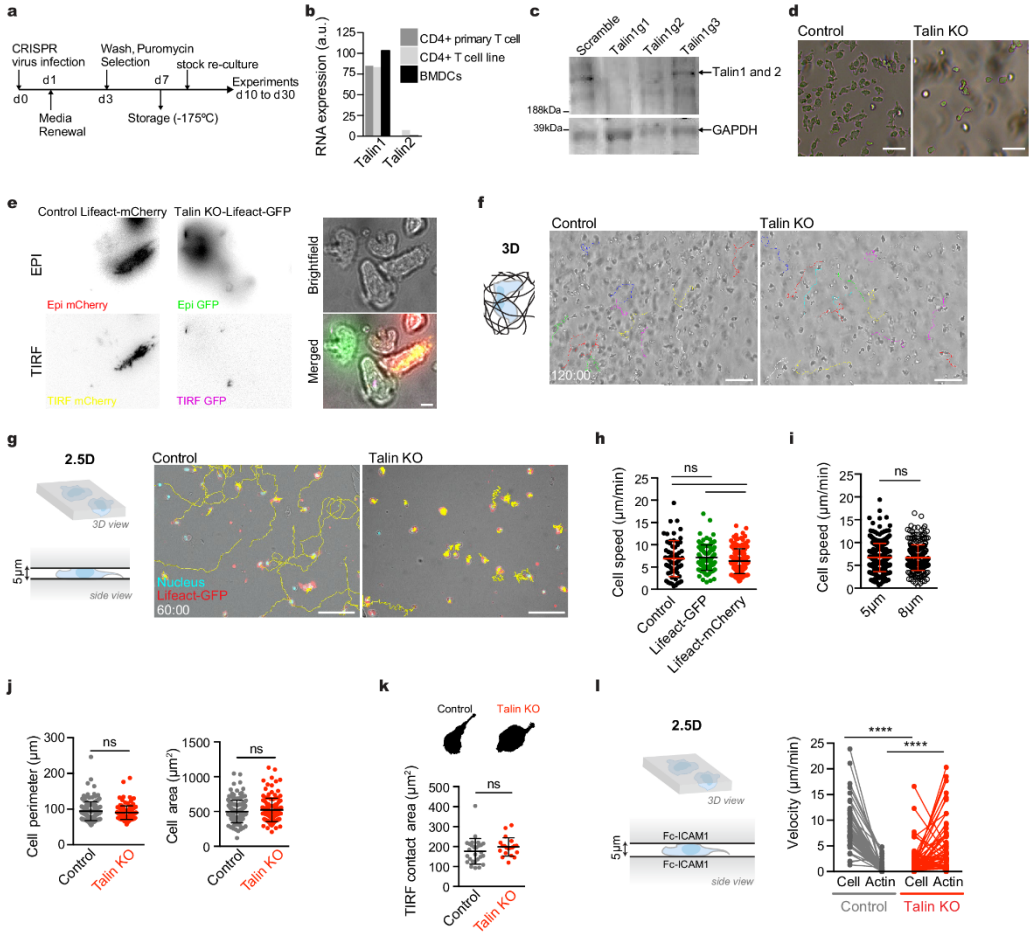
24. Riedl, J. et al. Lifeact: a versatile marker to visualize F-actin. *Nat. Methods* **5**, 605–607 (2008).
25. Leithner, A. et al. Diversified actin protrusions promote environmental exploration but are dispensable for locomotion of leukocytes. *Nat. Cell Biol.* **18**, 1253–1259 (2016).
26. Shalem, O. et al. Genome-scale CRISPR–Cas9 knockout screening in human cells. *Science* **343**, 84–87 (2014).
27. Leithner, A., Merrin, J., Reversat, A. & Sixt, M. Geometrically complex microfluidic devices for the study of cell migration. *Protoc. Exch.* https://doi.org/10.1038/protex.2016.063 (2016).
28. Schwarz, J. et al. A microfluidic device for measuring cell migration towards substrate-bound and soluble chemokine gradients. *Sci. Rep.* **6**, 36440 (2016).
29. Sixt, M. & Lämmermann, T. in *Cell Migration: Developmental Methods and Protocols* (eds. Wells, C. M. & Parsons, M.) 149–165 (Humana, 2011).
30. Képiró, M. et al. *para*-Nitroblebbistatin, the non-cytotoxic and photostable myosin II inhibitor. *Angew. Chem. Int. Ed. Engl.* **53**, 8211–8215 (2014).
31. Tinevez, J. Y. et al. TrackMate: an open and extensible platform for single-particle tracking. *Methods* **115**, 80–90 (2017).
32. Sommer, C., Straehle, C., Koethe, U. & Hamprecht, F. A. Ilastik: interactive learning and segmentation toolkit. In *2011 IEEE International Symposium on Biomedical Imaging: From Nano to Macro* 230–233 (IEEE, 2011).

Acknowledgements We thank A. Leithner and J. Renkawitz for discussion and critical reading of the manuscript; J. Schwarz and M. Mehling for establishing the microfluidic setups; the Bioimaging Facility of IST Austria for excellent support, as well as the Life Science Facility and the Miba Machine Shop of IST Austria; and F. N. Arslan, L. E. Burnett and L. Li for their work during their rotation in the IST PhD programme. This work was supported by the European Research Council (ERC StG 281556 and CoG 724373) to M.S. and grants from the Austrian Science Fund (FWF P29911) and the WWTF to M.S. M.H. was supported by the European Regional Development Fund Project (CZ.02.1.01/0.0/0.0/15_003/0000476). F.G. received funding from the European Union's Horizon 2020 research and innovation programme under the Marie Skłodowska-Curie grant agreement no. 747687.

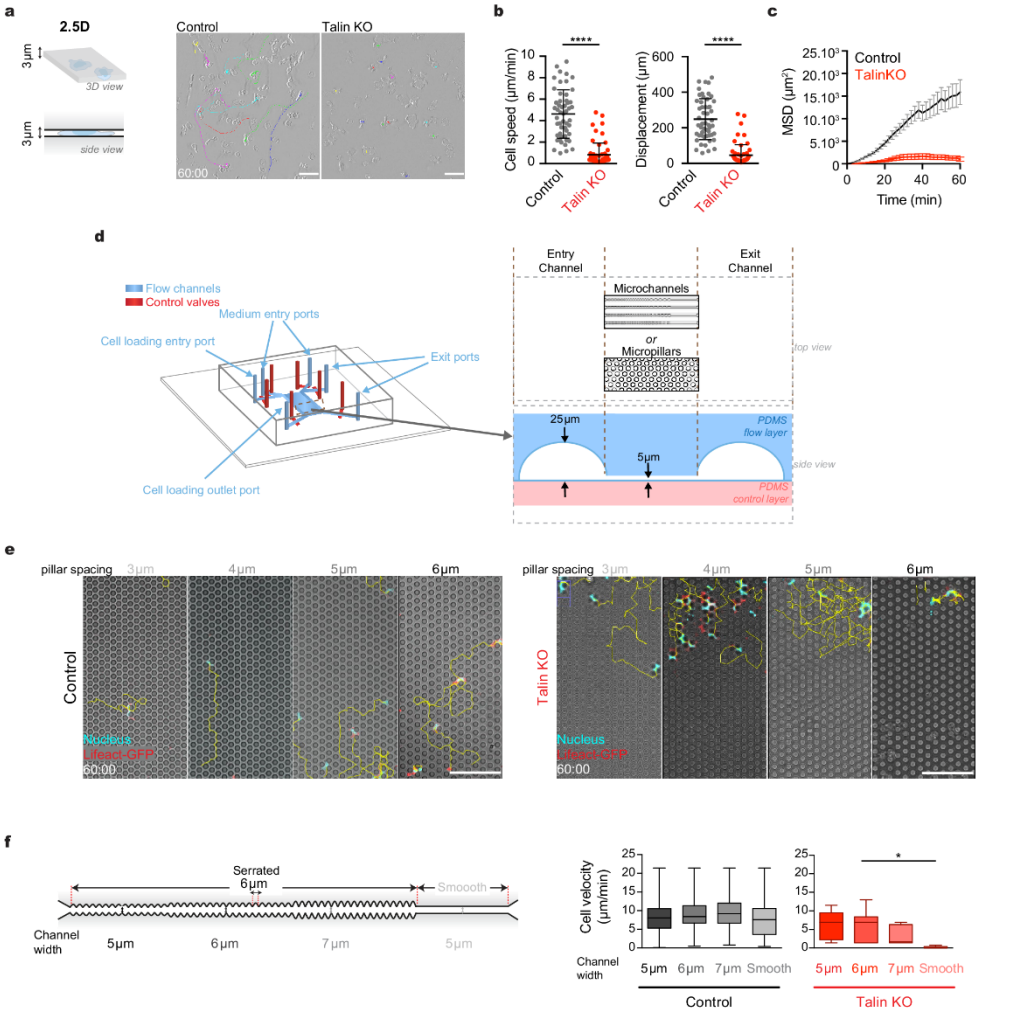
Author contributions A.R. and M.S. conceived the experiments and wrote the manuscript, with critical feedback from all authors. A.R. designed, performed and analysed the experiments, with the help of I.d.V., J.S., M.H., R.H. and S.T. A.R. and J.M. designed the microfluidic devices. J.M. performed the photolithography. F.G. designed and performed the nanoridge experiments. J.A. fabricated the nanoridge substrates. R.H. wrote the image analysis scripts. A.C.-J., R.V., J.M., R.H., M.S. and A.R. discussed the physical model. A.C.-J. and R.V. wrote the physical model.

Competing interests The authors declare no competing interests.

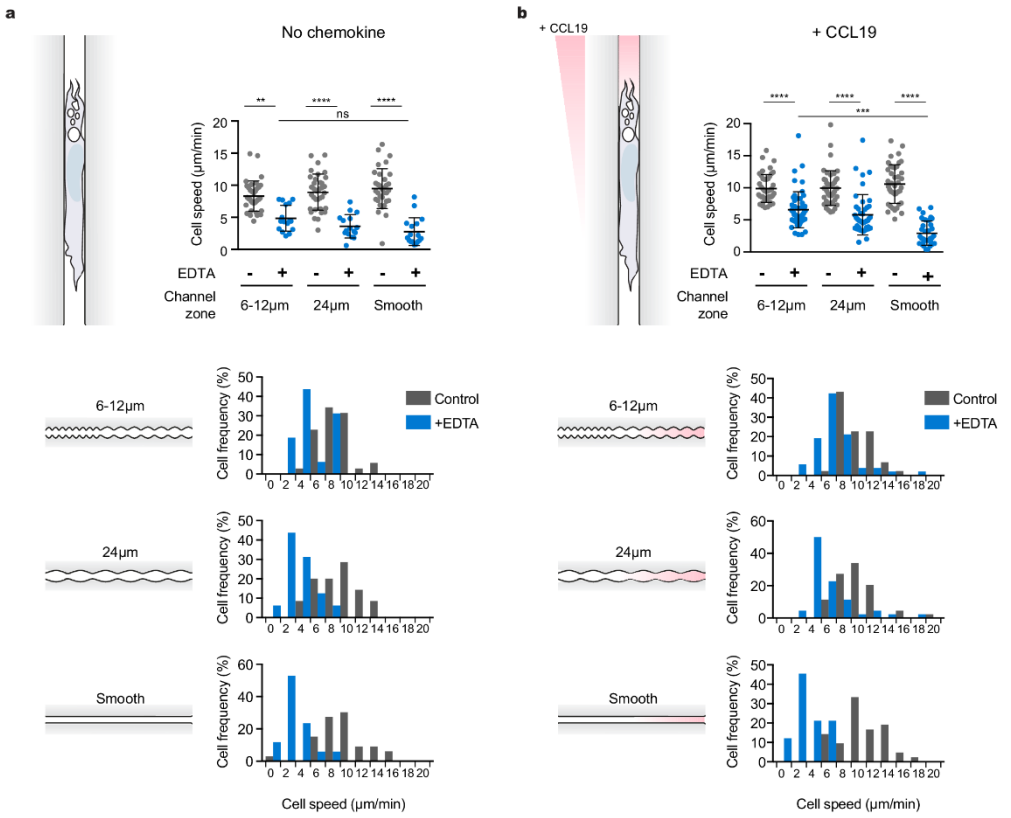
Additional information
Supplementary information is available for this paper at https://doi.org/10.1038/s41586-020-2283-z.
Correspondence and requests for materials should be addressed to A.R. or M.S.
Peer review information *Nature* thanks Kenneth Yamada and the other, anonymous, reviewer(s) for their contribution to the peer review of this work.
Reprints and permissions information is available at http://www.nature.com/reprints.



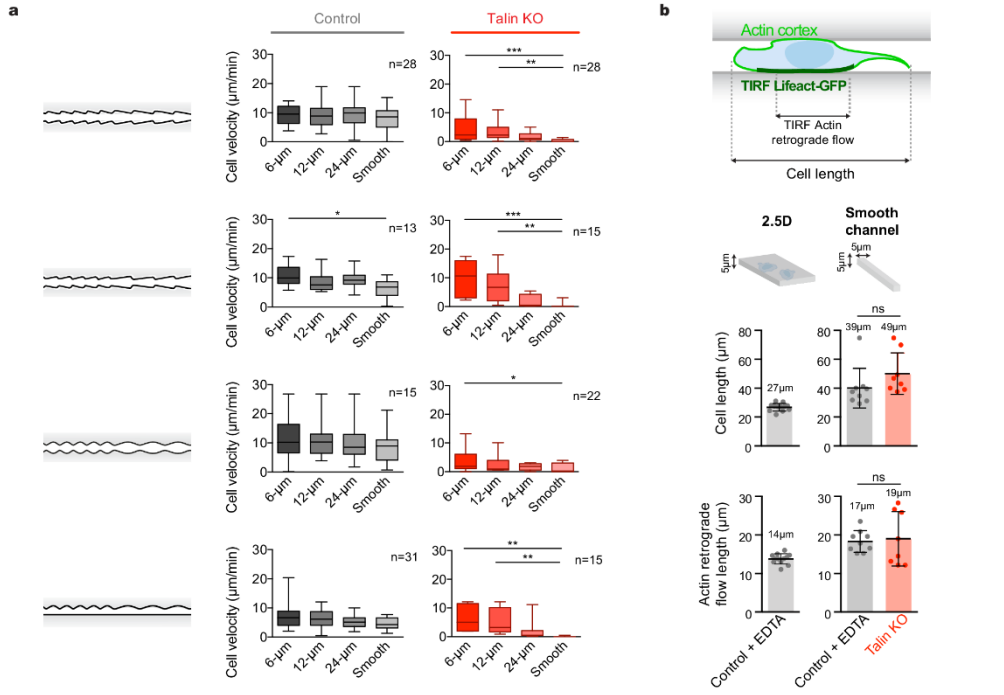
Extended Data Fig. 1 | Effects of *Tln1* deletion on T cell adhesion and migration. **a**, Workflow scheme of virus production, cell infection and analysis. d, day. **b**, RNA-seq analysis of talin 1 and 2 expression in mouse CD4$^+$ primary T cells, the T cell line and bone marrow-derived dendritic cells (BMDCs). **c**, Western blot analysis of talin 1 and talin 2 expression in T cells infected with lentivirus containing scrambled and talin 1-targeting CRISPR guides (guides 1–3 (Talin1g1–Talin1g3)). Data are representative of three independent experiments. **d**, Related to Fig. 1a. Phase-contrast images of control and talin-KO cells. Scale bars, 50 µm. Representative of four experiments. **e**, Related to Fig. 1b. Representative snapshots of epifluorescence (EPI) and TIRF microscopy of control cells (left) and talin-KO cells (middle) expressing mCherry and eGFP Lifeact fusions, respectively, plated on a Fc-ICAM1-coated surface. Representative of three experiments. The right panel shows bright field and merged fluorescence. Scale bar, 5 µm. **f**, Related to Fig. 1c. Representative snapshots of control and talin-KO cells embedded in 3D collagen gel at $t = 120$ min; individual tracks are displayed in different colours. Representative of three experiments. Scale bars, 100 µm. **g**, Related to Fig. 1d. Left, scheme of 5-µm high confinement used in **f**, **g** and **j**. Right, control cells (left) and talin-KO T cells (right) expressing Lifeact-GFP (red), stained with Hoechst (cyan), were placed under 5-µm height confinement and imaged by video microscopy. Representative of four experiments. Snapshot is at $t = 60$ min. Nucleus tracks are displayed in yellow. Scale bars, 50 µm. **h**, Cell speed of control T cells ($n = 62$) and T cells expressing Lifeact-GFP ($n = 100$) or Lifeact-mCherry ($n = 138$). Data are mean ± s.d.; ns $P = 0.0775$, Kruskal–Wallis one-way ANOVA followed by two-sided post hoc Dunn's test; control versus Lifeact-GFP or Lifeact-mCherry: $P > 0.999$; Lifeact-GFP versus Lifeact-mCherry: $P = 0.0717$. **i**, Speed of T cells placed under 5-µm ($n = 300$) or 8-µm ($n = 274$) confinement. Data are mean ± s.d.; ns $P = 0.8460$, two-sided Mann–Whitney *U*-test. **j**, Perimeter (left) and area (right) of control and talin-KO cells placed under 3-µm confinement (control cells: $n = 145$, talin-KO cells: $n = 127$). Representative of three experiments. Data are mean ± s.d.; ns $P = 0.4261$ for perimeter and $P = 0.2558$ for area, two-sided Mann–Whitney *U*-test. **k**, Spreading area observed by TIRF microscopy of control ($n = 27$) and talin-KO ($n = 20$) cells under 5-µm confinement. Representative of two experiments. Data are mean ± s.d.; ns $P = 0.2025$, two-sided Mann–Whitney *U*-test. **l**, Scheme of the 5-µm high Fc-ICAM1-coated confinement (left) used to measure velocities and F-actin retrograde flow (right) in control cells ($n = 49$) and talin-KO T cells ($n = 59$). Representative of five experiments. ****$P < 0.0001$, two-sided Mann–Whitney *U*-test.



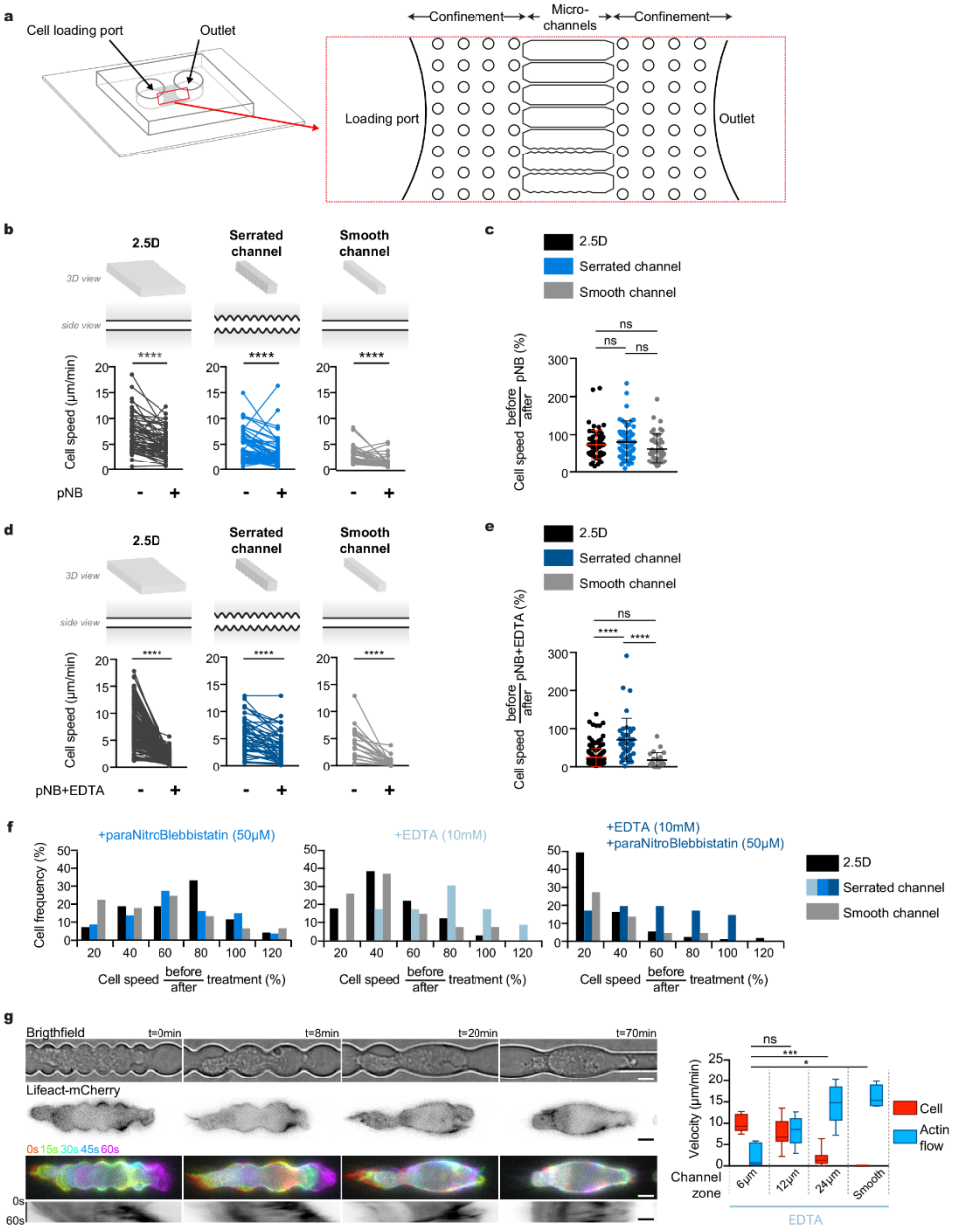
Extended Data Fig. 2 | Topography rescues T cell locomotion in the absence of adhesion. a–**c**, Migration of control ($n = 71$) and talin-KO ($n = 74$) cells under 3-µm confinement. Representative of four independent experiments. In **a**, the left panel shows the scheme of the 3-µm confinement used in **a**–**c**. The right panel shows representative snapshots of control and talin-KO cells under 3-µm confinement at $t = 60$ min. Individual tracks are displayed in different colours. Scale bars, 50 µm. In **b**, the speed and displacement of control and talin-KO cells under 3-µm confinement are shown. Data are mean ± s.d.; ****$P < 0.0001$, two-sided Mann–Whitney U-test. In **c**, the MSD of control cells (black) and talin-KO cells (red) is shown. Data are mean ± s.e.m.; $P < 0.0001$, two-sided Mann–Whitney U-test. **d**, Related to Fig. 2a–d. Scheme of multilayered microfluidic devices used to push cells into the pillar maze or into microchannels used in **e** and **f**. **e**, Snapshots of video microscopy at $t = 60$ min of control and talin-KO cells in the pillar device. The nucleus is shown in cyan (Hoechst), Lifeact-GFP reporter in red and the bright-field image in grey. Individual cell tracks are displayed in yellow. Scale bars, 50 µm. Time is in min:s. Representative of three experiments. **f**, Related to Fig. 2g, h. Velocities (µm/min) of control and talin-KO cells in serrated channels of different diameters (with a conserved serration period of 6 µm). Representative of three experiments. $n = 57$ for control cells and $n = 9$ for talin-KO cells. *$P = 0.0356$; otherwise not significant, Kruskal–Wallis one-way ANOVA followed by post hoc Dunn's test. Boxes extend from the 25th to the 75th percentiles, with the middle line showing the median and the whiskers representing the minimum to maximum values.



Extended Data Fig. 3 | Topography rescues dendritic cell locomotion in the absence of adhesion. a, Top left, scheme of a mature dendritic cell migrating in a channel designed for the EDTA experiment. Mature dendritic cells migrate in a device containing channels with different serration periods, with or without 30 mM EDTA. Top right, single-cell migration speed with (+, blue) and without (-, grey) EDTA treatment. Bottom, histograms of cell speed in different serrations with (blue) or without (grey) EDTA. Representative of three independent experiments. $n = 35$ cells without EDTA, $n = 17$ cells with EDTA. Data are mean ± s.d.; $^{**}P = 0.0022$, $^{****}P < 0.0001$ and ns $P = 0.6363$, one-way ANOVA with Kruskal–Wallis test followed by post hoc Dunn's test. **b**, Top left, scheme of a mature dendritic cell migrating in a channel designed for the EDTA experiment, along a CCL19 gradient (indicated in red). Mature dendritic cells migrate towards the chemokine CCL19 into a device that contains microchannels with different serration periods, with or without 30 mM EDTA. Top right, migration speed with (+, blue) and without (-, grey) EDTA treatment. Bottom, histograms of cell speed in the different serrated channels with (blue) or without (grey) EDTA. Representative of three independent experiments. Without EDTA: $n = 44$ cells; with EDTA: $n = 52$ (6–12 μm), $n = 44$ (24 μm), $n = 33$ (smooth channels). Data are mean ± s.d.; $^{***}P = 0.0001$ and $^{****}P < 0.0001$, one-way ANOVA with Kruskal–Wallis test followed by post hoc Dunn's test.

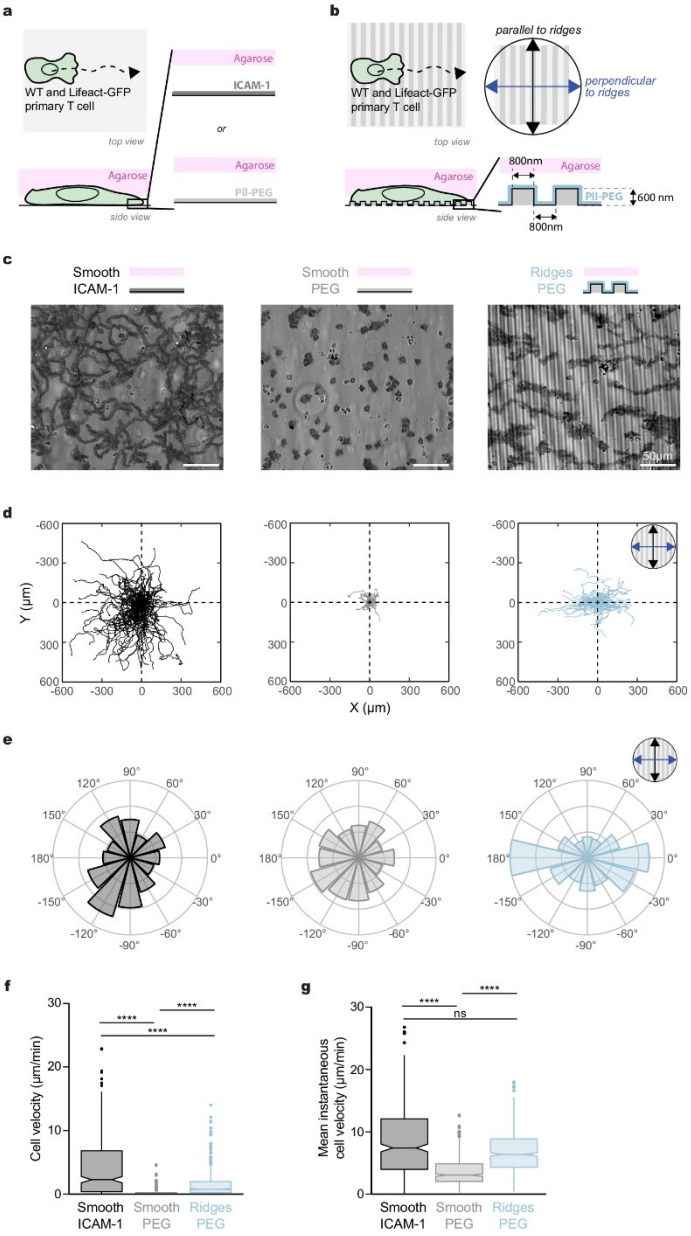


Extended Data Fig. 4 | Effect of topographical features on T cell migration. **a**, Related to Fig. 4d. Scheme of channel designs with decreasing complexity. In brief, serrations with a period of 6, 12 and 24 µm were arranged in consecutive zones of a 5-µm wide channel ending with a smooth zone. The left panel shows the different geometries. The right and middle panels show the velocity of cells migrating in zones with a different period. The total number of cells in each design is shown. Representative of four (control cells) and eight (talin-KO cells) independent experiments. Control: $^{*}P = 0.0415$. KO arrow 'right': $^{***}P = 0.0008$ and $^{**}P = 0.0013$; KO arrow 'left': $^{***}P = 0.0003$ and $^{**}P = 0.0018$; KO bulb: $^{*}P = 0.0344$; KO half-bulb: $^{**}P = 0.0016$ (6 µm versus smooth) and $^{**}P = 0.0013$ (12 µm versus smooth), otherwise not significant, one-way ANOVA with Kruskal–Wallis test followed by post hoc Dunn's test. Boxes extend from the 25th to the 75th percentiles, with the middle line showing the median and the whiskers representing the minimum to maximum values. **b**, Top, scheme of cell and actin retrograde flow length. Bottom, control cells expressing the Lifeact-GFP reporter with 10 mM EDTA (grey) or talin-KO cells (red), under 5-µm confinement (left, $n = 12$) or in a 5 × 5-µm channel (right, $n = 9$ for control cells and $n = 8$ for talin-KO cells), were observed by TIRF microscopy, and the mean cell length (ns $P = 0.0555$, two-sided Mann–Whitney U-test) and the actin retrograde flow length (ns $P = 0.7247$, two-sided Mann–Whitney U-test) were measured using kymograph analysis. Representative of two independent experiments. Data are mean ± s.d.



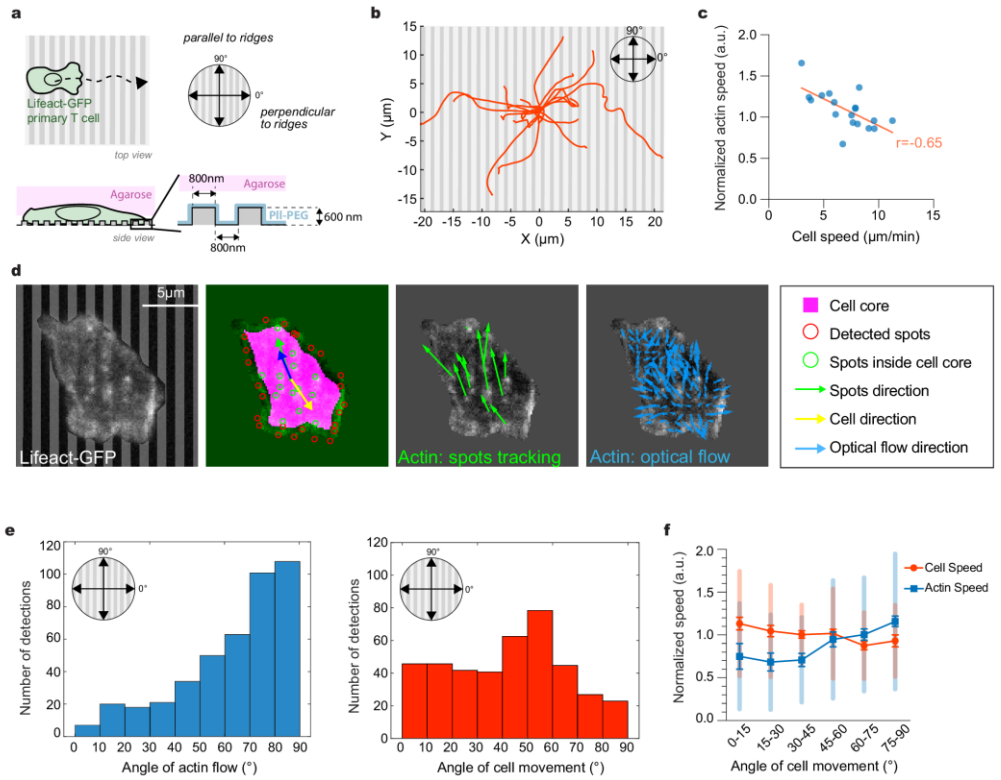
Extended Data Fig. 5 | See next page for caption.

Extended Data Fig. 5 | Actin polymerization versus contractility during topography-based locomotion. a, Scheme of the device used for the experiments in Fig. 2i, j and Supplementary Figs. 3, 5. **b**, Control T cells migrating under confinement (2.5D) or in smooth versus serrated channels as shown in the top panels. After 60 min, 50 µM para-nitroblebbistatin (pNB) was added. The migration speed before (-) and after (+) treatment is shown. Representative of four independent experiments. $n = 68$ for 2.5D, $n = 79$ for serrated channel and $n = 44$ for smooth channel. ****$P < 0.0001$, two-tailed, Wilcoxon matched-pairs signed-rank test. **c**, Migration speed change after versus before pNB treatment. Data are mean ± s.d. ns $P > 0.9999$ (2.5D versus serrated channel), ns $P = 0.1414$ (2.5D versus smooth channel) and ns $P = 0.1044$ (serrated vs smooth channel), one-way ANOVA with Kruskal–Wallis test followed by post hoc Dunn's test. **d**, Control T cells migrating under confinement or in smooth versus serrated channels as shown in the top panels. After 60 min, 50 µM pNB and 10 mM EDTA were added. The migration speed before (-) and after (+) treatment is shown. Representative of four independent experiments. $n = 166$ for 2.5D, $n = 45$ for serrated channel and $n = 22$ for smooth channel. ****$P < 0.0001$, two-tailed, Wilcoxon matched-pairs signed-rank test. **e**, Migration speed change after versus before pNB + EDTA treatment. Data are mean ± s.d. ns $P = 0.1170$ and ****$P < 0.0001$, one-way ANOVA with Kruskal–Wallis test followed by post hoc Dunn's test. **f**, Histogram of migration speed variation after versus before pNB treatment alone (left, see **b**, **c**), EDTA treatment alone (middle, related to Fig. 2i, j) or pNB + EDTA treatment (right, see **d**, **e**). **g**, Related to Fig. 4e–g. Left, snapshots of a control T cell expressing Lifeact-mCherry incubated with 10 mM EDTA in different channel zones. The left panel from top to bottom shows bright field, Lifeact-mCherry in black, colour-coded snapshots of F-actin in the different channel zones (15-s intervals), and the corresponding kymograph of a cell migrating in the channel. Scale bars, 5 µm. Right, cell and actin retrograde flow velocities observed by wide-field microscopy and measured with kymograph analysis. $n = 8$ cells; 3 cells in all zones, 4 cells in the 6–12–24-µm zone and 1 cell in the 12–24-µm zone. *$P = 0.0138$ and ***$P = 0.0002$, one-way ANOVA with Kruskal–Wallis test followed by post hoc Dunn's test. Boxes extend from the 25th to the 75th percentiles, with the middle line showing the median and the whiskers representing the minimum to maximum values.

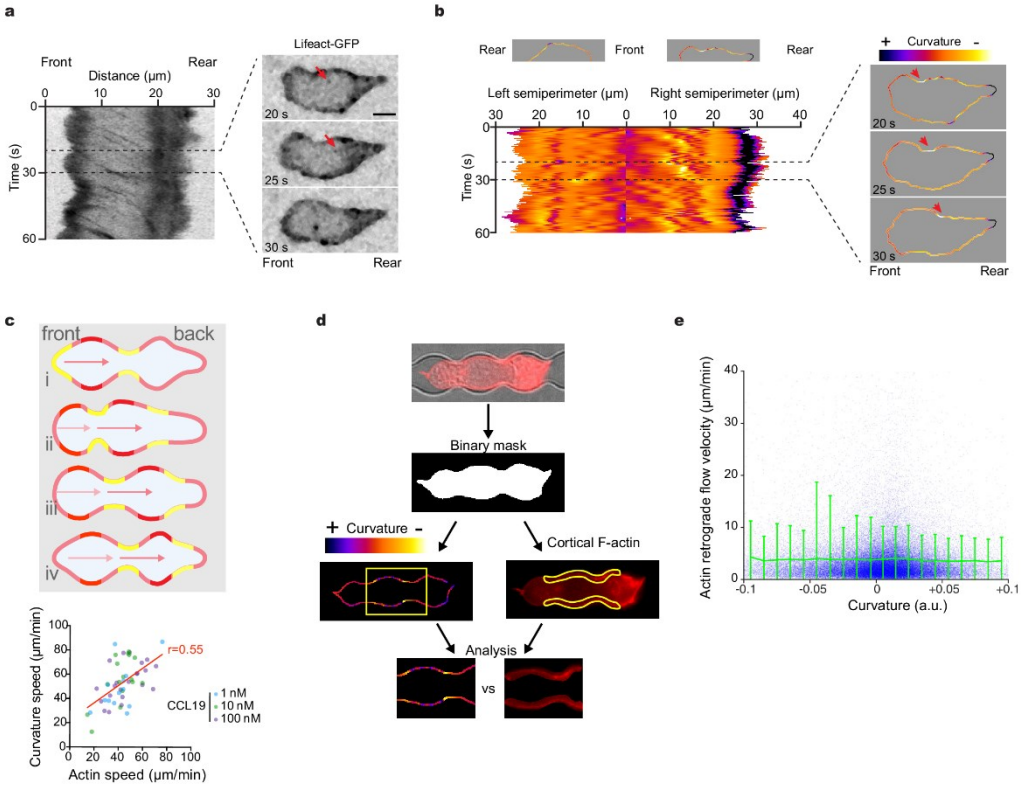


Extended Data Fig. 6 | See next page for caption.

Extended Data Fig. 6 | Topography-based migration of primary T cells. **a**, Scheme (top and side view) of control and Lifeact-GFP cells confined under agarose on a smooth surface coated with Fc-ICAM1 or passivated with PLL-PEG. WT, wild type. **b**, Scheme (top and side view) of control and Lifeact-GFP cells confined under agarose on a coverslip with linear ridges passivated with PLL-PEG. **c**, Minimum-intensity projection showing the trace of control cells migrating for 15 min under agarose on Fc-ICAM1-coated smooth surfaces (left), PLL-PEG-coated smooth surfaces (middle) and PLL-PEG-coated ridge-baring surfaces (right). Representative of six independent experiments. Scale bars, 50 µm. **d**, Randomly selected tracks of mixed control and Lifeact-GFP cells migrating under agarose on Fc-ICAM1-coated smooth surfaces (left, $n = 183$), PLL-PEG-coated smooth surfaces (middle, $n = 183$) and PLL-PEG-coated ridge-baring surfaces (right, $n = 183$). The orientation of ridges is indicated in the top right corner. **e**, Rose diagram (with circular lines from the centre showing 6%, 12% and 18% of total cells) of cells migrating on Fc-ICAM1-coated smooth surfaces (left, $n = 419$), PLL-PEG-coated smooth surfaces (middle, $n = 650$) and PLL-PEG-coated ridge-baring surfaces (right, $n = 687$). The orientation of ridges is indicated in the top right corner. $n = 6$ independent experiments. **f**, **g**, Velocities of cells migrating under agarose on Fc-ICAM1-coated smooth surfaces ($n = 419$), PLL-PEG-coated smooth surfaces ($n = 650$) and PLL-PEG-coated ridge-baring surfaces ($n = 687$). $n = 6$ independent experiments. Cell velocities (cell displacement divided by track duration) (**f**) and mean instantaneous velocities (**g**) are shown. ****$P < 0.0001$ and ns $P = 0.0757$, both one-way ANOVA with Kruskal–Wallis test followed by post hoc Dunn's test.



Extended Data Fig. 7 | Actin-based force transmission in primary T cells. **a**, Scheme (top and side view) of cells migrating under agarose on a non-adhesive, topography-baring substrate. **b**, Tracks of migrating cells analysed in **c**–**f**. $n = 18$; mean cell speed = 6.58 µm/min; mean actin retrograde flow speed = 6.53 µm/min. Starting points of tracks are shifted to the origin. **c**, Mean speed of cells in relation to their mean actin retrograde flow speed (in relation to the substrate). Pearson's rank correlation coefficient r = −0.6484. A drop in retrograde flow with increasing locomotion speed demonstrates that, as in the transmembrane clutch paradigm of force transmission, actin slippage is inversely related to locomotion. **d**, Snapshots of actin flow analysis on ridged surfaces of cells expressing Lifeact-GFP. Left, cell core segmented with Ilastik (pink); the yellow arrow indicates cell direction, the blue arrow indicates the mean optical flow direction and the green arrow indicates actin retrograde flow. Middle, optical flow analysis (obtained with a customized MATLAB code). Right, actin single-spot tracking (TrackMate). Representative of three independent experiments. **e**, Angular distribution of actin retrograde flow and forwards locomotion of cells migrating on nanoridges. Only frames where optical flow analysis was confirming automatic particle tracking (deviation of <30°; see **d**) were subjected to analysis. The histogram on the left shows predominant retrograde actin flow when aligned along the ridges (90°). Retrograde actin flow declines towards 0° (perpendicular to the ridges), while forwards locomotion (right histogram) steadily increases, indicating that retrograde actin flow couples to topographical barriers and drives locomotion. $n = 422$ events of actin flow and cell movements obtained in $n = 18$ cells from three independent experiments. **f**, Frame-to-frame speed of cells migrating on nanoridges increases when forwards locomotion aligns perpendicular to topographical barriers (90° → 0° ≃ 15% increase). The orientation-dependent increase of cell speed is paralleled by a steady decrease of retrograde actin flow (90° → 0° ≃ 55%), indicating that retrograde actin flow couples to topographical barriers and drives locomotion. Frame-to-frame cell speed and actin retrograde flow speed were recorded in 18 cells from 3 independent experiments, and pooled to $n = 412$ (cell speed) and $n = 422$ (actin retrograde flow speed) events. The centre shows the mean, and both s.e.m. (solid lines) and s.d. (thick transparent lines) are shown. Before pooling, cell speed was normalized to the mean speed of the tracked cell, and actin retrograde flow speed was normalized to the mean actin retrograde flow speed.



Extended Data Fig. 8 | Retrograde actin flow and shape changes in adhesion-free confinement. Related to Fig. 4h. **a**–**c**, Primary T cells expressing Lifeact-GFP confined on PLL-PEG. $n = 51$ cells from three independent experiments: $n = 22$ cells for 100 nM CCL19, $n = 16$ cells for 10 nM CCL19 and $n = 13$ cells for 1 nM CCL19. **a**, Representative snapshots (right, $t = 20$, 25 and 30 s) and kymographs (left), of primary T cells expressing Lifeact-GFP confined on PLL-PEG, showing actin retrograde flow (red arrows). Scale bar, 5 μm. **b**, Representative snapshots (right, $t = 20$, 25 and 30 s) of the cell outline and the colour-coded curvature. Kymograph analysis (left) of the migrating T cell shows retrograde movement of cell body deformations (right, red arrowhead). **c**, Top, scheme of the travelling cell body deformations. Bottom, retrograde actin flow versus curvature flow velocities in primary T cells confined on an inert substrate and exposed to the indicated chemokine (CCL19) concentrations. $n = 51$ cells from three independent experiments: $n = 22$ cells for 100 nM CCL19, $n = 16$ cells for 10 nM CCL19 and $n = 13$ cells for 1 nM CCL19. Pearson's rank correlation coefficient $r = 0.5542$. **d**, **e**, Cell curvature versus cortical actin retrograde flow analysis in channels (obtained from three cells in three experiments). A scheme of the segmentation used to measure channel-dependent cell curvature and cortical actin retrograde flow velocity used in **e** is shown (**d**). Fluorescent images were binarized and the local curvature was calculated from a spline fit to the cell outline. Measurement of channel-dependent cell curvature versus cortical actin retrograde flow shows no correlation (Pearson's correlation coefficient $c \approx -0.006425$) (**e**). The green line shows mean ± s.d.

7.1.5 Nuclear Positioning Facilitates Amoeboid Migration Along the Path of Least Resistance

Originally published in *Nature (2019)*. https://doi.org/10.1038/s41586-019-1087-5

LETTER

https://doi.org/10.1038/s41586-019-1087-5

Nuclear positioning facilitates amoeboid migration along the path of least resistance

Jörg Renkawitz[1,4]*, Aglaja Kopf[1], Julian Stopp[1], Ingrid de Vries[1], Meghan K. Driscoll[2,3], Jack Merrin[1], Robert Hauschild[1], Erik S. Welf[2,3], Gaudenz Danuser[2,3], Reto Fiolka[2,3] & Michael Sixt[1]*

During metazoan development, immune surveillance and cancer dissemination, cells migrate in complex three-dimensional microenvironments[1–3]. These spaces are crowded by cells and extracellular matrix, generating mazes with differently sized gaps that are typically smaller than the diameter of the migrating cell[4,5]. Most mesenchymal and epithelial cells and some—but not all—cancer cells actively generate their migratory path using pericellular tissue proteolysis[6]. By contrast, amoeboid cells such as leukocytes use non-destructive strategies of locomotion[7], raising the question how these extremely fast cells navigate through dense tissues. Here we reveal that leukocytes sample their immediate vicinity for large pore sizes, and are thereby able to choose the path of least resistance. This allows them to circumnavigate local obstacles while effectively following global directional cues such as chemotactic gradients. Pore-size discrimination is facilitated by frontward positioning of the nucleus, which enables the cells to use their bulkiest compartment as a mechanical gauge. Once the nucleus and the closely associated microtubule organizing centre pass the largest pore, cytoplasmic protrusions still lingering in smaller pores are retracted. These retractions are coordinated by dynamic microtubules; when microtubules are disrupted, migrating cells lose coherence and frequently fragment into migratory cytoplasmic pieces. As nuclear positioning in front of the microtubule organizing centre is a typical feature of amoeboid migration, our findings link the fundamental organization of cellular polarity to the strategy of locomotion.

During development and immune surveillance, trafficking cells typically follow chemotactic cues, which globally prescribe direction and destination of migration[8]. At the same time, cells have to negotiate the local physical environment[9] and traverse or circumnavigate obstacles within inhomogeneous tissues[4,5]. Rapidly migrating cells such as leukocytes rarely cause permanent tissue defects by proteolysis or rearrangement of the extracellular matrix[7,10], which suggests that they are able to adapt their migratory path to the physical constraints of their immediate environment.

As a model system for rapid amoeboid migration of leukocytes in 3D microenvironments, we imaged dendritic cells (DCs) that express LifeAct–GFP, embedded in fluorescent 3D collagen gels, by light-sheet microscopy with isotropic, subcellular 3D resolution[11]. Collagen fibres assembled into a 3D network with pore diameters that ranged between 1 μm and 5 μm (Extended Data Fig. 1a–c, Supplementary Video 1) into which DCs inserted multiple actin-rich protrusions (Fig. 1a, b, Extended Data Fig. 1d, Supplementary Video 1). To investigate how single cells respond to differential pore-size regimes, we spiked collagen gels with islands of higher network density and established gradients of the chemokine CCL19, which chemoattracts mature DCs (Fig. 1c–e). When chemotaxing DCs approached a dense island head-on (thus encountering a broad area of denser matrix), they steadily transited from the low-density matrix to the high-density matrix (Fig. 1c, Supplementary Video 2). Following this transition, they decelerated but continued to migrate towards the chemokine source (Fig. 1c, Extended Data Fig. 1e). By contrast, cells that approached a dense island on more tangential trajectories preferentially remained in regions of lower collagen density, thus deviating from the direct path as prescribed by the chemotactic gradient (Fig. 1c, Supplementary Video 2). These findings suggest that DCs follow the path of least resistance: whenever the option is available, they circumnavigate local areas of high matrix density, thereby trading the shortest path for migratory speed.

To test the mechanistic basis of local pathfinding, we established DC migration in microfluidic setups, which enable precise control over geometric parameters. We used a 'pillar forest', which represents a flattened approximation of a 3D collagen gel[12] (Extended Data Fig. 1f–l). To introduce inhomogeneity, we placed pillars at alternating 2-μm and 5-μm intervals, and found that DCs preferentially passed through the larger pores (79.89% ± 6.15%, mean ± s.d.) (Extended Data Fig. 2a–d and Supplementary Video 3). When we engineered islands of densely packed pillars into less-dense surroundings, DCs recapitulated the behaviour in heterogeneous collagen gels and bypassed dense areas (Extended Data Fig. 2e, Supplementary Video 2).

In a complex 3D scaffold, cells usually face multiple pores simultaneously (Fig. 1a). To investigate the capacity of cells to discriminate among several pore sizes, we engineered channels that guide the cells towards a decision point, at which they encounter four differently sized pores of between 2 and 5 μm in width. DCs showed a strong pore-size preference, migrating predominantly through larger pores and ignoring smaller pores (Fig. 1f, g, Extended Data Fig. 2f–i, Supplementary Video 3). Pore-size discrimination was comparable in the absence or presence of a chemokine gradient (Fig. 1g). When DCs faced a single pore, they passed through all pore sizes efficiently, albeit with longer passage times in smaller pore regimes (Extended Data Fig. 2j). To investigate whether pore-size selectivity is a general feature of amoeboid cells, we tested primary T cell blasts, a T cell line and neutrophil granulocytes and found behaviours equivalent to DCs (Fig. 1h and Extended Data Fig. 3a–g). On the basis of these data we conclude that amoeboid cells have the ability to distinguish between differently sized pores and—when given the option—they preferentially migrate along the path of least resistance.

When DCs extended actin-rich protrusions into differently sized pores (Fig. 1f, Extended Data Fig. 4a, b, Supplementary Video 3), protrusion–retraction dynamics did not correlate with ultimate pore choice (Extended Data Fig. 4c). This argued against a selector function of the cell's leading edge, which usually serves as the steering organelle. As the nucleus is often the bottleneck when cells migrate in 3D environments[9,13–17], we tested whether the nucleus is involved in active directional choices[18]. Imaging nuclear positioning revealed that pore choice temporally coincided with nuclear passage (Fig. 2a), and that, before passage, the nucleus massively deformed and protruded into multiple pores (Fig. 2b, Extended Data Figs. 4d–j, 5a–f, Supplementary Video 4). For the polymorph nucleus of neutrophil granulocytes[19], we even observed parallel penetration of nuclear lobes into different pores

[1]Institute of Science and Technology Austria (IST Austria), Klosterneuburg, Austria. [2]Department of Cell Biology, University of Texas Southwestern Medical Center, Dallas, TX, USA. [3]Department of Bioinformatics, University of Texas Southwestern Medical Center, Dallas, TX, USA. [4]Present address: Walter Brendel Center of Experimental Medicine, Institute of Cardiovascular Physiology and Pathophysiology, Biomedical Center (BMC), Klinikum der Universität, LMU Munich, Munich, Germany. *e-mail: joerg.renkawitz@med.uni-muenchen.de; michael.sixt@ist.ac.at

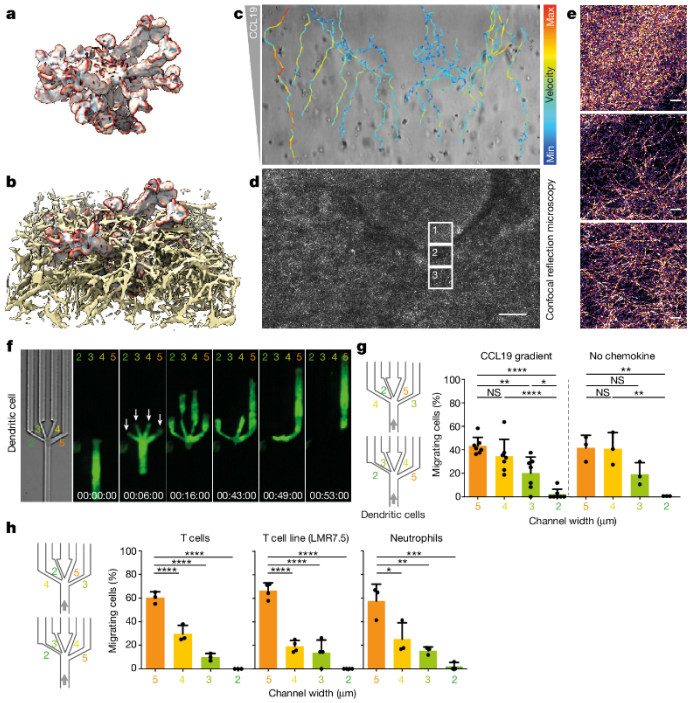


Fig. 1 | Migrating cells are selective for pore size. a, A DC (LifeAct–GFP-labelled) embedded in a 3D collagen matrix (Alexa Fluor 568-labelled) and imaged by light-sheet microscopy with isotropic, subcellular 3D resolution. Colouring on the DC surface indicates regions of large positive and negative curvature in red and blue, respectively. Image representative of 24 cells from 5 experiments. **b**, Subvolume of the collagen matrix surrounding the DC depicted in **a**. Image representative of 24 cells from 5 experiments. **c**, Migratory tracks (velocity colour coding) of DCs along a CCL19 chemokine gradient in a collagen matrix spiked with a region of higher collagen density (three experiments). **d**, Confocal reflection microscopy of the same collagen matrix shown in **b** (three experiments). Scale bar, 100 μm. **e**, Enlargement of regions in boxes 1, 2 and 3 in **c**, exemplifying regions of higher (top) and lower (middle and bottom) collagen densities. Scale bar, 10 μm. **f**, Protrusion dynamics of the leading edge of a DC, labelled with LifeAct–GFP, during migration in microchannels through a junction (decision point) with four differently sized pores (2-, 3-, 4- and 5-μm wide (4-μm height)). Arrows highlight early establishment of cell-front protrusions into all different pore sizes (three experiments). **g**, Quantification of pore-size preference of DCs treated as in **f**, with (left; 7 experiments, 119 cells; one-way ANOVA with Tukey's test; $^{****}P < 0.0001$, $^{**}P = 0.0029$, $^{*}P = 0.0225$) or without (right; 3 experiments, 81 cells; one-way ANOVA with Tukey's test; $^{**}P = 0.0049$) a CCL19 chemokine gradient. Pooled data from two devices with differently ordered sequences of pore size (2, 3, 4 and 5 μm or 4, 2, 5 and 3 μm, respectively). **h**, Migration of T cells, LMR7.5 hybridoma T cells and neutrophils in microchannels through a decision point of four differently sized pores of 2-, 3- ,4- and 5-μm wide (T cells, LMR7.5, 4-μm height; neutrophils, 2-μm height), and quantification of pore-size preference along a chemokine gradient (T cells (CCL19): 3 experiments, 68 cells; LMR7.5: 3 experiments, 40 cells; neutrophils (fMLP): 3 experiments, 46 cells; one-way ANOVA with Tukey's test; $^{****}P < 0.0001$, $^{***}P = 0.0007$, $^{**}P = 0.0043$, $^{*}P = 0.0193$). Pooled data from two devices with differently ordered sequences of pore size (2, 3, 4 and 5 μm or 4, 2, 5 and 3 μm, respectively). Data in **g** and **h** are mean ± s.d. Time is indicated as h:min.s.

(Fig. 2c–e, Supplementary Video 8). These observations suggest that cells may use their nucleus as a mechanical gauge to choose their path. To functionally test this hypothesis, we spatially decoupled the decision point (the channel split) from the site at which the leading edge senses pore size (channel constriction) (Fig. 2f). We placed differently sized constrictions 10 μm upstream of the decision point at which the channel splits into four equal branches. In these conditions, DCs lost their pore-size preference, even though the leading edges fully penetrated all constrictions (Fig. 2f, g). Together with observations that (i) DCs cannot distinguish pores larger than the nuclear diameter (Fig. 2h), (ii) overexpression of a stiffer mutant form of lamin A[20,21] resulted in an increased propensity to pass through bigger pores (Extended Data Fig. 6a–c), (iii) enucleated cells are not pore-size selective (Fig. 2i, j) and (iv) nuclear positioning is actively driven by cytoskeletal forces (Extended Data Figs. 6d–h, 8e–g, Supplementary Video 5), these results suggest that the nucleus is the decisive mechanical gauge mediating navigation along the path of least resistance, and that protrusive structures such as lamellipodia[22] act in a subordinate manner.

It has long been recognized that the organization of cellular polarity differs between amoeboid cells and mesenchymal cells: whereas mesenchymal cells often migrate with the microtubule-organizing centre (MTOC) and Golgi apparatus 'in front' of the nucleus[23] ('MTOC-first'), amoeboid cells preferentially migrate with the inverted configuration ('nucleus first') and only reorient once they stably dock onto other cells, as exemplified by immunological synapses[23–26]. The ultimate physiological foundations of this peculiar polarization remain unknown. Visualization of microtubules in DCs directionally migrating in channels, pillar forests, collagen gels and in the physiological environment of a mouse ear revealed a dynamically deforming 'frontward'-positioned nucleus (Fig. 3a, Extended Data Figs. 7a–k, 8a–c, Supplementary Videos 6, 7), directly trailed by the closely associated MTOC, which frequently caused nuclear indentations (Extended Data Fig. 8i, j) as if

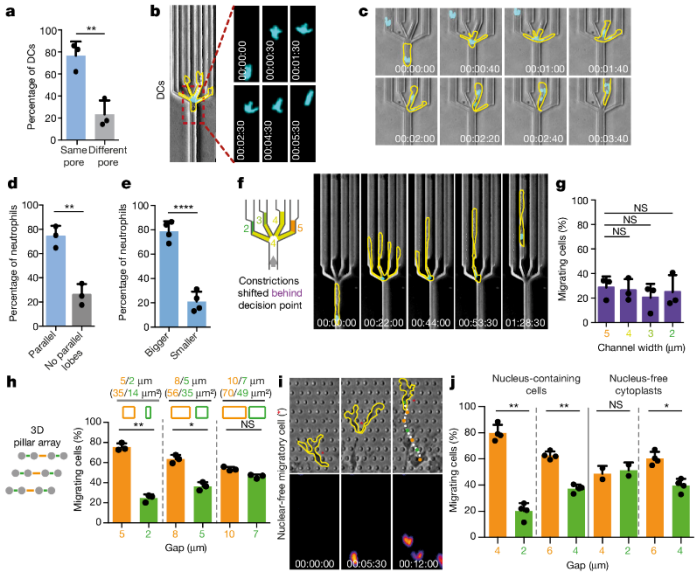


Fig. 2 | The nucleus functions as a mechanical guide along the path of least resistance. a, Correlation of initial nuclear translocation and final pore decision (3 experiments, 61 cells; unpaired *t*-test, $^{**}P = 0.0068$). **b**, Nuclear protrusion dynamics (Hoechst stain) during DC pore-size decision (cell outline in yellow, time indicated; representative of five experiments). **c**, Nuclear lobe dynamics (Hoechst stain) during neutrophil pore-size decision (cell outlines in yellow, time indicated; representative of three experiments). **d**, Quantification of parallel nuclear lobes into different pores during neutrophil pore-size decision (3 experiments, 46 cells; unpaired *t*-test, $^{**}P = 0.0027$). **e**, Pore-size selection by parallel nuclear lobes (4 experiments, 71 cells; unpaired *t*-test, $^{****}P < 0.0001$). **f**, Spatial decoupling of the decision point (the channel split) from the site where the leading edge senses pore size (channel constriction) by locating the differently sized constrictions 10 μm upstream of the decision point (cell outlines in yellow, nucleus (Hoechst stain) in cyan, time indicated; representative of three experiments). **g**, Quantification of cell 'decisions' from **f**; pooled data from two devices with differently ordered sequences of pore size (2, 3, 4 and 5 μm or 4, 2, 5 and 3 μm, respectively; 3 experiments, 120 cells; one-way ANOVA with Tukey's test). **h**, Pore-size preference of DCs in pillar arrays with pores of increasing size (3 experiments, 62 cells, 1,148 pore passages; paired *t*-test; $^{**}P = 0.0073$, $^{*}P = 0.0289$). **i**, Nucleus-free cell fragment (cytoplast; outlines in yellow) migrating in a pillar array of large (orange) and small (green) pores (representative of three experiments). **j**, Quantification of pore passages in **i** (3 experiments, 19 nucleus-free cytoplasts, 224 pore passages; paired *t*-test; $^{**}P = 0.0023$ (4 μm versus 2 μm, intact cells), $^{**}P = 0.0034$ (6 μm versus 4 μm, intact cells), $^{*}P = 0.0267$ (6 μm versus 4 μm, nucleus-free cytoplast)). Data are mean ± s.d. Time is indicated as h:min:s.

pushing the nucleus forward. To test whether the nucleus-first configuration relates to pore-size selection, we took advantage of cell-to-cell variation in our system: 72.23% ± 2.8% (mean ± s.d.) of DCs in microchannels migrated with the nucleus first, whereas 21.27% ± 2.9% migrated in the MTOC-first configuration (Fig. 3b, Extended Data Fig. 8c). Migration speed in non-constricted channels and through single pores was independent of polar configuration (Extended Data Fig. 8d, k, l). Whereas the leading edges of DCs that migrated nucleus-first were indistinguishable from those of cells that migrated MTOC-first, they exhibited more nuclear deformations, a stronger propensity to pass through larger pores and—consequently—a faster passage beyond the decision point (Fig. 3c–f, Extended Data Fig. 9a–c, Supplementary Video 8). Similarly, fibroblasts only showed a preference for larger pores when migrating in the nucleus-first configuration (Fig. 3g, Extended Data Fig. 9d–g, Supplementary Video 8). In neutrophils, the MTOC located itself predominantly in between nuclear lobes when cells moved through straight channels. However, during passage through decision points, the nucleus unfolded and at least one lobe passed the (preferentially largest) pore before the MTOC and the other nuclear lobes ultimately followed (Extended Data Fig. 10a–c, Supplementary Video 8). Thus, we conclude that the nucleus-first configuration—which is typical for amoeboid cells—facilitates migration along the path of least resistance, whereas cells migrating MTOC-first do not show this capacity.

The close proximity between MTOC and nucleus, the finding that in polymorphonuclear cells the MTOC specifies the nuclear lobe that leads the directional choice (Extended Data Fig. 10d), and evidence that the MTOC determines polarization in other cellular systems[27] raised the possibility that the nucleus acts as the mechanical gauge and the MTOC acts as the spatially associated directional selector. We therefore imaged the MTOC in DCs and found that once it followed the nucleus through a pore, all remaining protrusions were retracted (Fig. 4a). To functionally uncouple nucleus-based pore-selection from MTOC-based directional selection, we engineered microfluidic channels that split into two symmetric channels ('Y' junctions). This revealed that the MTOC is the superior predictor for side selection (Fig. 4b, Supplementary Video 10), which means that in the rare cases in which the MTOC and nucleus dissociate, the MTOC is a better indicator of the ultimate directional choice of the cell. It is well established that microtubule depolymerization triggers actomyosin contraction via activation of RhoA and myosinII[28], which provides a potential link between MTOC passage and trailing-edge retraction, such as via the RHOA guanine nucleotide exchange factor LFC–GEF-H1[29]. Imaging microtubule plus-end dynamics upon MTOC passage revealed that microtubules vanish from the trailing protrusion before or on retraction (Fig. 4c, Supplementary Video 9). On myosin II inhibition with blebbistatin and a ROCK inhibitor, cells showed slowed passage owing to a failure to retract supernumerary protrusions (Extended Data Fig. 10e–n); likewise, microtubule disruption by low-dose nocodazole treatment led to markedly increased passage times. Nocodazole-treated cells frequently failed to make any productive decision (Fig. 4d, e, Supplementary Video 10) and, instead, protrusions often advanced

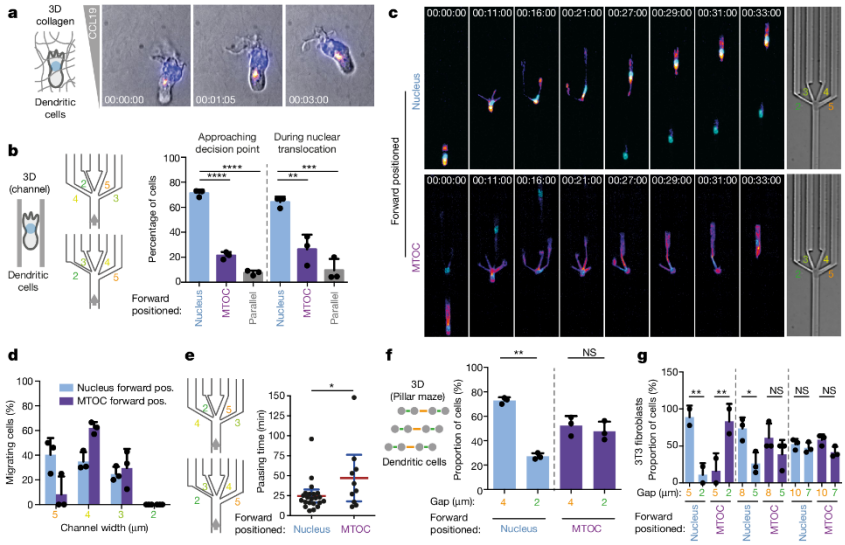


Fig. 3 | Nucleus-first cell polarity facilitates migration along the path of least resistance. a, Position of MTOC (indicated by EMTB–mCherry, with fire colour-coded intensity: black (minimum), magenta, orange, yellow to white (maximum)) and nucleus (Hoechst stain; cyan) in a DC migrating in a collagen matrix along a CCL19 gradient (time indicated; representative of three experiments). **b**, Quantification of relative position of nucleus and MTOC in DCs before and during pore-size decisions (3 experiments, 76 cells; one-way ANOVA with Tukey's test; $^{****}P < 0.0001$, $^{***}P = 0.0007$, $^{**}P = 0.0049$). **c**, Examples of DCs migrating through the decision point with the nucleus (top) or the MTOC (bottom) first (time indicated; representative of three experiments). **d**, Pore-size preference of DCs approaching a pore-size decision with nucleus or MTOC first (3 experiments, 76 cells). **e**, Time taken for cell to pass through a pore (passing time), based on whether the cell passes through in nucleus-first or MTOC-first configuration (3 experiments, 32 cells; unpaired *t*-test; $^{*}P = 0.0389$). **f**, Pore-size preference of DCs (nucleus-first versus MTOC-first configuration) migrating through pillar arrays with different pore sizes (3 experiments, 31 cells, 252 pore passages; paired *t*-test; $^{**}P = 0.0042$). **g**, Pore-size preference of fibroblasts (nucleus-first versus MTOC-first configuration) migrating through pillar arrays with different pore sizes (125 cells, 146 pore passages; one-way ANOVA with Tukey's test; $^{***}P = 0.0017$, $^{**}P = 0.0088$, $^{*}P = 0.0307$). Data in **b**, **d**, **f** and **g** are mean ± s.d.; data in **e** are mean ± 95% confidence interval (CI).

beyond the decision point, ultimately breaking the cell into fragments (Fig. 4d, f, Supplementary Video 10). Notably, nocodazole-treated DCs successfully passed through single constrictions (Extended Data Fig. 9o), which demonstrates that microtubules mediate decision-making rather than physical passage. Likewise, DCs in 3D collagen gels showed massive fragmentation when exposed to chemotactic stimuli

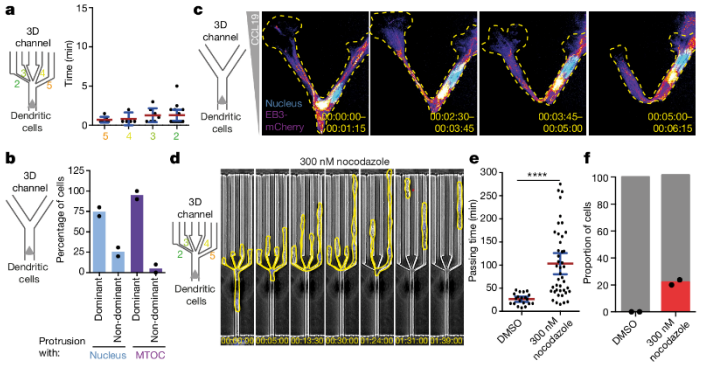


Fig. 4 | The microtubule cytoskeleton coordinates nuclear probing with cellular locomotion. a, Retraction of cellular protrusions (from non-chosen pores) on passage of the MTOC into the chosen pore (3 experiments, 34 cells). **b**, Path choice of DCs in Y-junction channels on translocation of the nucleus or the MTOC into one of the Y branches (2 experiments, 46 cells). **c**, Microtubule plus ends, labelled with EB3–mCherry (fire colour-coded intensity), and nucleus (Hoechst stain, cyan) in a DC migrating through a Y-junction channel (time indicated; representative of three experiments). Images depict maximal intensity projections of 15 frames (5-s intervals). **d**, DCs (outlined in yellow) migrating through a decision point with pores 2, 3, 4 and 5 μm wide in the presence of 300 nM nocodazole (representative of two experiments). The red star highlights loss of cellular integrity. **e**, Quantification of the passing time in the experiments represented in **d** (2 experiments, 63 cells; Mann–Whitney test; $^{****}P < 0.0001$). **f**, Quantification of the cellular integrity in the experiments represented in **d** (2 experiments, 61 cells). Data in **b** and **f** are mean; data in **a** and **e** are mean ± 95% CI.

(Extended Data Fig. 9p, Supplementary Video 10). These data demonstrate that MTOC-nucleated microtubules serve to signal successful nuclear passage to the trailing edge of the cell, decisively coordinating pathfinding and cellular coherence upon passage through pores.

Overall, we show that the nucleus-first configuration—a distinctive feature of amoeboid cells—facilitates rapid navigation along the path of least resistance. These cells use the nucleus as a mechanical gauge, providing the basis for fast and non-destructive tissue locomotion such as during immune surveillance. By contrast, the mesenchymal cell-body-first configuration does not allow such subtle navigation, but is likely to support the slow path-generating strategy of pericellular proteolysis[30]. Beyond its relevance in development, immunity and regeneration, this functional link between polar organization and the generic mode of locomotion might also serve to classify migration of metastatic cancer cells.

Online content

Any methods, additional references, Nature Research reporting summaries, source data, statements of data availability and associated accession codes are available at https://doi.org/10.1038/s41586-019-1087-5.

Received: 14 July 2017; Accepted: 1 March 2019;
Published online 3 April 2019.

1. Petrie, R. J. & Yamada, K. M. Multiple mechanisms of 3D migration: the origins of plasticity. *Curr. Opin. Cell Biol.* **42**, 7–12 (2016).
2. Friedl, P. & Weigelin, B. Interstitial leukocyte migration and immune function. *Nat. Immunol.* **9**, 960–969 (2008).
3. te Boekhorst, V., Preziosi, L. & Friedl, P. Plasticity of cell migration in vivo and in silico. *Annu. Rev. Cell Dev. Biol.* **32**, 491–526 (2016).
4. Weigelin, B., Bakker, G.-J. & Friedl, P. Intravital third harmonic generation microscopy of collective melanoma cell invasion: principles of interface guidance and microvesicle dynamics. *Intravital* **1**, 32–43 (2012).
5. Stoitzner, P., Pfaller, K., Stössel, H. & Romani, N. A close-up view of migrating Langerhans cells in the skin. *J. Invest. Dermatol.* **118**, 117–125 (2002).
6. Wolf, K. & Friedl, P. Extracellular matrix determinants of proteolytic and non-proteolytic cell migration. *Trends Cell Biol.* **21**, 736–744 (2011).
7. Wolf, K., Müller, R., Borgmann, S., Bröcker, E.-B. & Friedl, P. Amoeboid shape change and contact guidance: T-lymphocyte crawling through fibrillar collagen is independent of matrix remodeling by MMPs and other proteases. *Blood* **102**, 3262–3269 (2003).
8. Sarris, M. & Sixt, M. Navigating in tissue mazes: chemoattractant interpretation in complex environments. *Curr. Opin. Cell Biol.* **36**, 93–102 (2015).
9. Giordano, G. F. & Lichtman, M. A. Marrow cell egress. The central interaction of barrier pore size and cell maturation. *J. Clin. Invest.* **52**, 1154–1164 (1973).
10. Pflicke, H. & Sixt, M. Preformed portals facilitate dendritic cell entry into afferent lymphatic vessels. *J. Exp. Med.* **206**, 2925–2935 (2009).
11. Dean, K. M., Roudot, P., Welf, E. S., Danuser, G. & Fiolka, R. Deconvolution-free subcellular imaging with axially swept light sheet microscopy. *Biophys. J.* **108**, 2807–2815 (2015).
12. Renkawitz, J., Reversat, A., Leithner, A., Merrin, J. & Sixt, M. Micro-engineered "pillar forests" to study cell migration in complex but controlled 3D environments. *Methods Cell Biol.* **147**, 79–91 (2018).
13. Thiam, H.-R. et al. Perinuclear Arp2/3-driven actin polymerization enables nuclear deformation to facilitate cell migration through complex environments. *Nat. Commun.* **7**, 10997 (2016).
14. Raab, M. et al. ESCRT III repairs nuclear envelope ruptures during cell migration to limit DNA damage and cell death. *Science* **352**, 359–362 (2016).
15. Denais, C. M. et al. Nuclear envelope rupture and repair during cancer cell migration. *Science* **352**, 353–358 (2016).
16. Harada, T. et al. Nuclear lamin stiffness is a barrier to 3D migration, but softness can limit survival. *J. Cell Biol.* **204**, 669–682 (2014).
17. Irianto, J. et al. DNA damage follows repair factor depletion and portends genome variation in cancer cells after pore migration. *Curr. Biol.* **27**, 210–223 (2017).
18. Le Berre, M. et al. Geometric friction directs cell migration. *Phys. Rev. Lett.* **111**, 198101 (2013).
19. Rowat, A. C. et al. Nuclear envelope composition determines the ability of neutrophil-type cells to passage through micron-scale constrictions. *J. Biol. Chem.* **288**, 8610–8618 (2013).
20. Dahl, K. N. et al. Distinct structural and mechanical properties of the nuclear lamina in Hutchinson–Gilford progeria syndrome. *Proc. Natl Acad. Sci. USA* **103**, 10271–10276 (2006).
21. Verstraeten, V. L. R. M., Ji, J. Y., Cummings, K. S., Lee, R. T. & Lammerding, J. Increased mechanosensitivity and nuclear stiffness in Hutchinson–Gilford progeria cells: effects of farnesyltransferase inhibitors. *Aging Cell* **7**, 383–393 (2008).
22. Leithner, A. et al. Diversified actin protrusions promote environmental exploration but are dispensable for locomotion of leukocytes. *Nat. Cell Biol.* **18**, 1253–1259 (2016).
23. Luxton, G. W. & Gundersen, G. G. Orientation and function of the nuclear–centrosomal axis during cell migration. *Curr. Opin. Cell Biol.* **23**, 579–588 (2011).
24. Krummel, M. F. & Macara, I. Maintenance and modulation of T cell polarity. *Nat. Immunol.* **7**, 1143–1149 (2006).
25. Eddy, R. J., Pierini, L. M. & Maxfield, F. R. Microtubule asymmetry during neutrophil polarization and migration. *Mol. Biol. Cell* **13**, 4470–4483 (2002).
26. Yoo, S. K. et al. The role of microtubules in neutrophil polarity and migration in live zebrafish. *J. Cell Sci.* **125**, 5702–5710 (2012).
27. Bornens, M. Organelle positioning and cell polarity. *Nat. Rev. Mol. Cell Biol.* **9**, 874–886 (2008).
28. Liu, B. P., Chrzanowska-Wodnicka, M. & Burridge, K. Microtubule depolymerization induces stress fibers, focal adhesions, and DNA synthesis via the GTP-binding protein Rho. *Cell Adhes. Commun.* **5**, 249–255 (1998).
29. Kwan, K. M. & Kirschner, M. W. A microtubule-binding Rho-GEF controls cell morphology during convergent extension of *Xenopus laevis*. *Development* **132**, 4599–4610 (2005).
30. Infante, E. et al. LINC complex-Lis1 interplay controls MT1-MMP matrix digest-on-demand response for confined tumor cell migration. *Nat. Commun.* **9**, 2443 (2018).

Acknowledgements We thank F. Gärtner, E. Kiermaier and A. Casano for discussions and critical reading of the manuscript, A. Leithner for primary T cells, A. Reversat for LMR7.5 cell cultures, J. Schwarz and M. Mehling for sharing microfluidics knowledge, K. M. Dean for assistance with light-sheet imaging, T. Goddard from UCSF ChimeraX (P41-GM103311) for assistance with 3D rendering, and the Scientific Service Units of IST Austria for support. This work was supported by the European Research Council (ERC StG 281556 and CoG 724373), a grant from the Austrian Science Foundation (FWF) and the FWF DK 'Nanocell' to M.S., National Institutes of Health awards (F32GM116370, K25CA204526) to M.K.D. and E.S.W., the Cancer Prevention Research Institute of Texas recruitment award (R1225) to G.D., the Cancer Prevention Research Institute of Texas recruitment award (RR160057) to R.F., ISTFELLOW funding from the People Programme (Marie Curie Actions) of the European Union's Seventh Framework Programme (FP7/2007-2013) under REA grant agreement no. 291734 to J.R., and an EMBO long-term fellowship (ALTF 1396-2014) co-funded by the European Commission (LTFCOFUND2013, GA-2013-609409) to J.R.

Reviewer information *Nature* thanks Dennis Discher, Pakom Kanchanawong, Kenneth Yamada and the other anonymous reviewer(s) for their contribution to the peer review of this work.

Author contributions J.R. and M.S. conceived the experiments and wrote the manuscript. J.R. designed, performed and analysed all experiments with the help of A.K., J.S. and I.d.V: A.K. established EMTB–mCherry and EB3–mCherry Hoxb8-derived DCs, and performed high-magnification imaging of microtubule plus ends (EB3); J.S. established isolation, purification and microtubule-labelling (SiR–tubulin) of polymorphonuclear leukocytes; I.d.V. supported leukocyte cell cultures and established GFP–progerin HoxB8-derived DCs. M.K.D., E.S.W., G.D. and R.F. performed and analysed light-sheet microscopy. J.M. generated microfabricated channels and pillar arrays. R.H. wrote image-analysis scripts for collagen pore-size quantification, for quantification of cellular displacement in collagen gels, and for the analysis of nuclear and MTOC positioning.

Competing interests The authors declare no competing interests.

Additional information
Extended data is available for this paper at https://doi.org/10.1038/s41586-019-1087-5.
Supplementary information is available for this paper at https://doi.org/10.1038/s41586-019-1087-5.
Reprints and permissions information is available at http://www.nature.com/reprints.
Correspondence and requests for materials should be addressed to J.R. or M.S.
Publisher's note: Springer Nature remains neutral with regard to jurisdictional claims in published maps and institutional affiliations.

© The Author(s), under exclusive licence to Springer Nature Limited 2019

METHODS

Data reporting. No statistical methods were used to predetermine sample size. The experiments were not randomized. The investigators were not blinded to allocation during experiments and outcome assessment.

Mice. All mice used in this study were of C57BL/6J background and bred and maintained in accordance with the Austrian law for animal experimentation (*Österreichisches Tierschutzgesetz*) and euthanized at 6-to-12 weeks of age (male and female) for use in experiments. Permission was granted and all experimental protocols were approved by the Austrian federal ministry of science, research and economy (identification code: BMWF-66.018/0005-II/3b/2012). All experiments were performed in accordance with relevant guidelines and regulations.

Cell culture. All cells were grown and maintained at 37 °C in a humidified incubator with 5% CO_2 and routinely tested for mycoplasma contamination.

DCs. DCs were differentiated from bone marrow extracted from femur and tibia of six-to-eight-week-old male C57BL/6J wild-type (or LifeAct–GFP positive[31]) mice, or from immortalized haematopoietic precursors (as described in refs. [32,33]). In brief, haematopoietic precursors were differentiated in R10 culture medium (RPMI 1640 supplemented with 10% fetal calf serum (FCS), 2 mM L-glutamine, 100 U/ml penicillin, 100 mg/ml streptomycin and 0.1 mM 2-mercaptoethanol; all Gibco) supplied with 10% granulocyte–macrophage colony-stimulating factor (GM-CSF) hybridoma supernatant, with addition of fresh medium on differentiation days 3 and 6 (ref. [34]). For maturation and subsequent migration assays, either fresh (day 8) or thawed DCs were stimulated overnight with 200 ng/ml lipopolysaccharide (LPS; *Escherichia coli* 0127:B8 Sigma). For phagocytic uptake of polystyrene-based latex beads (Fluoresbrite yellow-green microspheres 6 μm, Polyscience), immature day-seven DCs were incubated for 2 h with one drop of the beads per DC culture plate, followed by LPS stimulation (as above) in the presence of the beads.

T cells. T cells were isolated from the spleen of male or female 6-to-12-week-old C57BL/6J mice, using the EasySep mouse naive T cell isolation Kit (Stemcell). Cells were seeded onto cell culture plates coated with 1 μg/ml CD3 antibody and 1 μg/ml CD28 antibody, and either used for experiments between differentiation days 3 and 6, or frozen at day 6 and thawed for experiments.

LMR7.5 hybridoma T cells. Cells were a gift from A. M. Lennon (U932, Institut Curie), used courtesy of N. Glaichenhaus (IPMC UMR7525, UNS) and cultured in R10 culture medium (RPMI 1640 supplemented with 10% FCS, 2 mM L-glutamine, 100 U/ml penicillin, 100 mg/ml streptomycin and 50 mM 2-mercaptoethanol; all Invitrogen).

Polymorphonuclear leukocytes. Human peripheral blood polymorphonuclear leukocytes (PMNs) were isolated from healthy donors (in accordance with relevant national guidelines and regulations, and informed consent of healthy volunteers: GS1-EK-4/543-2018) using EasySep Direct Human Pan-Granulocyte Isolation Kit (Stemcell). Purity and non-activated status of PMNs were validated using flow cytometry (FSC, SSC, CD11b, CD14, CD45, CD62L, CD66b, CD235a; Miltenyi). For short-term storage or staining, PMNs were kept in Hank's balanced salt solution without phenol red (Gibco), supplemented with 0.6% human serum albumin (Sigma) and 1% glutamine (Gibco), with gently agitation in a ventilated tube in a humidified incubator. For experiments, PMNs were resuspended in RPMI without phenol red, supplemented with 0.6% human serum albumin, 20 mM HEPES (Gibco) and 1% glutamine.

Fibroblasts. 3T3 Swiss fibroblasts were cultured in DMEM GlutaMax (Thermofisher) supplemented with 10% FCS, 100 U/ml penicillin and 100 mg/ml streptomycin, and collected with trypsin–EDTA for experiments.

Fluorescent reporter constructs. The fluorescent plasmid DNA reporter construct coding for EB3–GFP was a gift from V. Small (IMBA). LV-GFP plasmid encoding H2B–GFP was a gift from E. Fuchs (Addgene plasmid no. 25999)[35]. GFP-wt-laminA and GFP-progerin were gifts from T. Misteli (Addgene plasmid no. 17662 and 17663)[36]. The EMTB–3×mCherry constructs were a gift from W. M. Bement (University of Wisconsin)[37]. Gateway cloning technology was used to generate lentivirus from plasmid DNA constructs. In brief, corresponding DNA segments were amplified using primers containing overhangs with attB1 and attB2 recombination sites on the 3′- and the 5′-end respectively. To obtain an EMTB fusion construct carrying a single mCherry tag, the PCR product was separated by gel electrophoresis, and only the fragment of corresponding size (EMTB: 816 bp, mCherry: 705 bp) was further processed. Gel-purified PCR fragments were inserted into pcDNA221 entry vectors (Invitrogen) by BP recombination reaction generating the entry clone, and expression clones were obtained by the LR recombination reaction between entry clone and pLenti6.3 destination vector (Invitrogen).

Transgene delivery for reporter cell line generation. Fusion-protein-coding lentiviruses were produced in LX-293 HEK cells (Clontech) by co-transfection of the expression plasmids (pLenti6.3, Invitrogen) with pCMV-dR8.91 packaging- and pCMV-VSV-G envelope plasmids (a gift from B. Weinberg; Addgene plasmid no. 8454 (ref. [38])). The supernatant of virus-producing cells was collected 72 h after transfection for immediate use or stored at −80 °C after snap-freezing. For generation of stably expressing reporter cells, immortalized progenitor cells (for later differentiation into DCs) and LMR7.5 T cell hybridoma cells were spin-infected (1,500*g*, 1 h) in the presence of lentivirus coding for fluorescent reporter construct of interest and 8 μg/ml Polybrene (Sigma-Aldrich). Spin infection was carried out in a 12-well plate with 3×10^5 cells/ml per reaction plus 500 μl of undiluted virus. The 3T3 fibroblasts were infected without spin infection. Following transduction, cells were expanded for two days and subsequently selected for stable virus insertion using 10 μg/ml blasticidin (Gibco) for one week. Cells expressing fluorescent reporter constructs were sorted using fluorescence-activated cell sorting (FACS Aria III, BD Biosciences) before further experiments.

Flow cytometry analysis. Primary DCs and neutrophils were routinely checked for correct surface expression markers using antibodies against MHCII and CD11c (DCs; both eBiosciences) and CD11b, CD14, CD45, CD62L, CD66b, CD235a (Neutrophils; all Miltenyi). Stainings were done in FACS buffer (1 × PBS, 2 mM EDTA, 1% BSA) with Fc receptor blockage (anti-mouse CD16/CD32) for antibodies bearing an Fc part.

Micro-fabricated devices. Micro-fabricated devices were generated as recently described[12,39]. In brief, microfluidic photomask designs were drawn with Coreldraw X8 (Corel), converted to Gerber format with Linkcad, and printed on chrome photomask at a resolution of 1 μm (JD Photo Data & Photo Tools). For high-resolution structures, wafers were first coated with a sub-micrometre layer of SU8 as a sticky substrate for later SU8 structures. We used GM-1040 SU8 photoresist (Gersteltec) at 5,000 r.p.m. for 2 min with flood UV exposure. The feature layer was then applied with SU8-2005 (Microchem). According to the datasheet, a UV-absorbing glass plate and higher exposure were used to make sharp features. PL-360-LP from Omega Optical and 550 mJ/cm^2 with an EVG mercury lamp based mask aligner gave good results in the 3–7-μm-thickness range. The thick loading channels were made with Microchem SU8-3025 using the EVG mask aligner according to the Microchem data sheet without the PL-360-LP plate. The master wafers underwent vapour silanization for 1 h with (1H, 1H, 2H, 2H-perfluorooctyl) trichlorosilane. The final results were single hydrophobic master wafers containing several aligned layers. Polydimethylsiloxane (PDMS) devices were made with Sylgard 184 Elastomer Kit (Dow Corning) using a ratio of 10:1. The PDMS was mixed in a Thinky mixing machine and then poured on the wafer in an aluminium tray and further degassed several times in a vacuum chamber. The devices were baked at 80 °C overnight. The hardened devices were carefully peeled off the mould and cut into single devices using a razor blade. Holes were punched with a custom arbor press, and sticky tape was used to remove debris. Glass coverslips were sonicated for 5 min in 70% ethanol and blown dry. Devices were bonded to the glass slides by oxygen plasma then sealed together at 85 °C for 1 h to make the bond permanent.

Cell migration assays. For visualization of the nucleus in live cells, cells were pre-incubated for at least 30 min with NucBlue (Invitrogen), followed by washing. For live-cell MTOC or microtubule visualization in human granulocyte neutrophils, cells were incubated with 1 μM SiR–tubulin (Cytoskeleton). For cytoskeletal inhibition experiments, 300 nM nocodazole (Sigma), 1μM Y27632 (Sigma) or 50 μM *para*-nitroblebbistatin[40] (Optopharma) were used.

3D collagen migration assays. Matrix densities ranging from 1.7 mg/ml to 5.6 mg/ml were obtained by using different bovine collagen stock solutions (PureCol, Nutragen, Fibricol; all AdvancedBioMatrix) and dilutions, mixed in 1× minimum essential medium eagle (MEM, Sigma) and 0.4% sodium bicarbonate (Sigma) with 3×10^5 cells in R10 at a 2:1 ratio (as previously described[41]). Collagen–cell mixtures were casted in custom-made migration chambers. After 45 min polymerization of collagen fibres at 37 °C and 5% CO_2, gels were overlaid with 100 μl CCL19 (R&D Systems, 0.6 μg/ml). DC migration was recorded with time-lapse video microscopy and analysed by a custom-made tracking tool. Inhomogeneous collagen gels with spiked regions of higher collagen density were obtained by polymerizing a higher concentrated collagen mixture first (5.6 mg/ml), followed by cutting with a razor blade into very small pieces, and subsequent addition of the more-concentrated collagen gel pieces into a polymerizing mixture of lower-concentration collagen.

Immunofluorescence in 3D collagen migration assays. Three-dimensional collagen gels were cast as described above. Two hours after introduction of the CCL19 gradient, the gel was isolated from the chamber and immediately bathed in 4% paraformaldehyde for 10 min at room temperature. After three washes with PBS, the primary antibody (diluted in PBS, 0.2% BSA and 0.05% saponin) was incubated overnight at 4 °C. Then, after PBS washes, the secondary antibody (diluted in PBS, 0.2% BSA and 0.05% saponin) was incubated for 2 h at room temperature, washed three more times with PBS, and subsequently mounted using Fluoromount (Sigma) with DAPI (1:5,000).

Light-sheet imaging of DCs in collagen gel. Agarose sample chambers were made as described[11] and soaked in R10 medium before imaging. A collagen solution was prepared by mixing concentrated PBS and water with bovine collagen I (Advanced Biomatrix) at concentrations of 2.0 mg/ml or 5.6 mg/ml. Eight per cent of collagen was labelled by direct conjugation to Alexa Fluor 568. The collagen was neutralized with 1 M NaOH and mixed with DCs before incubation at 37 °C. Imaging was performed with or without CCL19 (R&D Systems, 10 μg/ml).

Cell migration in micro-fabricated devices. An overview of the devices used is shown in Extended Data Fig. 2a, b. For the hole-based assay shown in Extended Data Fig. 2b, a 2-mm biopsy puncher was used to punch holes. To ensure comparable confinement, the heights of the channels and pillar arrays were adjusted to the individual cell/nucleus sizes of the cell types used: 4 μm or 5 μm for DCs, T cells and LMR7.5 hybridoma T cells (4 μm: Figs. 1f–h, 2a, b, f, g, i, j, 3b–f, 4a–f, Extended Data Figs. 1h–l, 2c, d, f–j, 3a–e, 4a–j, 6a, b, d, 8b–l, 9a–c, 10e–o; 5 μm: Fig. 2h, Extended Data Fig. 2a, b, e), 2 μm for neutrophils (Figs. 1h, 2c–e, Extended Data Figs. 3f, g, 10a–d), 7 μm for fibroblasts (Fig. 3g; Extended Data Figs. 6c, 9d–g). Before the introduction of cells, the devices were flushed with the corresponding medium and incubated for at least 1 h at 37 °C, 5% CO_2. To visualize the CCL19 chemokine gradient, we mixed 2.5 μg/ml CCL19 with FITC–dextran (200 μg/ml in R10; hydrodynamic radius: 2.3 nm; Sigma Aldrich) as a proxy, as the diffusion profiles of FITC–dextran 10 kDa and the chemokine CCL19 are similar owing to similar hydrodynamic radii[42].

Ex vivo crawl-in assay. Four-to-six-week-old C57BL/6J mice were euthanized, ears were split and the cartilage-free ventral half was used as migration matrix as previously described[10]. Wild-type bone-marrow-derived DCs were labelled with 10 μM TAMRA (Invitrogen) and a total of 6×10^4 cells were applied to one ear sheet and incubated for 20 min to allow migration into the tissue. Subsequently, non-adherent cells were washed away and ear explants were incubated at 37 °C and lymphatic vessels of the ear explants were immunostained for LYVE1 (R&D).

Imaging. *Cell migration in micro-fabricated devices.* Cell migration was recorded with an inverted wide-field Nikon Eclipse microscope using 20×/0.5 PH1 air, 60×/1.4 PH3 oil and 100×/1.4 PH3 oil objectives, equipped with a Lumencor light source (390 nm, 475 nm, 542/575 nm) and an incubation chamber, heated stage and CO_2 mixer (Ibidi); or an Visitron epifluorescence microscope using a Plan-APOCHROMAT 20×/0.8 air objective, equipped with a lumencor light source (390 nm, 475 nm and 542/575 nm) and an incubation chamber, heated stage and CO_2 mixer (Ibidi).

Spinning-disc microscopy. High-magnification EB3 dynamics were imaged with an inverted TILL photonics spinning disc using a 60×/1.35 oil objective equipped with an Andor 885 camera, laser lines (405, 445, 488, 561 and 640 nm) and an incubation chamber, heated stage and CO_2 mixer (Ibidi).

Confocal reflection microscopy. Collagen matrix analysis by confocal reflection microscopy was done as described[34] by using an inverted Leica SP5 confocal/multiphoton microscope.

Ex vivo crawl-in assay. Labelled DCs within the explants were visualized using a LSM700 upright confocal microscope (Zeiss) with a plan apochromat 40×/1.1 water objective and 405-, 488- and 555-nm laser lines.

Light-sheet imaging. DCs embedded in 3D collagen were imaged with axially swept light-sheet microscopy[11], which has an isotropic resolution of ~390 nm.

Image analysis. Fiji[43] was used for image processing, including using the Trackmate plugin for manual cell tracking[44]. Generally, only single, non-interacting cells were quantified to exclude the influence of neighbouring cells on pore-size decision, cell path and cell speed.

Quantification of displacement towards chemokine source and average speed in 3D collagen gels. The average displacement of all cells towards the chemokine source was calculated with a custom-made script[22] in ImageJ. In brief, cell migration image sequences were background-corrected by subtracting the average of the sequence. Particle filtering was used to discard objects smaller or larger than the cells. For each image, the lateral displacement that optimizes its overlap with the previous frame was determined. Finally, the displacement towards the chemokine source was calculated from the optimal y displacement in pixels, divided by the time between two consecutive frames.

Analysis of nucleus and MTOC positioning. Nuclear (Hoechst) and MTOC (major EB3–mCherry signal) signals were segmented with ilastik v.1.1.5 (https://ilastik.org) to generate binary images of nucleus and MTOC positioning, which were subsequently analysed by a custom-made Matlab script (available upon request) to determine the cell speed in relation to the nucleus–MTOC axis configuration.

Light-sheet image analysis. To extract the DC surface, we used custom-built Matlab tools to combine three transformations of the deconvolved image that each detected different components of the cell. First, we generated a lamellipodia-enhanced image by applying a multiscale surface filter[45] that accentuates planar features that are two or three pixels thick. This image was normalized by subtracting the intensity value two standard deviations above the mean. Second, we enhanced the cell cortex by calculating the Otsu threshold[46] of the deconvolved image and subtracting this value from the deconvolved image. Third, we enhanced the cell interior by applying a gamma correction of 0.8, smoothing with a Gaussian filter of width two pixels, Otsu thresholding, morphologically dilating with a sphere of radius seven pixels, filling the holes in each x–y plane, morphologically eroding with a sphere of radius five pixels and, finally, smoothing with a Gaussian filter of width one pixel. The three images were combined by finding the maximum value at each pixel, and a triangle mesh was generated as an isosurface of the combined image. The surface curvature of the mesh was calculated as previously described[47]. To better visualize the collagen matrix, a multiscale steerable filter[47,48] was applied to detect linear features that are two or three pixels wide. ChimeraX was used for rendering.

Analysis of 3D collagen pore sizes. Collagen matrix information from light-sheet microscopy images was used to analyse pore sizes of the collagen fibre network. The collagen network was segmented from the raw light-sheet images using ilastik[49]. The segmentation threshold was chosen such that the volume of the segmented network matched the volume fraction of collagen in the gel. The pore-size distribution was obtained analogously to the 2D pore-size analysis described in ref. [50]: 3D spheres were consecutively positioned into fitting corresponding gaps of the network (starting with the largest spheres) using a custom-made Matlab script (available upon request). To exclude edge artefacts, the outer sector (with a width of the largest overall filling spheres) was not included into the pore-size analysis.

Statistics. Figures represent pooled data from independent biological replicates as indicated in the figure legends. Appropriate control experiments were performed for each biological replicate. All replicates were validated independently and pooled only when all showed the same result. All statistical analyses were performed with GraphPad Prism using the appropriate tests according to normal or non-normal data distribution: unpaired t-tests (Figs. 2a, d, e, 3e, Extended Data Figs. 6g, h, 8h, j), paired t-tests (Figs. 2j, l, 3g, Extended Data Figs. 2b, 10c), one-way ANOVA with Tukey's test (Figs. 1g, h, 2g, 3b, h, 4b, Extended Data Figs. 2f, h, 3b, e, g, 4a, d, f, 6f, 8e, f, 9a, 10b), two-way ANOVA (Extended Data Figs. 6b, c, 9c), Mann–Whitney (Fig. 4e, Extended Data Figs. 9b, c, 10h, i, l, m), Kruskal–Wallis with Dunn's test (Extended Data Figs. 2g, h, 3c, 4e, 8d, l, 10o). $^*P < 0.05$, $^{**}P < 0.01$, $^{***}P < 0.001$ and $^{****}P < 0.0001$.

Reporting Summary. Further information on experimental design is available in the Nature Research Reporting Summary linked to this article.

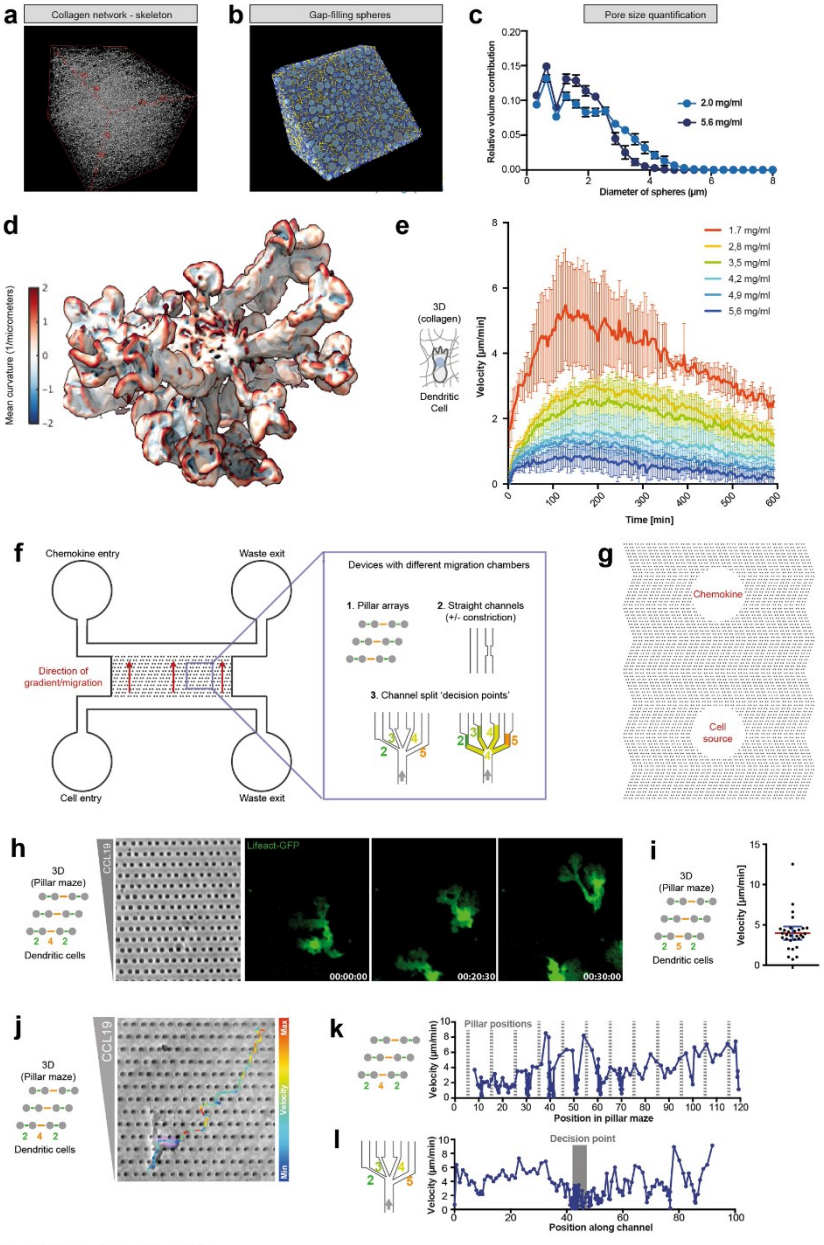
Data availability

All data that support the conclusions of this paper are available from the authors on request.

Code availability

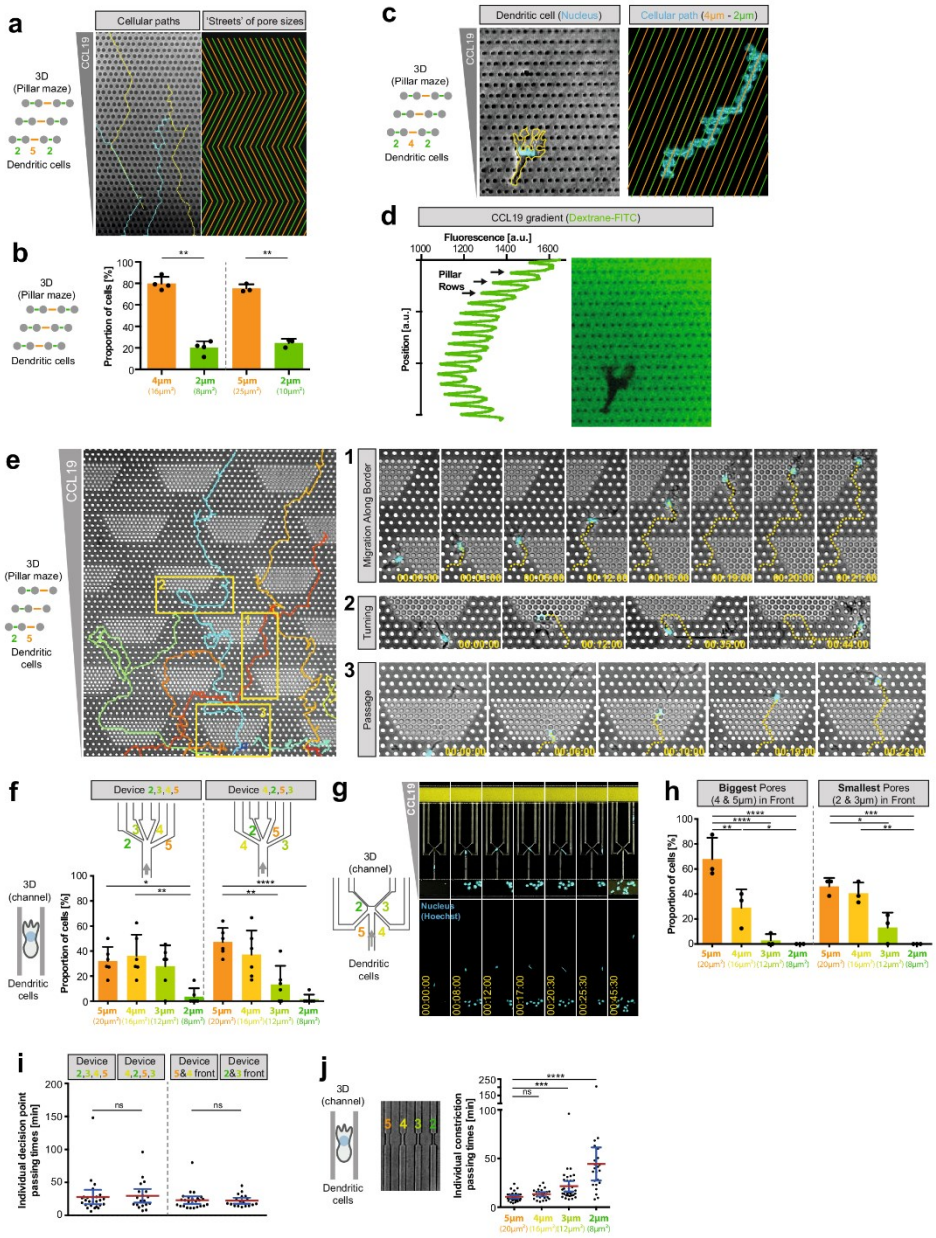
All custom-made scripts are available from the authors on request.

31. Riedl, J. et al. Lifeact mice for studying F-actin dynamics. *Nat. Methods* **7**, 168–169 (2010).
32. Redecke, V. et al. Hematopoietic progenitor cell lines with myeloid and lymphoid potential. *Nat. Methods* **10**, 795–803 (2013).
33. Leithner, A. et al. Fast and efficient genetic engineering of hematopoietic precursor cells for the study of dendritic cell migration. *Eur. J. Immunol.* **48**, 1074–1077 (2018).
34. Sixt, M. & Lämmermann, T. *In vitro* analysis of chemotactic leukocyte migration in 3D environments. *Methods Mol. Biol.* **769**, 149–165 (2011).
35. Beronja, S., Livshits, G., Williams, S. & Fuchs, E. Rapid functional dissection of genetic networks via tissue-specific transduction and RNAi in mouse embryos. *Nat. Med.* **16**, 821–827 (2010).
36. Scaffidi, P. & Misteli, T. Lamin A-dependent misregulation of adult stem cells associated with accelerated ageing. *Nat. Cell Biol.* **10**, 452–459 (2008).
37. Miller, A. L. & Bement, W. M. Regulation of cytokinesis by Rho GTPase flux. *Nat. Cell Biol.* **11**, 71–77 (2009).
38. Stewart, S. A. et al. Lentivirus-delivered stable gene silencing by RNAi in primary cells. *RNA* **9**, 493–501 (2003).
39. Leithner, A., Merrin, J., Reversat, A. & Sixt, M. Geometrically complex microfluidic devices for the study of cell migration. *Protoc. Exch.* https://doi.org/10.1038/protex.2016.063 (2016).
40. Képiró, M. et al. *para*-Nitroblebbistatin, the non-cytotoxic and photostable myosin II inhibitor. *Angew. Chem. Int. Ed. Engl.* **53**, 8211–8215 (2014).
41. Lämmermann, T. et al. Rapid leukocyte migration by integrin-independent flowing and squeezing. *Nature* **453**, 51–55 (2008).
42. Schwarz, J. et al. A microfluidic device for measuring cell migration towards substrate-bound and soluble chemokine gradients. *Sci. Rep.* **6**, 36440 (2016).
43. Schindelin, J. et al. Fiji: an open-source platform for biological-image analysis. *Nat. Methods* **9**, 676–682 (2012).
44. Tinevez, J.-Y. et al. TrackMate: an open and extensible platform for single-particle tracking. *Methods* **115**, 80–90 (2017).
45. Elliott, H. et al. Myosin II controls cellular branching morphogenesis and migration in three dimensions by minimizing cell-surface curvature. *Nat. Cell Biol.* **17**, 137–147 (2015).
46. Otsu, N. A threshold selection method from gray-level histograms. *IEEE Trans. Syst. Man Cybern.* **9**, 62–66 (1979).
47. Welf, E. S. et al. Quantitative multiscale cell imaging in controlled 3D microenvironments. *Dev. Cell* **36**, 462–475 (2016).
48. Aguet, F., Jacob, M. & Unser, M. *IEEE International Conference on Image Processing 2005* (IEEE, 2005).
49. Sommer, C., Straehle, C., Koethe, U. & Hamprecht, F. A. *IEEE International Symposium on Biomedical Imaging: from Nano to Macro* (IEEE, 2011).
50. Acton, S. E. et al. Dendritic cells control fibroblastic reticular network tension and lymph node expansion. *Nature* **514**, 498–502 (2014).



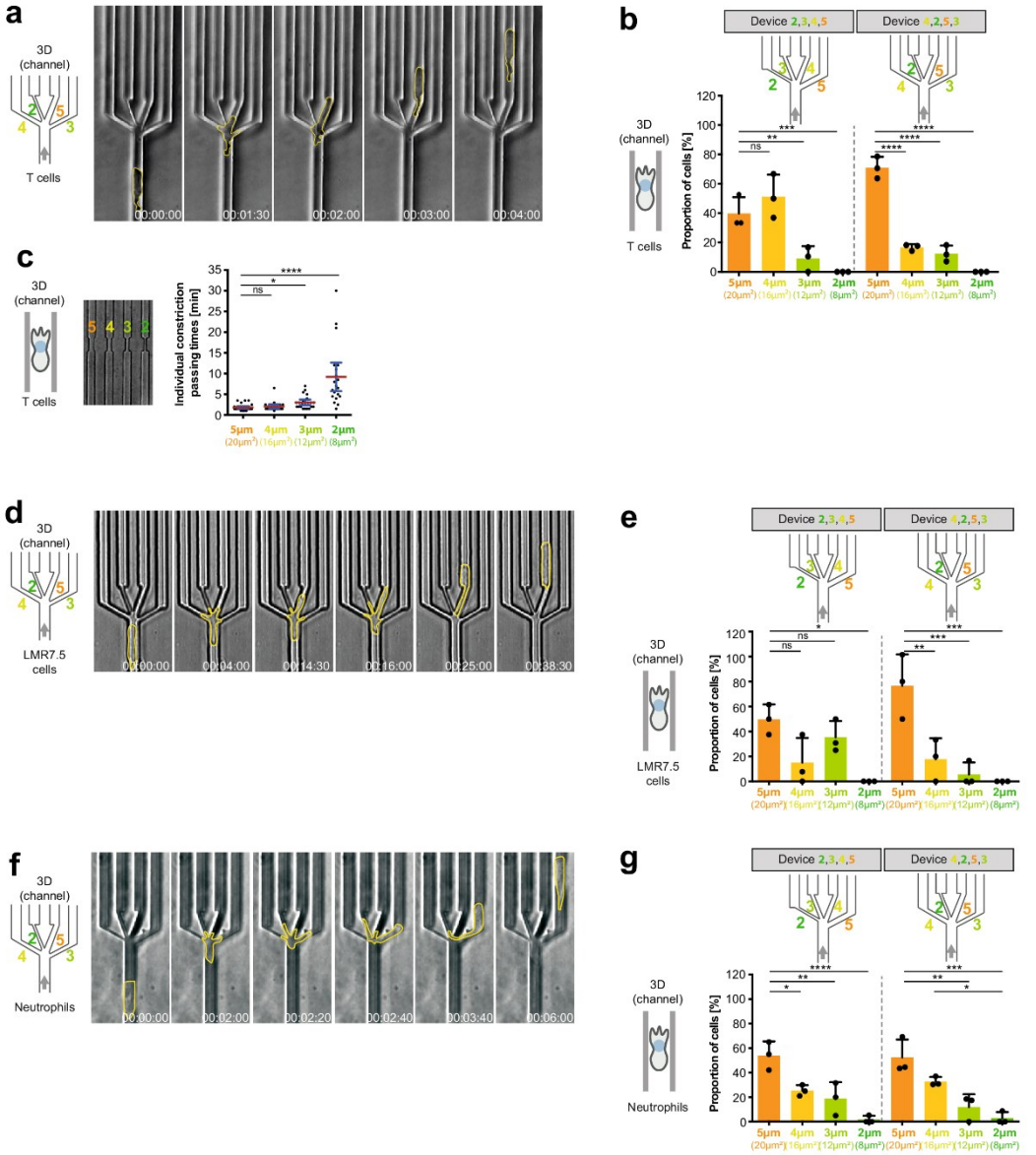
Extended Data Fig. 1 | See next page for caption.

Extended Data Fig. 1 | DC migration in 3D collagen matrices of different densities and microfluidic assays to study cell migration through defined inhomogeneous spaces. a, Skeleton representation of the collagen matrix (labelled with Alexa Fluor 568) imaged by light-sheet microscopy with isotropic, subcellular 3D resolution (four experiments). **b**, Pore-size analysis by filling 3D spheres (blue) between the collagen fibres (yellow) based on the skeleton representation in **a**. **c**, Quantification of pore sizes as in **b** for two different collagen concentrations (2.0 and 5.6 mg ml^{-1}; $n = 4$ cells each; mean ± s.d.). **d**, Magnification of Fig. 1a, showing an example of a DC (labelled with LifeAct–GFP) with multiple protrusions (with veil-like shapes) embedded in a 3D collagen matrix and coloured by surface curvature (regions of large positive and large negative curvature in red and blue, respectively; see scale bar). **e**, Migration velocities (average displacement in direction of the chemokine gradient over time) of DCs in collagen matrices of different collagen concentrations (1.7–5.6 mg ml^{-1}) along a CCL19 gradient, highlighting the ability of DCs to migrate even in high collagen densities (5.6 mg ml^{-1}), but with a reduced velocity. Data are mean ± s.d. ($n = 4$ experiments). **f**, Scheme of the PDMS-based microfluidic setup used to analyse cell migration in different defined microenvironments. In brief, cells and chemokine were flushed separately from two different entrances into two main channels, which are connected either by pillar arrays or different types of channels. On stopping the flow, a chemokine gradient was established and cells migrated into the connecting area (Methods). **g**, Alternative PDMS-based migration chamber setup, in which cells are placed in one hole and a chemokine is placed in the other; the holes are connected by arrays of pillars (Methods). **h**, Typical shape of a DC (labelled with LifeAct-GFP) with multiple cell fronts, migrating in a CCL19 gradient (left) through a pillar array with 2-μm and 4-μm pores, arranged to generate 'streets' of large (orange) and small (green) pores (2 experiments). **i**, Migration velocities of DCs through a pillar array of 2-μm and 5-μm pores (30 cells); data are mean ± 95% CI. **j**, Velocity (colour-coded) of a representative DC migrating through a pillar array of 2-μm and 4-μm pores (2 experiments). **k**, Quantification of **e**, showing cellular deceleration before pore translocation even before passing large pores (two experiments). **l**, DC velocity before, during and after pore-size decision, when migrating in a microchannel through a junction (decision point) of four differently sized pores of 2-, 3-, 4- and 5-μm width (2 experiments). During this 'decision time', DCs feature multiple parallel cell fronts and cellular protrusions (see Fig. 1).



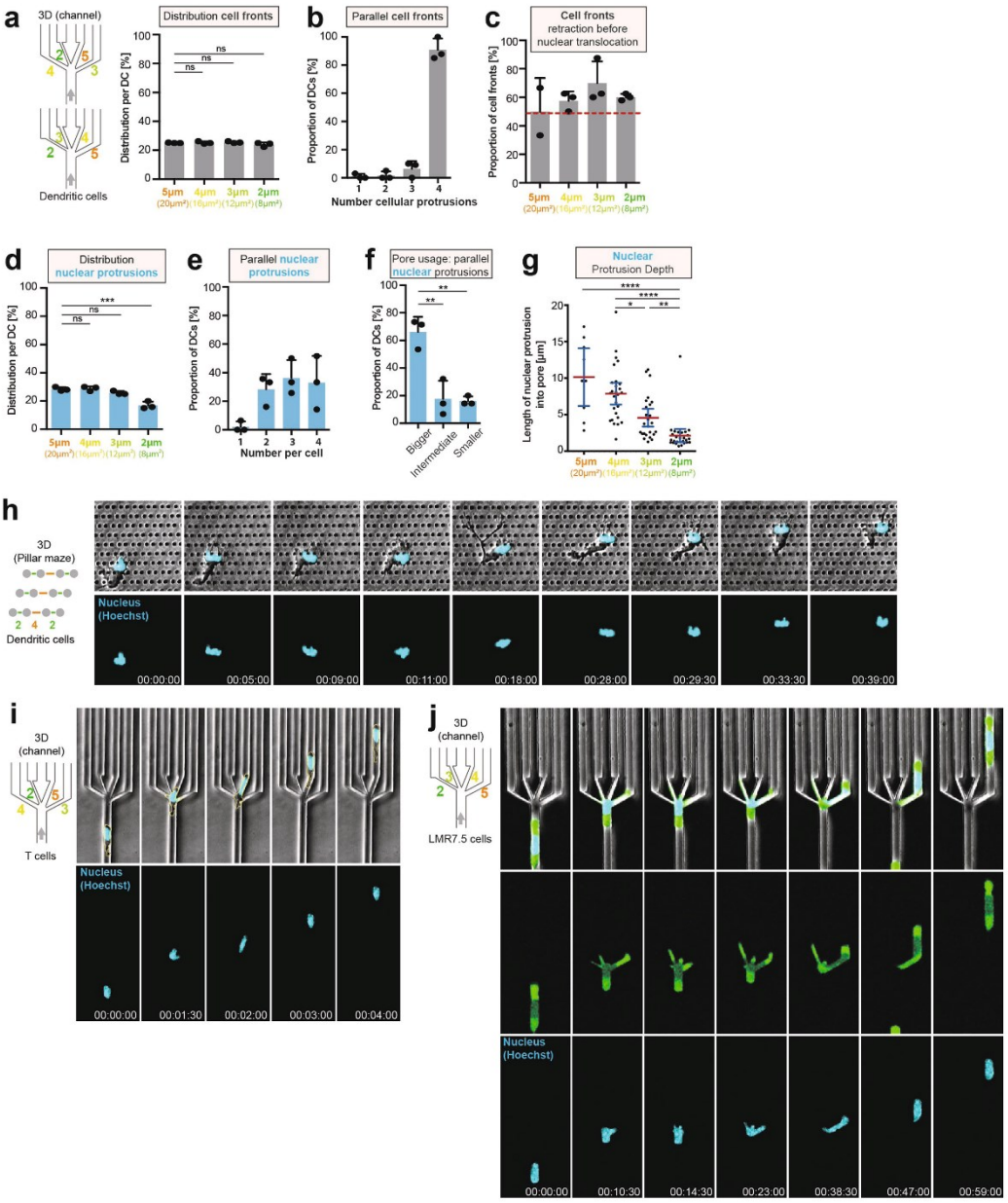
Extended Data Fig. 2 | See next page for caption.

Extended Data Fig. 2 | DC migration through defined inhomogeneous spaces. a, Tracks (left; blue, yellow) of DCs migrating long distances through pillar arrays (2-μm and 5-μm pores; 5-μm height), in which 'streets' of pore size change orientation after ten pores (right, streets of large and small pores in orange and green, respectively) (3 experiments). **b**, Left, quantification of DC pore-size preference in pillar forests depicted in **c** (4 experiments, 23 cells, 231 pore passages; paired *t*-test, $^{**}P = 0.0023$). Right, quantification of DC pore-size preference in **a** (3 experiments, 21 cells, 312 pore passages; paired *t*-test, $^{**}P = 0.0073$). **c**, Similar to **a**, but with different pore sizes and pillar arrangements, showing that DCs (nucleus (Hoechst stain) in cyan, cell outlines in yellow) can deviate from the most-direct chemokine gradient (CCL19) along the path of least resistance (2-μm and 4-μm pores; arranged to generate streets (top right) of large (orange) and small (green) pores) (3 experiments). **d**, CCL19 gradient in **a** visualized by dextran–FITC (three experiments). **e**, Pillar forests with dense pillar islands (2-μm pores) within a surrounding area with lower pillar density (5-μm pores). Insets are expanded on the right, showing examples of small-pore avoidance by migration along boundaries of small-pore islands (1) or turning (2), and small-pore translocation when cells encounter dense pillar islands head-on (3) (three experiments). **f**, As in Fig. 1g (left), but showing the results of the pore-size preference of DCs in individual devices with different orders of pore sizes (3 experiments, 27 cells in device 1, 30 cells in device 2); one-way ANOVA with Tukey's test; $^{****}P < 0.0001$, $^{**}P = 0.0016$, $^{*}P = 0.0159$). **g**, DC migration through microchannels with a decision point with 2 small pores (2-μm and 3-μm wide) directly in the migration direction, and two larger pores (4-μm and 5-μm wide) diagonally against the direction of migration (3 experiments). **h**, Quantification of **g**, comparing alternative orientations (small pores in front versus in the back) (3 experiments, 61 cells; one-way ANOVA with Tukey's test; left: $^{****}P < 0.0001$, $^{**}P = 0.0037$, $^{*}P = 0.0389$; right panel, $^{***}P = 0.0007$, $^{**}P = 0.0025$, $^{*}P = 0.0157$). **i**, Quantification of passing times in devices with different pore-size arrangements as in **f** and **h** (3 experiments; 26, 29, 25 and 18 cells, left to right, respectively; Kruskal–Wallis with Dunn's test). **j**, DC passing times through the same pore sizes as in **d**, **f** and Fig. 1g, but without the possibility of pore selection (single pores; 3 experiments, 114 cells; Kruskal–Wallis with Dunn's test; $^{****}P < 0.0001$, $^{***}P = 0.0002$). Data in **b**, **f** and **h** are mean ± s.d.; data in **i** and **j** are mean ± 95% CI.



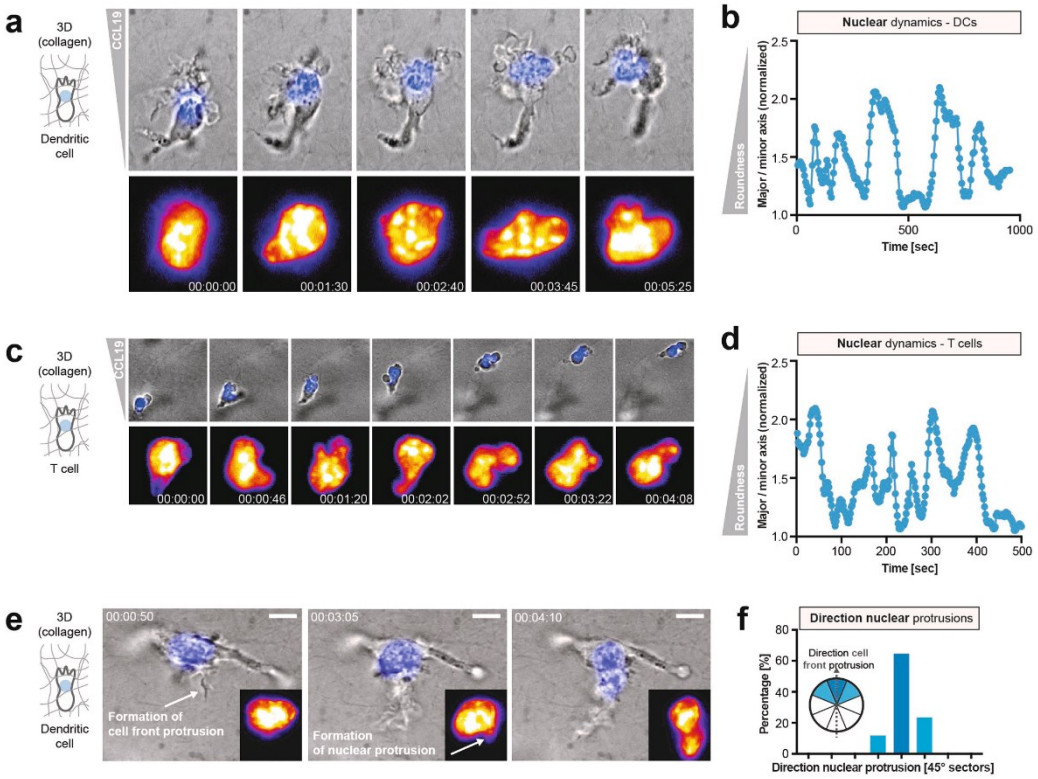
Extended Data Fig. 3 | See next page for caption.

Extended Data Fig. 3 | Migration of T cells, LMR7.5 cells and neutrophils through defined inhomogeneous spaces. a, Image sequence of a representative T cell (cell outlines in yellow) migrating in microchannels through a junction (decision point) with pores 2-, 3-, 4- and 5-μm wide (3 experiments). **b**, As in Fig. 1h, but showing the results of the pore-size preference of T cells in individual devices with different sequences of pore sizes (3 experiments, 37 (left) or 42 (right) cells; one-way ANOVA with Tukey's test; $^{****}P < 0.0001$, $^{***}P = 0.0003$, $^{**}P = 0.0045$). **c**, Passing times for T cells through the same pore sizes as in Fig. 1h, but without the possibility of pore choice (single pores; 3 experiments, 90 cells; Kruskal–Wallis with Dunn's test; $^{****}P < 0.0001$, $^{*}P = 0.0128$). **d**, Image sequence of a representative LMR7.5 T cell hybridoma cell (cell outlines in yellow) migrating in microchannels through a decision point with exits 2, 3, 4 and 5 μm wide (3 experiments). **e**, As in Fig. 1h, but showing the results of the pore-size preference of LMR7.5 T cell hybridoma cells in individual devices with different sequences of pore sizes (3 experiments, 23 (left) or 17 (right) cells; one-way ANOVA with Tukey's test; $^{***}P = 0.0002$, $^{***}P = 0.0004$, $^{**}P = 0.0030$, $^{*}P = 0.0132$ (left to right), respectively). **f**, Image sequence of a representative neutrophil (cell outlines in yellow) migrating in microchannels through a decision point with pores 2-, 3-, 4- and 5-μm wide (height 2 μm) (3 experiments). **g**, As in Fig. 1h, but showing the results of the pore-size preference for neutrophils in individual devices with different sequences of pore sizes (3 experiments, 59 (left) or 63 (right) cells; one-way ANOVA with Tukey's test; left: $^{****}P < 0.0001$, $^{**}P = 0.0054$, $^{*}P = 0.0284$; right: $^{***}P = 0.0002$, $^{**}P = 0.0014$, $^{*}P = 0.0212$). Data in **b**, **e** and **g** are mean ± s.d.; data in **c** are mean ± 95% CI.

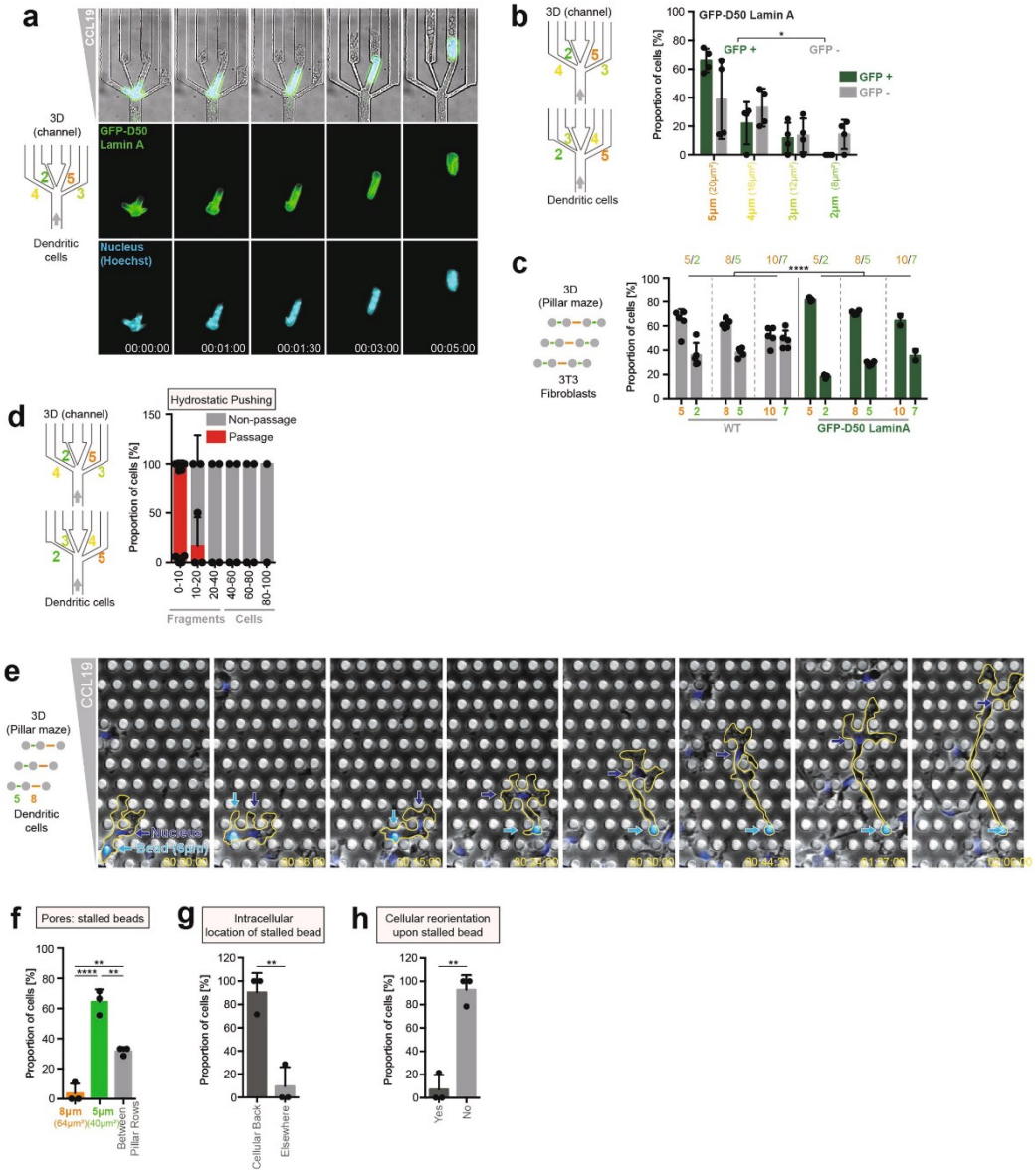


Extended Data Fig. 4 | See next page for caption.

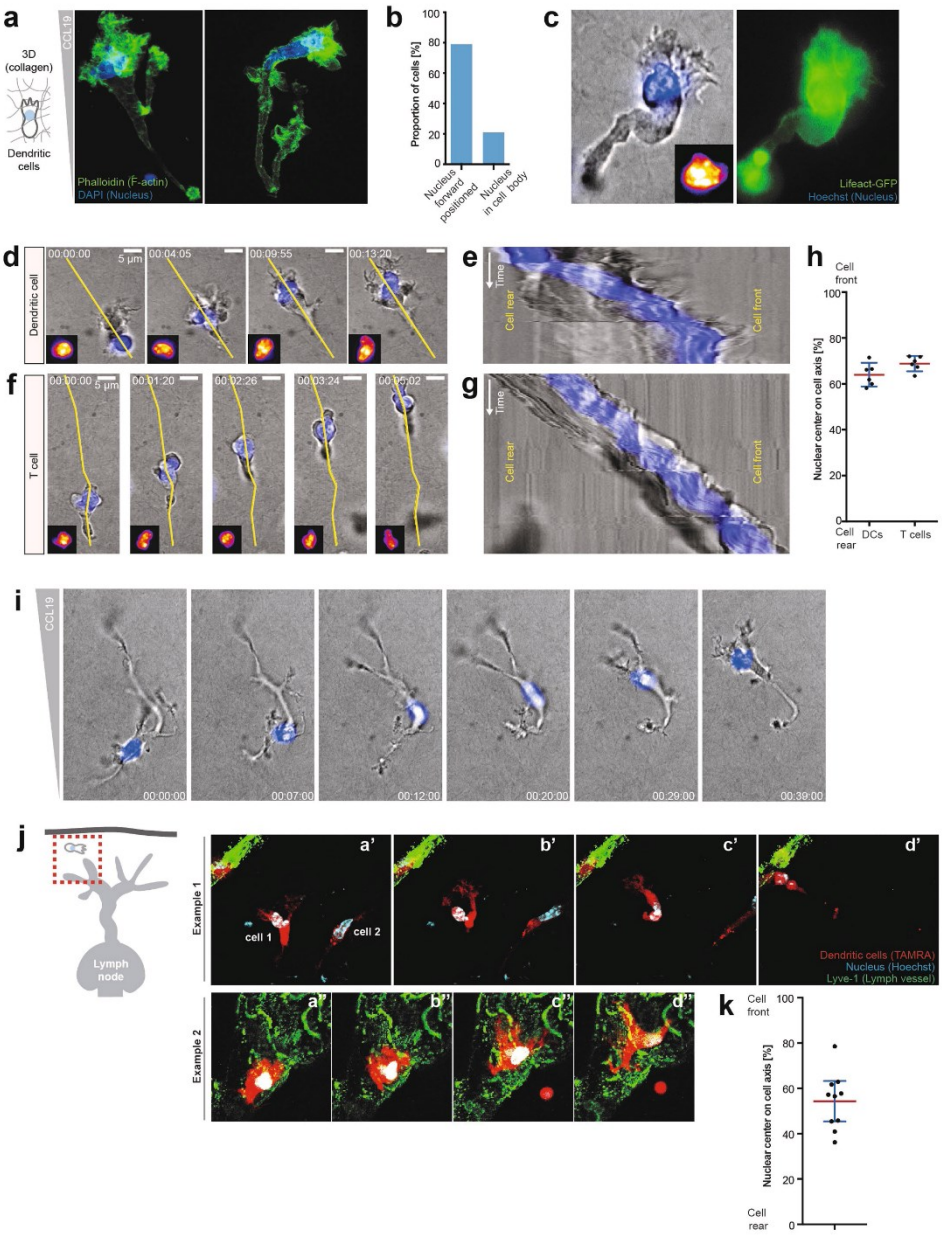
Extended Data Fig. 4 | Dynamic nuclear protrusions during pore-size decisions. **a**, Quantification of the translocation of cell fronts through the differently sized pores (3 exeriments, 71 cells, 237 lamellipodia; one-way ANOVA with Tukey's test). **b**, Number of cell front protrusions per cell during four-way pore-size decision (3 experiments, 62 cells). **c**, Quantification of cell front protrusion retractions before cell body (nuclear) passage (3 experiments, 101 lamellipodia). **d**, Quantification of initial nuclear protrusions into the different pore sizes during pore-size decision (3 experiments, 51 cells, 164 nuclear protrusions; one-way ANOVA with Tukey's test; $^{***}P = 0.0003$). **e**, Number of parallel nuclear protrusions per cell during pore-size decision (3 experiments, 51 cells). **f**, Pore-size selection for the larger, intermediate or smaller pore when there are parallel nuclear lobes (3 experiments, 50 cells; one-way ANOVA with Tukey's test; $^{**}P = 0.0025$ (bigger versus intermediate), $^{**}P = 0.0021$ (bigger versus smaller)). **g**, Maximal nuclear protrusion depth into non-chosen pores (9 cells (5 μm), 27 cells (4 μm), 25 cells (3 μm) and 27 cells (2 μm); Kruskal–Wallis with Dunn's test; $^{****}P < 0.0001$, $^{**}P = 0.0058$, $^{*}P = 0.0474$). **h**, Frequent and parallel nuclear protrusions (nucleus (Hoechst) in cyan) of migrating DCs navigating through a pillar array with 2-μm and 4-μm pores (3 experiments). **i**, Nuclear protrusions of a T cell (nucleus (Hoechst) in cyan; cell outlines in yellow) migrating in microchannels through a decision point of four differently sized pores of 2-, 3-, 4- and 5-μm width (3 experiments). **j**, Nuclear protrusions of a LMR7.5 T cell hybridoma (nucleus (Hoechst) in cyan; EB3–mCherry in green) migrating in microchannels through a decision point of four differently sized pores of 2-, 3-, 4- and 5-μm width (3 experiments). Data in **a**–**f** are mean ± s.d.; data in **g** are mean ± 95% CI.



Extended Data Fig. 5 | Dynamic nuclear protrusions during 3D migration in collagen matrices. a, Nuclear-labelled (top panels, blue; bottom panels, fire colour-coded intensity) DC migrating in a collagen matrix along a CCL19 gradient, depicting the various shapes adopted by the nucleus (three experiments). **b**, Nuclear shape changes over time of a DC migrating in a 3D collagen matrix, highlighting the dynamic transitions between rounded and more deformed shapes (three experiments). **c**, Nuclear-labelled (top panels, blue; bottom panels, fire-colour-coded intensity) T cell migrating in a collagen matrix along a CCL19 gradient, highlighting the various shapes adopted by the nucleus (three experiments). **d**, Nuclear shape changes over time of a T cell migrating in a 3D collagen matrix, highlighting the dynamic transitions between rounded and more deformed shapes (three experiments). **e**, DC during formation of a new cell front protrusion, followed by a nuclear protrusion in the direction of the new cell front (three experiments). **f**, Quantification of the direction of nuclear protrusion in relation to the direction of new cell front protrusions ($n = 17$ cells).

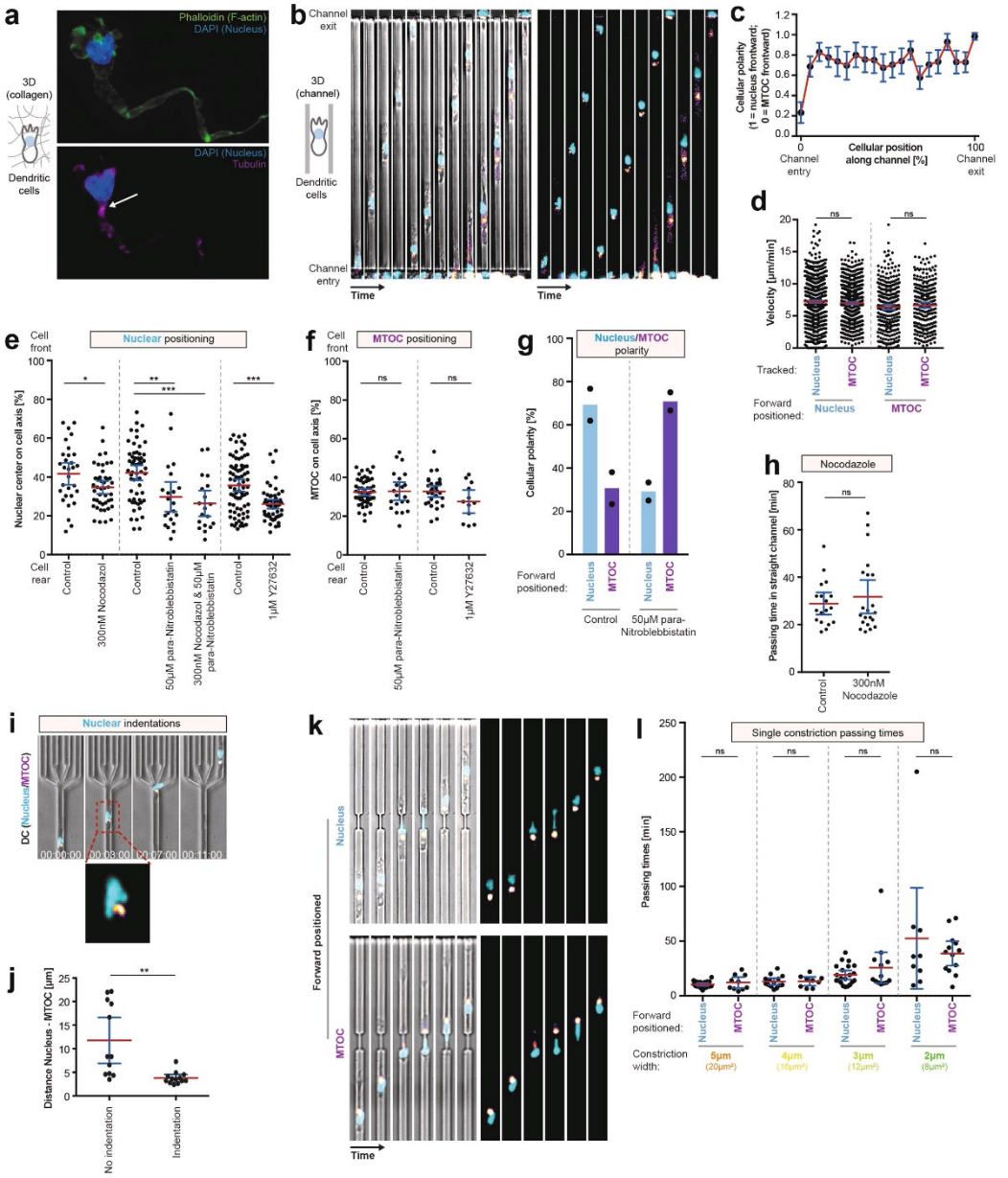


Extended Data Fig. 6 | Nuclear function as a mechanical guide. a, DC expressing lamin(D50)–GFP (lamin(D50) is also known as progerin) migrating through a four-way pore-size decision (four experiments). **b**, Quantification of pore-size preference in **a**, divided into GFP^+ and GFP^- regions (4 experiments, 293 cells; unpaired *t*-test; $^*P = 0.0118$). **c**, Pore-size preference of 3T3 fibroblasts expressing lamin(D50)–GFP (or wild-type lamin–GFP as control) migrating in pillar arrays with differently sized pores (3 experiments, 606 pore passages; two-way ANOVA with Tukey's test; $^{****}P < 0.0001$). **d**, Low hydrostatic pushing of cells and cellular fragments through 4-way pore-size decision ($n = 66$). **e**, DC (nucleus labelled, Hoechst, blue) loaded with a 6-µm polystyrene bead (cyan) migrating through a pillar array with 5-µm and 8-µm pores (3 experiments). **f**, Graph showing where the intracellular bead gets stuck (3 experiments, 29 cells; one-way ANOVA with Tukey's test; $^{****}P < 0.0001$, $^{**}P = 0.0016$ (8 µm versus between pillar rows), $^{**}P = 0.0035$ (5 µm versus between pillar rows)). **g**, Graph showing intracellular location of the bead when it gets stuck (3 experiments, 29 cells; unpaired *t*-test; $^{**}P = 0.0039$). **h**, Frequency of cellular reorientation of DCs with an intracellular bead after getting stuck (3 experiments, 29 cells; unpaired *t*-test; $^{**}P = 0.0011$). Data are mean ± s.d.



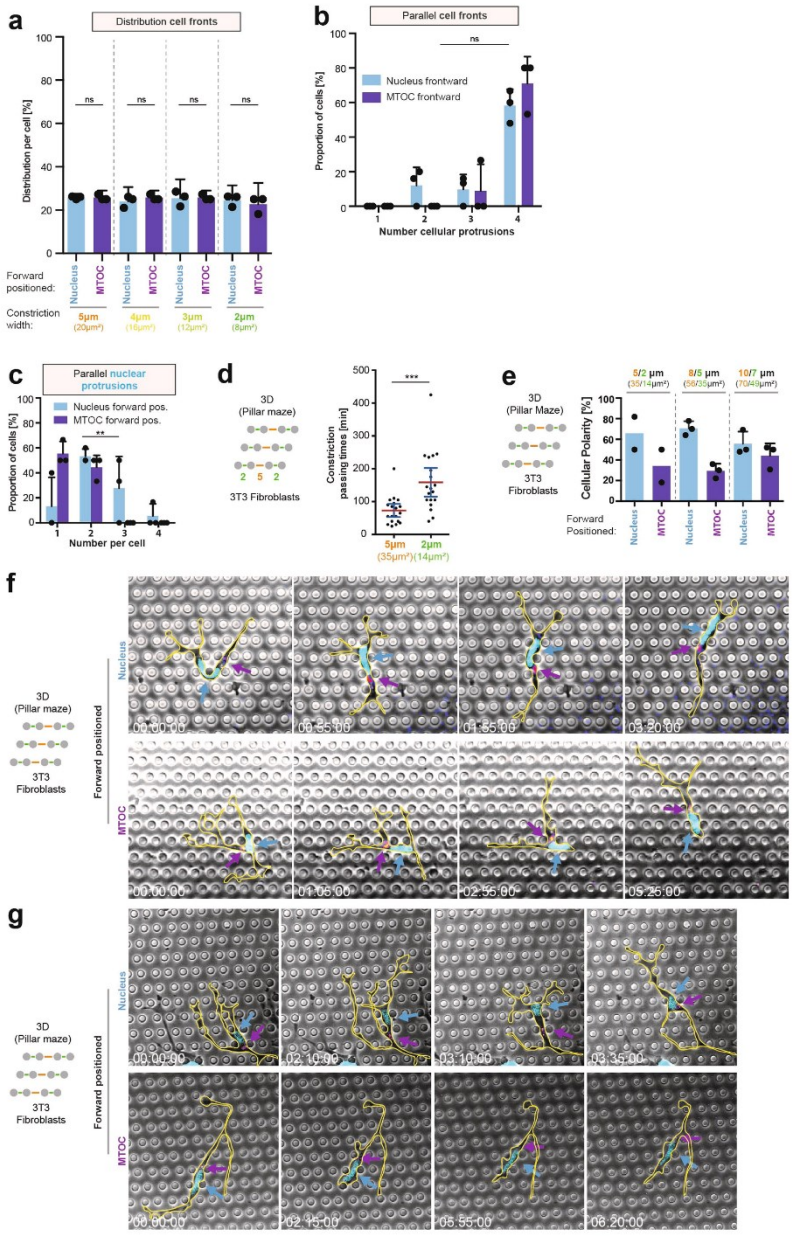
Extended Data Fig. 7 | See next page for caption.

Extended Data Fig. 7 | Nuclear positioning during amoeboid cell migration. a, DCs migrating in a 3D collagen matrix along a CCL19 gradient, fixed with paraformaldehyde and stained with phalloidin (green) and DAPI (blue). Two examples are shown; note the nuclear positioning close to the cell front directly behind the F-actin-rich lamellipodium (three experiments). **b**, Quantification of the nuclear location in **a** (62 cells). **c**, Live-cell imaging of a DC labelled with LifeAct–GFP (green) and Hoechst nuclear stain (blue), showing nuclear positioning close to the cell front directly behind the actin-rich lamellipodium (three experiments). **d**, Temporal analysis of nuclear positioning during DC migration in a 3D collagen matrix along a CCL19 gradient (yellow line depicts the kymographic axis in **e**). Note that the cell polarizes at time point 0, after which the nucleus quickly positions close to the cell front (three experiments). **e**, Kymographic analysis of **d** (three experiments). **f**, Temporal analysis of nuclear positioning during T cell migration in a 3D collagen matrix along a CCL19 gradient (yellow line depicts the kymographic axis in **e**) (three experiments). **g**, Kymographic analysis of **f**. Note the nuclear positioning close to the cell front (three experiments). **h**, Quantification of nuclear positioning along the cell axis ($n = 6$ cells; data are mean ± 95% CI). **i**, Representative of a repolarizing DC (the former front becomes the new back edge) migrating in a 3D collagen matrix along a CCL19 gradient. Note that the nucleus translocates through the entire cell body to position to the new cell front ($n = 3$ experiments). **j**, Ex vivo DC (TAMRA, red) migration in mouse skin ear explants (scheme, left) towards lymphatic vessels (LYVE1, green). Two exemplary image sequences ($n = 3$ experiments). **k**, Quantification of nuclear positioning along the cell axis in **j** ($n = 10$ cells; data are mean ± 95% CI).



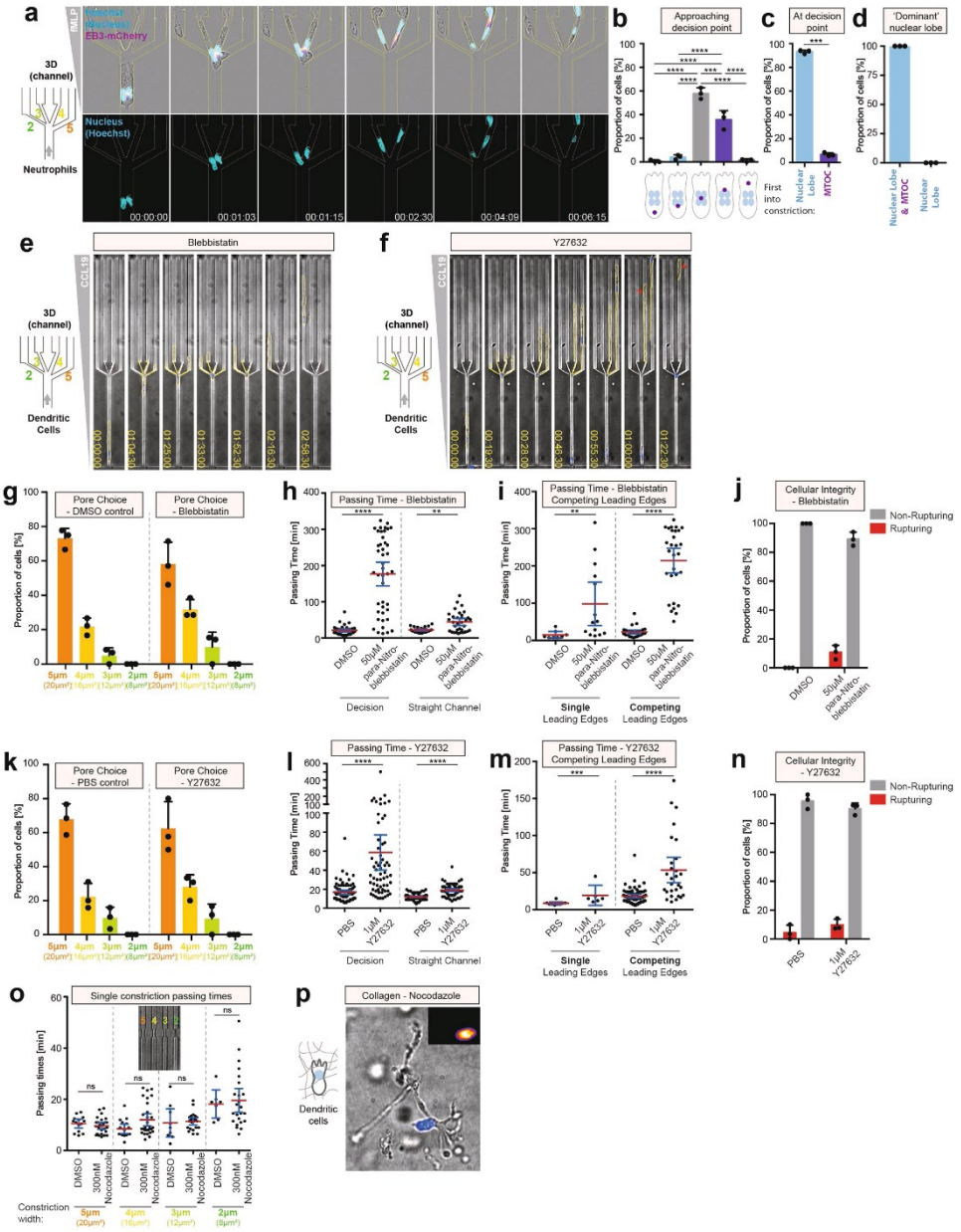
Extended Data Fig. 8 | See next page for caption.

Extended Data Fig. 8 | MTOC positioning during DC migration. **a**, DCs migrating in a 3D collagen matrix along a CCL19 gradient were fixed with paraformaldehyde and stained with DAPI (blue), phalloidin (green) and for tubulin immunofluorescence (magenta). The arrow highlights the major tubulin signal ($n = 3$ experiments). **b**, Image sequence of three exemplary DCs (Hoechst, nucleus, cyan; EB3–mCherry, fire colour-coded intensity) migrating consecutively in a microchannel along a CCL19 gradient. Note that cells 1 and 3 (counting from left to right) initially enter the channel with forward positioning of the MTOC; however, after a short migration distance the nucleus positions in front of the MTOC (nucleus-first configuration) ($n = 5$ experiments). **c**, Quantification of **b** ($n = 1{,}148$ events). **d**, Quantification of the velocity of the cells, depending on the orientation of the nucleus–MTOC axis, tracking the nucleus or the MTOC location as a velocity reference point ($n = 830, 323, 787, 262$ events, respectively, left to right; Kruskal–Wallis with Dunn's test). **e**, Nuclear positioning in DCs along the cell axis, in the presence of 300 nM nocodazole (with DMSO control), 50 μM *para*-nitroblebbistatin (with DMSO control) or 1 μM Y27632 (with PBS control) in straight microchannels without constrictions ($n = 30, 45, 56, 21, 19, 77, 54$ cells, respectively, left to right; one-way ANOVA with Tukey's test; $^{***}P = 0.0002$, $^{**}P = 0.0051$, $^{*}P = 0.0269$). **f**, MTOC positioning in DCs along the cell axis in the presence of 300 nM nocodazole (with DMSO control), 50 μM *para*-nitroblebbistatin (with DMSO control) or 1 μM Y27632 (with PBS control) in straight microchannels without constrictions ($n = 53, 21, 29, 12$ cells, respectively, left to right; one-way ANOVA with Tukey's test). **g**, Nuclear–MTOC polarity in the presence of 50 μM *para*-nitroblebbistatin (with DMSO control) in straight microchannels without constrictions (e = 2 experiments). **h**, Quantification of the passing time of DCs migrating through straight channels in the presence of 300 nM nocodazole (DMSO control) ($n = 18$ (control) or 21 (nocodazole) cells; unpaired *t*-test). **i**, Exemplary DCs migrating in a microchannel with a nuclear indentation in close proximity to the MTOC localization (three experiments). **j**, Quantification of **i** (25 cells; unpaired *t*-test; $^{*}P = 0.0012$). **k**, Image sequences of DCs (Hoechst, nucleus, cyan; EB3–mCherry, fire colour-coded intensity) migrating along a CCL19 gradient in a microchannel with a 2-μm-wide individual pore. Top panels depicts an exemplary DC migrating through the 2-μm pore with the nucleus first, the bottom panels depicts an exemplary DC migrating through the 2-μm pore with the MTOC first (3 experiments). **l**, Quantification of **k**, and of DC migration through individual pores 3-, 4- or 5-μm wide ($n = 20, 10, 14, 9, 21, 13, 9, 13$ cells, respectively, left to right; Kruskal–Wallis with Dunn's test). Data are mean ± 95% CI.



Extended Data Fig. 9 | See next page for caption.

Extended Data Fig. 9 | Nucleus-first versus MTOC-first cell polarity during pore-size decisions in DCs and fibroblasts. a, Quantification of cell-front pore preference as a function of nucleus–MTOC axis orientation (3 experiments, 26 cells; one-way ANOVA with Tukey's test). **b**, Quantification of parallel cell fronts as a function of nucleus–MTOC axis orientation (3 experiments, 26 cells; Mann–Whitney test). **c**, Number of parallel nuclear protrusion in DCs with nucleus first (cyan) or MTOC first (magenta). (3 experiments, 28 cells; two-way ANOVA, $^{**}P = 0.0029$). **d**, Constriction passing times of fibroblasts (38 cells; Mann–Whitney test, $^{***}P = 0.0002$) during migration through a pillar array with 2-μm and 5-μm pores. **e**, Pore-size preference of fibroblasts in pillar arrays with pores of increasing size as a function of the nucleus–MTOC polarity (5/2 μm: 2 experiments; 8/5 μm and 10/7 μm: 3 experiments). **f**, **g** Image sequence of two exemplary fibroblasts (nucleus (H2B–GFP) in cyan, EB3–mCherry in magenta, cell outlines in yellow) positioning either the MTOC (lower panel) or the nucleus (upper panel) forward, while migrating in a pillar array with 5-μm and 8-μm pores. Arrows indicate the area of highest EB3–mCherry signal (MTOC; fire colour-coded intensity) and the nucleus (cyan) (three experiments). Data in **a**, **b**, **c** and **e** are mean ± s.d.; data in **d** are mean ± 95% CI.



Extended Data Fig. 10 | See next page for caption.

Extended Data Fig. 10 | Myosin inhibition during pore decisions in DCs and nucleus-first versus MTOC-first cell polarity during pore-size decisions in neutrophils. **a**, Nuclear lobe dynamics (Hoechst stain) and MTOC localization (SiR–tubulin) during neutrophil pore-size decision (three experiments). **b**, Quantification of **a**, immediately before the decision point (3 experiments; 143 cells; one-way ANOVA with Tukey's test; $^{****}P < 0.0001$, $^{***}P = 0.0005$, respectively). **c**, Quantification of **a** during pore-size decision (3 experiments; 45 cells; paired *t*-test; $^{***}P = 0.0003$). **d**, Quantification of cells following the nuclear lobe closest to the MTOC when nuclear lobes translocate in parallel in different pores (3 experiments, 26 cells). **e**, DC migration in the presence of 50 μM *para*-nitroblebbistatin through a decision point of four pores of 2-, 3-, 4- and 5-μm wide (3 experiments). **f**, DC migration in the presence of 1 μM Y27632 through a decision point of 4 pores 2-, 3-, 4- and 5-μm wide (3 experiments). The red star highlights loss of cellular integrity. **g**, Quantification of pore preference in **e** (3 experiments, 79 cells). **h**, Quantification of passing time in **e** (3 experiments, 79 cells; Mann–Whitney test; $^{****}P < 0.0001$, $^{**}P = 0.0020$). **i**, Quantification of the passing time in **e**, depending on whether cells establish a single or multiple competing leading edges during pore decisions (3 experiments, 79 cells; Mann–Whitney test; $^{****}P < 0.0001$, $^{**}P = 0.0017$). **j**, Quantification of cellular integrity in **e** (3 experiments, 79 cells). **k**, Quantification of pore choice preference in **f** (3 experiments, 140 cells). **l**, Quantification of passing time in **f** (3 experiments, 140 cells; Mann–Whitney test; $^{****}P < 0.0001$). **m**, Quantification of passing time in **f**, depending on whether cells establish a single or multiple competing leading edges during pore decisions (3 experiments, 140 cells; Mann–Whitney test; $^{****}P < 0.0001$, $^{***}P = 0.0008$). **n**, Quantification of cellular integrity in **f** (3 experiments, 140 cells). **o**, DC passing times through the same pore sizes as in Fig. 4d, but without pore choice possibility, in the presence of 300 nM nocodazole (3 experiments, 147 cells; Kruskal–Wallis test). **p**, DC migration in a collagen matrix in the presence of nocodazole (three experiments). Data in **b**–**d**, **g**, **j**, **k** and **n** are mean ± s.d.; data in **h**, **i**, **l**, **m** and **o** are mean ± 95% CI.